5-2005

Crystallization of Random Propylene-Ethylene Copolymers at Atmospheric and High Pressures

Anita Dimeska
University of Tennessee - Knoxville

To the Graduate Council:

I am submitting herewith a dissertation written by Anita Dimeska entitled "Crystallization of Random Propylene-Ethylene Copolymers at Atmospheric and High Pressures." I have examined the final electronic copy of this dissertation for form and content and recommend that it be accepted in partial fulfillment of the requirements for the degree of Doctor of Philosophy, with a major in Polymer Engineering.

Paul J. Phillips, Major Professor

We have read this dissertation and recommend its acceptance:

Joseph E. Spruiell, Roberto Benson, John Collier

Accepted for the Council:

Carolyn R. Hodges

Vice Provost and Dean of the Graduate School

(Original signatures are on file with official student records.)

To the Graduate Council:

I am submitting herewith a dissertation written by Anita Dimeska entitled "Crystallization of Random Propylene-Ethylene Copolymers at Atmospheric and High Pressures". I have examined the final electronic copy of this dissertation for form and content and recommend that it be accepted in partial fulfillment of the requirements for the degree of Doctor of Philosophy, with a major in Polymer Engineering.

Paul J. Phillips

Major Professor

We have read this dissertation
and recommend its acceptance:

Joseph E. Spruiell

Roberto Benson

John Collier

Accepted for the Council:

Anne Mayhew

Vice Chancellor and
Dean of Graduate Studies

(Original signatures are on file with official student records)

CRYSTALLIZATION OF RANDOM PROPYLENE–ETHYLENE COPOLYMERS AT ATMOSPHERIC AND HIGH PRESSURES

A Dissertation

Presented for the

Doctor of Philosophy

Degree

The University of Tennessee, Knoxville

Anita Dimeska

May 2005

DEDICATION

This dissertation is dedicated to

my parents

Марија и Методија Димески

and

my husband

Nikola Zisi

whose love, support and patience

helped me complete this work

ACKNOWLEDGMENTS

I would like to thank my major advisor, Dr. Paul J. Phillips, for his important contributions, suggestions and guidance, and for providing me the opportunity to work on an interesting research project. Working with him has been a wonderful and rewarding experience. I would also like to thank the other committee members, Dr. Joseph Spruiell, Dr. Roberto Benson, and Dr. John Collier, for their suggestions and comments regarding my research. Special gratitude is extended to Dr. Spruiell for invaluable help on the x–ray scattering experiments and for serving as my advisor during the last year of my study. I owe a special thanks to Dr. Benson for many insightful discussions and advice. The entire Materials Science and Engineering faculty has been a great aid to my studies, and I would not have reached this point without them.

I would especially like to thank Dr. J. S. Lin for his valuable advices and discussions on small angle x–ray scattering. Dr. Alessandro Triolo of Instituto per i Processi Chimico–Fisici, Italy, is greatly acknowledged for his advice and assistance in dealing with the bimodal distributions in the SAXS data. I am also grateful to Dr. Claudia Rawn and the research staff at the HTML in ORNL for their time and help with the high temperature x–ray diffraction experiments. My appreciation also extends to Dr. John Clavier and Dr. Hongjun Pan for conducting measurements of the ^{13}C NMR data, and Dr. Marek Pyda and Mr. Tom Malgrem for performing the GPC and DSC experiments. My thanks go to Mr. Greg Jones and Dr. John Dunlap for their help with the SEM and AFM experiments.

I would also like to acknowledge Dr. Alexander VanHook and Dr. Mark Dadmun for letting me use the hot press in the Chemistry Department. Special thanks are extended to all graduate students in Dr. Dadmun's research group, especially Nathan and Deepali for their unselfish assistance.

My appreciation also goes to Sandy and Carla in the departmental office for their extreme efficiency in getting important paperwork completed and helping me with many details along the way. Both Frank and Randy were extremely helpful with ordering all the necessary equipment and supplies. This research would not be completed without the technical support provided by Mike and Greg from the electronic shop, and Doug, Larry and Dan from the machine shop.

I am thankful to all my colleagues for their moral support, friendship, and helpful technical conversations, especially to John Wagner, Xiaoping Guan, Samir Abu Iqyas, Xiaoyun Ling, Xiaolin Luo, George Jacob, Chris Stephens, and Songqing Wen. I would like to specifically mention those who I started my studies with at UT. Kislaya Gautam, Ketan Panse, Gyanendra Dutt, Yuenhong Zhang, Niraaj Khanna, and last but not least my roommate Mrunalini Dhamdhere who thought me everything I know about India.

The financial help from the National Science Foundation and Material Science and Engineering Department is highly acknowledged.

Most importantly, I would like to extend my sincere gratitude to my extended family for their constant encouragement and love, without which this would not have been possible.

Abstract

One of the main goals of the polymer research is to modify the properties of polymers in order to increase the range of their end–use applications. This is especially true in the case of isotactic polypropylene (*i*–PP). By simple modification of the molecular structure of *i*–PP with small amount of comonomer a variety of polymer grades with different characteristics can be produced. Random propylene copolymers with low ethylene content have lower crystallinity and melting temperatures than the homopolymer, as well as ability to crystallize into γ–crystal form of *i*–PP at atmospheric pressure. Isothermal crystallization of *i*–PP under high pressure can significantly affect the resulting crystallographic structures. While at atmospheric pressure it crystallizes exclusively in α–crystal from, when crystallized isothermally under high pressure a mixture of α– and γ–crystals, as well as pure γ–crystals form.

Random propylene copolymers with low ethylene content synthesized by Ziegler–Natta catalysts were used is this study to investigate their isothermal crystallization at atmospheric and high pressure. Copolymers were fractionated and their microstructure analyzed in detail by ^{13}C NMR to determine the concentration and distribution of defects since they have crucial role in the crystallization behavior and polymorphism of these copolymers.

Isothermal crystallization and melting studies showed that these random propylene-ethylene copolymers crystallize in a mixture of α– and γ–crystals. Their observed linear growth rates at atmospheric pressure were found to be dependent on the copolymer composition. Crystallization kinetic data were analyzed using the Lauritzen–Hoffman secondary nucleation theory. Copolymers exhibited two or three crystallization regimes depending on their defect content and molecular weight.

Combined DSC, WAXD and SAXS experiments were used to evaluate the copolymer crystallization models on these random copolymers. It was found that even though the exclusion model fairly well describes the behavior of copolymers with lower defect content some defect inclusion has to occur to account for the lowering of their equilibrium melting temperatures. Defect inclusion increased considerably with the increase of the total defect content in the case of copolymers.

It was shown that γ–phase content in the copolymer crystals increases with increasing defect content, crystallization temperature and pressure. Temperature-pressure-composition α–γ phase diagram of *i*–PP was constructed based on the Gibbs free energy approach. This diagram enabled the extrapolation of the equilibrium melting temperatures of both phases for defect free *i*–PP.

TABLE OF CONTENTS

SECTION **PAGE**

SECTION **PAGE**

SECTION **PAGE**

SECTION **PAGE**

List of Tables

TABLE **PAGE**

TABLE **PAGE**

List of Figures

FIGURE **PAGE**

FIGURE **PAGE**

FIGURE **PAGE**

FIGURE **PAGE**

FIGURE **PAGE**

FIGURE **PAGE**

FIGURE **PAGE**

FIGURE **PAGE**

FIGURE **PAGE**

FIGURE **PAGE**

FIGURE **PAGE**

FIGURE **PAGE**

1. INTRODUCTION

Isotactic polypropylene (*i*–PP) is one of the most important commercial polymers. Since the discovery of Ziegler–Natta catalyst systems and their subsequent industrial application, this polymer has received increasing scientific and commercial attention. The amount of interest that *i*–PP has received is due to the low cost of the monomer and polymerization techniques, it's properties, as well as the ease of fabrication.[1] The properties of polypropylene are closely dependent on its molecular structure (isotacticity, molecular weight, molecular weight distribution), which is related to the used catalyst and polymerization process. Some of it's attractive properties are high melting temperature, high chemical resistance, low density, and high strength to weight ratio. It is also a very versatile material because it can be compounded with high amount of fillers, reinforcing agents, and other polymeric materials.

The increasing use of this material for different applications requires good combination of properties over a wide temperature range. Although *i*–PP has many outstanding thermal, physical and mechanical properties, one of its disadvantages is its reduced low–temperature impact strength. One method for improving the impact properties of *i*–PP is copolymerization with other olefins, such as ethylene. The introduction of small amount of ethylene units in the macromolecular chain of *i*–PP decreases the length of isotactic segments leading to reduced melting temperature and degree of crystallinity. Random propylene copolymers with low ethylene content are commercially important materials because they have improved properties, such as improved clarity, flexibility, toughness, and melt flow rate, without seriously reducing other desirable properties.[2-5]

It is well known that *i*–PP can exist in three polymorphic crystalline forms, α–, β–, and γ–form, which can be produced using different preparation methods. α–form is the most common crystal form, that is observed for both solution and melt crystallized

samples prepared at atmospheric pressure. The metastable β–form is obtained sporadically at high supercoolings or in the presence of selective β–nucleating agents. The γ–form can be produced by using several methods, such as crystallization of low molecular weight fractions of *i*–PP, high pressure crystallization, as well as the crystallization of random propylene copolymers with low comonomer content.

Extensive study on the γ–form of high molecular weight *i*–PP with high isotacticity crystallized under high pressures was done by Mezghani.[6] With this analysis it was confirmed that the formation of γ–form is preferred at high pressures and low supercoolings (high crystallization temperatures). Additionally, the equilibrium melting temperature and heat of fusion of pure γ–form at atmospheric and high pressures was determined. Based on the melting behavior and polymorphism Mezghani calculated and constructed the phase diagram of *i*–PP, which enables the thermodynamic prediction of pure γ–form as a function of crystallization temperature and pressure.

One objectives of this study was to investigate the melting behavior, crystallization kinetics, and polymorphism of a series of fractionated random propylene–ethylene copolymers with low ethylene content at atmospheric pressure. The equilibrium melting temperature which is an essential parameter in the analysis of the crystallization kinetics was determined from Hoffman–Weeks and Gibbs–Thomson approach for both crystalline phases of *i*–PP.

Another objective of this research was to evaluate the effect of comonomer content and crystallization pressure on the development of γ–phase. It has been established that the γ–crystals preferentially form during high pressure crystallization of *i*–PP, and this study confirmed that presence of defects and high pressure enhance the formation of γ–crystals in random propylene–ethylene copolymers. Based on these results temperature–pressure–composition α–γ phase diagram of *i*–PP was constructed that enabled the extrapolation of the equilibrium melting temperatures of α– and γ–phases for defect free *i*–PP

2. THEORETICAL BACKGROUND

2.1. Polymer Morphology

The subject of polymer crystallization and morphology has received great amount of interest over the decades and still provides exciting opportunities for future research. Polymer crystallization is influenced by a range of factors such as the regularity of the polymer structure, presence of substituents, comonomers and branching. One characteristic that distinguishes polymers from other polycrystalline materials is their semi–crystallinity. It has been determined that the density of semi–crystalline polymer is between that of the fully crystalline and that of the fully amorphous polymer. Polymers that are capable of crystallizing can form ordered structures from melt or from dilute solutions. The crystallization process of polymers involves transformation of the disordered amorphous state into ordered crystalline state.

2.1.1. Models of the structure of semi–crystalline polymers

The first model that attempted to describe the semi–crystalline character of polymers was the 'fringed micelle' model by Hermann *et al.*[7] According to this model, semi–crystalline polymers consist of amorphous and crystalline regions that are 50–500 Å in size. It was proposed that since polymer molecules have long chain character they contribute to several crystalline and amorphous regions. In the crystalline regions the chain segment is aligned with segments from other polymer chains, while in the amorphous regions chain segments have random conformations. This model was able to explain the mechanical properties of semi–crystalline polymers because of the physical connections (fringes) between the crystalline and amorphous regions. However, it is

difficult to use this model for explaining the polymer morphological features, such as the radial symmetry of spherulites.

The fringed–micelle model was displaced by the chain–folding model. Evidence for a chain–folded crystals were first reported independently by Till,[8] Keller[9] and Fischer[10] in 1957. These findings were based on electron diffraction studies of lamellar single crystals of linear polyethylene grown from dilute solution. In these studies it was found that polymer chains are normal to the lamellae, which means that they are oriented parallel to the thinnest dimension of the crystal lamellae – it's thickness. Because the polymer chain length is of the order of several thousand angstroms and the typical crystalline thickness is only approximately 100 Å, it was suggested[9,11] that polymer chains must fold back and forth on themselves in an adjacent re–entering manner. In this model the nature of the folds results in a regularly folded surface, as shown in Figure 2.1.1 (a).

The adjacent re–entry folding model was subsequently challenged by Flory[12] who proposed the so–called switchboard model (Figure 2.1.1 (b)). In this model, although the folding of the molecules exist, the molecules re–enter the crystal predominantly in a non–adjacent manner, and sometimes some molecules may enter several lamellae. The resulting fold surface is somewhat irregular with loops of various lengths due to random re–entry, entanglements, etc. Another proposed model is the interzonal model (Figure 2.1.1 (c)), in which an interfacial zone exists between the ordered crystalline and disordered amorphous regions.[13]

Different crystallization conditions lead to rather different polymer morphologies, so it is reasonable to assume that polymer molecules will have different fold structures. The more realistic model for melt crystallized polymers would incorporate features of all three models, but should recognize that the chemical structure of the polymer (chain stiffness, molecular weight) and the crystallization conditions (temperature, cooling rate, stress, crystallization from melt or solution) will determine the type and frequency of the certain emergence and re-entry type.[14]

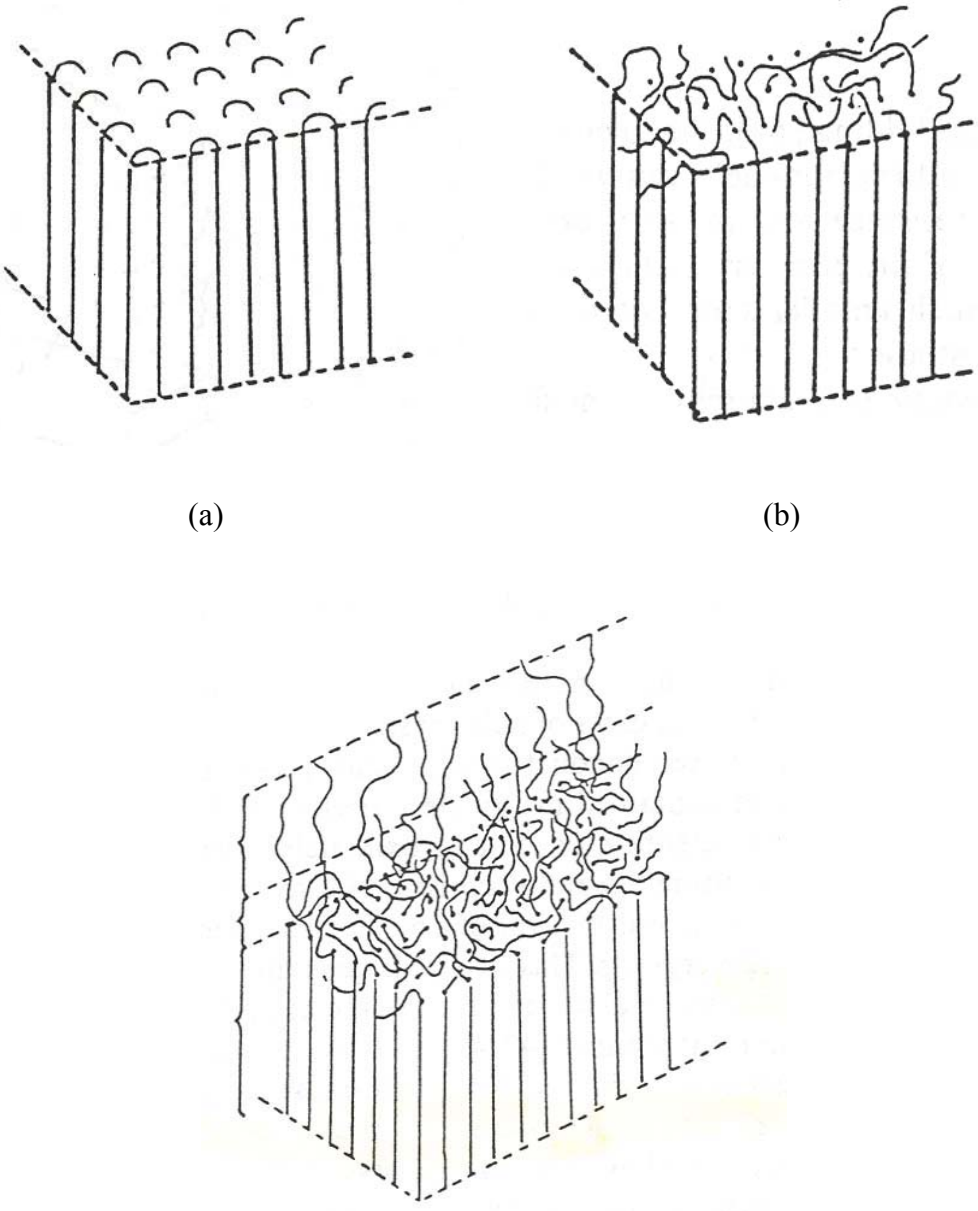

(a) (b)

(c)

Figure 2.1.1. Molecule re–entry folding models: (a) adjacent, (b) switchboard, and (c) interzonal model.[14]

2.1.2. Semi–crystalline Morphology

The most dominant morphological form of polymers crystallized from quiescent melt are spherulites. Electron microscopy data indicate that they consist of chain folded lamellae radiating outward from a central nucleus (Figure 2.1.2). The ribbon–like lamellae that make up the spherulites have thickness of the order of 100 Å, while their width is much larger – several hundreds or even thousands of angstroms. The nature of the spherulite nucleus can be heterogeneous (impurity or specially added nucleating agent) or homogeneous (polymer itself). In primary crystallization the homogeneous nucleus is considered to be composed of a sheaf–like stack of lamellae which achieves spherical shape at some finite size.[15] The radial spreading continues uniformly in all directions by the growth, branching and splaying of individual lamella until neighboring spherulites impinge on each other. The schematic representation of the growth path of the homogeneous nucleated spherulite is shown in Figure 2.1.3. Secondary crystallization occurs within the spherulite, transforming a portion of the interlamellar material into crystalline material.

The texture of spherulites can be described as (a) compact or open, and (b) coarse or fine.[15] In the compact texture, a large portion of the material within the spherulite boundary is crystallized, while in the open texture lamellae are separated by large regions of uncrystallized melt. A coarse structure refers to the texture in which bundles of lamellae have relatively large cross–sections, while a fine structure has more tenuous radial fibrils.

Another type of semi–crystalline morphology form are axialites. They can form from polymer melts under certain conditions. High crystallization temperatures and low molecular weights favor formation of axialites in certain polymers. They are crystal lamellae grouped in such a way that they resemble two slightly open books placed back to back.[16,17] These crystalline objects resemble sheaving shapes of immature spherulites.

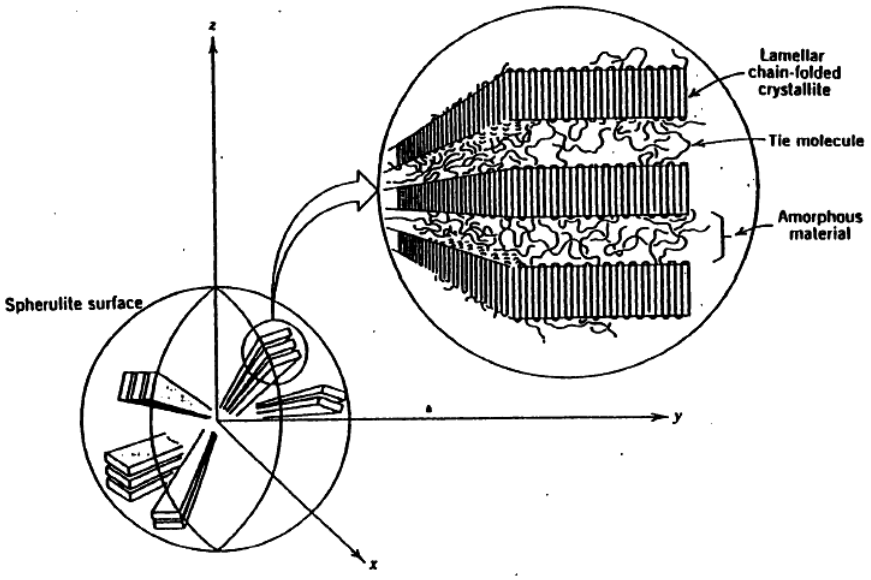

Figure 2.1.2. Schematic of a polymer spherulite with radial growth of lamellae.[18]

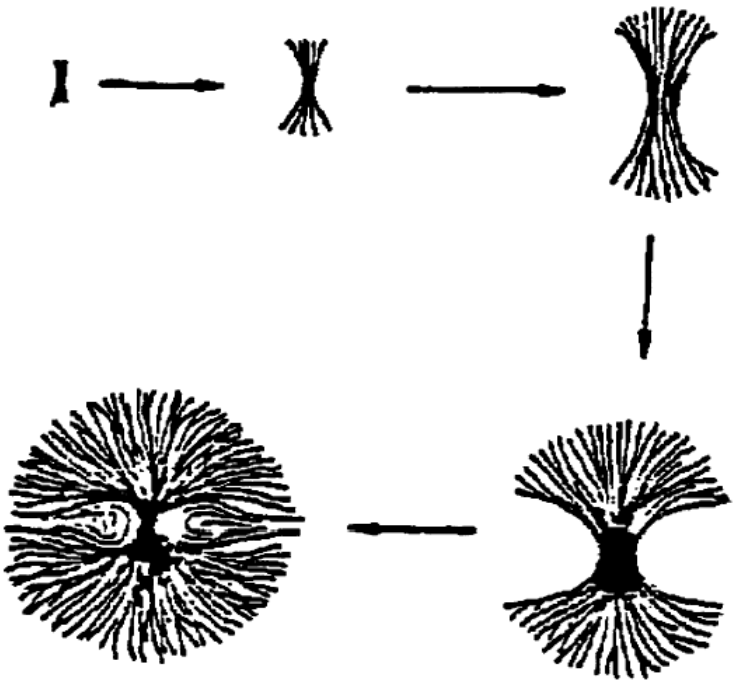

Figure 2.1.3. Schematic representation of spherulite growth path.[16]

2.2. Polymorphism in Polypropylene

Polypropylene is produced by polymerizing the monomer propylene. Prior to 1950's, propylene polymerization proceeded without any consistent addition and arrangement of the monomer units. The resulting product was branched low molecular weight oil without any practical interest.

The discovery of Ziegler–Natta catalysts for stereospecific polymerization of olefins made it possible to synthesize stereoregular polypropylene with high molecular weight which was capable of crystallizing. This breakthrough in the propylene polymerization opened the possibilities for wide range of end–use applications. Continuous improvements in catalyst systems and polymerization processes have greatly broadened its properties and utilization.

2.2.1. Isomerism of Polypropylene

The chemical structure of polypropylene is very similar to that of polyethylene, except that one of the hydrogen atoms is replaced by a methyl group on every other carbon atom. The methyl group gives a side group arrangement and handedness to the polypropylene chain. There are two different types of isomerism stemming from the way monomer unit are added to the main chain and the arrangement of the methyl groups: positional and stereo–isomerism.

Positional isomerism, also known as regio–isomerism, describes the orientation of the repeat unit when it is added to the growing polymer chain. Propylene unit can be added in a head–to–tail, head–to–head, or tail–to–tail type organization, as shown in Figure 2.2.1. A polymer chain is regio–regular when its repeat units are in the head–to–tail arrangements, while head–to–head or tail–to–tail defects cause interruptions in the regular monomer sequence in the polymer chain.

1. head–to–head

2. HEAD–TO–TAIL

3. TAIL–TO–TAIL

Figure 2.2.1. Propylene insertion mode in the polymer chain.

Stereo isomerism arises from the orientation of the methyl group in the polymer chain; whether it is in the *cis*– or *trans*–position with respect to the polymer backbone. Isotactic chains result from the addition in which the methyl groups always have *cis*–configuration, while the syndiotactic chains have *trans*–configuration. Atactic chains do not have any consistent placement of the methyl groups. Figure 2.2.2 shows the schematic illustration of isotactic, syndiotactic and atactic polypropylene chains.

2.2.2. Crystallographic Structures of Isotactic Polypropylene

Bulkiness of the methylene group in the isotactic polypropylene (*i*–PP) chain prevents the formation of planar conformation. The repulsion of the electron clouds rotates the methyl groups into a conformation with minimum energy. The resulting conformation has a threefold (3_1) helix, which can be either right– or left–handed, with the repeat periodicity of 6.5 Å and methyl group at every 120^o.[19,20] The position of the methyl group with respect to the chain axis can be either up or down. Therefore, four possibilities can occur for the *i*–PP helix in the crystalline state as shown in Figure 2.2.3. Different packing geometries of the helices lead to formation of four crystal structures: the monoclinic (α) form,[21] the hexagonal (β) form,[21-23] the triclinic (γ) form,[23,24] and the smectic form.[20] α–, β–, and γ–crystalline forms are identified with specific peaks in the x–ray pattern, as shown in Figure 2.2.4.

α–form

The structure of the most common crystal form of *i*–PP, the α–form, was first identified by Natta and Corradini.[20] They concluded that the geometry of the structure is monoclinic with unit cell parameters: a = 6.65 Å, b = 20.96 Å, and c = 6.50 Å, with $\alpha = \gamma = 90^o$ and $\beta = 99.3^o$, as shown in Figure 2.2.5.

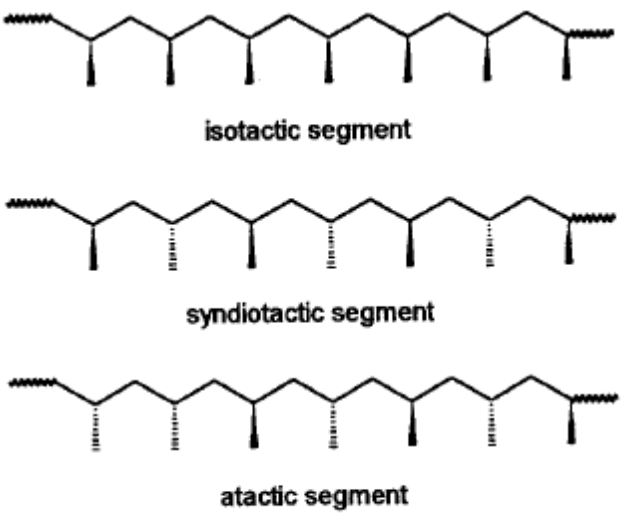

Figure 2.2.2. Schematic illustration of the stereochemical configurations of polypropylene.

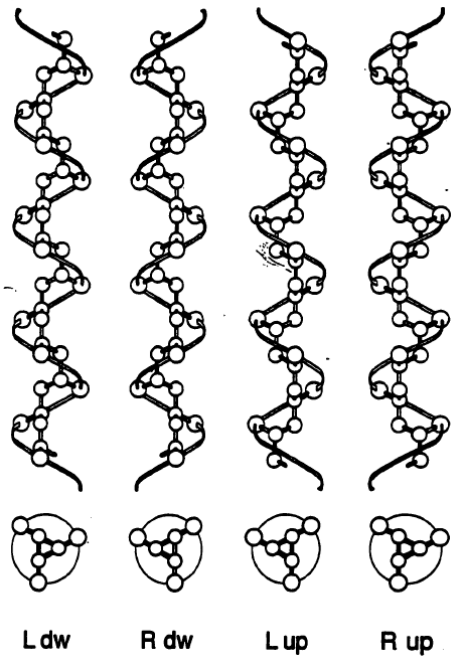

Figure 2.2.3. Chain conformations in isotactic polypropylene.

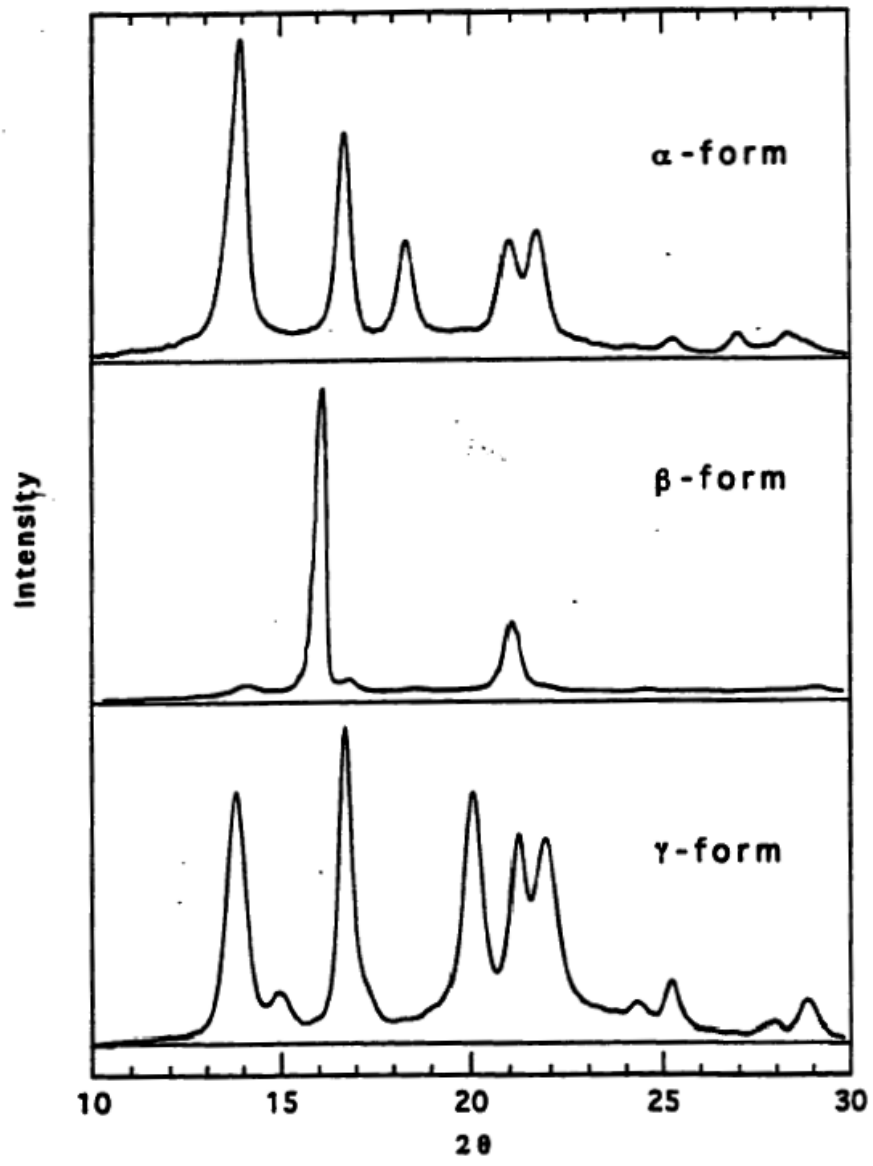

Figure 2.2.4. WAXD of different crystal structures of *i*–PP.[25]

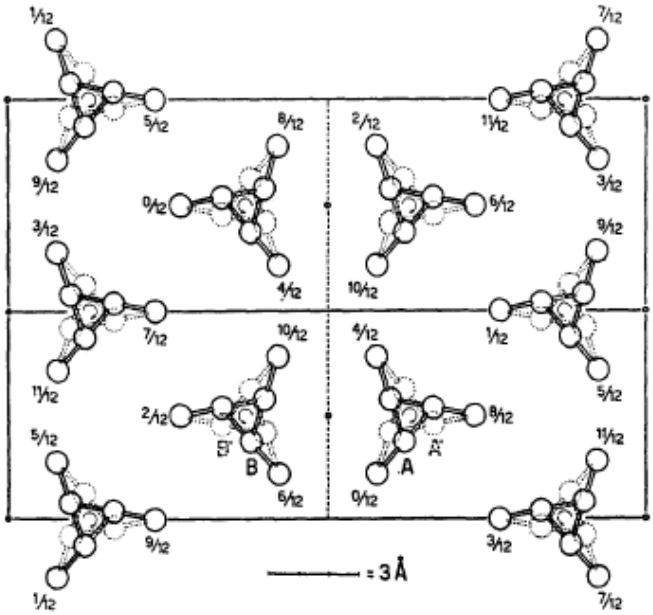

Figure 2.2.5. Crystal structure of the α–form of *i*–PP as determined by Natta and Corradini.[21]

The space group has been assigned as C2/c and Cc for the statistically ordered arrangement of up and down helices in the unit cell. This structure has been confirmed by later studies, although small adjustments to the cell parameters were made. Turner Jones and coworkers[23] proposed the following unit cell parameters: a = 6.66 Å, b = 20.78 Å, and c = 6.495 Å, with $\alpha = \gamma = 90^{o}$, and $\beta = 99.62^{o}$. Hikosaka and Seto[26] reported that α–form can be recrystallized or annealed from a less ordered α_1 form with a random distribution of up and down chain packing of methyl group to a more ordered α_2 form with well–defined deposition of up and down helices in the crystal unit cell. However, the unit cell dimensions and the arrangement of the helices in the cell remained substantially unchanged.

α–form is observed for both melt and solution crystallized samples prepared at atmospheric pressure. Several research groups have reported their findings of its morphology for a wide range of crystallization temperatures.[27-29] They classified the

spherulites into three types depending on their birefringence. Type I (α_I) spherulites exhibit positive birefringence, and can be developed at isothermal crystallization temperatures below 132 ^oC. Type II (α_{II}) spherulites have negative birefringence and exist at temperatures above 138 ^oC. However, most common type are spherulites of mixed birefringence (α_m) which do not possess distinct Maltese cross.

On a morphological level, α–form lamellae exhibit an unique lamellar branching which is very different from any other semi–crystalline polymer.[27-31] This branching is characterized by a constant angle of 80^o between the radial (parent) lamellae and the tangential (daughter) lamellae. The degree of branching depends on the crystallization temperature, as well as the tacticity of the polymer.[28,32] This behavior which results in the 'cross–hatched' morphology is found in isotactic polypropylene spherulites grown from melt or solution. The mechanism for the radial–tangential branching was explained by Lotz and Wittman[30,31] as epitaxial growth of the tangential lamella on the radial, due to crystallographic and structural interactions. The normal crystal structure, shown in Figure 2.2.5, requires that two successive *ac* layers are made up of chains with opposite handedness. If the consecutive layer has the same helical hand, then chain axes are rotated by the β monoclinic angle, and a daughter lamella is formed from this initial nucleus. Therefore, lamellar branching is a result of a 'mistake' in the strict alteration of helical hands in consecutive *ac* layers.

β–form

The metastable β–form of *i*–PP was first observed in 1959 by Keith *et al.*,[22] but hasn't been fully characterized. The difficulty of determining the crystal unit cell is due to the fact that the β form is thermodynamically and mechanically less stable than the α–form under normal crystallization conditions. These features, coupled with the substantial lower density and higher growth rate compared with the other crystalline forms of *i*–PP indicate that high degrees of disorder must exist in this structure.[33] In most

cases, the β–form can only be partially formed in samples mixed with other crystal forms. Numerous unit cell structures for β–form have been reported in the literature.[22-24,33] The simplest model proposed for β–form is hexagonal $P3_121$ with $a = b = 11.03$ Å and $c = 6.49$ Å.[33] Conditions that promote formation of rich or even pure β–form are rapid quenching,[22] zone solidification,[34] or use of selective nucleating agents.[35]

γ–form

The γ–form is probably the most interesting among crystal forms of *i*–PP. It is known that several factors can lead to the formation of the γ–form: (i) crystallization under high pressure,[36-39] (ii) crystallization of low molecular weight fractions,[24,40] (iii) slow cooling from the melt,[23] (iv) presence of chain defects or chemical heterogeneity caused by atacticity,[41] (iv) presence of the comonomer units in the chain,[42-44] and (v) melt vibration.[45]

Since the first discovery of the γ–form[22,23] its crystal structure has been considered as triclinic with the unit cell similar to that of the α–form, with a slip along the c–axis direction ($a = 6.54$ Å, $b = 21.40$ Å, $c = 6.50$ Å, $\alpha = 89^o$, $\beta = 99.6^o$, $\gamma = 99^o$).[40] However, according to Bruckner and Meille[46,47] this structure does not account for the diffraction peak at $2\theta = 24.5^o$. They noted that the triclinic cell is a sub–cell of a much larger face–centered orthorhombic unit cell with parameters: $a = 8.54$ Å, $b = 9.93$ Å, $c = 42.41$ Å. This new structure is unique in that the chain axis in the structure are not parallel. It contains sheets of parallel molecules, but the molecular orientation between adjacent sheets is nonparallel every two sheets (Figure 2.2.6). The angle between the nonparallel stems is approximately 80^o. Figure 2.2.7 represents the schematic arrangement of chain stems for γ–triclinic and γ–orthorhombic unit cells.

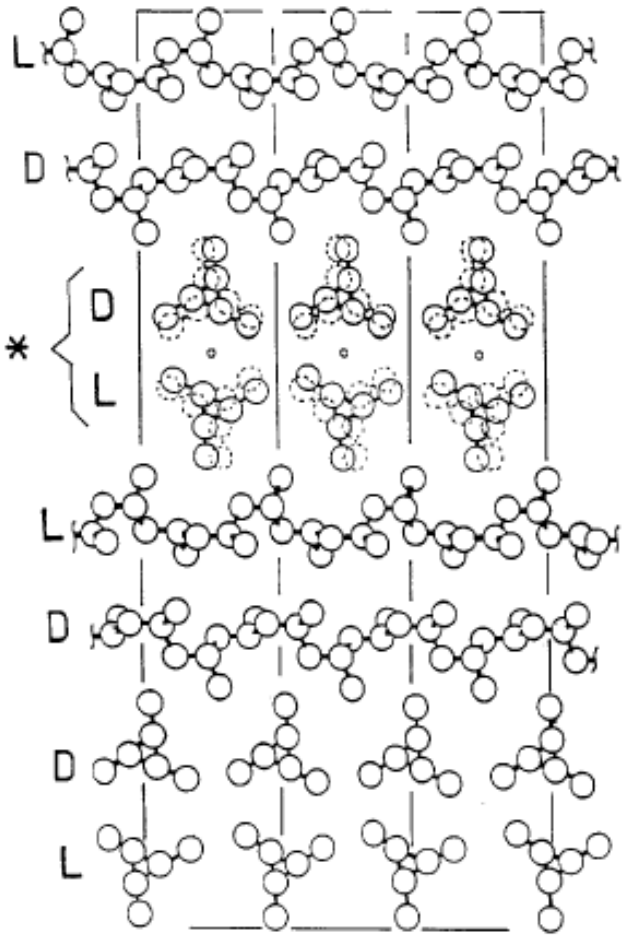

Figure 2.2.6. Projection of the γ–orthorhombic unit cell along one diagonal of the *a*–*b* plane as reported by Bruckner and Mielle.[47]

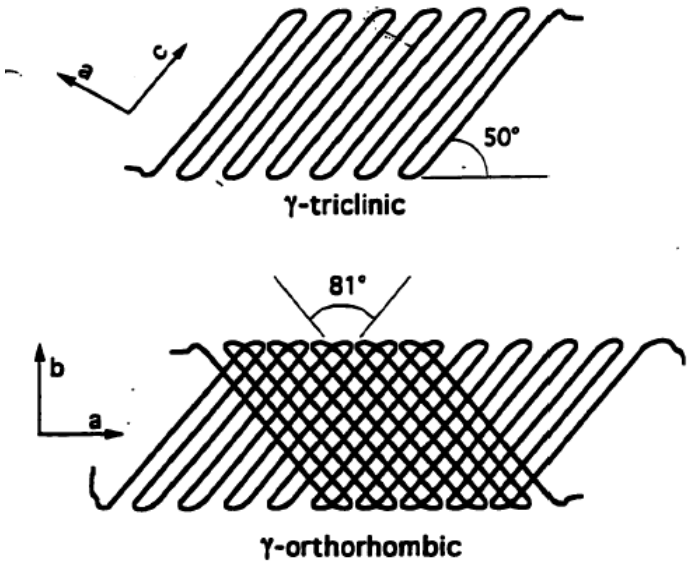

Figure 2.2.7. Schematic arrangement of chain stems in γ–triclinic and γ–orthorhombic unit cells.

On a spherulite level, studies of high pressure crystallized *i*–PP[39] indicated that similarly to the α–form, 100 % γ–form exhibits same spherulite types depending on the sign of the birefringence. Positive spherulites were observed at the lowest and highest crystallization temperatures, while negative spherulites formed at intermediate temperatures. Spherulites of the mixed type were observed at crystallization temperatures in–between positive and negative spherulites. On the lamellar level, pure γ–form that exhibited positive spherulites was composed of distinct 'feather–like' structures spreading radially from the spherulite centers. The individual lamellae in these 'feathers' were inclined at an approximate 70^{o} angle to the backbone of the feather (radial direction). SEM and AFM experiments indicated that the feather–like structure was developed by self–epitaxial growth of the γ–lamellae.

Studies of Thomann *et al.*[48] conducted on metallocene *i*–PP (M_w = 18,000 g/mol) with high content of stereo– and regio–irregularities showed that pure γ–crystals formed

mainly bundle–like structures. They argued that even in the case of samples completely crystallized in the γ–form, the morphology is widely affected by very small amount of α–phase crystals.

It has been shown that γ–form has an epitaxial relationship with the α form such that either can grow onto the lamellae of the other phase.[49,50] In general, α–form is observed to grow first followed by epitaxial growth of the γ–form at an angle of 40^{o}. The angle of 40^{o} between the daughter (γ–branch) and the parent α–lamella can be explained by the same mechanism proposed for α–α branching, that is epitaxial deposition of chains with an 80^{o} tilt with respect to those of the mother lamella. The crosshatching phenomenon that is common for the α–form has not been observed in the γ–form,[38,49,50] however, it should be noted that the process leading to branching in α–phase involves normal growth in the γ–phase.

Smectic form

Natta and Corradini[21] described this structure as 'smectic' and suggested that it is composed of parallel 3_1 helices, but that disorder exists in the packing of the chains perpendicular to their axes. The smectic form was first characterized by an intermediate order between those found in the crystalline and amorphous phases. It has been suggested that this phase is composed of very small hexagonal crystals,[51] or microcrystals of the monoclinic form.[52] On the other hand Miller[53] and Zannetti *et al.*[54] proposed that the order that exist in this form is paracrystalline. Corradini *et al.*[55] claimed that this structure cannot be described by only one type of unit cell, and that the chain correlations on the local level resemble more those of the monoclinic from, than the hexagonal form.

Smectic form can be obtained by quenching thin *i*–PP films from the melt into ice water. This form is metastable since on annealing at temperatures higher than 70 ^{o}C it transforms into the α–form. Its density is low, 0.88 g/cm^3, slightly higher than the density

of the atactic polypropylene (0.85 g/cm^3) which indicates that the smectic phase has higher molecular order.

2.3. Polymer Crystallization

The crystallization process of polymers is controlled by primary nucleation and crystal growth (secondary nucleation). Primary nucleation is the process by which molten polymer chains become aligned to form nuclei when the polymer melt is cooled down below its equilibrium melting temperature. Secondary nucleation is defined as a surface nucleation on an existing crystal nuclei growth plane, which is responsible for further growth of the activated nucleus.[56]

2.3.1. Lauritzen–Hoffman Secondary Nucleation Theory

This theory[57] and it's various modifications[58-61] represent perhaps the most comprehensive and widely used methodology to interpret and model crystallization behavior of large number of polymers. According to this theory the rate of nucleation is dependent on the crystallization temperature (degree of supercooling) which results in the observation of three regimes of crystal growth (I, II and III).

The crystal growth process is determined by two competing terms, diffusion–controlled at low crystallization temperatures, and nucleation–controlled at high crystallization temperatures.[62] The general expression of the crystal growth in the Lauritzen–Hoffman theory is expressed by the following equation:

$$G = G_0 \exp\left(-\frac{U^*}{R(T_c - T_\infty)}\right)\exp\left(-\frac{K_g}{T_c \Delta T f}\right) \tag{2.3.1}$$

where G is the observed linear growth rate, G_0 is the growth rate constant, U^* is the activation energy for polymer diffusion, R is the universal gas constant, T_c is the crystallization temperature (K), $T_\infty = T_g - 30$ (K), T_g is the glass transition temperature (K), $\Delta T = (T_m^0 - T_c)$ is the degree of supercooling (K), T_m^0 is the equilibrium melting temperature of lamellae with infinite thickness (K), and f is a correction factor for the change of the heat of fusion at high supercoolings.

$$f = \frac{2T_c}{T_c + T_m^0} \tag{2.3.2}$$

K_g is the secondary nucleation rate constant defined as:

$$K_g = \frac{j b_0 \sigma \sigma_e T_m^0}{k \Delta H_f} \tag{2.3.3}$$

where b_0 is the width of the chain, σ is the lateral surface free energy, σ_e is the fold surface free energy, k is the Boltzmann constant, and ΔH_f is the heat of fusion. j is constant depending on the operating regime; for regimes I and III $j = 4$, while for regime II $j = 2$. In Lauritzen–Hoffman theory which regime type will be observed is determined by the competition between the rate of deposition of secondary nuclei (i) and the rate of the lateral surface spreading (g) (Figure 2.3.1).

Regime I is characteristic for high crystallization temperatures (low supercoolings). Here, the rate of surface nucleation is much lower than the rate of lateral growth, $i << g$, and after the deposition of one surface nucleus the entire substrate is completed before new nucleation act occurs. The overall growth rate will be nucleation controlled and proportional to i.

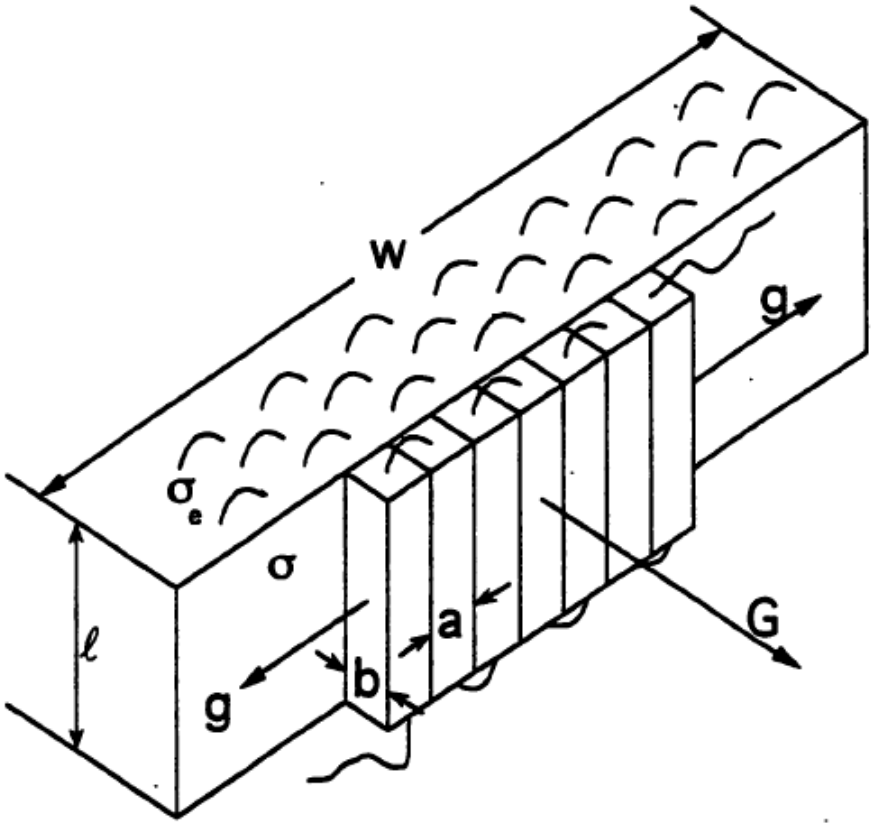

Figure 2.3.1. Schematic representation of an ideal growth front.[59]

Regime II is characteristic for moderate temperatures, where both rates of nucleation, *i*, and surface spreading, *g*, are of the same order of magnitude. This results in depositionof multiple surface nuclei on the same crystallizing surface before the previous layer is completed. The overall growth rate is proportional to $(ig)^{1/2}$.

Regime III, is characteristic for low crystallization temperatures (high supercoolings), where the rate of surface nucleation is much larger than the rate of substrate completion because of the decreased mobility of the polymer chains. The crystallization is accomplished by nucleation of stems on the surface. The overall growth rate will be diffusion controlled and proportional to *i*.

For various polymers the transition between regimes occurs at different temperatures (degrees of supercooling). A schematic diagram of polymer exhibiting all three regimes is shown in Figure 2.3.2.

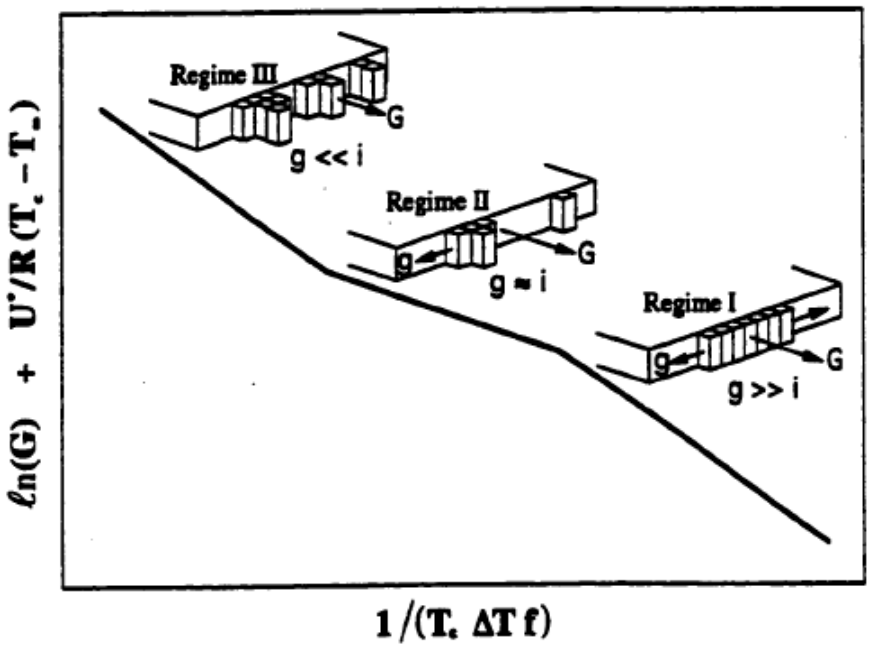

Figure 2.3.2. Schematic representation of the three growth regimes.

The slopes of regimes I and III are identical, and theoretically twice the slope in regime II, as seen from the following equations:

$$K_{g(I,III)} = \frac{4b_0\sigma\sigma_e T_m^0}{R\Delta H_f} \quad ; \quad K_{g(II)} = \frac{2b_0\sigma\sigma_e T_m^0}{R\Delta H_f} \tag{2.3.4}$$

Regime transitions for a particular polymer can be observed by plotting $\ln G + U^*/R(T_c - T_\infty)$ versus $1/(T_c \Delta T f)$. The transitions between regimes are shown as distinctive changes in the slopes on this plot as seen in Figure 2.3.2. K_g can be determined directly from the graph as the slope in particular regime, while G_0 can be estimated from the intercept which is equal to $\ln G_0$. Once K_g is known, other parameters characteristic for the crystal growth can be determined from equation (2.3.4).

The lateral surface free energy can be calculated from the Hoffman modification of Thomas–Stavely equation:

$$\sigma = \alpha \Delta H_f \sqrt{a_0 b_0} \tag{2.3.5}$$

where a_0 is the width, and b_0 is the thickness of the chain stem. For most polymers the factor α is usually 0.1.

The work, q, done by the chain to form a fold can be calculated using the following equation:

$$q = 2\sigma_e a_0 b_0 \tag{2.3.6}$$

2.3.2. Copolymer Crystallization Theories

Introducing units that are chemically or structurally different from the main repeating unit of a crystallizable homopolymer will change its crystallization behavior. Also, the concentration of the co−units, as well as their sequence distribution along the chain are of primary importance.

Random copolymers can crystallize in two extreme ways with regard to the location of the comonomer units, as shown in Figure 2.3.3, following the total exclusion or the uniform inclusion model. In the first case (Figure 2.3.3 (a)), the non−crystallizable comonomer is completely rejected from the crystal during the crystallization. Flory[63] described the exclusion model based on the equilibrium thermodynamic relationships.

In the second model (Figure 2.3.3 (b)) developed by Sanchez and Eby,[64] the comonomer is uniformly included in the crystalline phase, and the comonomer concentration in the crystal is the same as that in the initial melt. They considered that there is an excess enthalpy associated with forming the inclusion or defect in the crystalline lattice.

For an intermediate case, where the comonomer concentration in the crystal phase, X_c, is less than the overall comonomer concentration, X, the free energy of crystallization is given by:[65]

$$\Delta G = \Delta G^0 - RT\left\{\frac{\varepsilon X_c}{RT} + (1 - X_c)\ln\left[\frac{1 - X_c}{1 - X}\right] + X_c \ln\frac{X_c}{X}\right\} \qquad (2.3.7)$$

where ΔG^0 is the free energy of crystallization of the homopolymer, $\Delta G^0 = \Delta H_f^0(1 - T/T_m^0)$. T_m^0 is the equilibrium melting temperature of the homopolymer, and ΔH_f^0 is the enthalpy of fusion of the homopolymer. ε is the excess free energy of the defect created by incorporation of the comonomer unit in the crystal lattice.

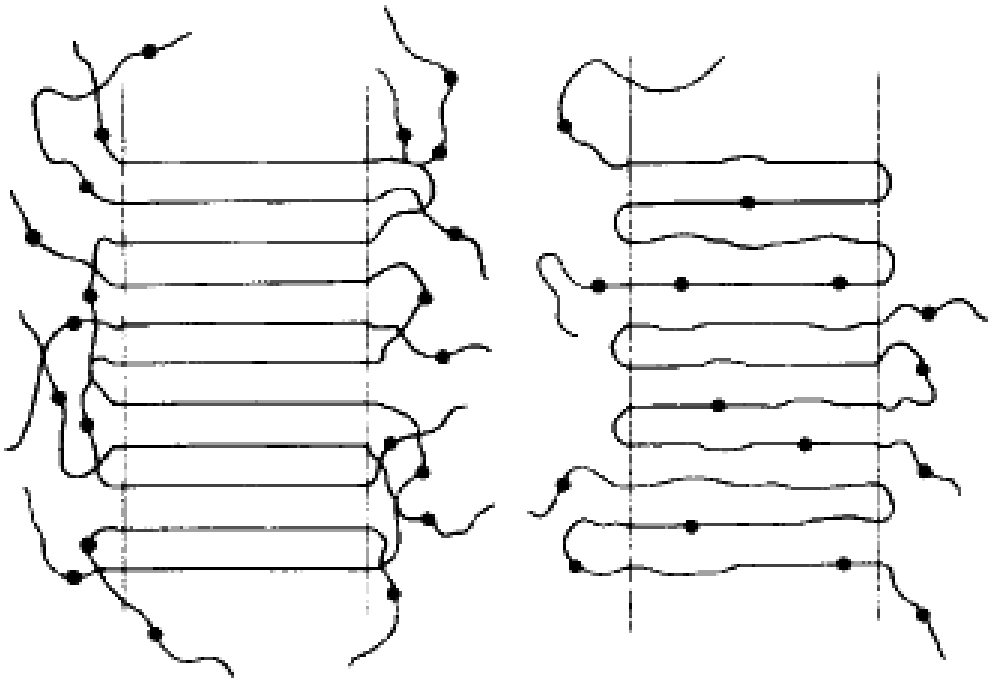

(a) (b)

Figure 2.3.3. Schematic representation of the extreme models of semi−crystalline random copolymers: (a) complete exclusion and (b) uniform inclusion model.[64]

As seen from equation (2.3.7), the free energy of crystallization consists of three terms, the first of which is an enthalpic term, while the remaining two are entropic in nature. For equilibrium condition (ΔG = 0) equation (2.3.7) yields the equilibrium melting temperature of an infinitely large crystal of composition X_c.

$$\frac{1}{T_m^0} - \frac{1}{T_m^0(X_c)} = -\frac{R}{\Delta H_f^0}\left\{\frac{\varepsilon X_c}{RT_m^0(X_c)} + (1-X_c)\ln\frac{(1-X_c)}{(1-X)} + X_c \ln\frac{X_c}{X}\right\} \qquad (2.3.8)$$

where $T_m{}^0$ and $T_m{}^0(X)$ are the equilibrium melting temperatures of the homopolymer and that of the copolymer, respectively. X and X_c are the mole fraction of the overall concentration of the comonomer in the copolymer and the mole fraction of the comonomer incorporated into the crystalline phase, respectively. R is the universal gas constant.

For complete exclusion of the comonomer units from the crystalline phase, $X_c = 0$, above equation reduces to Flory's equation:

$$\frac{1}{T_m^0} - \frac{1}{T_m^0(X)} = \frac{R}{\Delta H_f^0}\ln(1-X) \qquad (2.3.9)$$

For $X_c = X$ where all comonomer units are completely included in the crystalline lattice the equation reduces to that of uniform inclusion:

$$\frac{1}{T_m^0} - \frac{1}{T_m^0(X)} = -\frac{\varepsilon X}{\Delta H_f^0 T_m^0(X)} \qquad (2.3.10)$$

Both models predict depression of the equilibrium melting temperature of the copolymer with increasing comonomer concentration. For the inclusion model, the equilibrium melting temperature depression is caused by the lower heat of fusion resulting from the incorporation of the defects into the crystal lattice (enthalpy effect), while in the exclusion model the reason for the depression is the requirement for

preferential ordering of the copolymer chains which raises the entropy of fusion (entropy effect).

By assuming that the fold surface energy, σ_e, and the lamellar thickening at the crystallization temperature are independent of the comonomer content, Sanchez and Eby showed that the observed lamellar thickness at a given crystallization temperature increases linearly with the comonomer content, while the growth rate decreases. It should be noted that Flory's equilibrium theory also predicts that the lamellar thickness increases with the comonomer content. This seems counterintuitive for the exclusion model. However, even as the comonomer concentration increases there will still be sequences long enough to crystallize into larger thickness, although the average sequence length has decreased. This means that the lamellar thickness can increase, but here will be decrease in the crystallinity. Also, the actual thickness will be a function of the temperature, as well as of the composition.

Results from thermal analysis and x–ray crystallinity studies, in principle, can point out which model is more appropriate for certain copolymer system. If an assumption is made that the enthalpies are additive, observed enthalpies of the two models can be calculated according to the following equations:[64]

For the inclusion model:

$$\frac{\Delta H^*}{\omega_c} = \Delta H_f^0 - X\Delta H_d - \frac{2\Delta H_e}{\ell} \tag{2.3.11}$$

For the exclusion model:

$$\frac{\Delta H^*}{\omega_c} = \Delta H_f^0 - \frac{2\Delta H_e}{\ell} \tag{2.3.12}$$

where ΔH^* is the observed heat of fusion, ω_c is the degree of crystallinity, ΔH_d is an excess enthalpy associated with the formation of a defect in the crystal, ΔH_e is the excess enthalpy associated with the forming the basal surfaces of the crystal. For the inclusion model, comonomer concentration linearly affects the observed enthalpy, while the exclusion model is unaffected once the enthalpy is normalized with the degree of crystallinity.

Comonomers have been used to tailor the morphology and properties of semicrystalline polymers. It is agreed that increased comonomer concentration leads to lower crystallinity, while the melting range becomes broader and shifts to lower temperatures. Also, the presence of the comonomer remarkably reduces the rates of crystallization.

2.4. Melting of Polymer Crystals

It is known that semi–crystalline polymers do not exhibit single melting temperature, but rather a range of melting temperatures. The melting temperature of polymer crystals is controlled by several factors, among which the most important are the lamellar thickness and the surface free energies. With the increase of the lamellar thickness, polymer melting temperature also increases. Based on the Gibbs–Thomson equation for lamellae whose length is much larger than their thickness, the polymer experimental melting temperature, T_m, is defined as:

$$T_m = T_m^0\left(1-\frac{2\sigma_e}{\Delta H_f \ell}\right) \tag{2.4.1}$$

where σ_e is the fold surface free energy, ΔH_f is the heat of fusion per unit volume of crystal, and ℓ is the lamellar thickness. T_m^0 is the equilibrium melting temperature.

Equation (2.4.1) points out that the melting temperature of a thin crystal is depressed below that of the infinite crystal T_m^0 by the amount $2\sigma_e / \Delta H_f \ell$. For this equation to be used the plot of T_m versus $1/\ell$ must be linear, with T_m^0 as intercept and σ_e determined from the slope.

When the equilibrium melting temperature is estimated from experimentally determined relation between the melting and crystallization temperatures errors can occur due to the lamellar thickening. Generally it has been recognized that lamellar thickening can occur at the crystallization temperature and during the heating to obtain the melting curve.[62] Hoffman–Weeks[66,67] equation provides the relationship between the melting and crystallization temperatures:

$$T_m = T_m^0\left(1 - \frac{1}{\gamma}\right) + \frac{T_c}{\gamma} \qquad (2.4.2)$$

where γ is the thickening factor above the initial lamellar thickness ℓ_g^*.

The equilibrium melting temperature can also be determined using the Hoffman–Weeks plot, on which the observed melting temperature is plotted as a function of crystallization temperature. The equilibrium melting temperature is determined as the extrapolation of this line to the line $T_m = T_c$, while the thickening factor can be found from the slope $(1/\gamma)$ of the line. The existence of linear T_m vs T_c plot implies that the thickening factor is independent of the temperature. Also, the steeper slope in Hoffman–Weeks plot indicates that the polymer sample does not thicken as much as the one that has smaller slope. Crystals obtained at high supercoolings are thinner than those obtained from low supercoolings, therefore, it can be expected that the thickening process will raise their melting points in greater extent compared with those produced at lower supercooling. However, Mezghani *et al.*[68] demonstrated that for *i*–PP the thickening process favors thicker lamellae crystallized at low supercoolings.

2.5. Propylene–Ethylene Random Copolymers

Propylene can form copolymers with a number of other olefins, such as ethylene, 1–butene, hexene, octene, etc. Depending on the catalyst system used and the comonomer concentration, propylene-ethylene copolymers can be either semi–crystalline or amorphous rubbery materials. Crystal structures of propylene copolymers with low ethylene content (up to 30 mol%) are similar to those of polypropylene, and to that of the polyethylene for high ethylene content.[69,70]

Commercial random propylene–ethylene copolymers usually contain 1 – 7 wt% ethylene. The introduction of small amounts of ethylene comonomer units reduces the crystallinity of the copolymer, which in turn is responsible for the modification of the thermal, mechanical and processing properties compared with the homopolymer. Random copolymers have reduced stiffness and Young modulus, higher impact resistance, and much better clarity than the homopolymer.[3,5] They also have lower melting temperatures which give them advantages in some applications, such as special sealing layers in coextruded film structures. Random propylene copolymers are used in blow molding, injection molding, and film and sheet extrusion applications. They are used in food and medical packaging, as well as for consumer products.

2.5.1. Polymorphism

In the early 1970's Turner–Jones[71] showed that introducing small amount of comonomer units in the isotactic polypropylene chains promotes the formation of γ–phase crystals. This phenomenon was associated with the presence of the heterogeneity in the polypropylene chain caused by atacticity or copolymerization. The fact that copolymers used in this study contained atactic material and had broad molecular weight and comonomer distribution additionally complicated the results due to the problem with

fractionation during crystallization. The effect of atacticity on the γ–phase formation could not be separated from the copolymer effect.

Subsequent work on propylene–ethylene copolymers that did not contain atactic material,[43] or were fractionated[72-74] confirmed that there is correlation between the formation of the γ–crystalline phase and the content of short isotactic segments in the copolymer chains. It was also found that with increasing ethylene concentration a maximum is observed in the γ–phase content.[75] Most of these studies were performed at very slow cooling from the melt. For isothermal crystallization of unfractionated copolymers Mezghani and Philips[43] concluded that an important factor for the formation of γ–phase besides the presence of microstructural heterogeneities (comonomer or stereo defects) is the degree of supercooling. Lower degrees of supercooling (high crystallization temperatures) encourage the development of γ–phase crystals.

2.5.2. Inclusion or exclusion of ethylene units in propylene copolymers

One important question that needs to be answered when dealing with these copolymers is whether the ethylene units are incorporated into the crystalline phase or rejected into the amorphous region. The extent to which the comonomer units are included or excluded from the crystalline phase depends on their size, thus on the free energy change associated with vacancies or with the steric repulsion they create in the lattice structure. For ethylene–propylene copolymers it has been reported that propylene units can be accommodated into the polyethylene lattice.[76] On the other hand, in the literature there is no apparent agreement concerning the inclusion or exclusion of ethylene units from the crystal lattice of propylene ethylene copolymers.

In agreement with Flory's exclusion model, Monasse and Haudin[77] and Feng and Hay[78] reported that ethylene units are excluded from the crystal judging from the decrease of the crystallinity and melting temperature with increasing ethylene content.

Based on x–ray diffraction and thermal analysis data Zimmerman[42] also concluded that ethylene units are completely rejected from the crystalline phase. His argument was that the heat of fusion corrected with the degree of crystallinity and the difference of electron densities between the amorphous and crystalline phases do not change with increasing ethylene content. Also, he reported that dimensions of the α–unit cell are independent of the comonomer content. He concluded that the decrease of the crystallinity of the copolymers is due to the severe disturbance of helical regularity by the ethylene units.

In contrast with the findings that support exclusion model, there are many reports that propose partial inclusion of the ethylene units in the crystalline phase. Avella *et al.*[79] on the basis of the systematic contraction of the α–crystal unit cell with increasing ethylene content concluded that during the crystallization small fraction of ethylene units is incorporated as defect in the crystal lattice. However, this conclusion by the authors is somewhat ambiguous since the original data were not presented in that paper. In another study[75] of propylene copolymers with 4–20 mol% ethylene it was also found that the unit cells for both α– and γ–phase are independent of the ethylene content, suggesting exclusion. However, in the same report it was noted that the observed crystallinities are much higher than what might be expected for the complete exclusion model, therefore suggesting partial inclusion of ethylene units in the crystal.

Molecular mechanic calculations on model compounds were the basis on which Starkweather *et al*.[69] suggested that the copolymer molecule with low concentration of ethylene is equivalent to *i*–PP from which a few methyl groups have been removed. Therefore, isolated ethylene units can be incorporated into *i*–PP 3_1 helix and consequently the crystalline phase. According to these authors, with increasing ethylene concentration the propagation of the helix will depend on the randomness of the copolymer. The ethylene inclusion will be less likely to happen in copolymers with blocky character since the ethylene blocks will hinder the *i*–PP 3_1 helix.

From infra–red spectroscopy results Laihonen *et al*.[72] reported that the average length of 3_1 helices of the copolymer is shorter than that of the homopolymer, and that it

decreases with increasing ethylene concentration. Based on their results, as well as the decrease of crystallinity and enthalpy of fusion with comonomer content they reached the conclusion that ethylene unit to some extent is included in the crystals.

It can be seen from these reviewed reports that the subject of the inclusion or exclusion of ethylene units in the polymer crystals was treated indirectly using density, x–ray scattering, and thermal analysis data. More recently, two studies were published dealing with methods for direct determination of the concentration of ethylene comonomer in the crystalline phase, both of them on copolymers synthesized with metallocene catalyst systems.

Alamo and coworkers[80] implemented solid-state ^{13}C NMR technique to determine the partitioning of the ethylene defects within the semicrystalline morphology of the series of propylene copolymers with 0.8 – 7.5 mol% ethylene. They found that the concentration of ethylene in the crystalline regions increases proportionally with the overall ethylene content in the copolymer. They gave qualitative evaluation of the ethylene distribution within the crystal, as well as the crystalline/amorphous interface. This study was conducted on slow cooled samples (dT/dt = 1 ^{o}C/min), although authors expect the same behavior for isothermally crystallized samples. However, the limitations of the solid–state NMR spectroscopy include the difficulties in accurate chemical shift assignments, as well as the small differences in both the chemical shifts and relaxation time between the comonomer in the crystalline phase and in the amorphous phase, as suggested for ethylene/α–olefin copolymers.[81]

Hosoda and coworkers[82] studied the degree of comonomer inclusion in the crystal phase for a series of quenched samples of propylene copolymers with ethylene, as well as butene–1, hexane–1, and octene–1. The comonomer location was investigated using the fuming nitric acid etching technique to remove amorphous component, followed by DSC and ^{13}C NMR measurements in solution. They obtained similar results as Alamo *et al*.[80] concerning the ethylene defect partitioning. It is interesting to mention that they found that the degree of inclusion of ethylene unit in much less than that of butene–1.

2.5.3. Multiple Melting Behavior

Propylene–ethylene random copolymers exhibit multiple melting behavior analogous to that of isotactic polypropylene which has been attributed to different factors. Some researchers suggested that the multiple melting peaks are due to the partial melting and recrystallization during the heating of the sample in the DSC.[73,79] They argued that crystals grown at high cooling rates or under isothermal conditions at high supercoolings are small and imperfect; on heating these crystals will perfect and/or recrystallize thus giving rise to multiple peaks.

One other possibility that has been considered is the melting of thin and thick lamellae.[43,83] Vaughan *et al*.[83] and Weng *et al.*[84] associated the high temperature melting peak with the thicker crystals formed during the primary crystallization, while the low temperature peak to the thinner crystals that form during the secondary crystallization.

However, majority of the published studies on multiple melting associate this behavior to the presence of different crystalline phases.[72,74,85-87] The low melting endotherm is associated with the melting of the γ–crystals, and the high melting endotherm with α–crystals. These findings were supported with wide–angle x–ray scattering data at different temperatures, which show that the γ polymorph indeed melts at lower temperatures compared with α–form.

2.6. The Effects of Pressure

Hydrostatic pressure is known to affect the crystallization and physical properties of polymers. The density (or specific volume) of polymers is dependent on pressure, much more than metals and ceramics. Crystallization, melting and glass transition temperatures of polymers are also dependent on the applied pressure. Typically, the pressure dependence of the glass transition temperature is in the range of 20–75 ^{o}C per

100 MPa, and the dependence of the melting temperature is in the range of 10–95 ^{o}C per 100 MPa.[88] Other properties of polymer melts, such as melt viscosity and thermal conductivity are also affected by pressure. Crystallization under pressure may also result in a new morphology (such as chain–extended crystals) or different polymorphism (γ–phase in *i*–PP).

In 1960's the development of γ–form of *i*–PP crystallized under high pressures was observed for the first time. Kardos *et al.*[37] reported the formation of γ–form in samples isothermally crystallized, as well as slow cooled from the melt at pressures above 320 atm. With increasing pressure larger portion of the samples crystallized in the γ–form until at 5000 atm where only the γ–form was present. Sauer and Pae[89] investigated the crystal structure, thermal and melting behavior, and the morphology of the pressure crystallized *i*–PP. For all studied temperatures and pressures the material crystallized into the γ–form, which was stable for low degrees of supercooling. They suggested that for pressure–crystallized samples γ–form was the most stable one, which was also suggested by other authors.[37,90] The rate of γ→α transformation was found by Pae[91] to be a function of time and temperature. In addition, based on the DSC studies Pae noted that the γ–phase melted without conversion into the α–phase.

In a more recent study[38] on *i*–PP it was reported that with increasing crystallization pressure γ–form starts to coexist with the α–form until it becomes dominant at 2 kbar. In this study a crystallization model was proposed in which the two crystal phases are epitaxially deposited in the same lamella.

Extensive studies on the morphology and melting of the pure γ–form of high molecular weight *i*–PP with high isotacticity crystallized under high pressures were published by Mezghani and Phillips.[39,92] They confirmed that the formation of γ–form is preferred at high pressures and low supercoolings. With the purpose of answering the question why γ–form is preferentially developed at these conditions Gibbs free energy approach was used. The Gibbs free energies of both α– and γ–phase were calculated

separately as a function of temperature at constant pressure. Consequently, the phase that had lower Gibbs free energy had higher probability for nucleation and growth. Their results obtained for atmospheric pressure and 200 MPa are presented in Figure 2.6.1.

From Figure 2.6.1 (a) it is obvious that at atmospheric pressure below the transition temperature α–phase is more stable, while the range of lower free energy of the γ–phase is limited to temperatures close to the equilibrium melting temperature. On the other hand, at crystallization pressure of 200 MPa shown in Figure 2.6.1 (b), the range in which the γ–phase has the lowest free energy is significantly larger and shifted to lower temperatures. This thermodynamic prediction of pure γ–form showed good agreement with their experimental results. Based on the results for different crystallization temperatures and pressures authors calculated and constructed the α–γ phase diagram of *i*–PP as shown in Figure 2.6.2.

Foresta and coworkers[86] used the same principle of Gibbs free energy to estimate the stability of the phases in the case of *i*-PP copolymer with 3% ethylene crystallized at atmospheric pressure. Their analysis is qualitative since the parameters they used, such as equilibrium melting temperature, heat of fusion, density, and surface free energy were not experimentally determined, but rather approximated. Using the Gibbs–Thompson equation (2.4.1) and the approximate parameters, they calculated the temperature regions of stability of both phases based on the lamellar thickness, as shown in Figure 2.6.3.

In the region above the transition line γ–phase is more stable than α–phase, while below it the α–phase is more stable. Figure 2.6.3 shows that the temperature region in which the γ–phase has lower free energy is considerably larger compared with the homopolymer. The slopes of the melting and transition lines are almost the same because they assumed similar ratios of surface free energy to the heat of fusion. This diagram is consistent with the observations that the formation of γ–phase takes place at slower cooling and lower degrees of supercooling.

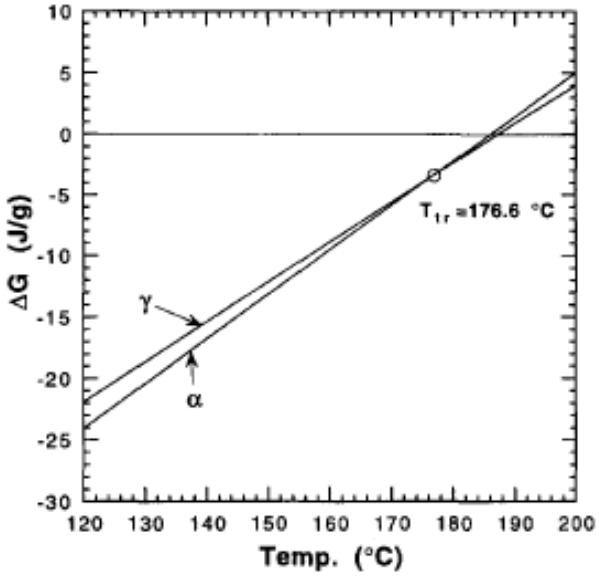

(a)

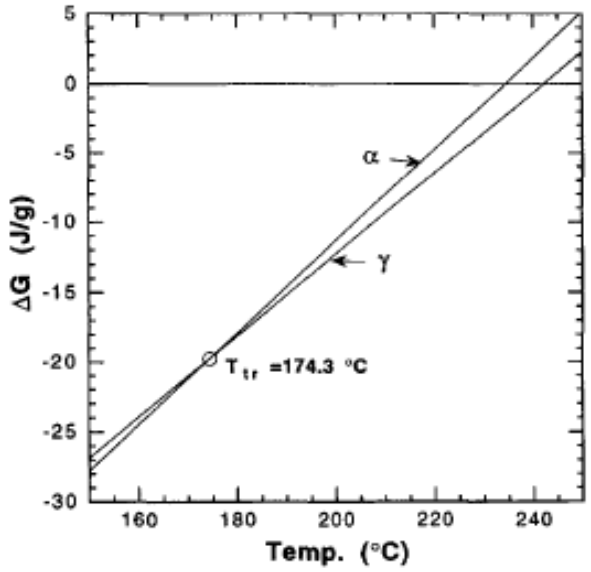

(b)

Figure 2.6.1. Gibbs free energy as a function of temperature for the α– and γ–forms of *i*–PP at (a) atmospheric pressure, and (b) 200 MPa.[92]

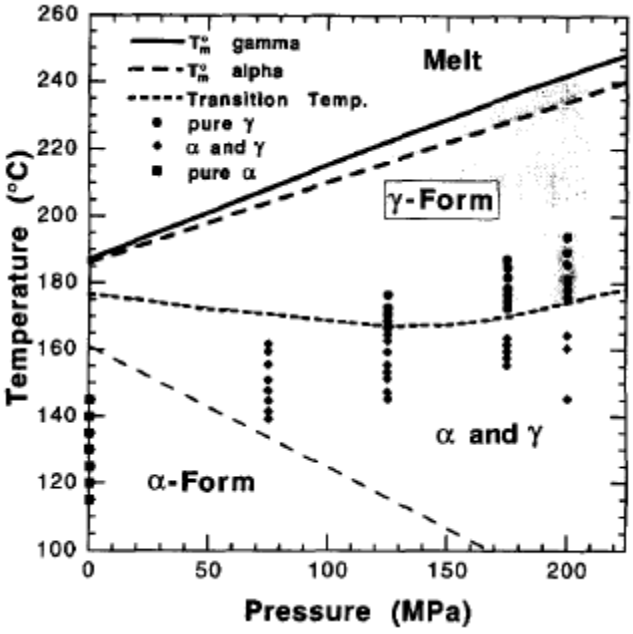

Figure 2.6.2. Theoretical prediction of pure γ–form as a function of temperature and pressure.[92]

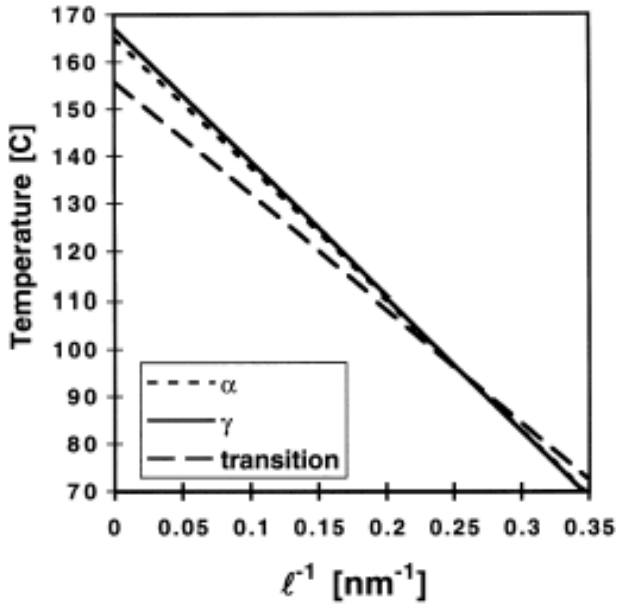

Figure 2.6.3. Schematic phase stability diagram of *i*–PP copolymer with 3 % ethylene, showing the melting lines of the α– and γ–phases, and the transition line between the two phases.[86]

2.7. Tacticity and Copolymer Content Analysis

^{13}C Nuclear magnetic resonance (^{13}C NMR) spectroscopy is an important method for materials characterization and for studying structure–property relationships of numerous polymer systems. This importance is partly due to the possibility to assign signals to specific atoms along the polymer backbone and side chains.

Chemical shift assignments are important factor to a successful analysis of the polymer structures. Oligomers and polymers with rigorously controlled structures offer the best model systems for establishing chemical shift assignments.[93,94] Also, the assignments can be calculated using empirical parameters, such as Grant and Paul parameters.[95] Some alternative additive schemes and improvements have been given in the literature.[96-98]

Chemical shift differences in ^{13}C NMR polymer spectra are related to the number, type and relative configuration of nearest–neighbor carbon atoms. The three carbon atoms nearest to the carbon of interest strongly affect the chemical shift while weaker contributions arise from carbons in the fourth and fifth positions away.[95] Therefore, using ^{13}C NMR spectroscopy the configurations up to pentads can be identified.

For polypropylene stereoregularity of the chains depends on the catalyst system used for the polymerization. It is known that polypropylenes synthesized with Ziegler–Natta type catalysts have high isotacticity, but broad tacticity and molecular weight distribution. In addition, there is a broad distribution of defects from chain to chain, and also defect distribution within the chains that differs strongly from the random behavior. It has been shown that defects are more concentrated in the molecules with lowest molecular weight.[96] Also, most heterogeneous Ziegler–Natta catalysts are highly regioselective in propylene insertion. This means that the resulting polymer does not contain regio–defects, at least in amount above the detection limit of the NMR instruments (0.1 % mol).

Figure 2.7.1 shows an example of spectra of propylene–ethylene copolymer. It is obvious that there are three sharp peaks at approximately 48, 30, and 23 ppm, which correspond to the three different carbon atoms in the propylene monomer unit, methyl, methine and methylene, respectively.

Information about the tacticity of polypropylenes can be obtained from the methyl carbon resonances at 20–23 ppm. Chemical shift assignment of ten pentads (shown in Figure 2.7.2) and statistical analysis of polypropylene stereostructure can be performed using the methyl region assignment by Busico *et al.*[96,99] The usual nomenclature is adapted from Bovey,[100] where *meso* (*m*) and *racemic* (*r*) designate consecutive monomer pairs with either like (*m*) or opposite (*r*) configurations.

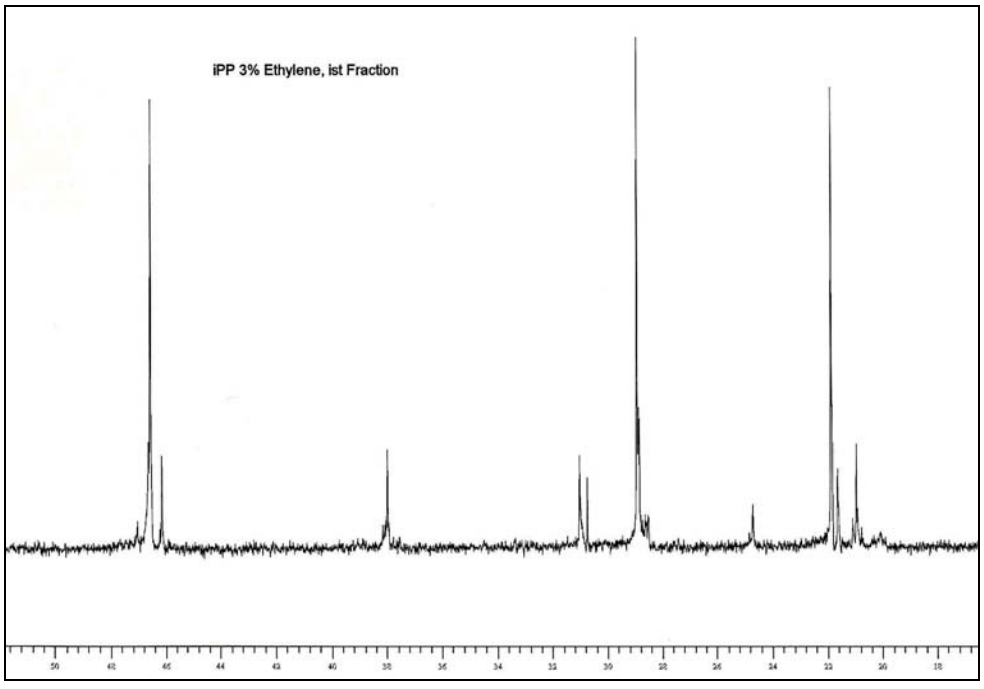

Figure 2.7.1. ^{13}C NMR spectra of random propylene–ethylene copolymer.

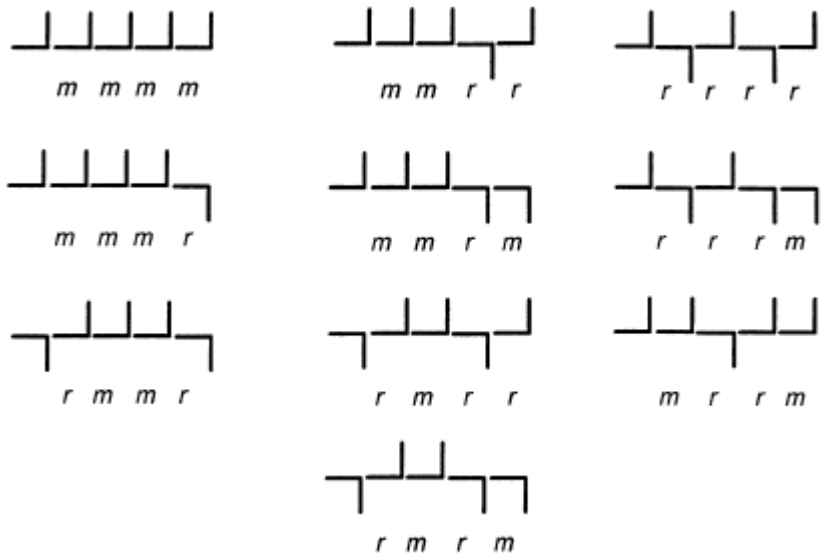

Figure 2.7.2. Schematic representation of isotactic polypropylene pentads.[96]

According to Randall,[98] number average sequence length from pentads is given by the following equation:

$$\bar{n} = \frac{rrrr + rrrm + mrrm + rmrr + rmrm + 3rmmr + 2mmmr + mmmm}{rrrr + rrrm + mrrm + ½\,rmrr + ½\,rmrm + rmmr + ½\,mmmr} \qquad (2.7.1)$$

The structure of copolymers of propylene with ethylene becomes quite complex, especially when inverted propylene units are present. ^{13}C–NMR is powerful tool for illuminating the detailed sequence structure of these copolymers. Extensive studies have been carried out on propylene–ethylene copolymers for determining the comonomer content and sequence distribution.[78,101-105]

For the interpretation of ^{13}C NMR spectra of propylene–ethylene copolymers, the monomer distribution is expressed in terms of combinations of adjacent structural units, such as dyads or triads. For example, the copolymer chain can be visualized as being derived from any one or all of the six exclusive types of triads, that is, PPP, PPE, PEP,

EEP, EPE or EEE. Knowledge of the triad concentrations, leads to the propylene and ethylene fractions, as well as their average sequence lengths.

Comonomer molar composition can be calculated as:

$$\text{ethylene}\% = \frac{[\text{E}]}{[\text{E}]+[\text{P}]} \times 100 \tag{2.7.2}$$

where [P] and [E] are the mole fractions of the propylene and ethylene units, respectively, and can be determined from triads using the relationships given by Bovey.[100]

Number–average sequence lengths of propylene and ethylene units can be determined from the triad concentrations as:

$$\bar{n}_P = \frac{[\text{PPP}]+[\text{PPE}]+[\text{PEP}]}{[\text{PEP}]+½[\text{PPE}]} \quad ; \quad \bar{n}_E = \frac{[\text{EEE}]+[\text{PPE}]+[\text{PEP}]}{[\text{PEP}]+½[\text{EEP}]} \tag{2.7.3}$$

In terms of ethylene and propylene contents, the number–average sequence length of uninterrupted methylene carbons is given by:[106]

$$n_o = 1 + 2\frac{[\text{E}]}{[\text{P}]} \tag{2.7.4}$$

2.8. Diffraction and Scattering of X–rays

Wide–angle x–ray diffraction (WAXD) and small–angle x–ray scattering (SAXS) are powerful methods for obtaining information about the internal structure of polymers. WAXD is used to determine the crystal structure of a crystalline polymer, such as the size and shape of the unit cell and the crystal space group. Additionally, WAXD is used to

determine the degree of crystallinity and crystal orientation of semicrystalline polymers. SAXS is mostly used to disclose information about a larger scale. It can be used to determine the lamellar thickness, crystal size, and radius of gyration of semi–crystalline polymers.

The basic principles of scattering for both methods are due to the scattering of single atoms. Single atom scatters an incident beam of x–rays in all directions in space. Crystals, which are regularly ordered three–dimensional periodic arrangements of atoms scatter the incident x–ray beam in relatively few directions. This happens because the periodic arrangement of atoms causes destructive interference of the scattered rays in all except those predicted by Bragg's law, and in these directions constructive interference occurs.

2.8.1. Wide Angle X–ray Diffraction (WAXD)

WAXD is frequently used for determining the crystalline structure of crystalline or semi–crystalline materials using Bragg's law:

$$n\lambda = 2d_{hkl}\sin\theta \qquad (2.8.1)$$

where n is an integer and indicated the order of diffraction, λ is the wavelength of the scattering radiation, d_{hkl} is the distance between (hkl) planes, and θ is the Bragg scattering angle.

WAXD is also used to determine the degree of crystallinity of a polymeric materials. This is the only method that directly measures the crystalline component of the polymer sample, while all other techniques measure properties related to the degree of crystallinity. However, WAXD is not an absolute method because of the arbitrary nature of constructing the baseline that defines the crystalline and amorphous scattering.

The procedure of determining the degree of crystallinity involves separating the diffraction pattern into background, amorphous and crystalline components. After the subtraction of the background, the amorphous halo is drawn underneath the prominent crystalline peaks. The degree of crystallinity is calculated from the relative areas of the crystalline and amorphous components using the following equation:

$$X_c = \frac{A_{crystal}}{A_{crystal} + KA_{amorphous}} \times 100 \qquad (2.8.2)$$

where K is typically set to unity. A_{crystal} is the area of the all crystalline peaks, and $A_{\text{amorphous}}$ represents the area of the amorphous halo. Possible errors that arise when using this method to calculate crystallinity include the uncertainty of defining the baseline and the shape and position of the amorphous halo.

2.8.2. Small Angle X–ray Scattering (SAXS)

It is well established that semi–crystalline polymers form lamellar structures that are defined as ordered structures with thickness in the range of 20 to 500 Å. Stacked lamellar structures will produce areas with electron density fluctuations due to the differences in the electron densities of the crystalline and amorphous phases. SAXS technique is sensitive to the differences in the electron density, therefore it can be used to measure the long period parameter, which represents the center–to–center distance of the stacked lamellae averaged over the entire irradiated volume of the sample. In order to apply Bragg's law to the semicrystalline polymer, the polymer should consist of parallel lamellae and have sharp phase boundary between the crystalline and amorphous phases as shown in Figure 2.8.1.

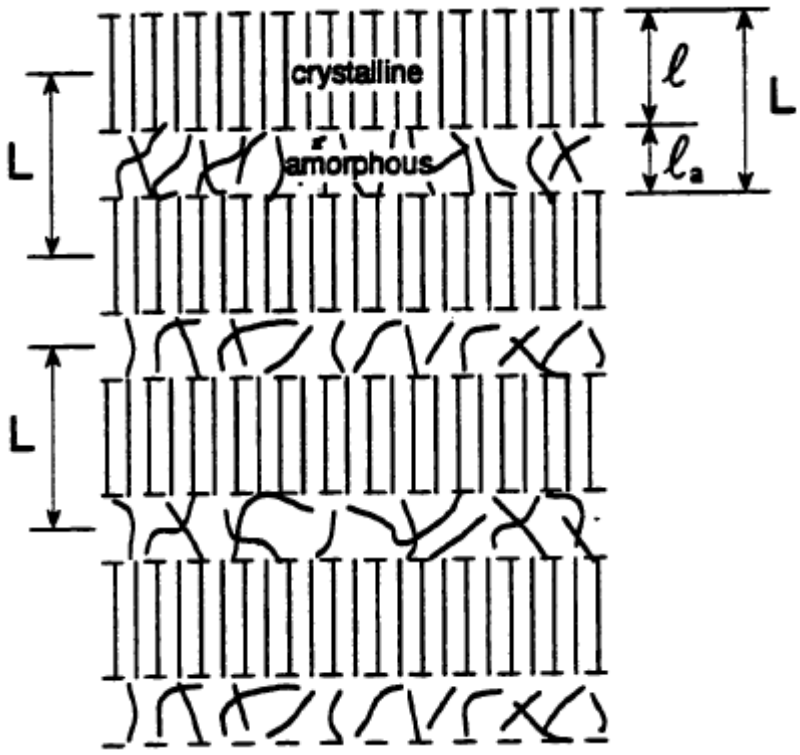

Figure 2.8.1. Crystalline and amorphous domains in two–phase lamellar structure.

The long period will have a scattering maximum where the population of spacings of a given distance occurs most often. It can be calculated by applying the Bragg's law to the intensity maximum at a specific angle using the following equation:

$$L = \frac{2\pi}{q_{\text{peak}}} \tag{2.8.3}$$

The long period value calculated from the intensity maximum obtained from the $I(q)$ versus q plot is only an estimate of the interlamellar spacing, because the thickness of the amorphous layers that separate the lamellae is not known. So, for semicrystalline polymer Lorentz correction can be applied, which requires correction of the intensity by multiplication factor q^2. According to this method, the long period can be determined from the maximum of the plot of $q^2I(q)$ versus q. The lamellar thickness, ℓ, can be obtained by multiplying the long period by the volume crystallinity.[107]

One dimensional correlation function

Assuming that the lamellae crystals are essentially flat and parallel, the Lorentz corrected scattering intensity $I_{\text{LC}}(q)$ can be related to the one–dimensional correlation function $K(z)$ defined as:

$$K(z) = \int_{\xi=0}^{\infty} \eta(\xi - z)\eta(\xi)d\xi \tag{2.8.4}$$

where $\eta(\xi)$ is the difference between the average and the local electron density, and z is the coordinate in the direction perpendicular to the surfaces of the lamellae.

The one dimensional correlation function can be obtained by Fourier transform of the Lorentz corrected scattering intensity:

$$K(z) = \frac{1}{2\pi^2} \int_{q=0}^{\infty} I_{\text{abs}}(q) \cdot q^2 \cos(qz) dq \tag{2.8.5}$$

where $I_{\text{abs}}(q)$ is the measured absolute intensity. In the case that the absolute intensity cannot be obtained, the one–dimensional correlation function can be normalized. From equation (2.8.4) it can be seen that for $z = 0$, $K(z=0)$ will be equal to the average of the square of the local electron density, and in equation (2.8.5) the cosine function for $z = 0$ will be equal to one. Therefore, the correlation function $K(z)$ can be normalized by dividing it with the correlation function at $z = 0$, $K(0)$, which is also called the invariant:

$$K_1(z) = \frac{\int_{q=0}^{\infty} q^2 I_{\text{abs}}(q) \cos(qz) dq}{\int_{q=0}^{\infty} q^2 I_{\text{abs}}(q) dq} \tag{2.8.6}$$

The invariant is the total scattering power of the sample and is defined for pinhole–collimation in the case of ideal two–phase model as follows:

$$K(0) = Q = \frac{1}{2\pi^2} \int_{q=0}^{\infty} q^2 I_{\text{abs}}(q) dq \tag{2.8.7}$$

In order to obtain the $K_1(z)$, Lorentz corrected data should be integrated in the interval ranging from $q = 0$ to $q = \infty$. However, the experimental data cannot go to zero because of the beam stop, or to infinity because of the physical limits of the two dimensional detector. Therefore, the intensity data has to be extrapolated to both low and high values of q so that the whole range is covered. For the range between zero and the lowest experimental q value, the intensity function can be approximated by a line connecting two points. For the extrapolation to infinity, usually it is assumed that the

intensity data follows Porod's law for a system with sharp phase boundaries. According to the Porod's law, the intensity $I(q)$ is directly proportional to q^{-4} as q goes to infinity, thus the plot of $I(q)$ versus $1/q^4$ will provide the proportionality constant.

The application of a graphical extrapolation procedure in the one–dimensional correlation function, $K(z)$, allows direct determination of the structure parameters such as, crystallinity, specific inner surface, average lamellar thickness, long period, and the electron density difference if the absolute values of the scattering intensities are measured.[108]

A summary of the information derived from the schematic graph of $K(z)$ is shown in Figure 2.8.2. From Figure 2.8.2 it can be observed that in the $K(z)$ curve, there is a section between $z = 0$ and $z = \bar{d}$ where the slope $dK(z)/dz$ is constant. This slope, that forms the 'self–correlation triangle' is related to the specific inner surface O_s as follows:

$$\frac{dK(z)}{dz} = -\frac{O_s}{2}(\eta_c - \eta_a)^2 \tag{2.8.8}$$

By extrapolating the slope to $z = 0$ the invariant Q is obtained:

$$Q = w_c(1 - w_c)(\eta_c - \eta_a)^2 \tag{2.8.9}$$

where w_c is the fraction of the crystalline phase, and η_c and η_a are the crystalline and amorphous electron densities.

If the $K(z)$ curve has a flat section at the first minimum, then it can be used as the base of the 'self–correlation triangle'. The baseline coordinate can be calculated as:

$$A = -w_c^2(\eta_c - \eta_a)^2 \tag{2.8.10}$$

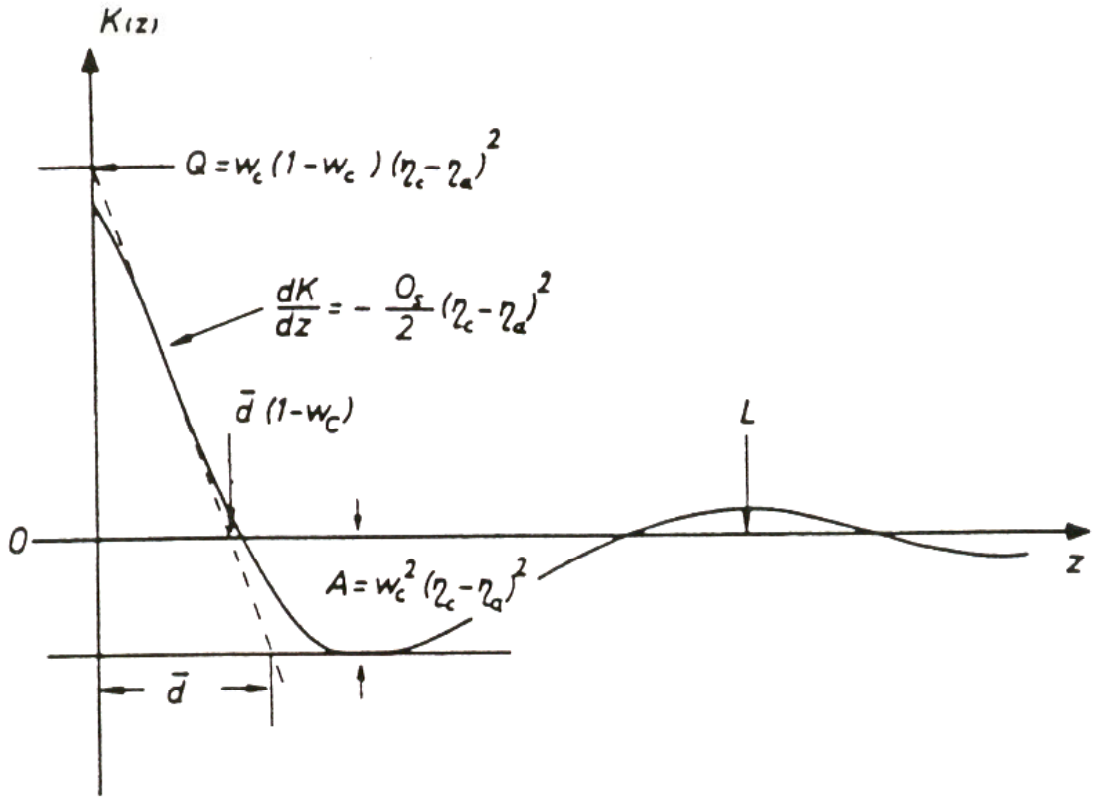

Figure 2.8.2. Schematic graph of $K(z)$ showing the 'self–correlation triangle'.

To determine the average lamellar thickness, an extrapolation of the same slope to the other side is required. The extrapolated line cuts the baseline at $z = \bar{d}$ (where $\bar{d}$ is the number average lamellar thickness) for $w_c < 50\%$, and the abscissa at $z_0 = \bar{d}(1 - w_c)$

Above method is based on absolute intensities, which require calibration with sample of known scattering power. Vonk *et al.*[107,109] developed similar method using relative intensities and the normalized one–dimensional correlation function $K_1(z)$. In this case $-A$ is equal to $-w_c/(1- w_c)$, and the value of z at $K_1(z) = -A$ remains the number average lamellar thickness $\bar{d}$. For the relative intensity method, the calculation of the value of A involves prior knowledge of the crystallinity by some other method, such as WAXD, w_{cw}. From this the SAXS crystallinity, w_{cs}, can be determined by the following equation:

$$w_{cs} + (B-1)w_{cs} - Bw_{cw} = 0 \tag{2.8.11}$$

where

$$B = \frac{1}{3} + \frac{1}{E\left(\frac{dK_1(z)}{dz}\right)_{z=E}} \quad ; \quad E = -\frac{4}{R}\left(\frac{dK_1(z)}{dz}\right) \quad ; \quad R = \frac{\int_{q=0}^{\infty} q^4 I(q) dq}{\int_{q=0}^{\infty} q^2 I(q) dq} \tag{2.8.12}$$

The value for the average lamellar thickness at A is equal to $\Delta + \bar{d}$. Δ is the correction for the width of the transition layer and is equal to:

$$\Delta = \frac{E\left(\frac{2}{3} - w_{cs}\right)}{1 - w_{cs}} \tag{2.8.13}$$

Both these methods are based on the crystallinity being less than 50%, $w_c<0.5$. The equations can be adjusted for degrees of crystallinity above 50% by switching w_c to $w_a(1- w_c)$, and η_a to η_c.

3. EXPERIMENTAL PROCEDURES

3.1. Materials

In this study two commercial random propylene copolymers with low ethylene content were used as starting materials. These unfractionated copolymers were provided by ExxonMobil Chemical Company, who also carried out their molecular characterization, details of which are listed in Table 3.1. According to the manufacturing company, the copolymers were synthesized using a slurry based Ziegler–Natta type catalyst, similar to those used in the production of linear low density polyethylenes. In the case of propylene–ethylene copolymers such catalysts produce an almost random copolymers. This result is due to the fact that propylene and ethylene comonomers have similar diffusion behaviors into the pores of the surfaces of the slurry.

Table 3.1.1. Characteristics of unfractionated propylene–ethylene copolymers.

Sample ID	Ethylene (wt.%)	M_w (g/mol)	MFR (g/10 min)
iPPu3%	3.0	300,000	4.0
iPPu5%	5.0	300,000	2.7

3.2. Fractionation

With the purpose of studying the effect of copolymer microstructure on the crystallization and polymorphic behavior of propylene–ethylene copolymers, fractions of the copolymer with different ethylene content and tacticity were obtained by fractionating the starting copolymers by direct solvent extraction.

The fractionation of the iPPu3% and iPPu5% copolymers was performed in a Soxhlet extractor using solvents with increasing boiling points. In order to achieve rapid dissolution equilibrium in the extractor, there has to be a large interface between the polymer and solvent vapor. For this, the copolymer sample was prepared in a powder form, by dissolving the copolymer pellets in xylene containing antioxidant (butyrated hydroxyl toluene 1.5 – 2 g/dm^3) at 140 ^{o}C under constant stirring. The resulting solution was cooled to room temperature, and then the copolymer was precipitated in cold methanol. The recovered copolymer was filtered using a cellulose filter and dried under vacuum until constant weight was achieved. The solvents used for the fractionation were hexanes (69 ^{o}C) and cyclohexanes (80 ^{o}C).

The schematic of the extraction–fractionation apparatus used is shown in Figure 3.2.1. It consisted of a three necked flask, Soxhlet extractor, water cooled condenser, cellulose thimble, thermometer, glass wool, glass beads and heating mantle. The sample was mixed with glass wool and placed in the cellulose extraction thimble. The purpose of the glass wool was to prevent the clumping of the swelled polymer. Glass wool was also placed on the top of the extraction thimble to prevent the direct dripping of the condensate on the copolymer sample. The thimble was placed in the insulated Soxhlet extractor, then the extractor was placed on top of the flask and the condenser was put on top of the extractor. The insulated Soxhlet extractor was capable of keeping the extraction temperature within 2 ^{o}C of the boiling point of the solvent. The extraction solvent, along with the antioxidant and the glass beads, was placed in the flask.

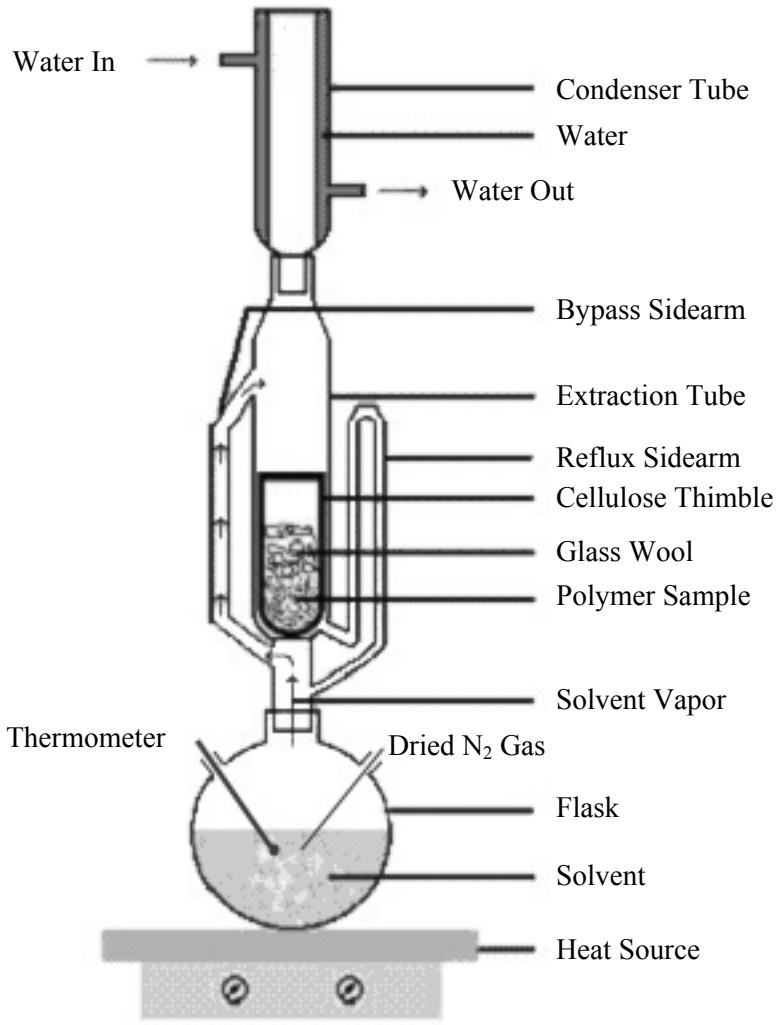

Figure 3.2.1. Schematic representation of Soxhlet extraction fractionation.

To prevent the oxidative degradation of the copolymers it is important to remove any trace of oxygen from the solution. For this purpose, in addition to the antioxidant, dried nitrogen gas was bubbled into the solvent. The solvent was brought to boil sufficiently to allow the extraction cup to fill and empty every 10 minutes. In order to achieve steady state the extraction was continued for 24–30 hours. After cooling, the copolymer fraction was recovered by precipitation in cold methanol, and then dried at room temperature under vacuum until constant weight was achieved. This procedure was carried out for both solvents, thus obtaining four fractions. Fractions were labeled according to the ethylene molar content determined from ^{13}C NMR experiments, as outlined in section 4.1. Table 3.2.1 displays the identification labels of the fractionated copolymers.

Table 3.2.1. Propylene–ethylene fractions identification.

Starting copolymer	Extraction solvent	Fraction	Sample ID
iPPu3%	hexanes	First	iPP10.45
iPPu3%	cyclohexanes	Second	iPP2.62
iPPu5%	hexanes	First	iPP15.57
iPPu5%	cyclohexanes	Second	iPP4.38

3.3. Molecular Characterization

3.3.1. Composition and Tacticity Determination with ^{13}C NMR

Ethylene concentration and triad distribution, as well as pentad isotacticity of the fractionated copolymer samples were determined by solution ^{13}C NMR spectroscopy. Samples were prepared by dissolving the copolymer fraction in *o*–dichlorobenzene to make solutions with concentration of 10% (w/v). Such high concentrations were necessary in order to obtain reasonable signal–to–noise ratio. d_6–benzene (DMSO) was used for the internal lock.

^{13}C NMR experiments were performed on a Bruker AMX–400 NMR spectrometer at 112 ^{o}C with frequency of 100.64 MHz. For all measurements an acquisition time of 2 s and pulse interval of 10 s was chosen to allow for sufficient relaxation, since it has been shown[110] that the pulse spacing should be five times the spin–lattice relaxation time of the slowest relaxing nucleus. About 1000 repetitions for each sample were used to improve the overall signal to noise ratio.

3.3.2. Molecular Weight Determination

The molecular weight of the fractionated copolymers was determined by gel permeation chromatography (GPC) at the Polymer Characterization Laboratory in the Chemistry Department at UT. Measurements were performed on Polymer Laboratories PL–GPC 220, equipped with Precision Detector PD2040 dual angle (90^{o} and 15^{o}) light scattering detector, refractometer detector, and Viscotec 220 R four capillary viscometer detector. Experiments were carried out at 145 ^{o}C in 1,2,4–trichlorobenzene as solvent. Dr. Marek Pyda and Mr. Tom Malgrem are acknowledged for these measurements.

3.4. Sample Preparation

Polymer samples were prepared as thin films in a Mettler FP52 hotstage with Mettler FP80 temperature control unit. A small amount of the copolymer was placed between two clean Kapton sheets, which were placed between two cover slips. The whole setup was heated to 190 ^{o}C for 10 minutes to ensure complete melting, followed by quenching in ice water. The sample preparation was conducted under the flow of nitrogen gas to prevent any thermo–oxidative degradation. Films with thickness of 50–100 μm were prepared for polarized light microscopy studies, while for WAXS and SAXS studies thicker samples were prepared by isothermal crystallization.

Thick film samples of the fractionated copolymers with thickness ranging from 0.5–1 mm were prepared using a Wabash Hydraulic Press. The polymer sample was placed between Kapton sheets, which in turn were placed between two chrome coated stainless steel plates. The temperature was raised to 190 ^{o}C, and after 15 minutes of melting the pressure was applied. The molten sheet of sample within the plates was taken out of the hot press and quenched in ice water. The thickness of the film was controlled by the melt temperature and applied pressure.

3.5. High Pressure Experiments

Copolymer polymorphism studies were carried out on thick film samples prepared by isothermal crystallization in a custom piston–cylinder type high pressure cell, shown in Figure 3.5.1. The whole high pressure experimental setup is shown in Figure 3.5.2. High pressure crystallization was performed on copolymers iPP2.62 and iPP4.38.

A Carver hydraulic press equipped with heated platens was used in this experiment. The press capacity was 110 kN. Two 15 x 15 cm, 5 mm thick steel plates were placed on both sides of the high–pressure cell to prevent damage of the press

Figure 3.5.1. High–pressure cell components.

① Carver Hydraulic Press

② High–Pressure Cell Assembly

③ Press Temperature Controller

④ High–Pressure Cell Temperature Controller

Figure 3.5.2. High–pressure isothermal crystallization experimental setup.

platens by the cell pistons. The cell cylinder and the pistons were made of VascoMax 300 CVM maraging steel, which was heat–treated to a hardness of 55 Rockwell C. The dimensions of the cell were 63.5 mm × 38 mm (diameter × height), and a 25.4 mm diameter hole was bored through the cell to fit the pistons and the sample. A hole with 1.5 mm diameter was bored at the center of the cell's wall to a depth of ½ of the cell height (19 mm) for temperature measurement. The clearance between the cell and the pistons was 25 μm. The whole cell was designed to take pressures of up to 1,000 MPa and temperatures beyond 300 ^{o}C. Thick copolymer sample was placed in the cell between two tightly fitting teflon spacers that were used to provide the initial sealing at lower pressures. Brass delta rings were put on the pistons to seal the cell at high pressures.

The heating of the cell was accomplished primarily by a mica band heater, which was clamped on an aluminum ring that tightly fitted the outside of the cell. The temperature of the cell was measured by an Omega K–type thermocouple, and it was controlled through an Omega temperature control unit. The press' platens were used as a secondary heater. The temperature of the top platen was measured by a thermocouple, and the temperature of the both platens was controlled through Bernant temperature controller. Insulation surrounding the cell was used to improve the temperature stability.

After the sample was properly mounted into the cell, the cell assembly was placed between the press platens and heated to an appropriate melting temperature for a time sufficient to ensure complete melting, typically 15 minutes. The cell temperature was then lowered to the desired crystallization temperature. The pressure was applied after the crystallization temperature was stabilized. Sufficient time was provided to ensure complete crystallization of the sample under constant pressure and temperature. Afterwards the temperature of the cell was lowered to room temperature and the pressure was released.

3.6. Differential Scanning Calorimetry

The melting behavior of the samples was obtained using TA Q1000 V7.3 differential scanning calorimeter (DSC). The temperature and heat capacity calibrations were performed with pure standards. Pure indium standard was used for temperature calibration, while sapphire standard was used for heat capacity calibration. In all melting experiments, the heating rate in the DSC was 10 ^{o}C/min, unless otherwise stated. Peak temperature was chosen as the melting temperature.

Samples were melted at 190 ^{o}C for 10 minutes, then quenched to the crystallization temperature, and after the isothermal run was completed they were melted from the crystallization temperature. Peak temperature was chosen for the melting temperature. Melting curves of samples isothermally crystallized under the same conditions in the hot stage and quenched in ice water were also obtained.

3.7. Polarized Light Microscopy

Polarized light microscopy (PLM) studies were carried out in order to determine the linear growth rates of the copolymer samples at atmospheric pressure. For this purpose a Mettler FP82 hot stage mounted on an Olympus BX50 polarizing microscope, equipped with a Sony video camera, was used. The hot stage was calibrated with standard substances which undergo sharp melting around the temperature range of interest. The sample was melted at 190 ^{o}C for 10 minutes to erase its thermal history. Then, the sample was rapidly transferred to another calibrated hot stage preset to the desired crystallization temperature, and crystallized at that temperature for an amount of time that allows complete crystallization. The melting and crystallization studies of the samples were performed under a nitrogen atmosphere to prevent any thermo–oxidative degradation. The process of crystallization was recorded either by the Sony video camera on an

accompanying VCR (for fast crystallization rates) or by an Olympus 35 mm film camera (for slow crystallization rates).

For the growth rate determination, the radii of the growing spherulites were measured as a function of crystallization time. These measurements were made on at least five spherulites per crystallization temperature. Linear growth rates were obtained as the slope of the plot of the average spherulite radius versus time using the least square method. The linear growth rate data were further analyzed using the secondary nucleation theory of Lauritzen and Hoffman.

3.8. Wide Angle X–ray Diffraction

Wide–angle x–ray diffraction (WAXD) studies were conducted on a Philips X'Pert Plus Diffractometer in the reflection mode, with CuKα radiation of an X–ray source operated at 40 kV and 45 mA. The patterns were acquired from $2\theta = 5$ to 35^{o} with a step size of 0.02^{o} and scan rate of 0.2 ^{o}/min. Experimental data were analyzed with Philips X'Pert Plus and Philips Profile Fit analysis software provided with the Philips system. Peak assignment given by Bruckner and Meille[46] was used for the γ–phase, while assignments given by Turner *et al*.[23] were used for the α–phase.

To calculate the degree of crystallinity it is necessary to separate the amorphous halo from the crystalline reflections. The method described by Natta *et al*.[111] was applied for the defining and extraction of the amorphous halo. The Profile Fit software was used to fit the amorphous halo by scaling the intensities of the 2θ regions at 10, 16.3 and ~30^{o}. The same standard plotting procedure was used for both atmospheric and high pressure crystallized samples. An example of the plotting procedure is shown in Figure 3.8.1. The degree of crystallinity of the copolymers was calculated from the relative areas of the amorphous and crystalline peaks according to the equation (2.8.2).

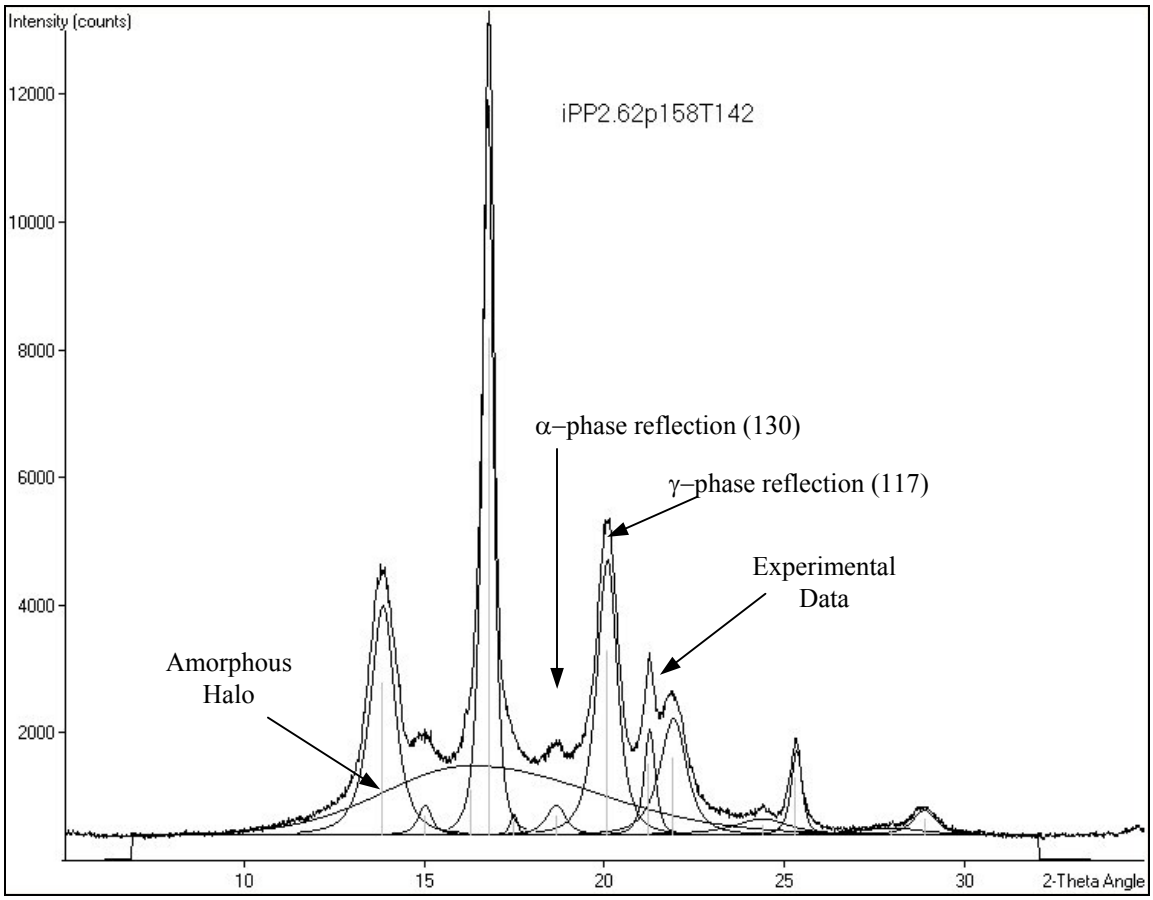

Figure 3.8.1. X–ray diffractogram of propylene–ethylene copolymer.

The fraction of the γ–form of each sample was determined from the heights of the (117) Bragg peak of the γ–form and the (130) Bragg peak of the α–form according to the method given by Turner–Jones[71] and the equation (3.8.1):

$$\gamma\% = \frac{I_{117}}{I_{117} + I_{130}} \times 100 \qquad (3.8.1)$$

To determine the presence of different crystalline phases as a function of temperature, high–temperature WAXD (HTWAXD) experiments were conducted at Oak Ridge National Laboratory. The HTWAXD data were collected using a PANalytical X'Pert PRO MPD θ – θ diffractometer with an Anton–Paar XRK–900 high temperature stage. The diffractometer was equipped with an X'celerator detector that allows ultrafast data collection. The data were collected using Cu K_α radiation at operating voltage and current of 45 kV and 40 mA, respectively. Data were collected between 10–25° (2θ) with a count time of 30 s so that each scan took less than 5 minutes.

3.9. Small Angle X–ray Scattering

Small angle x–ray scattering (SAXS) measurements were performed on Molecular Metrology SAXS system. It consists of monochromatic x–ray source, three pinholes, two sample chambers, and a two dimensional detector. The x–ray generator was a copper microfocused x–ray beam, normally operated at 45 kV and 0.66 mA. The sample–to–detector distance (SDD) for the first sample chamber was 1.5m, and 0.5 m for the second sample chamber. SAXS experiments on this system can be performed under room temperature as well as high temperature of up to 300 ºC.

The scattering vector, q (nm^{-1}), at SDD = 1.5 m was in the range 0.07 – 1.5 nm^{-1}. Also, in order to obtain higher scattering vector q, SDD = 0.5 m whose q range is 1.0 – 5.0 nm^{-1} was used.

3.9.1. Raw Data Treatment

The MPA–3 Server and MPANT program (from Fast ComTec) record the scattering intensity at each pixel of the two dimensional area detector. The SAXS software written in Matlab (from Molecular Metrology) was used for pattern analysis. With this program, raw experimental data were corrected for the background, and converted from pixels to quantum units. The data output from this program is the scattering intensity of the sample, $I_{s,}$ versus the scattering vector, q. Correction of the scattering data was carried out to eliminate the effects associated with the background air scattering and the electronic noise in the detector (dark current). Also, absolute intensity factor correction was essential for performing correct splicing of the two SSD data, as well as obtaining the net corrected absolute scattering intensity (cm^2/cm^3). In order to make this correction first the transmission coefficient, $T_{m,s}$, of each sample has to be determined. For this, the intensity of the sample, the intensity of the x–ray beam without a sample (empty beam), as well as the intensity with no x–ray beam (dark current), have to be measured for each sample. The transmission coefficient of the sample was calculated with the following equation:

$$T_{m,s} = \frac{I_s - I_{dc}}{I_{mt} - I_{dc}} \tag{3.9.1}$$

where I_s, I_{mt}, and I_{dc} are the scattered intensity of the sample, empty beam and dark current, respectively.

Then, the absolute intensity factor, F_{abs}, used to convert the scattering intensity into absolute units was obtained using two different secondary standard materials. In the case of 1.5 m geometry S-2907 standard ($T_{m,std}$ = 0.538, thickness = 1.713 mm) was used. It's absolute intensity factor was found from the maximum intensity, corrected for the standard transmission factor, thickness and time, and the equations (3.9.2) and (3.9.3).

$$F_{\text{abs}}(1.5\text{m}) = \frac{I_{\max}(q)}{\left(\frac{d\Sigma}{d\Omega}\right)_{\text{peak}}} \tag{3.9.2}$$

$$\left(\frac{d\Sigma}{d\Omega}\right)_{\text{peak}} = 24.5 \text{ cm}^{-1} \tag{3.9.3}$$

where $(d\Sigma/d\Omega)_{\text{peak}}$ is the scattering cross–section per unit volume obtained by calibration against the primary standard.

For the 0.5 m geometry, a glassy carbon GC–UTK ($T_{\text{m,std}}$ = 0.463, thickness = 1.044 mm) was used as secondary standard. The F_{abs}, was obtained from the ratio of the intercept of the linear region (2 nm^{-2} < q^2 < 12 nm^{-2}) in the Debye–Bueche plot ($1/\sqrt{I(q)}$ versus q^2) to the known $I(q=0)$= 3.805 cm^{-1}.

The scattering intensity of the sample was corrected for the transmission coefficient, sample thickness, scanning time and the absolute intensity factor, by multiplication with the correction factor calculated by the equation (3.9.4):

$$CF = \frac{1}{T_{\text{m,s}} \times th_{\text{s}} \times t \times F_{\text{abs}}} \tag{3.9.4}$$

where $T_{\text{m,s}}$ is the transmission factor of the sample, th_s is the sample thickness in mm, t is the scanning time in seconds, and F_{abs} is the absolute intensity factor calculated for the standard in cm^2/cm^3. Which F_{abs} was utilized depended on the type of geometry used to measure the scattering intensity.

3.10. Scanning Electron Microscopy

The morphology of the copolymer samples crystallized at atmospheric and high pressures was studied using the scanning electron microscopy (SEM). SEM pictures were taken on a LEO 1525 field emission high–resolution scanning electron microscope. This electron microscope is designed to run at high vacuum and low electron beam voltages. This limits the damage to the polymer samples by the electron beam, and reduces the possibility of charging the sample, even at high magnification. Because of this there is no need of sample coating to get pictures, however, to avoid charging at very high magnifications some of the samples were lightly coated with gold. The gold coating was approximately 3 nm in thickness. Prior to the SEM experiments all samples were etched for 30 minutes in permanganic acid solution, according to procedure published in the literature for polyolefins.[112]

4. RESULTS

4.1. NMR

The ^{13}C NMR spectra of the four propylene–ethylene copolymer fractions positioned from front to back according to decreasing ethylene content are shown in Figure 4.1.1. The spectra for all four fractions contain three sharp peaks at approximately 47 ppm, 29 ppm, and 22 ppm, which correspond to the three different carbon atoms in the propylene monomer unit, methylene, methine and methyl, respectively.

The nomenclature of Carman and Wilkes[113] was adopted for the ^{13}NMR peak assignments, where the primary (methyl), secondary (methylene), and tertiary (methine) carbon atoms were designated as P, S, and T, respectively. Two Greek subscripts indicate the carbon atom distances in both directions from the nearest tertiary carbons (methine carbon bearing a methyl group). Few typical structures with the used nomenclature are given in Figure 4.1.2.

Because of the high resolution of the measured spectra, it was possible to assign pentad or hexad sequences[114] to the NMR peaks for each of the copolymer fractions. Chemical shift assignments for different carbon atoms in the copolymer chains are listed in Table 4.1.1. The pentads and hexads were expressed in terms of dyad and triad using the relationships given by Bovey.[100]

Freeware software MestRe–C[115] was used to analyze the experimental data. The obtained results in terms of the chemical shifts and peak areas of the fractionated copolymers in the ^{13}C NMR spectra are given in Table 4.1.2.

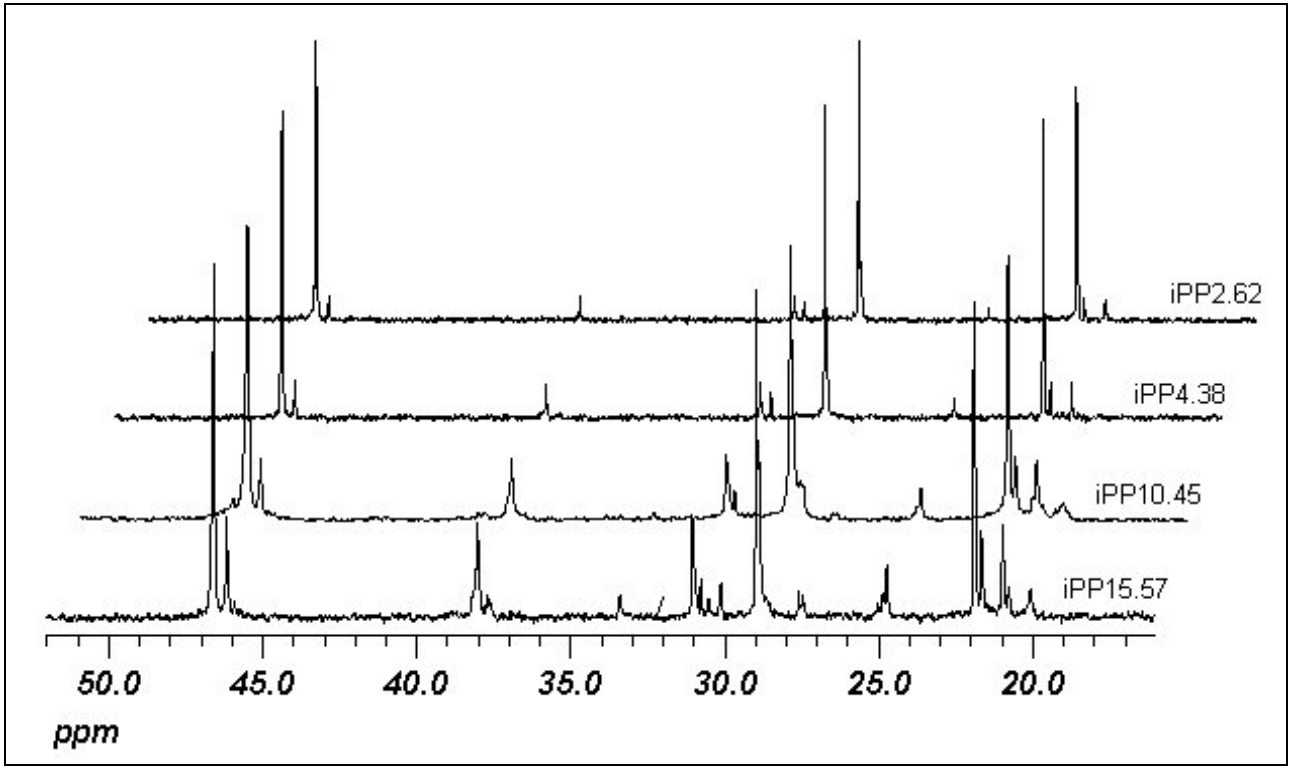

Figure 4.1.1. ^{13}C NMR spectra of the fractionated propylene–ethylene copolymers.

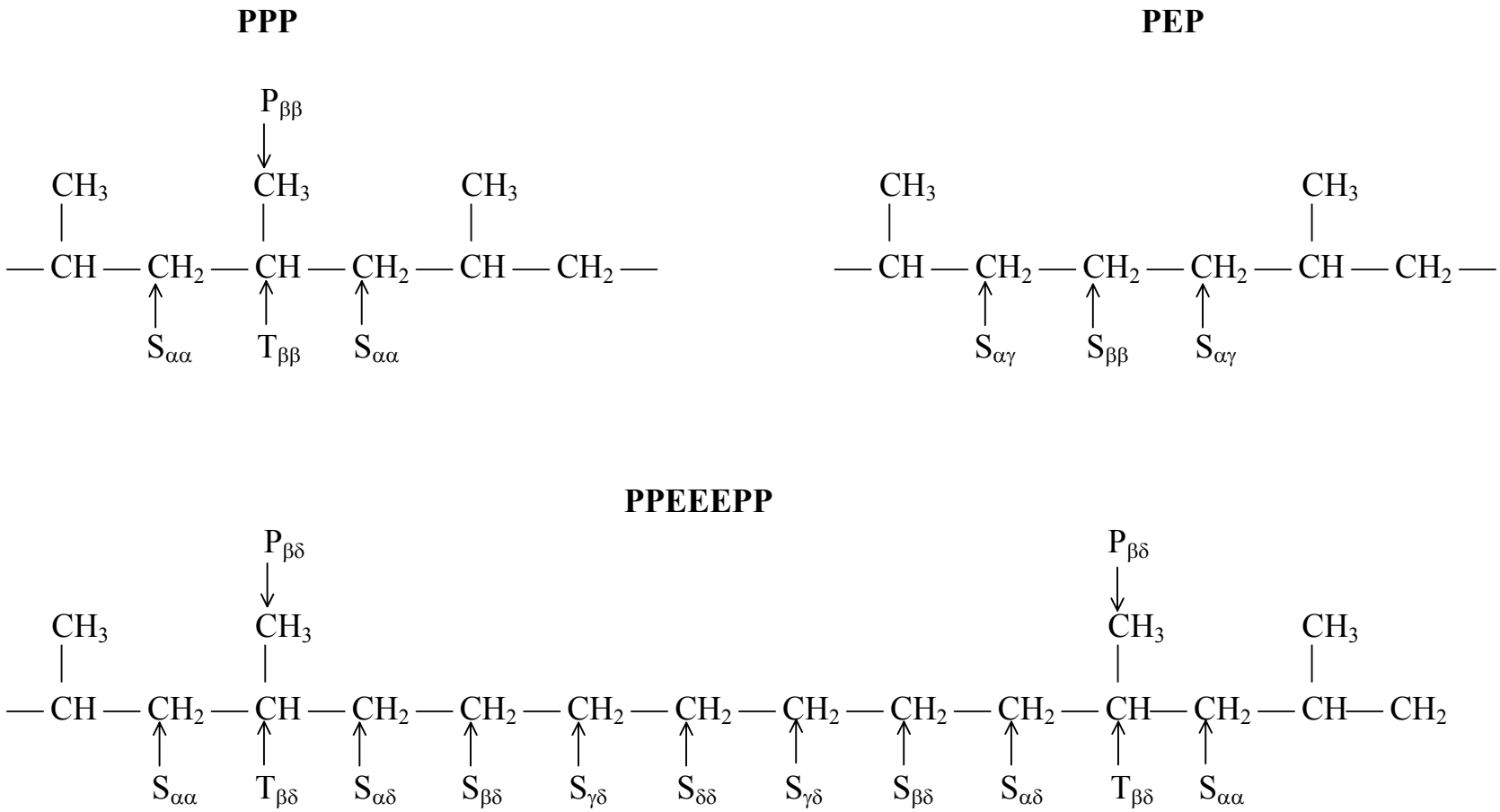

Figure 4.1.2. Nomenclature used for the methyl (P), methylene (S) and methine (T) carbons of propylene–ethylene copolymers.

Table 4.1.1. Chemical shift assignments in propylene–ethylene copolymers.

Carbon type	Chemical shift[a] (ppm)	Sequence
$S_{\alpha\alpha}$	46.8–45.8	PPP
	46.66	PPPPPE
	46.60	PPPPPP
	46.26	PPPPEE
	46.17	PPPPEP
	45.92	PEPPEP
$S_{\alpha\gamma}$	38.4–37.9	PEP
	38.2	EPPEPP
	38.12	EPPEPE
	38.08	PEPEPP
	38.02	PPPEPP
	37.97	PPPEPE
$S_{\alpha\delta}$	37.6–37.7	PEE
	37.69	PPPEEP+PPPEEE
$T_{\delta\delta}$	33.40	EPE
$T_{\beta\delta}$	30.7–31.1	PEPP
$S_{\gamma\gamma}$	30.77	PPEEPP
$S_{\gamma\delta}$	30.54	PPEEEP
$S_{\delta\delta}$	30.13	PEEEP
$T_{\beta\beta}$	29.0–28.8	PPP
	28.98	PPPPP
	28.90	PPPPE
	28.84	EPPPE
$S_{\beta\delta}$	27.6–27.4	PEE
	27.60	EPEEP
	27.46	PPEEP
$S_{\beta\beta}$	24.6–25.1	PEP
	25.03	EPEPE
	24.86	PPEPE
	24.74	PPEPP
$P_{\beta\beta} + P_{\beta\delta}$	21.9–21.8	mmmm
	21.7–21.6	mmmr
	21.03	mmrr
	21–20.9	mrmm
	20.8	mrmr
	20.12–20.05	mrrm

a) The chemical shift scale is in ppm downfield of DMSO.

Table 4.1.2. Chemical shifts and peak area for fractionated copolymers.

Carbon type	Peak Area, %			
	iPP2.62	iPP4.38	iPP10.45	iPP15.57
$S_{\alpha\alpha}$	47.79	28.10	41.75	38.02
$S_{\alpha\gamma}$	2.65	2.62	7.59	10.31
$S_{\alpha\delta}$	0	0	1.67	2.48
$S_{\beta\delta}$	0	0	1.67	2.48
$S_{\gamma\delta}$	0	0	0	1.11
$S_{\delta\delta}$	0	0	0	0.66
$T_{\beta\beta}$	44.71	24.95	36.26	32.53
$T_{\beta\delta}$	4.85	2.86	9.66	11.11
$T_{\delta\delta}$	0	0	1.39	1.30

Dyad sequence concentrations were determined from the area of the methylene peaks using the following equations:[106]

$$PP = S_{\alpha\alpha} \tag{4.1.1}$$

$$PE = S_{\alpha\gamma} + S_{\alpha\delta} \tag{4.1.2}$$

$$EE = \tfrac{1}{2}\left(S_{\beta\delta} + S_{\delta\delta}\right) + \tfrac{1}{4}S_{\gamma\delta} \tag{4.1.3}$$

Triad comonomer distributions were determined with the calculation scheme given by Cheng *et al*.[103] Only total methylene (S) and methine (T) carbons were used for these calculations:

$$PPP = T_{\beta\beta} \tag{4.1.4}$$

$$PPE = T_{\beta\delta} \tag{4.1.5}$$

$$EPE = T_{\delta\delta} \tag{4.1.6}$$

$$PEP = S_{\beta\beta} = \tfrac{1}{2}S_{\alpha\gamma} \tag{4.1.7}$$

$$EEP = S_{\alpha\delta} = S_{\beta\delta} \tag{4.1.8}$$

$$EEE = \tfrac{1}{2}S_{\delta\delta} + \tfrac{1}{4}S_{\gamma\delta} \tag{4.1.9}$$

Ethylene and propylene content was calculated from both dyad and triad concentrations from the equations:

$$P = PP + \tfrac{1}{2}PE = PPP + PPE + EPE \tag{4.1.10}$$

$$E = EE + \tfrac{1}{2}PE = EEE + EEP + PEP \tag{4.1.11}$$

Ethylene content and number–average sequence lengths of propylene and ethylene runs for each sample were calculated using equations (2.7.2) and (2.7.3). The pentad isotacticity was determined from the methyl peak assignments according to Busico *et al*.[96,99] and equation (2.7.1).

Table 4.1.3 summarizes the sequence distributions of the fractionated copolymers in terms of dyads and triads, copolymer compositions, as well as the number average sequences of propylene, $\overline{n}_p$, and ethylene units, $\overline{n}_e$.

Chemical shift assignment for the statistical analysis of copolymer chain stereostructure was performed on the basis of ten pentads shown in Figure 2.7.2 by using the methyl region (20–23 ppm) assignments by Busico *et al.*[96,99] for the homopolymer, and by Hayashi *et al.*[114] for the propylene–ethylene copolymers. The usual nomenclature was adopted where *meso* (*m*) and *racemic* (*r*) designate consecutive monomer pairs with either like (*m*), or opposite (*r*) configurations.[100]

Pentad isotacticity data calculated from the methyl region are shown in Table 4.1.4. The summary of the molecular characteristics of the four copolymer fractions are given in Table 4.1.5.

4.2. Molecular Weight

Molecular weight characteristics were determined by GPC and are reported in Table 4.2.1. The results indicate that copolymers had fractionated based on ethylene content and molecular weight. Fractions extracted with the lower boiling solvent (hexanes) have higher ethylene content, lower molecular weight, and slightly higher polydispersity.

Table 4.1.3. Sequence distributions of fractionated copolymers.

Sequence	iPP2.62	iPP4.38	iPP10.45	iPP15.57
	(mol%)	(mol%)	(mol%)	(mol%)
PPP	87.87	85.68	68.70	61.17
PPE	9.52	9.82	18.31	20.89
PEP	2.61	4.50	7.19	9.69
EPE	0	0	2.63	2.45
EEP	0	0	3.16	4.65
EEE	0	0	0	1.15
PP	94.74	91.47	80.53	72.21
PE	5.26	8.53	17.86	24.28
EE	0	0	1.61	3.51
P	97.38	95.62	89.55	84.43
E	2.62	4.38	10.45	15.57
$\overline{n}_p$	37.03	22.45	10.02	6.95
$\overline{n}_e$	1.0	1.0	1.18	1.29

Table 4.1.4. Pentad distribution and isotacticity of the copolymer fractions.

Sequence	iPP2.62	iPP4.38	iPP10.45	iPP15.57
	(mol%)	(mol%)	(mol%)	(mol%)
mmmm	87.42	76.00	64.05	56.84
mmmr	6.32	7.11	14.26	14.55
rmmr	0	0	0	0
mmrr	0	0	4.51	1.31
mrmm	6.25	16.89	15.04	16.76
mrmr	0	0	2.14	3.58
mrrm	0	0	0	6.96
rmrr	0	0	0	0
rrrm	0	0	0	0
rrrr	0	0	0	0
m	96.86	92.78	89.30	82.22
r	3.14	7.22	10.70	17.78
$\overline{n}_m$	32	25.4	11.6	6

Table 4.1.5. Summary of the molecular characteristics of the fractionated samples.

Sample ID	ethylene (mol%)	stereo defects (mol%)	total defects (mol%)
iPP2.62	2.62	3.14	5.76
iPP4.38	4.38	7.22	11.60
iPP10.45	10.45	10.70	21.15
iPP15.57	15.57	17.78	33.35

Table 4.2.1. Molecular weight characteristics of propylene–ethylene copolymers.

Sample ID	M_w (g/mol)	M_n (g/mol)	M_z (g/mol)	Polydispersity
iPP2.62	252,200	120,600	520,150	2.09
iPP4.38	287,100	145,100	512,200	1.98
iPP10.45	86,190	36,140	199,450	2.39
iPP15.57	74,940	31,850	150,750	2.37

4.3. Wide Angle X–ray Diffraction at Ambient Temperature

WAXD studies were performed at ambient temperature on copolymer samples that were prepared by isothermal crystallization at atmospheric and high pressures. Degree of crystallinity and γ–crystal content were determined from these experiments by using equations (2.8.2) and (3.8.1).

4.3.1. WAXD of copolymers crystallized at atmospheric pressure

Each of the crystal forms of *i*–PP has distinctive reflection in the WAXD pattern. These characteristic reflections are found in the 2θ angle range of 18–19^o for the α–monoclinic form, 15–16^o for the β–hexagonal form, and 19.2–20.5^o for the γ–orthorhombic form. The presence or absence of each of these peaks indicates the existence of that particular structure.

WAXD patterns of propylene–ethylene copolymers crystallized at atmospheric pressure are shown in Figures 4.3.1 – 4.3.4. For these copolymers only the characteristic peaks of the isotactic polypropylene were observed, since ethylene sequences in the copolymers were not long enough to crystallize into polyethylene crystals. The presence of the diffraction peaks at 2θ = 18.6^o (α–phase (130) reflection) and 2θ = 20.1^o (γ–phase (117) reflection) in the patterns indicates that these copolymers crystallize only in α– and γ–crystals.

WAXD analysis of copolymer samples isothermally crystallized at atmospheric pressure shows that the lower the supercooling the higher the amount of γ–phase produced. In addition, as the ethylene content increases in the copolymer samples, the

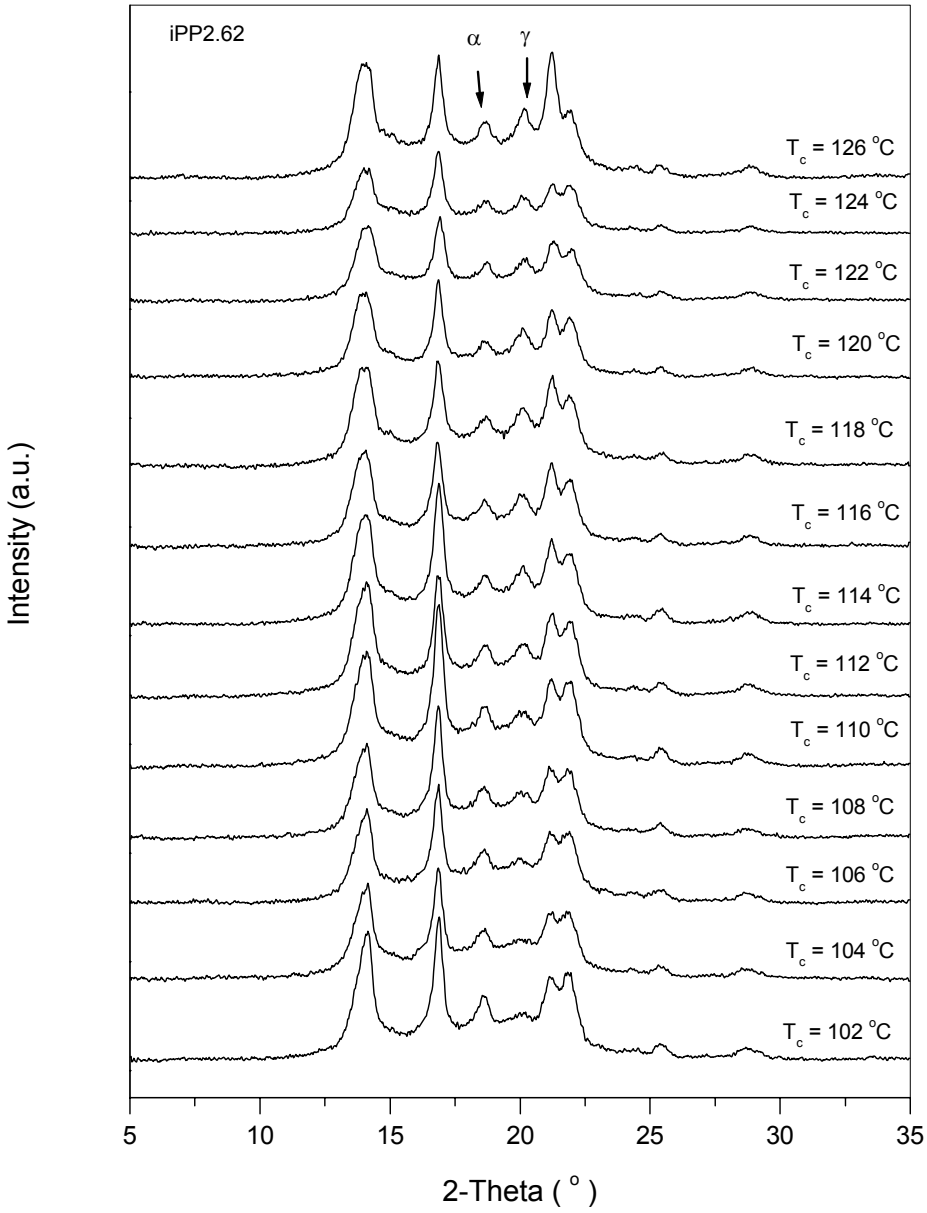

Figure 4.3.1 WAXD pattern of iPP2.62 at different crystallization temperatures.

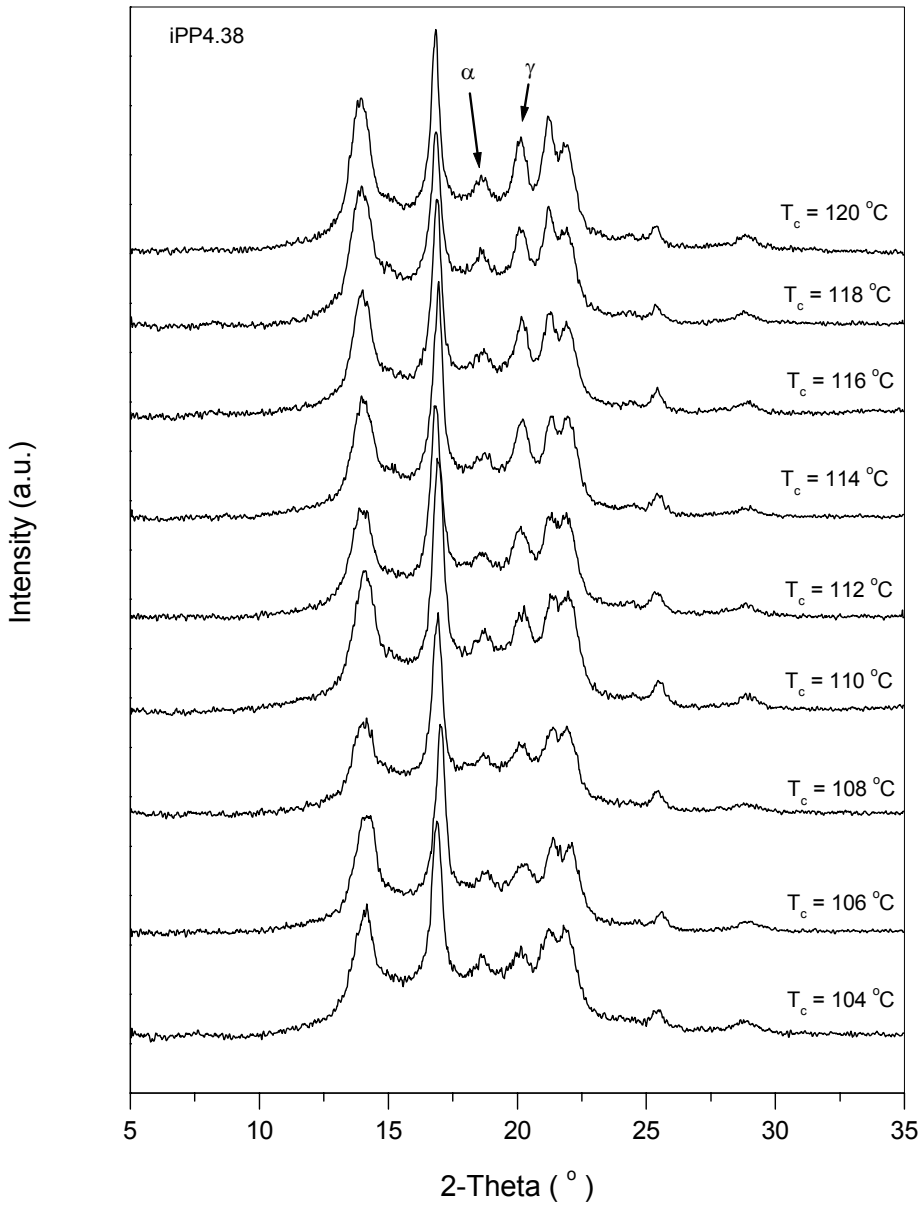

Figure 4.3.2 WAXD pattern of iPP4.38 at different crystallization temperatures.

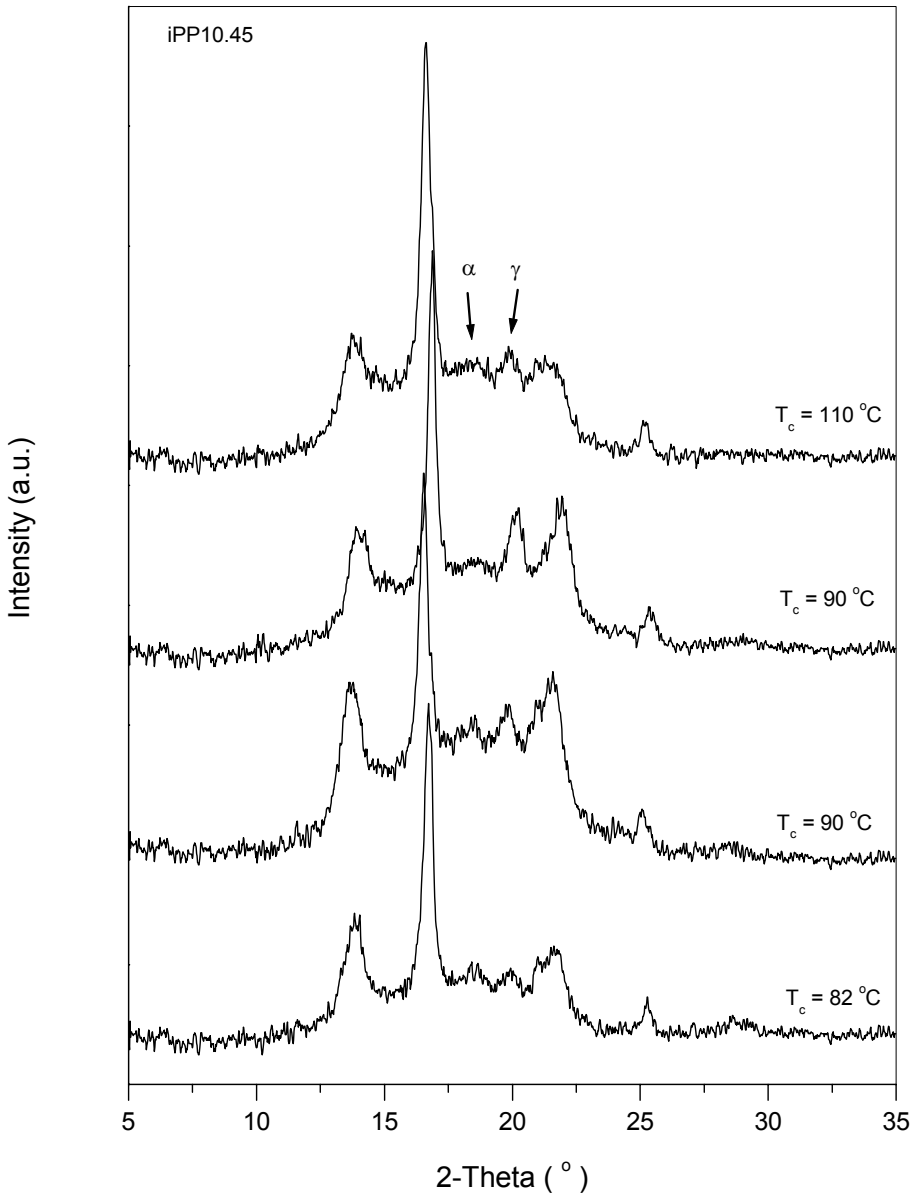

Figure 4.3.3 WAXD pattern of iPP10.45 at different crystallization temperatures.

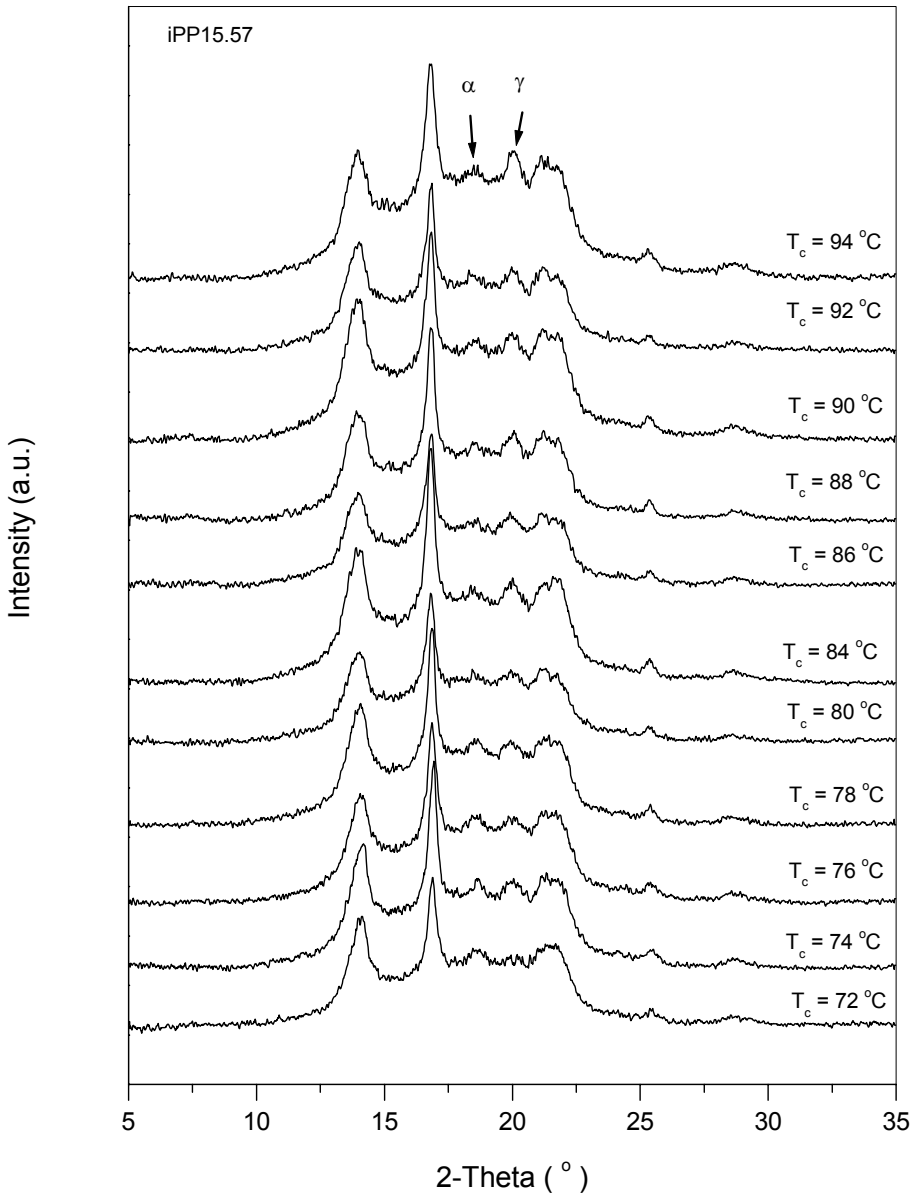

Figure 4.3.4 WAXD pattern of iPP15.57 at different crystallization temperatures.

amount of the γ–phase also increases. Calculated degrees of crystallinity are shown in Figure 4.3.5. The increase of the crystallization temperature results in higher degree of crystallinity of the samples.

4.3.2. WAXD of copolymers crystallized at high pressures

WAXD analysis of the copolymer samples crystallized at high pressures was carried out at room temperature and atmospheric pressure. WAXD patterns of copolymer iPP2.62 as a function of crystallization temperature and pressure are shown in Figures 4.3.6 – 4.3.9. The diffractogram of iPP2.62 crystallized at the lowest crystallization pressure (p_c = 88 MPa) shows that these samples crystallize into both α– and γ–crystal phases. At this pressure, even at very high crystallization temperatures only a mixture of these phases was produced. However, for all other pressures, 123 MPa, 158 MPa and 193 MPa, pure γ–crystal phase was obtained at higher crystallization temperatures.

WAXD patterns of the iPP4.38 samples as a function of crystallization temperature and pressure are shown in Figures 4.3.10 – 4.3.13. These samples exhibited the same behavior as iPP2.62, namely, the γ–phase content increased with increasing crystallization temperature and pressure. In contrast with iPP2.62, this copolymer crystallized into pure γ–form even at the lowest crystallization pressure of 88 MPa. Because this sample had higher ethylene content of 4.38 mol% (or total defect content of 11.6 mol%) the crystallization temperature range and the crystallization temperature at which pure γ–phase was produced were shifted to lower values. Therefore, for this propylene–ethylene copolymer the increase in ethylene content shifted the onset of pure γ–crystal formation to lower temperature values.

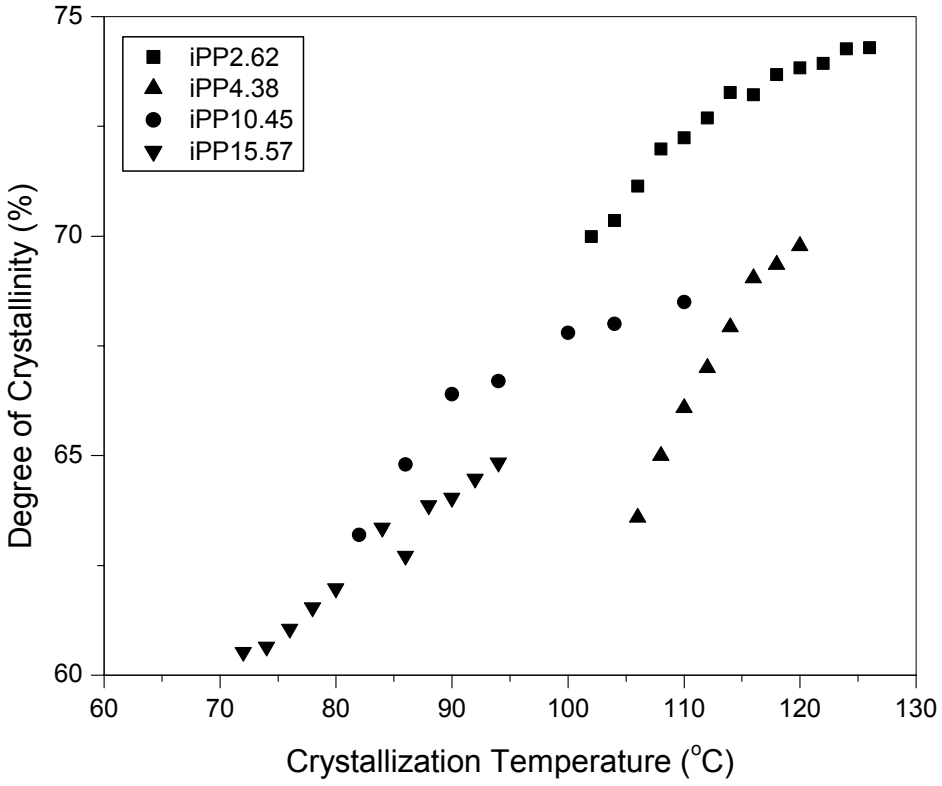

Figure 4.3.5. Degree of crystallinity as a function of the crystallization temperature for the four copolymer fractions.

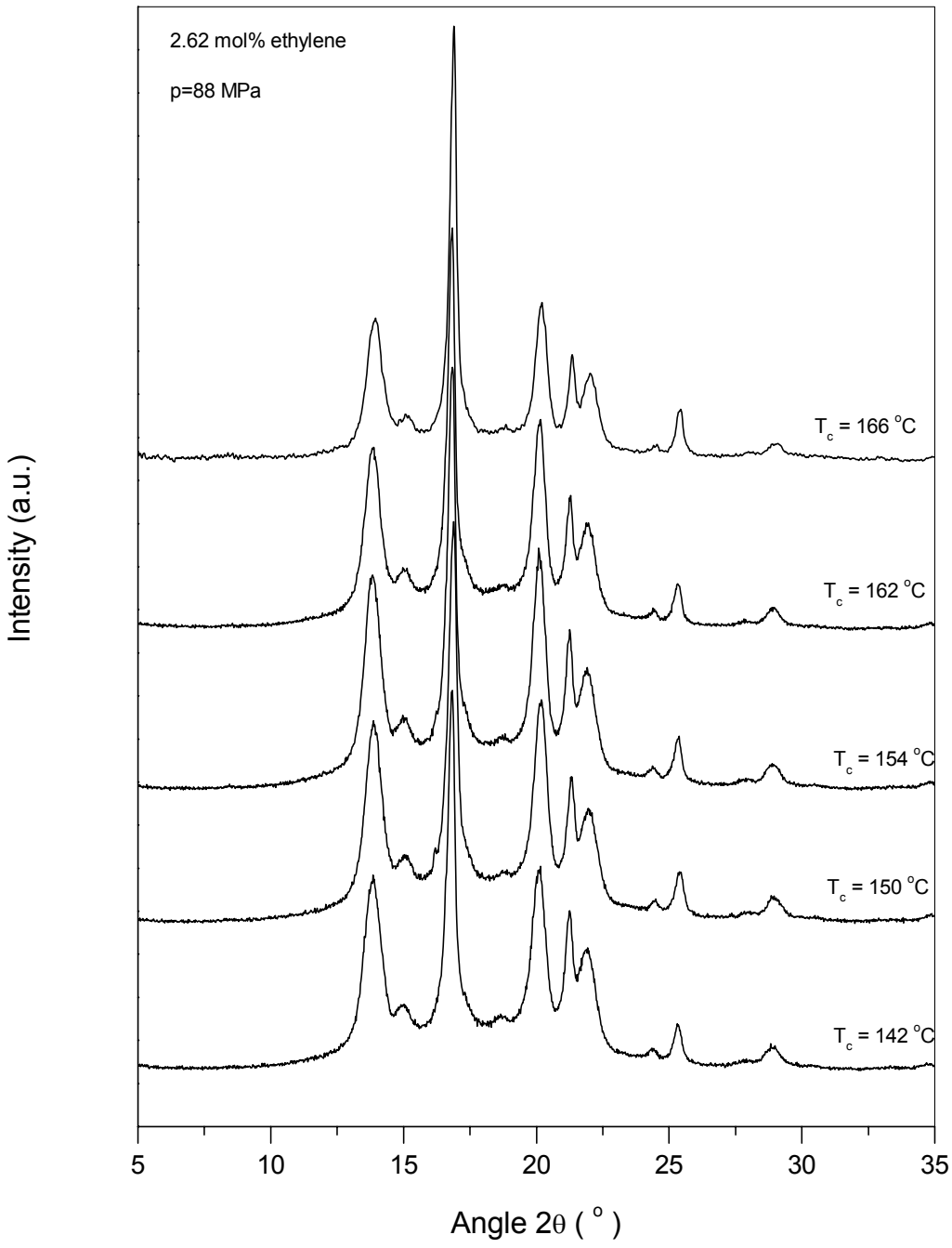

Figure 4.3.6. WAXD patterns of iPP2.62 isothermally crystallized at 88 MPa.

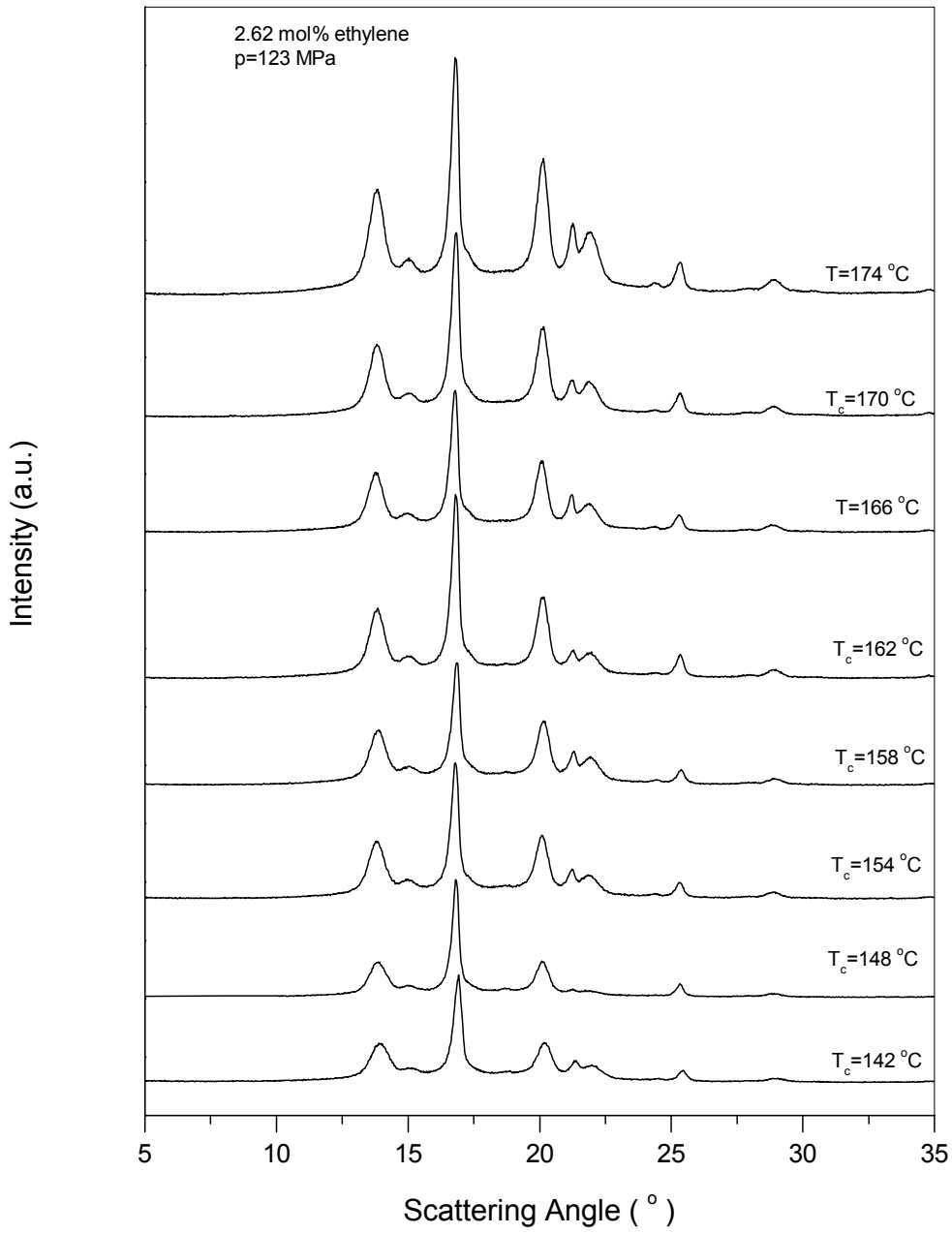

Figure 4.3.7. WAXD patterns of iPP2.62 isothermally crystallized at 123 MPa.

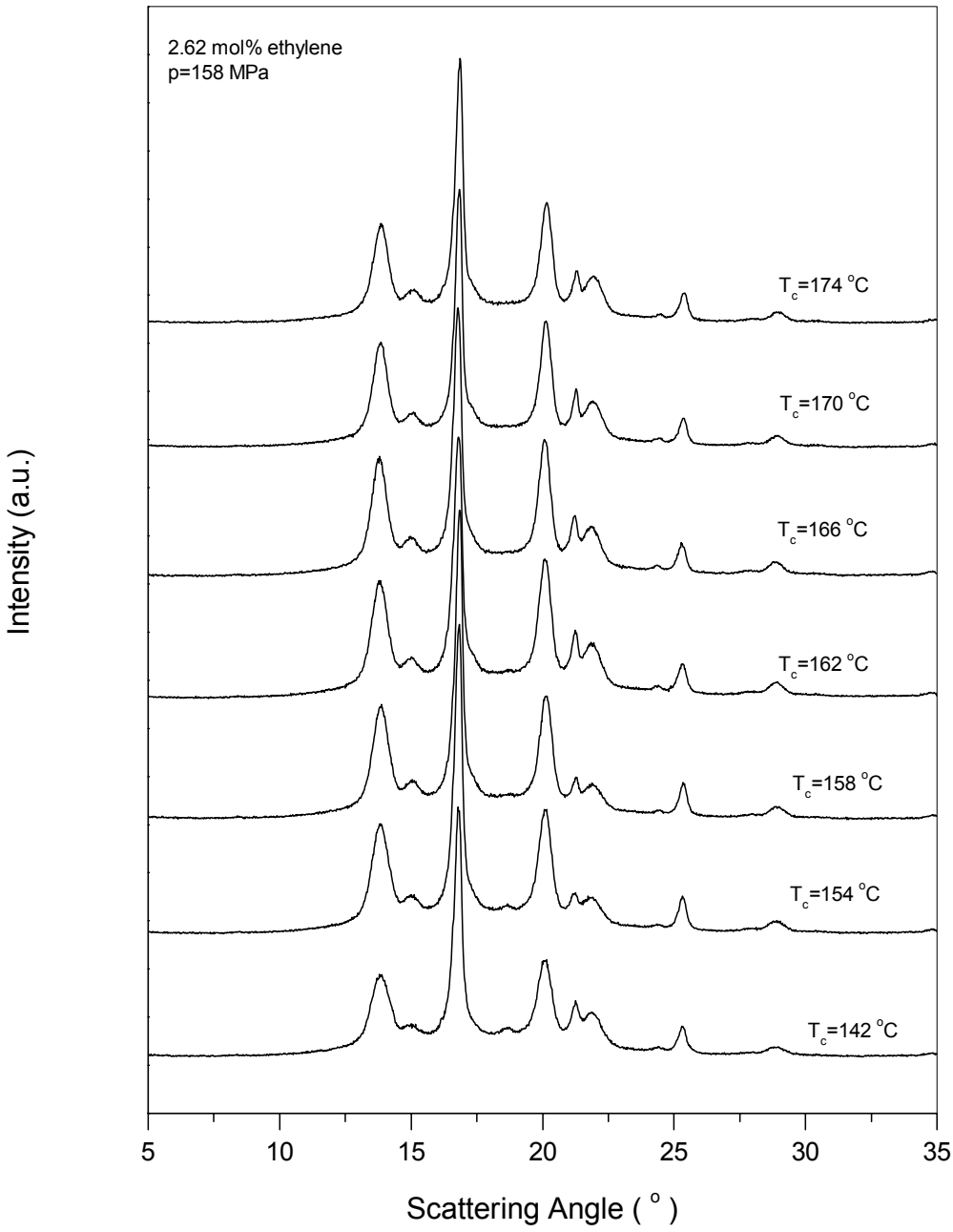

Figure 4.3.8. WAXD patterns of iPP2.62 isothermally crystallized at 158 MPa.

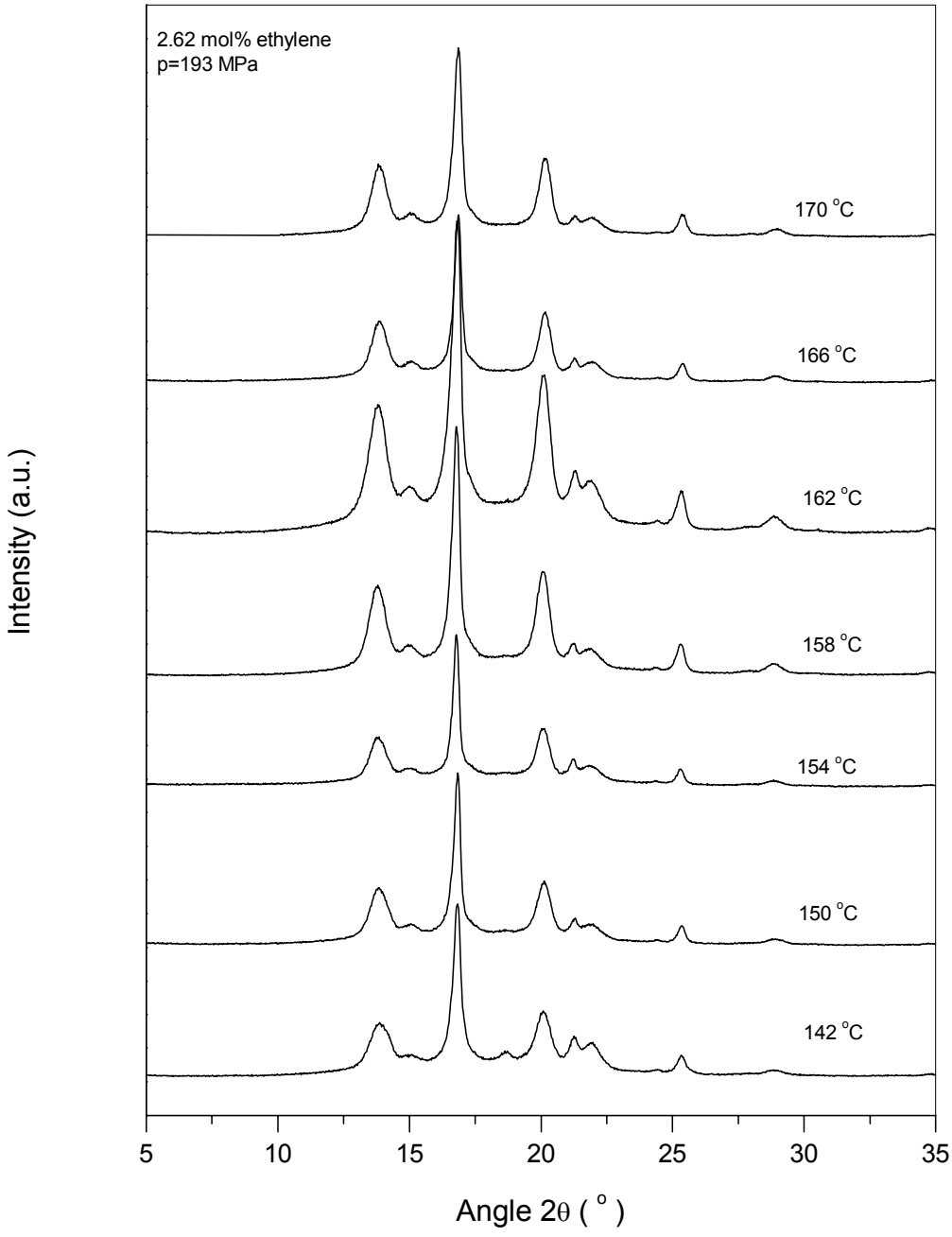

Figure 4.3.9. WAXD patterns of iPP2.62 isothermally crystallized at 193 MPa.

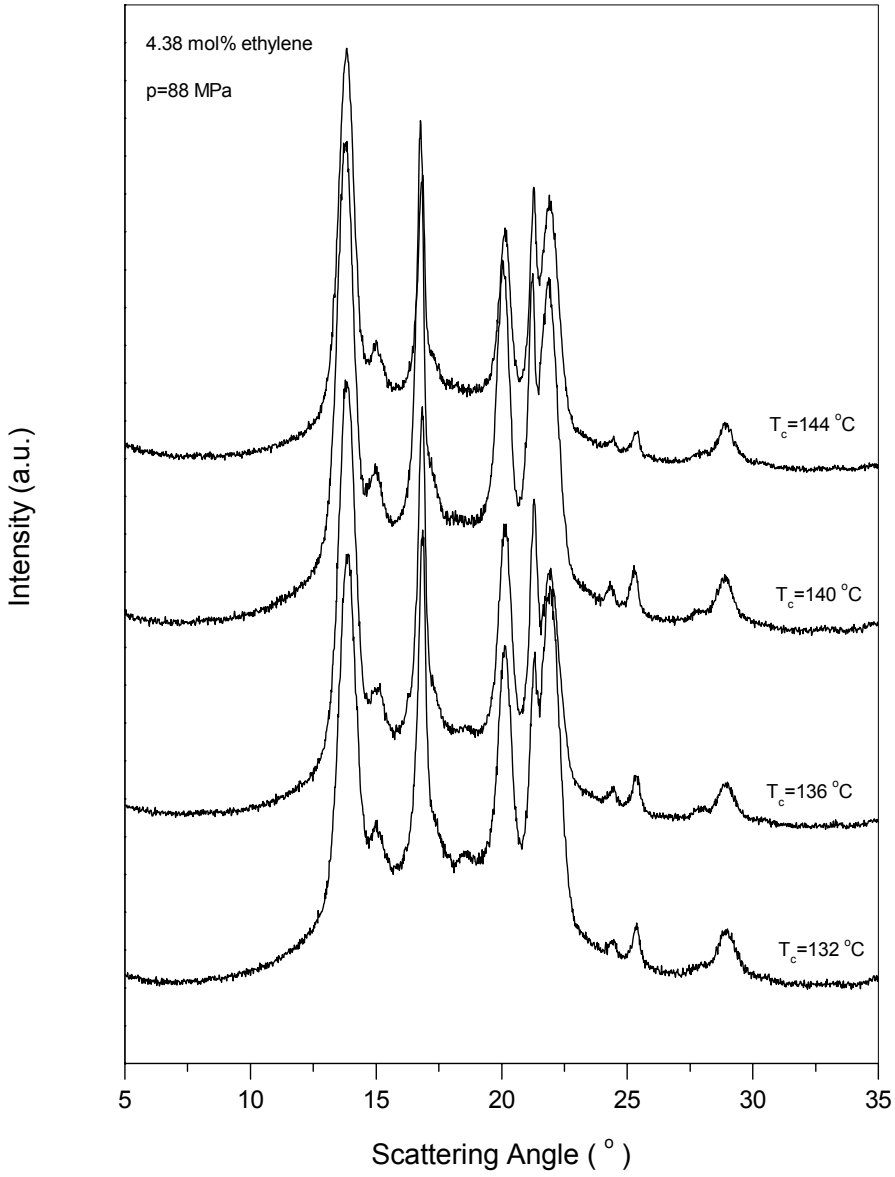

Figure 4.3.10. WAXD patterns of iPP4.38 isothermally crystallized at 88 MPa.

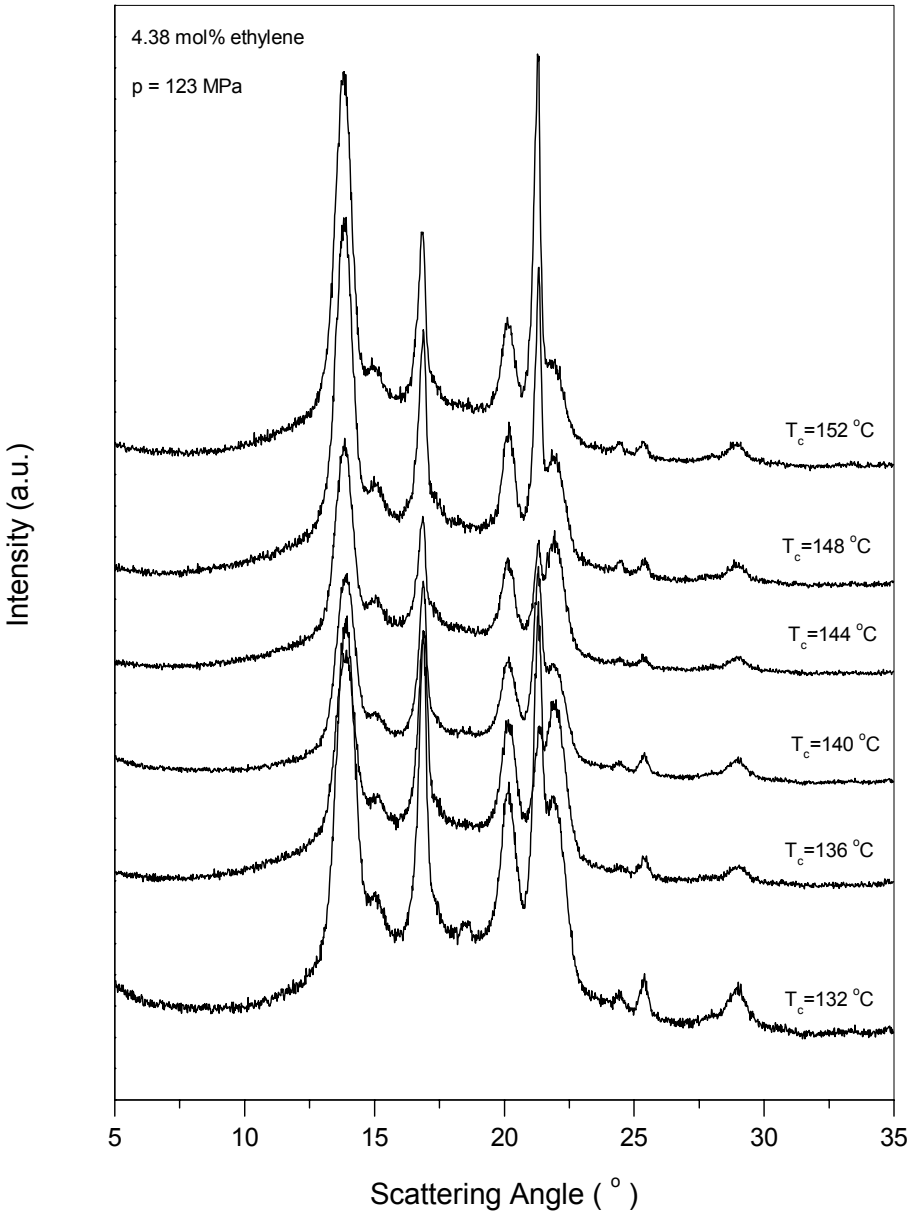

Figure 4.3.11. WAXD patterns of iPP4.38 isothermally crystallized at 123 MPa.

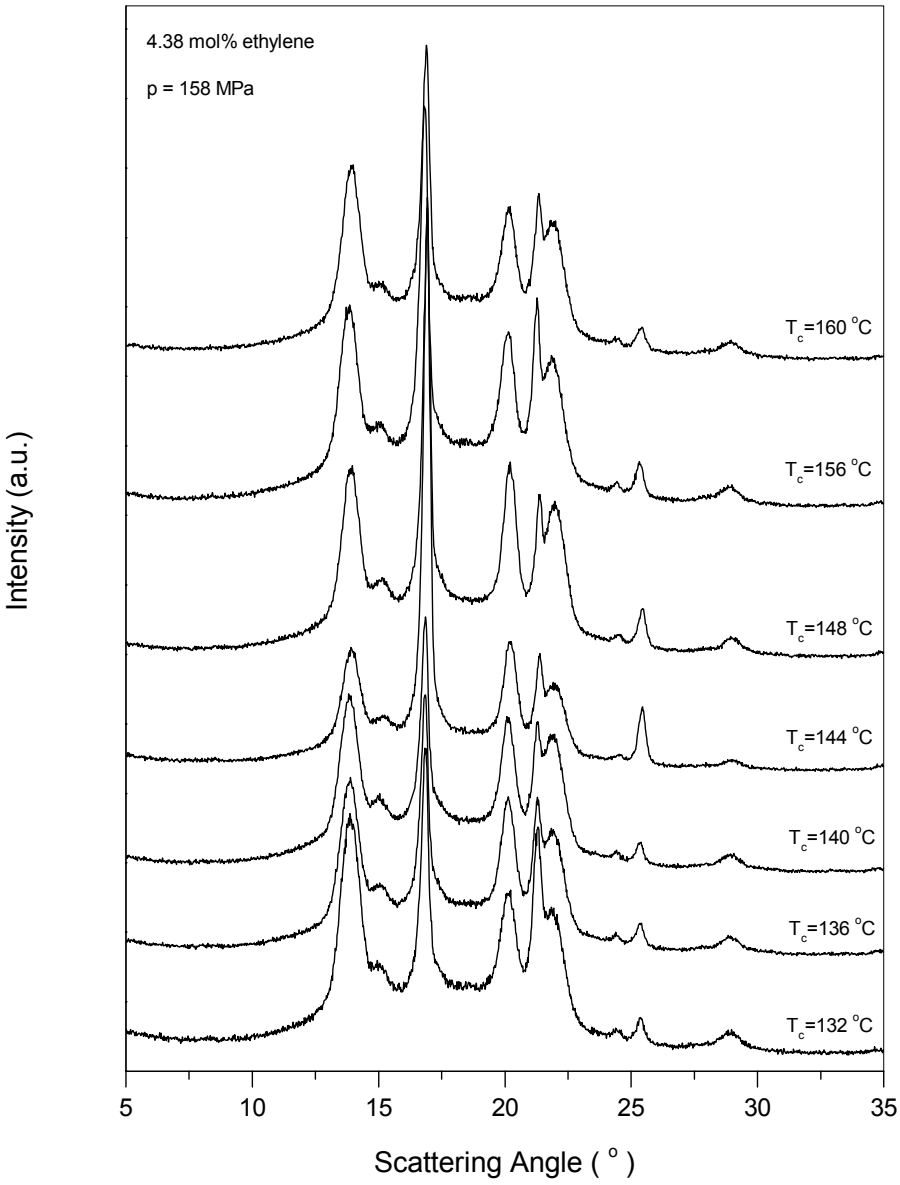

Figure 4.3.12. WAXD patterns of iPP4.38 isothermally crystallized at 158 MPa.

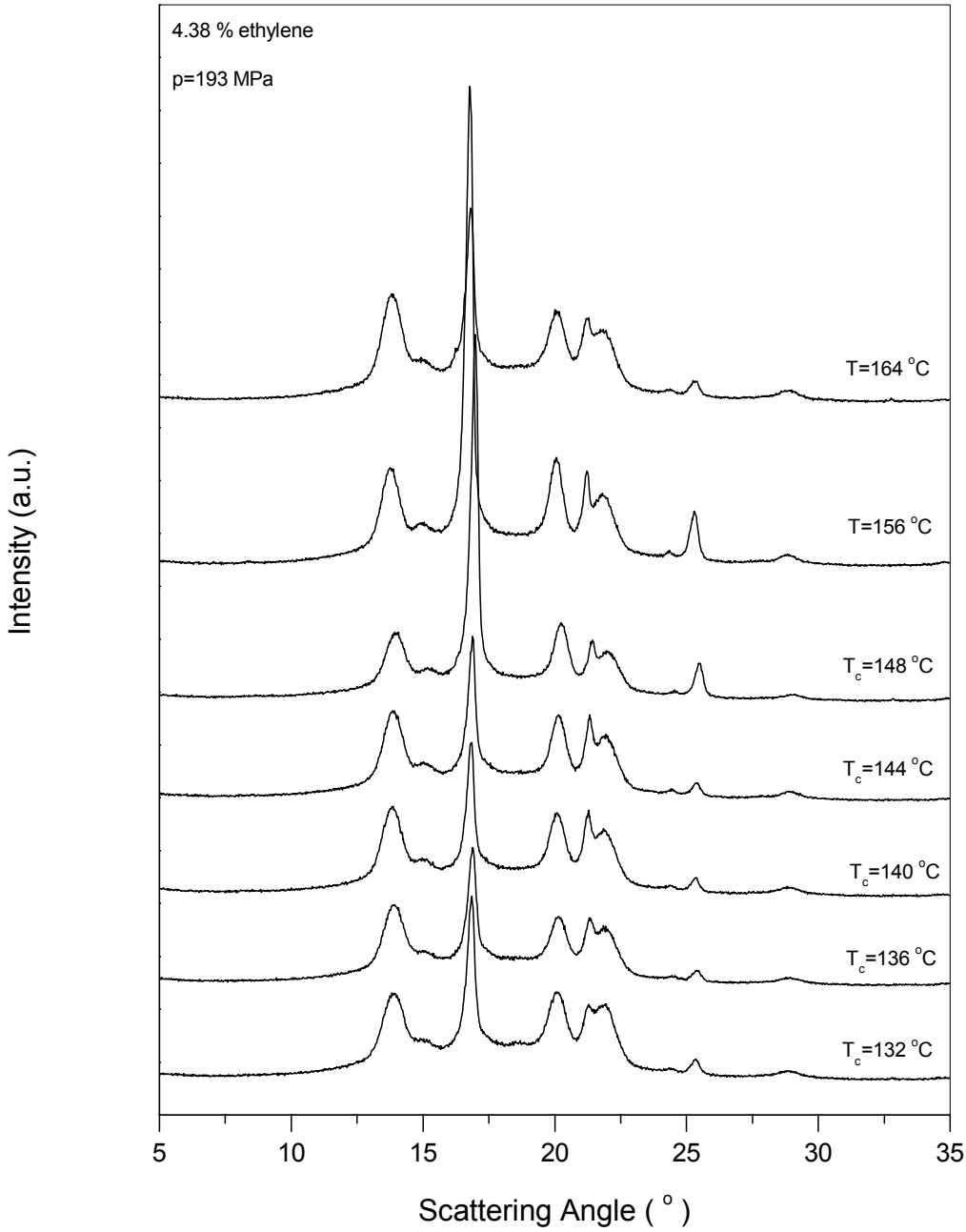

Figure 4.3.13. WAXD patterns of iPP4.38 isothermally crystallized at 193 MPa.

Plots of the degree of crystallinity of copolymers iPP2.62 and iPP4.38 as a function of crystallization temperature and pressure are shown in Figures 4.3.14 and 4.3.15. The results indicate that the crystallinity values of pressure crystallized samples remained almost unchanged with increasing temperature and pressure.

4.4. Thermal Analysis

4.4.1. Non–isothermal Crystallization

Before studying the isothermal crystallization of random propylene–ethylene copolymers it is necessary to determine the crystallization temperature range. This experiment can be done easily by non–isothermal crystallization in the DSC. In general, the isothermal crystallization should be performed above the non–isothermal crystallization temperature. Figures 4.4.1 and 4.4.2 show the crystallization and melting curves of the copolymers, recorded during cooling and heating at a rate of 10 ^{o}C/min. Crystallization and melting curves of *i*–PP homopolymer are also shown for comparison purposes.

It is evident that both crystallization and melting peak temperatures depend on ethylene content. These copolymers exhibit only one peak during the non–isothermal crystallization and melting, and the peak position shifts to lower temperatures as the ethylene content increases. The intensity of the peaks is reduced with increasing ethylene content, while the width of the crystallization and melting ranges does not change. The presence of the ethylene units in the polypropylene chain decreases the crystallization temperature from 114 ^{o}C for the homopolymer to 66.5 ^{o}C for the copolymer with 15.57 mol% ethylene. The decrease of the crystallization temperature is approximately 3 ^{o}C per mol% ethylene, or 1.5 ^{o}C per mol% total defects. A similar tendency is observed for the melting temperatures, as shown in Figure 4.4.3.

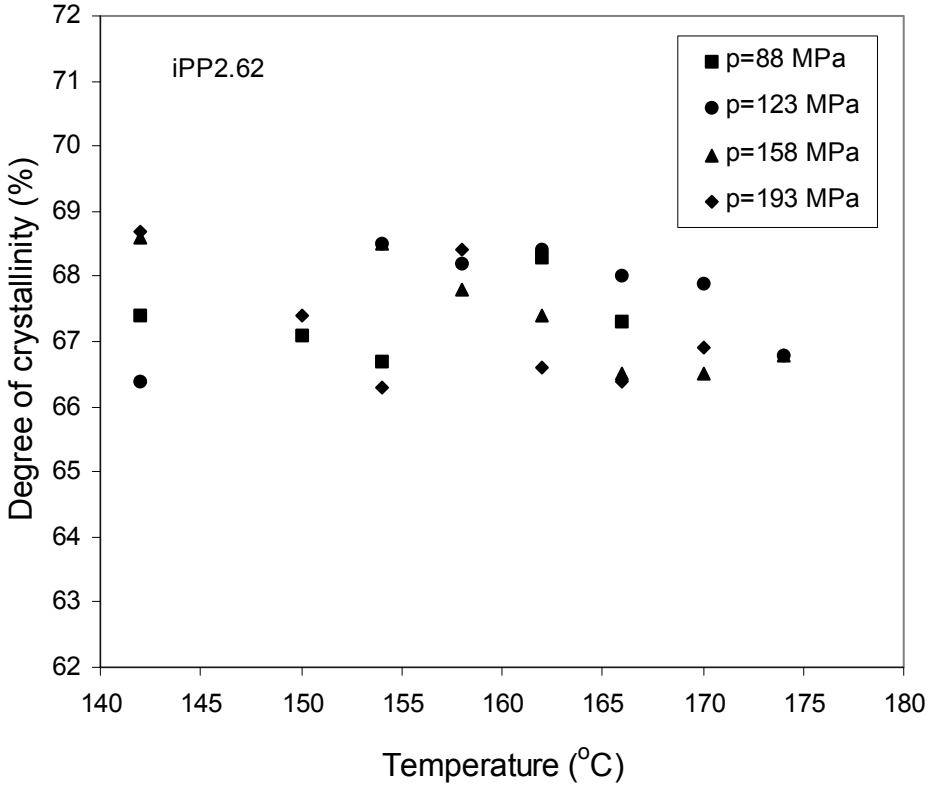

Figure 4.3.14. Degree of crystallinity of copolymer iPP2.62 as a function of the crystallization temperature and pressure.

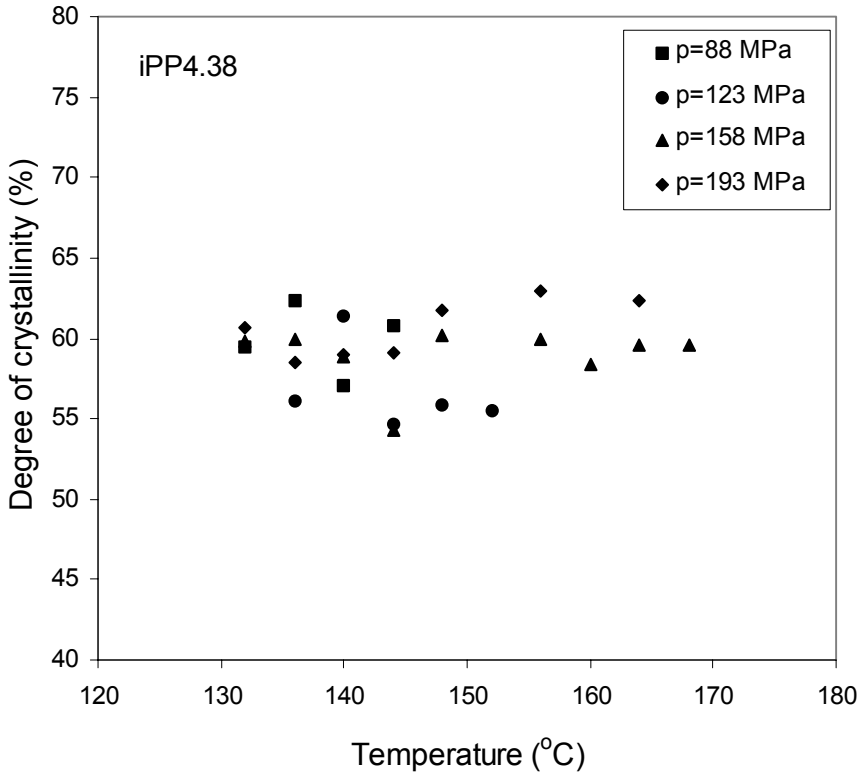

Figure 4.3.15. Degree of crystallinity of copolymer iPP4.38 as a function of the crystallization temperature and pressure.

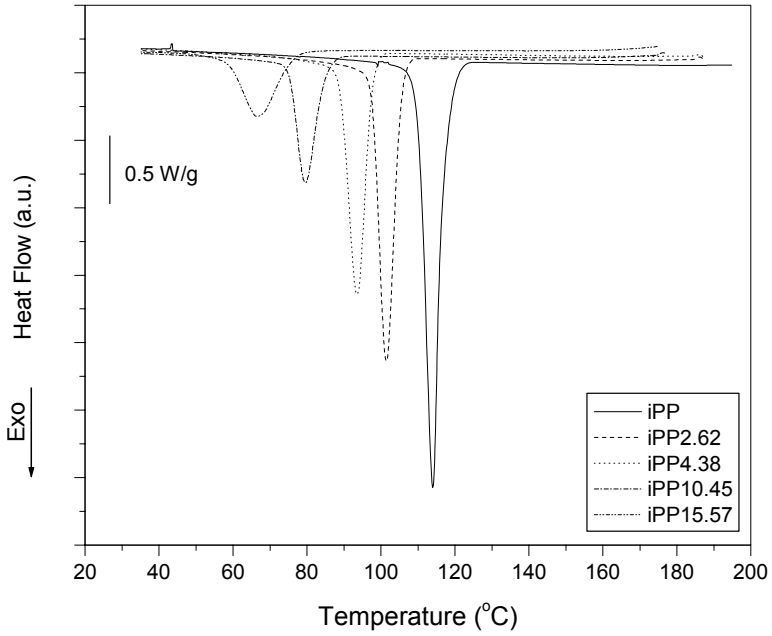

Figure 4.4.1. DSC exotherms of propylene–ethylene copolymers and *i*–PP recorded during crystallization at a cooling rate of 10 °C/min.

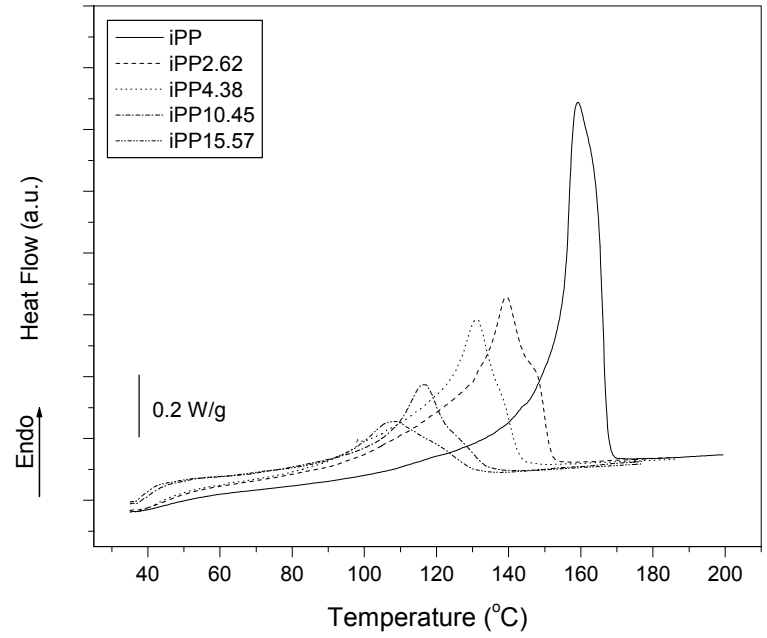

Figure 4.4.2. DSC melting curves of propylene–ethylene copolymers and *i*–PP crystallized at a cooling rate of 10 °C/min (heating rate 10 °C/min).

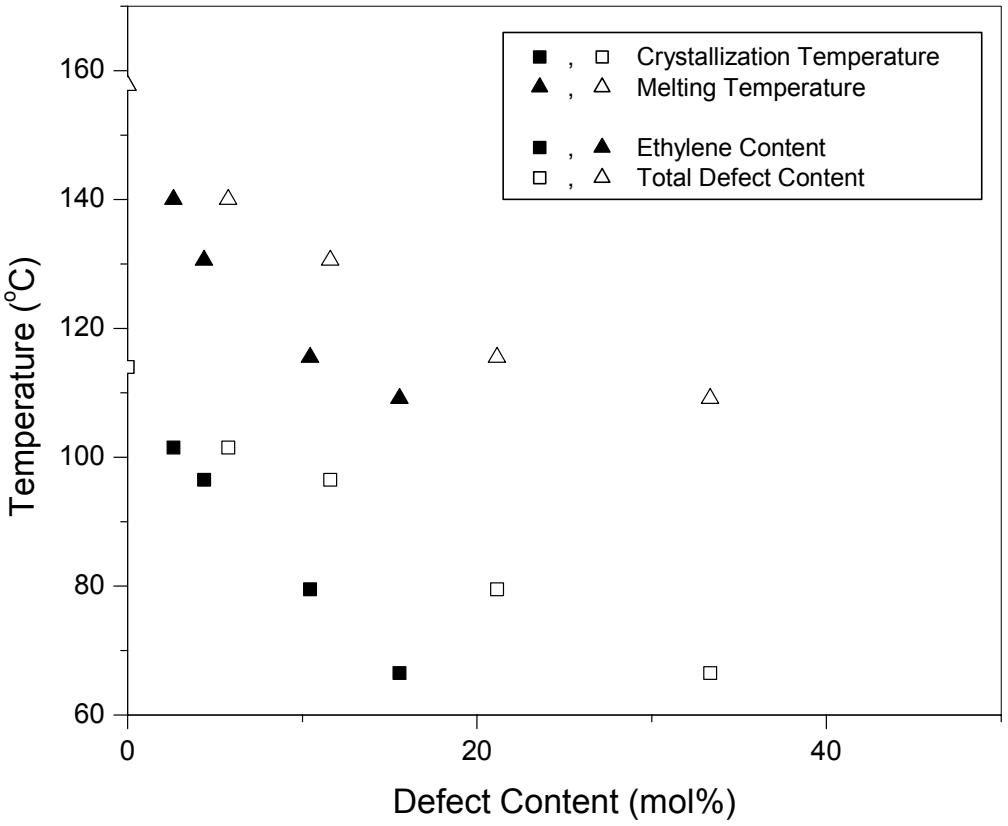

Figure 4.4.3. Crystallization and melting peak temperatures as a function of ethylene and total defect content (cooling and heating rate at 10 °C/min).

4.4.2. Melting of copolymers crystallized at atmospheric pressure

Melting endotherms of the four copolymer fractions that were crystallized in the hot stage for different isothermal crystallization temperatures are shown in Figures 4.4.4 – 4.4.7. Samples exhibit multiple melting peak behavior, as well as melting over a broad temperature range. Melting endotherms were recorded at heating rate of 10 ^{o}C/min.

The complex melting behavior of iPP2.62 copolymer samples is displayed in Figure 4.4.4. For crystallization temperatures of up to 112 ^{o}C they exhibit a low–temperature melting 'hump' at a temperature slightly above the crystallization temperature, followed by a high–melting temperature endotherm. This 'hump' increases in size with increasing crystallization temperature. Additionally, these samples have another small shoulder above the high–temperature peak which decreases with increasing crystallization temperature. As the crystallization temperature is increased above 114 ^{o}C the 'hump' becomes a well defined low–temperature endotherm that further increases at the expense of the high–temperature endotherm. In the crystallization temperature range of 114 – 126 ^{o}C samples have an additional low–temperature endotherm at a temperature just below the crystallization temperature that increases in height and becomes more defined as the crystallization temperature is increased. This low–temperature endotherm is probably due to melting of the material which did not crystallize isothermally for long crystallization times, but crystallized during the quenching. For all iPP2.62 samples, an increase in the crystallization temperature led to shift of both melting endotherms to higher temperatures.

Similar melting behavior was observed for the iPP4.38 copolymer shown in Figure 4.4.5. The observed low–temperature 'hump' becomes a well defined peak at T_c = 110 ^{o}C, and it continues to increase in height with increasing crystallization temperature. Unlike the copolymer iPP2.62, the low–temperature peak starts to dominate the

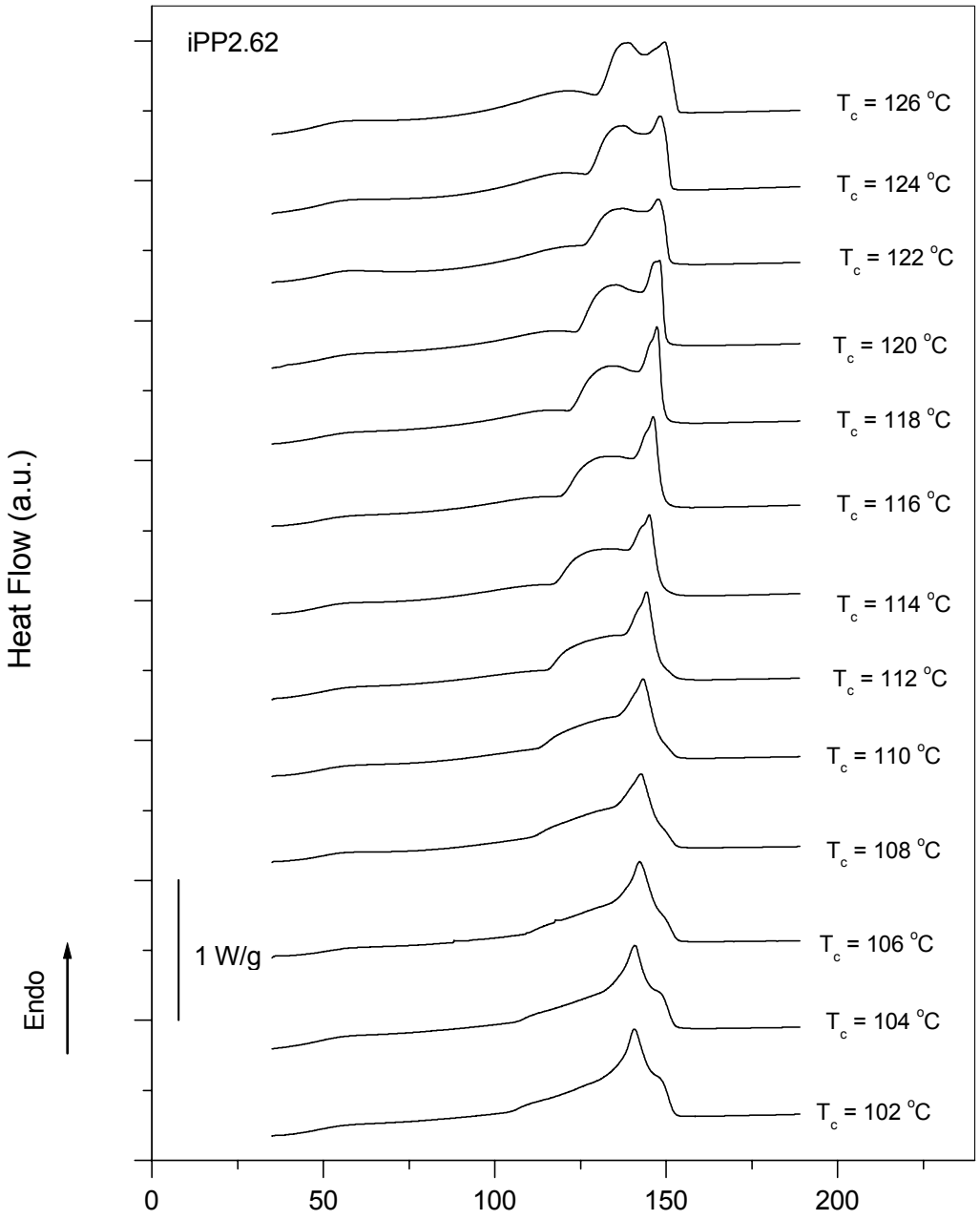

Figure 4.4.4. DSC melting behavior of copolymer iPP2.62 as a function of isothermal crystallization temperature.

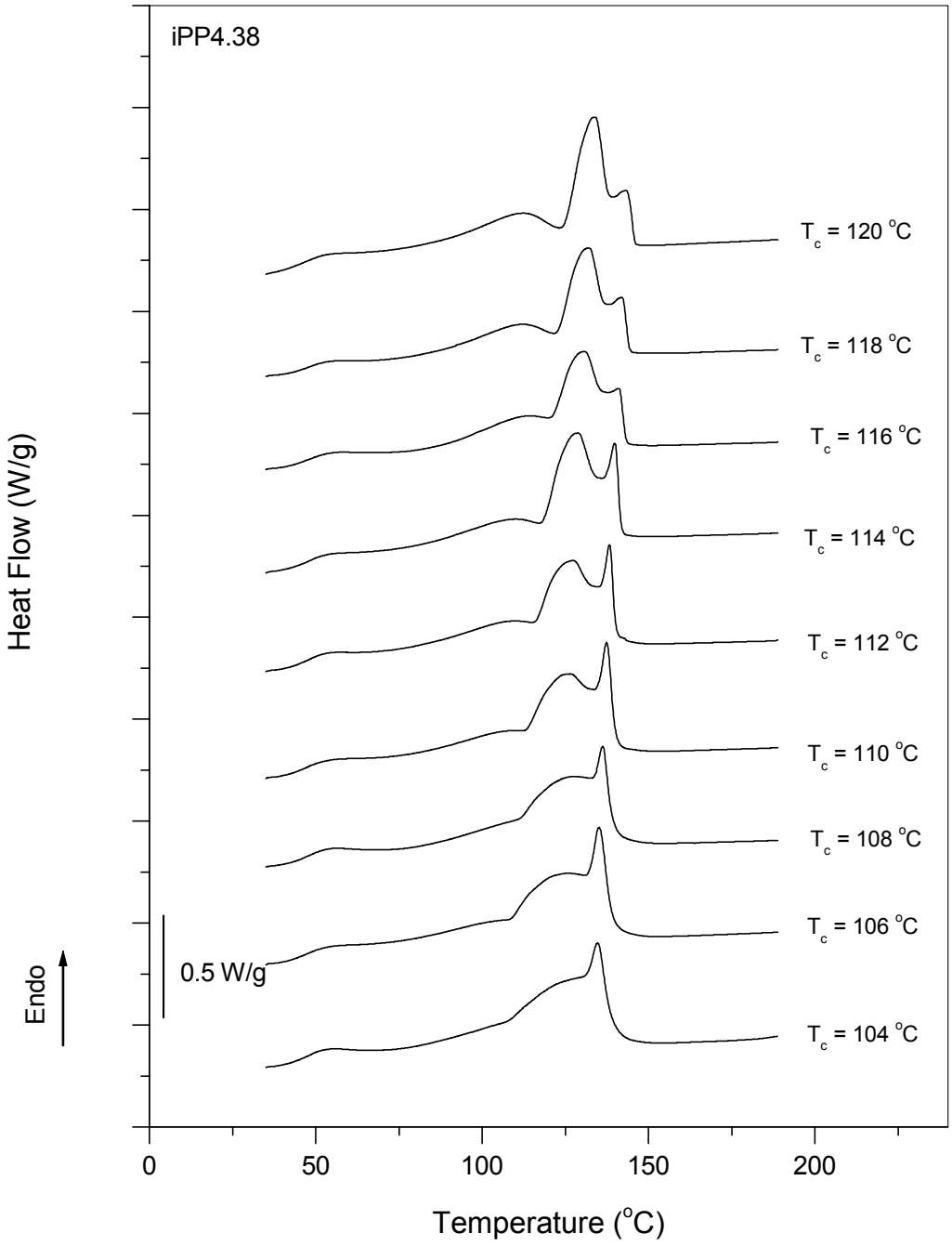

Figure 4.4.5. DSC melting behavior of copolymer iPP4.38 as a function of isothermal crystallization temperature.

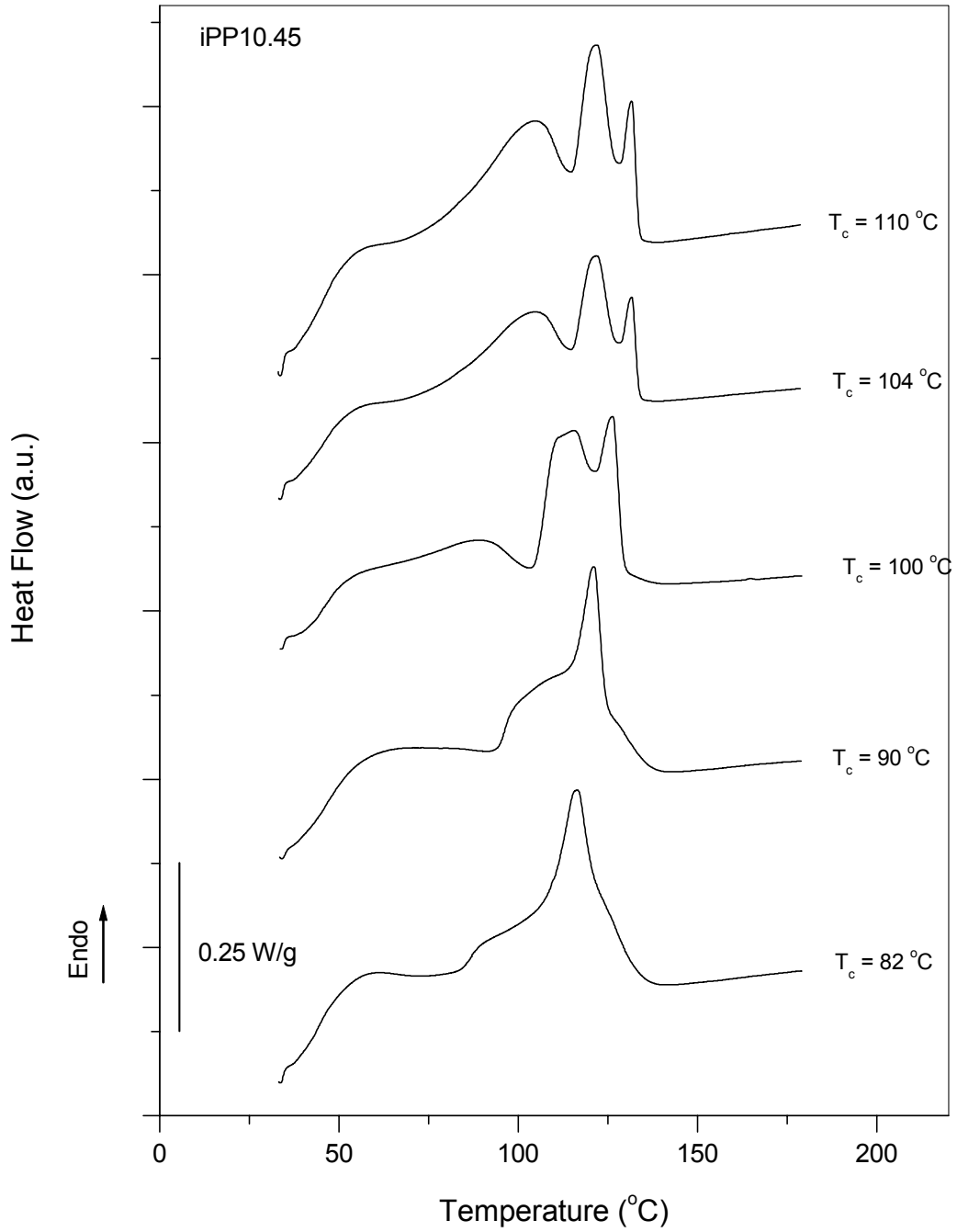

Figure 4.4.6. DSC melting behavior of copolymer iPP10.45 as a function of isothermal crystallization temperature.

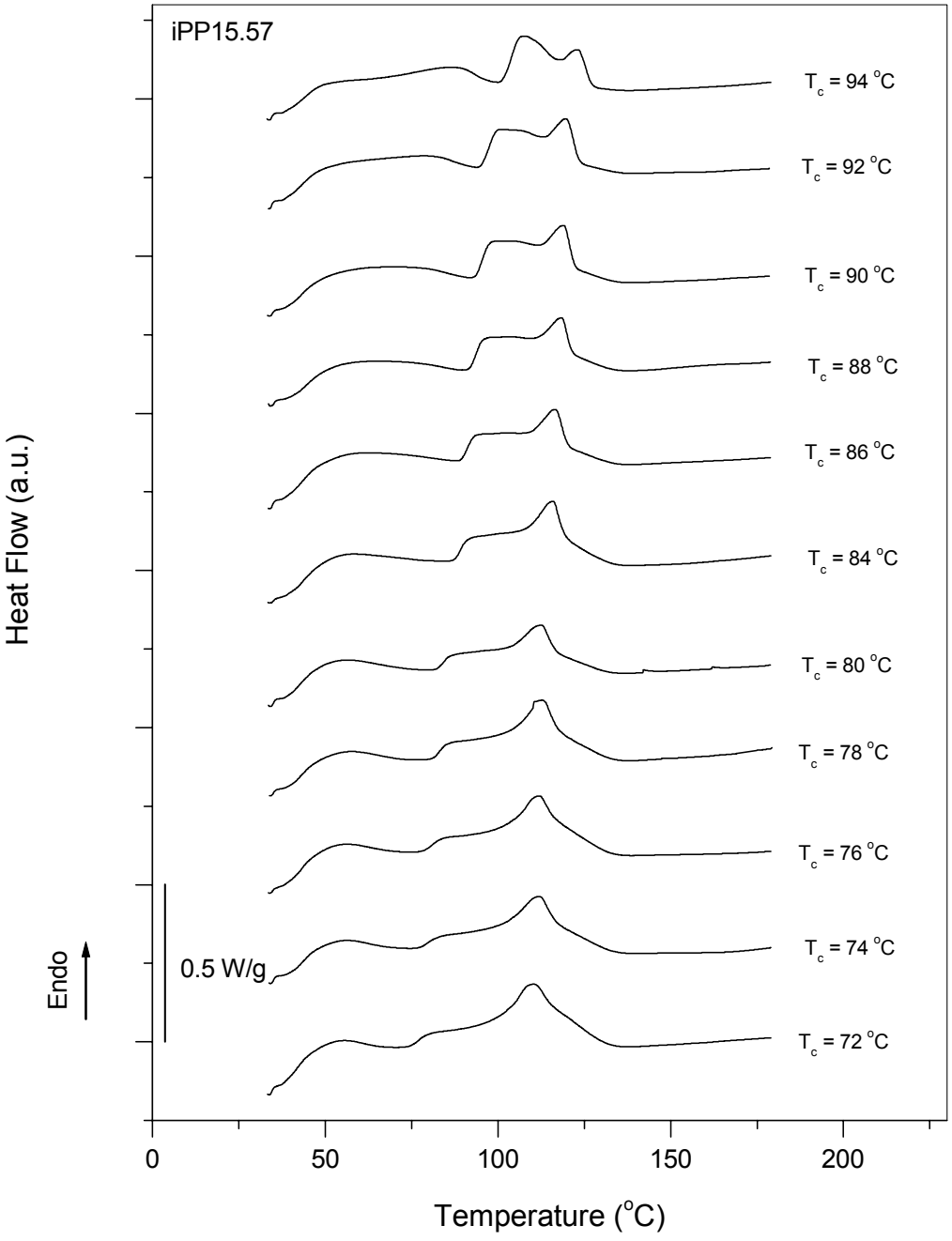

Figure 4.4.7. DSC melting behavior of copolymer iPP15.57 as a function of isothermal crystallization temperature.

high–temperature peak at T_c = 116 ^oC. This behavior is also characteristic of copolymers iPP10.45 and iPP15.57 as seen in Figures 4.4.6 and 4.4.7, respectively.

In order to better illustrate the effect of ethylene content on the melting behavior of propylene–ethylene copolymers, melting endotherms of iPP2.62, iPP4.38 and iPP10.45 crystallized at T_c = 110 ^oC are plotted in Figure 4.4.8. It can be seen that the increase of ethylene content from 2.62 mol% to 10.45 mol% decreases the peak melting temperatures and broadens the low–temperature tail of the endotherm. In addition, increasing ethylene content promotes the intensity of the low–temperature peak which for iPP10.45 becomes higher than the high–temperature peak. This last observation is similar to the effect that increasing crystallization temperature has on the intensity of the low–temperature peak at constant ethylene content. This can be easily explained with the fact that the presence of ethylene units in the polypropylene chains shifts the crystallization temperature range of these copolymers to lower temperatures (Figure 4.4.3). This means that for iPP10.45 crystallization temperature of 110 ^oC corresponds to much lower degree of supercooling compared to the iPP2.62.

The multiple melting behavior of the propylene–ethylene copolymers can be attributed to any of the following: melting of the α– and γ–phase crystals, existence of two crystalline lamellar thickness populations which have different melting temperatures, or melting–recrystallization–remelting process. The first hypothesis was tested using high temperature WAXD experiments on several samples at temperatures determined from DSC, such as peak temperatures and saddle temperatures in–between the peaks. The results from these experiments are presented in section 4.5.

In order to evaluate whether a melting–recrystallization–remelting process was responsible for multiple melting peaks, DSC scans were performed at different heating rates: 1, 2, 5, 10, 20 and 40 ^oC/min. The experiments were performed for three iPP2.62 samples crystallized isothermally at 102 ^oC, 112 ^oC and 126 ^oC, and are shown in Figures 4.4.9, 4.4.10, and 4.4.11, respectively.

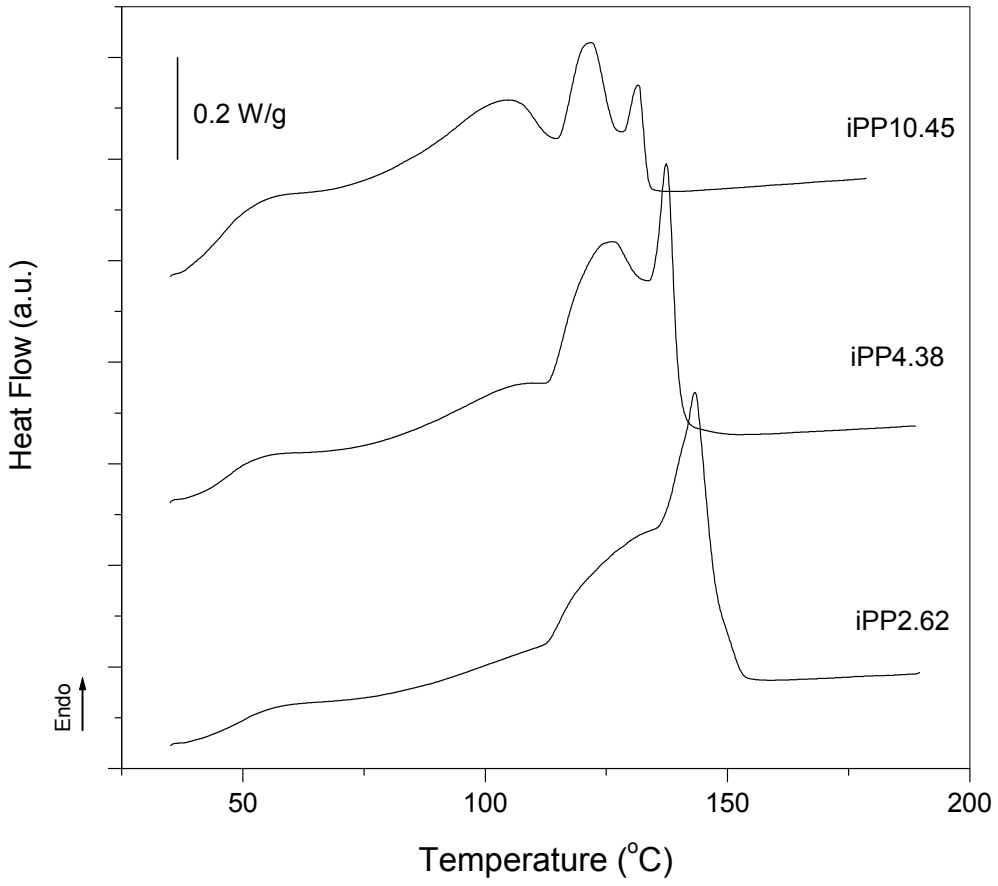

Figure 4.4.8. DSC scans of copolymer fractions crystallized at 110 °C.

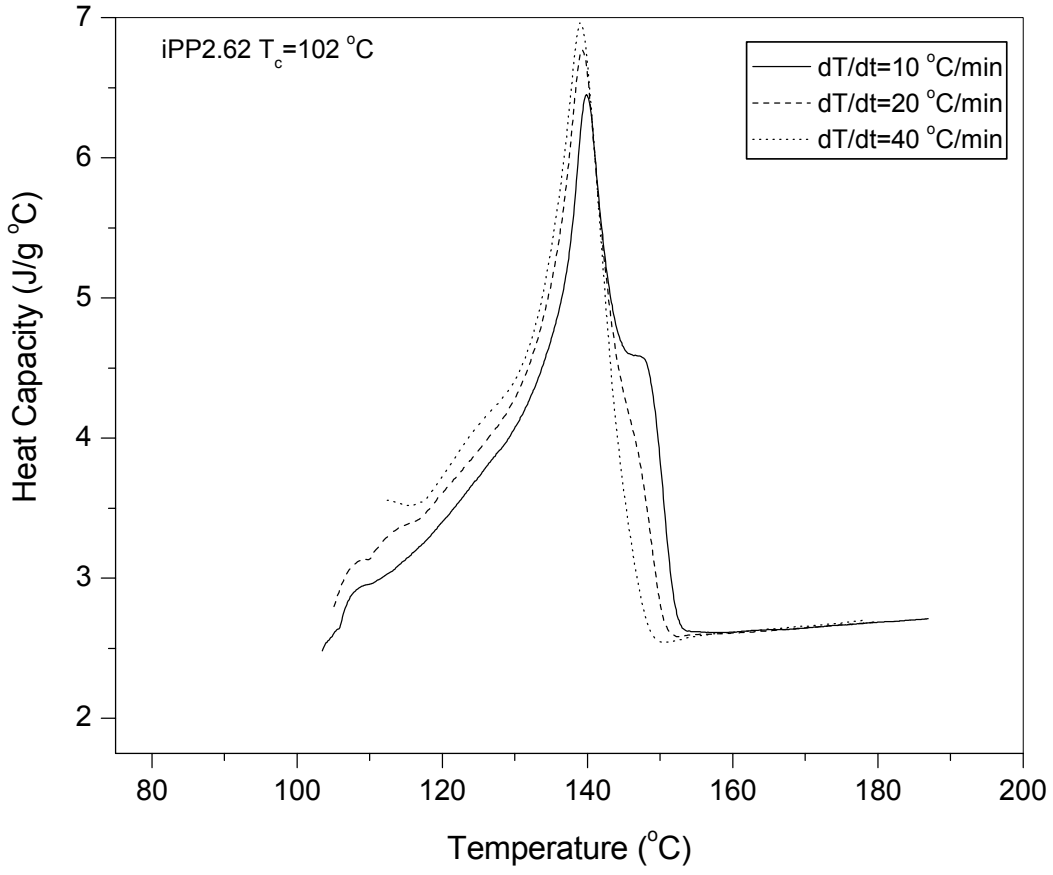

Figure 4.4.9. Effect of heating rate on the melting of copolymer iPP2.62 crystallized at 102 °C.

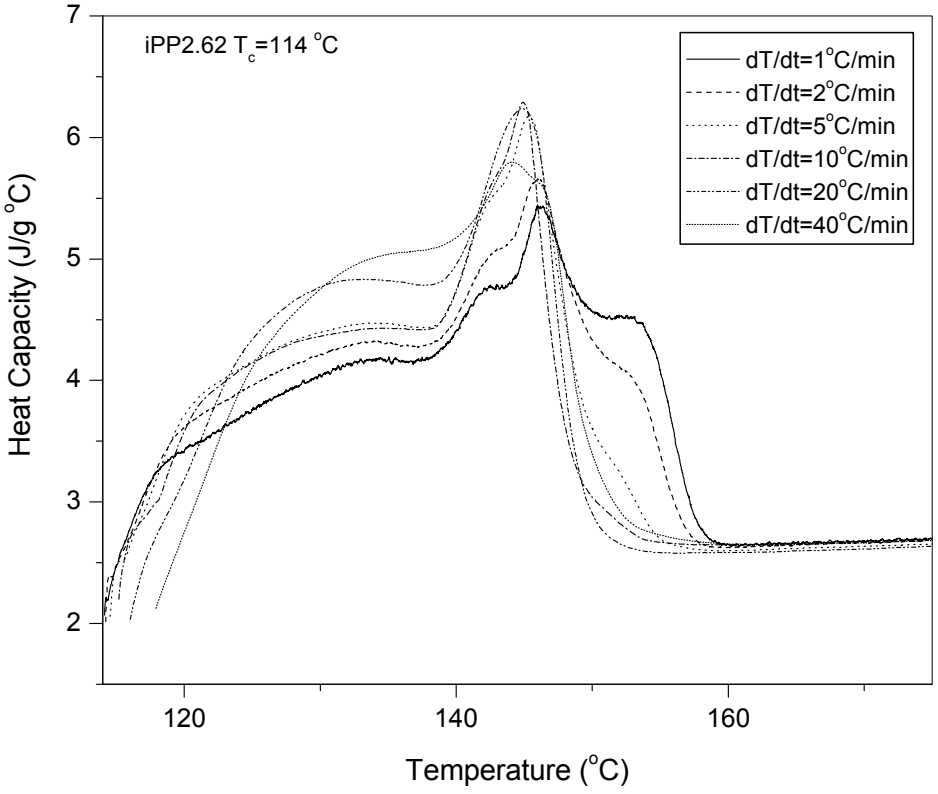

Figure 4.4.10. Effect of heating rate on the melting of copolymer iPP2.62 crystallized at 114 °C.

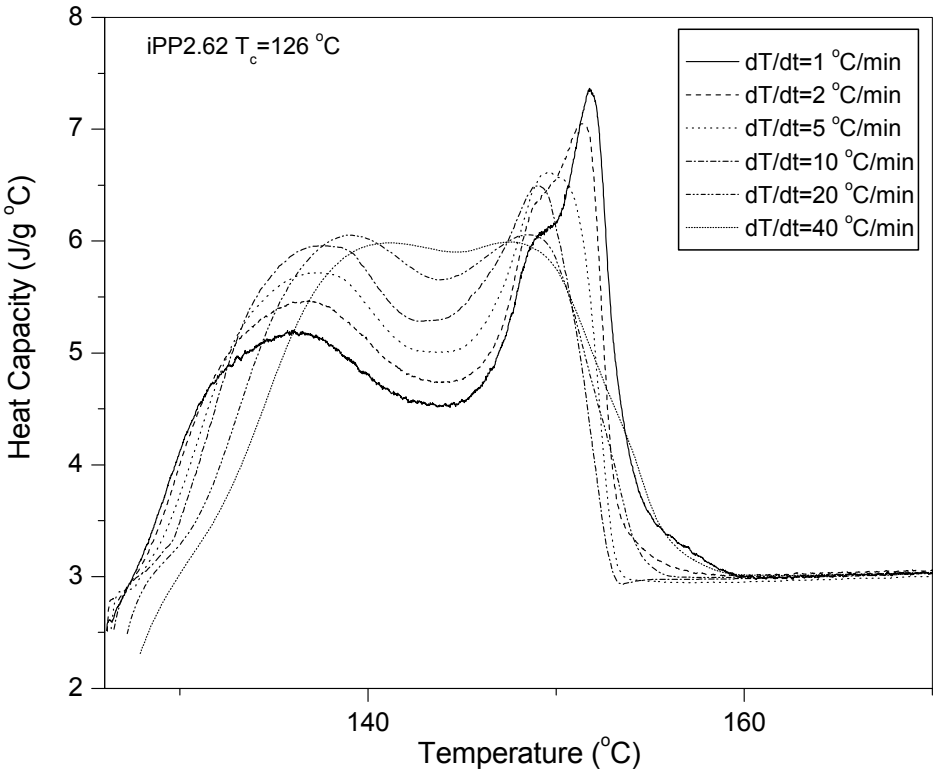

Figure 4.4.11. Effect of heating rate on the melting of copolymer iPP2.62 crystallized at 126 °C.

Figure 4.4.9 shows that for the iPP2.62 sample crystallized at low T_c = 102 ^oC the shoulder above the main melting peak decreases with increasing heating rate, and is not observed for the highest heating rate. This shoulder is also observed in Figure 4.4.10 for iPP2.62 crystallized at 114 ^oC for the low heating rates of 1 – 5 ^oC/min, and is absent for iPP2.62 crystallized at the highest crystallization temperature.

The effect of the heating rate on the overall heat of fusion (ΔH_f), the individual heat of fusion associated with the lower ($\Delta H_{f,1}$) and upper ($\Delta H_{f,2}$) endotherm and the peak melting temperatures can be determined from the analysis of the DSC melting curves shown in Figures 4.4.9 – 4.4.11. Figure 4.4.12 shows the results of this analysis for copolymer iPP2.62 crystallized at 126 ^oC. The following observations were made from this figure. The overall heat of fusion is independent of the heating rate, as is expected. The heat of fusion of the lower endotherm increases with heating rate, while the heat of fusion of the higher endotherm decreases. The lower endotherm peak shifts to higher temperatures and the higher endotherm peak shifts to lower temperatures with increasing heating rate. All of these changes are more significant at lower heating rates, and the changes level off for heating rate of approximately 10–20 ^oC.

4.4.3. Melting of copolymers crystallized at high pressures

Melting behavior of copolymer samples isothermally crystallized at high pressures was studied in DSC at atmospheric pressure. Figures 4.4.13–4.4.20 show the melting endotherms of copolymers iPP2.62 and iPP4.38 crystallized at different temperatures and pressures. All DSC melting curves were recorded at a heating rate of 10 ^oC/min. From these figures it can be seen that copolymers crystallized at high pressures display multiple melting similar to samples crystallized at atmospheric pressure, although less prominent.

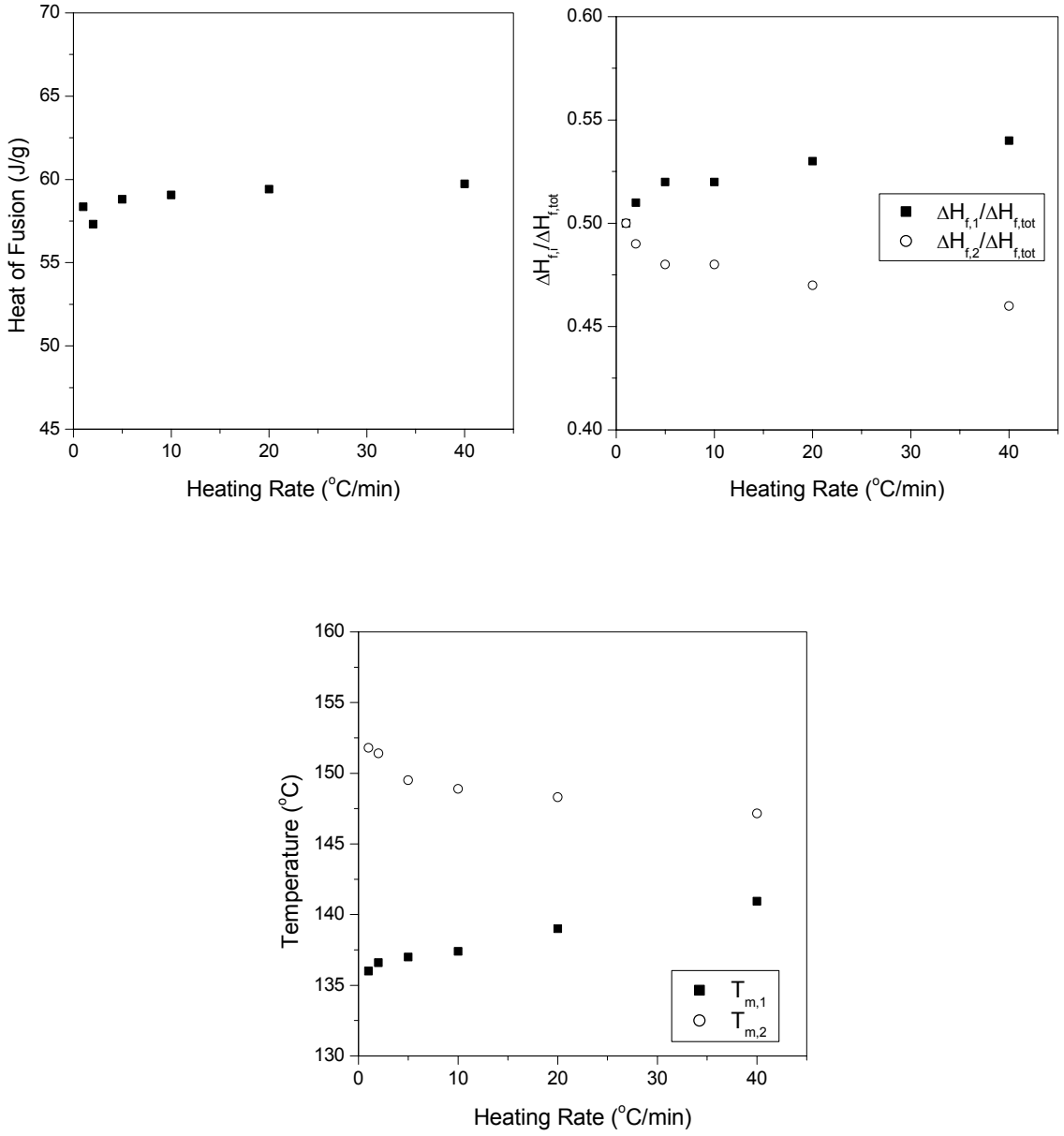

Figure 4.4.12. Effect of heating rate on (a) total heat of fusion, (b) low endotherm ($\Delta H_{f,1}$) and high endotherm heat of fusion ($\Delta H_{f,2}$), and (c) low–melting peak ($T_{m,1}$) and high–melting peak ($\Delta T_{m,2}$) temperatures for iPP2.62 sample crystallized at 126 °C.

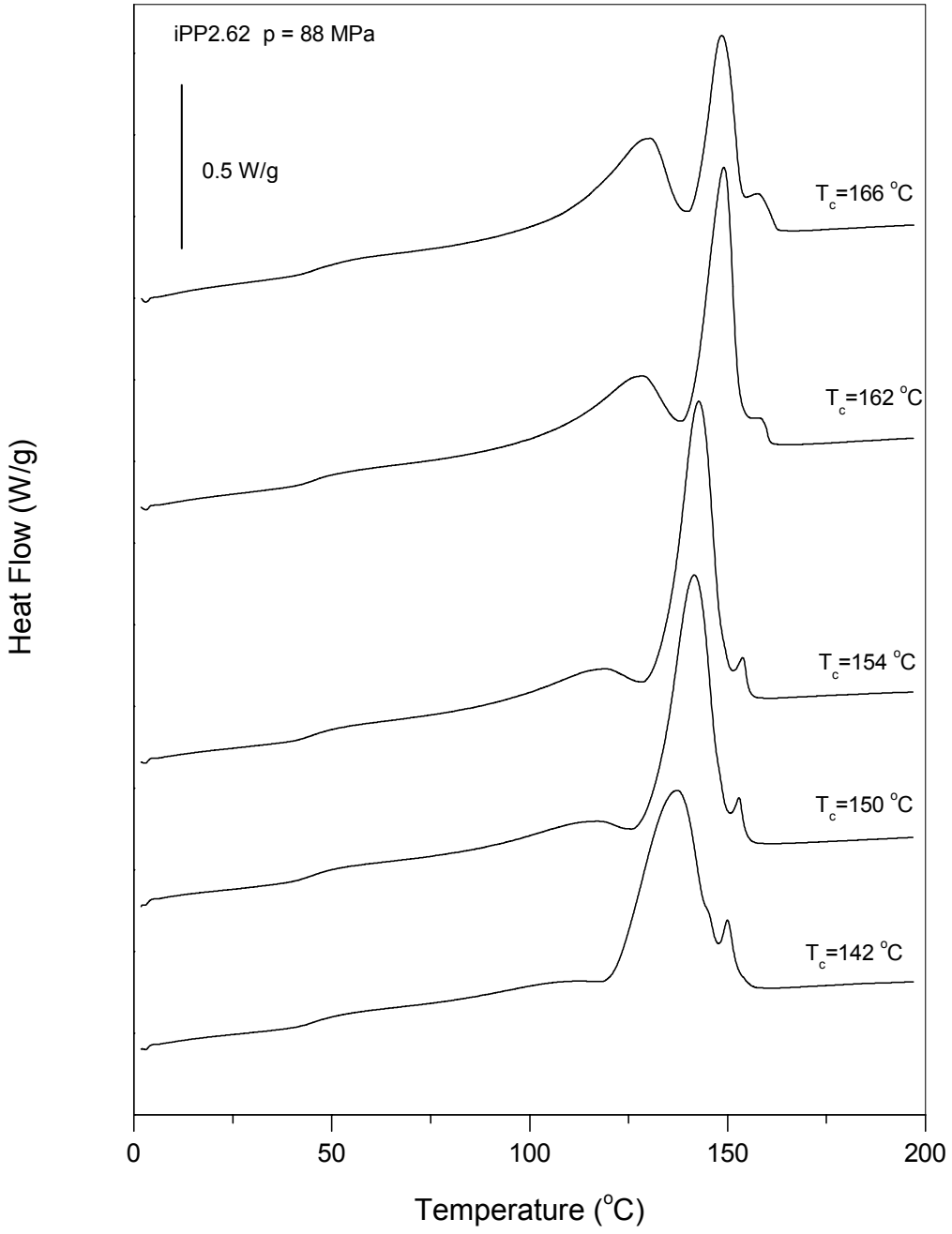

Figure 4.4.13. DSC endotherms for iPP2.62 crystallized at 88 MPa as a function of isothermal crystallization temperature.

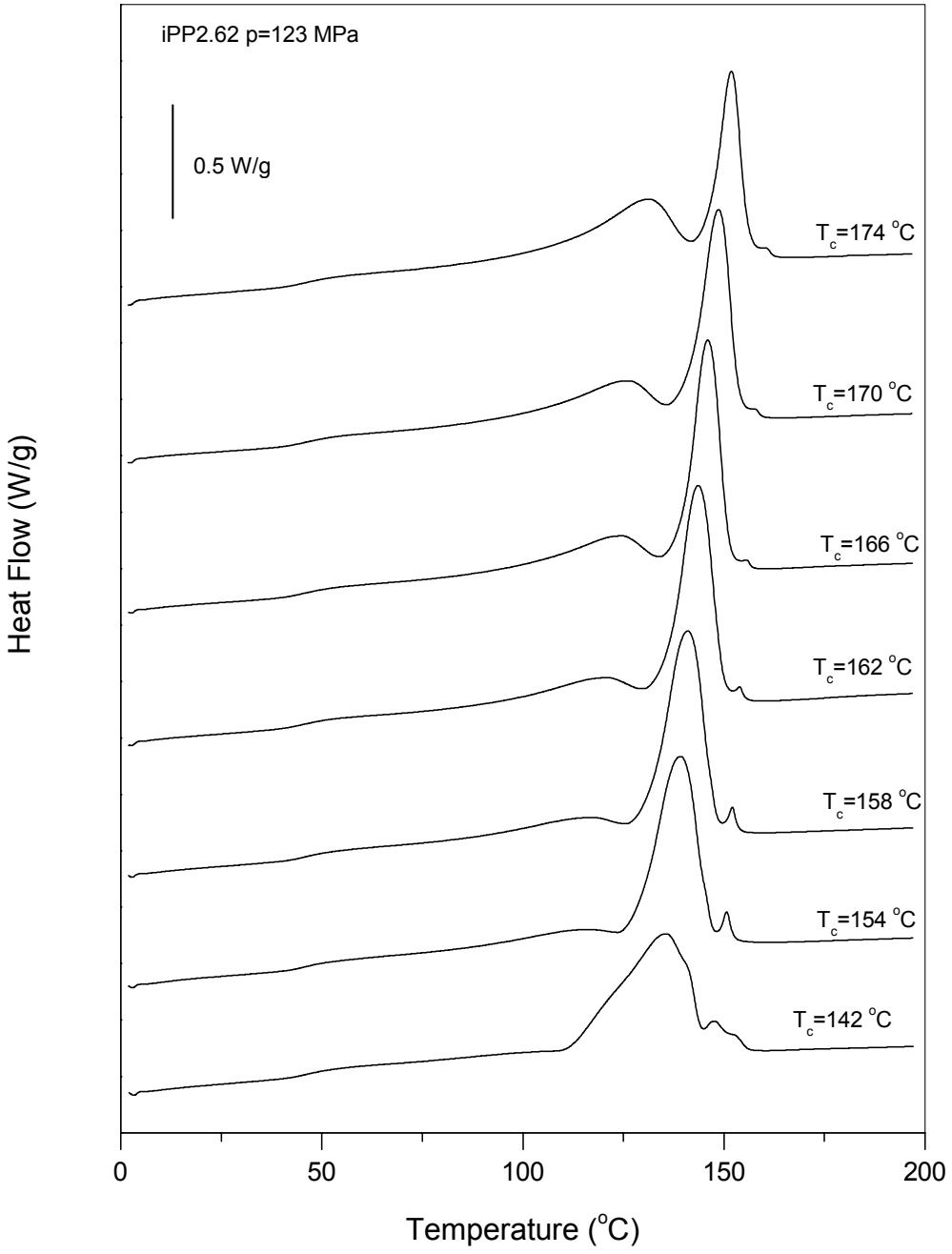

Figure 4.4.14. DSC endotherms for iPP2.62 crystallized 123 MPa as a function of isothermal crystallization temperature.

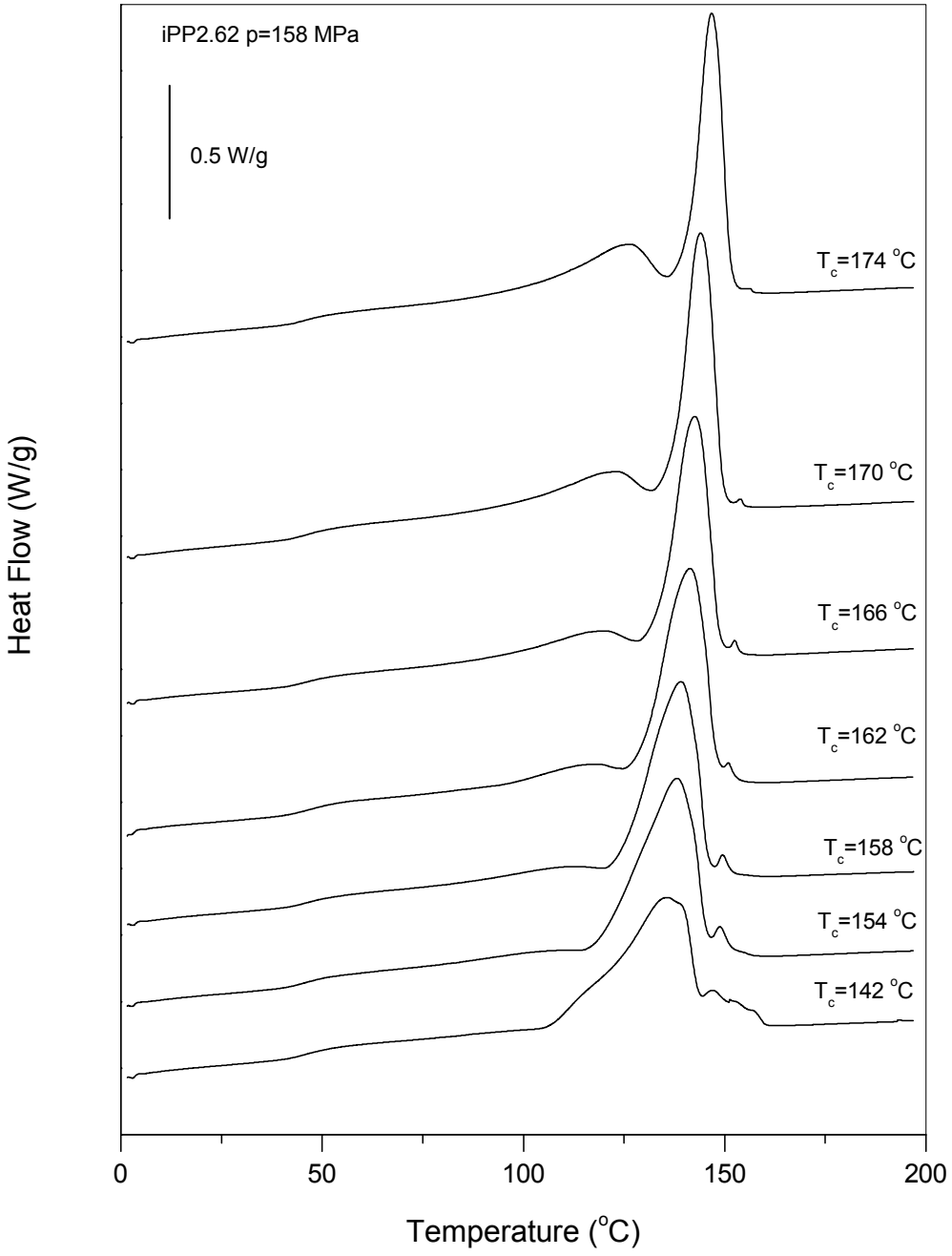

Figure 4.4.15. DSC endotherms for iPP2.62 crystallized at 158 MPa as a function of isothermal crystallization temperature.

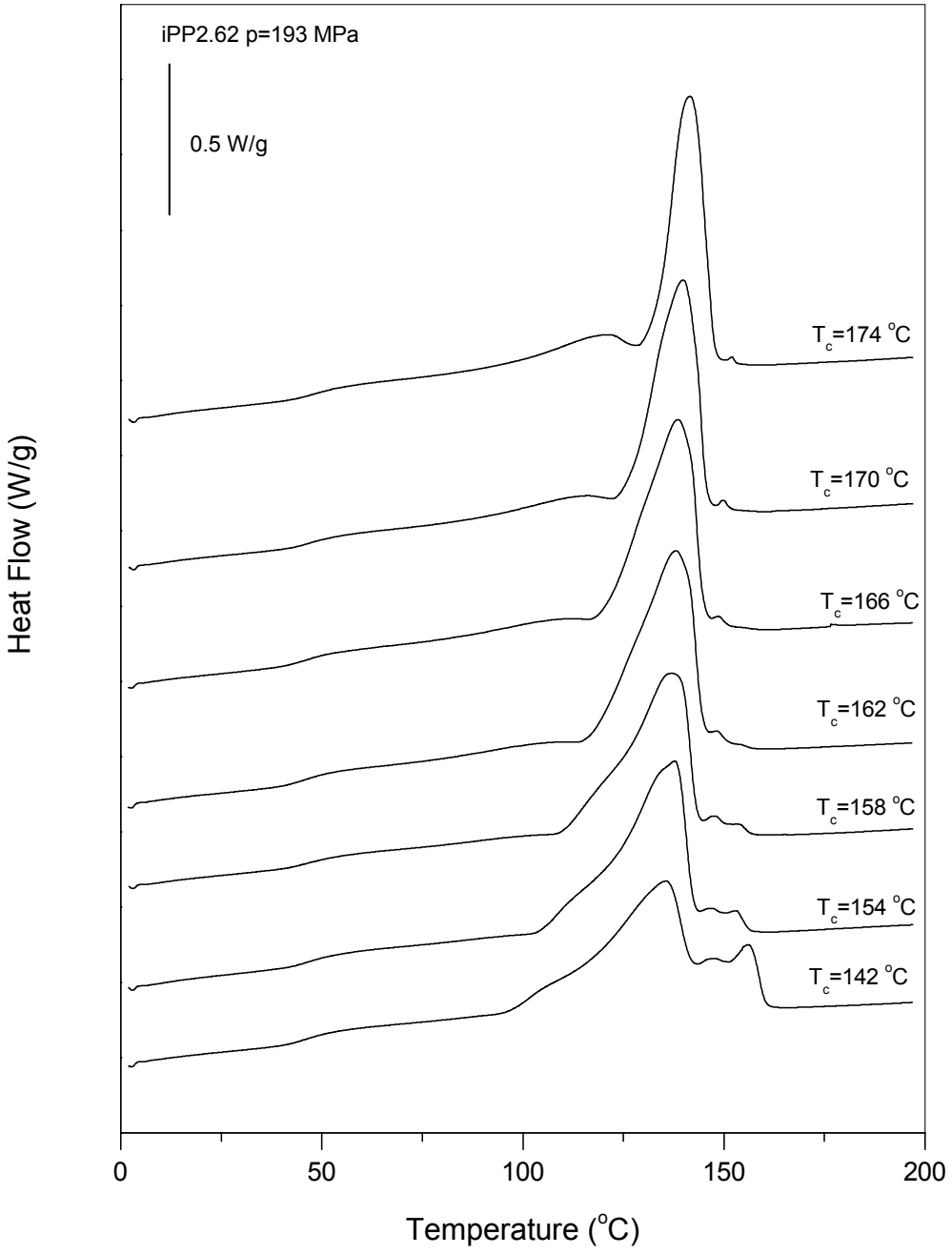

Figure 4.4.16. DSC endotherms for iPP2.62 crystallized at 193 MPa as a function of isothermal crystallization temperature.

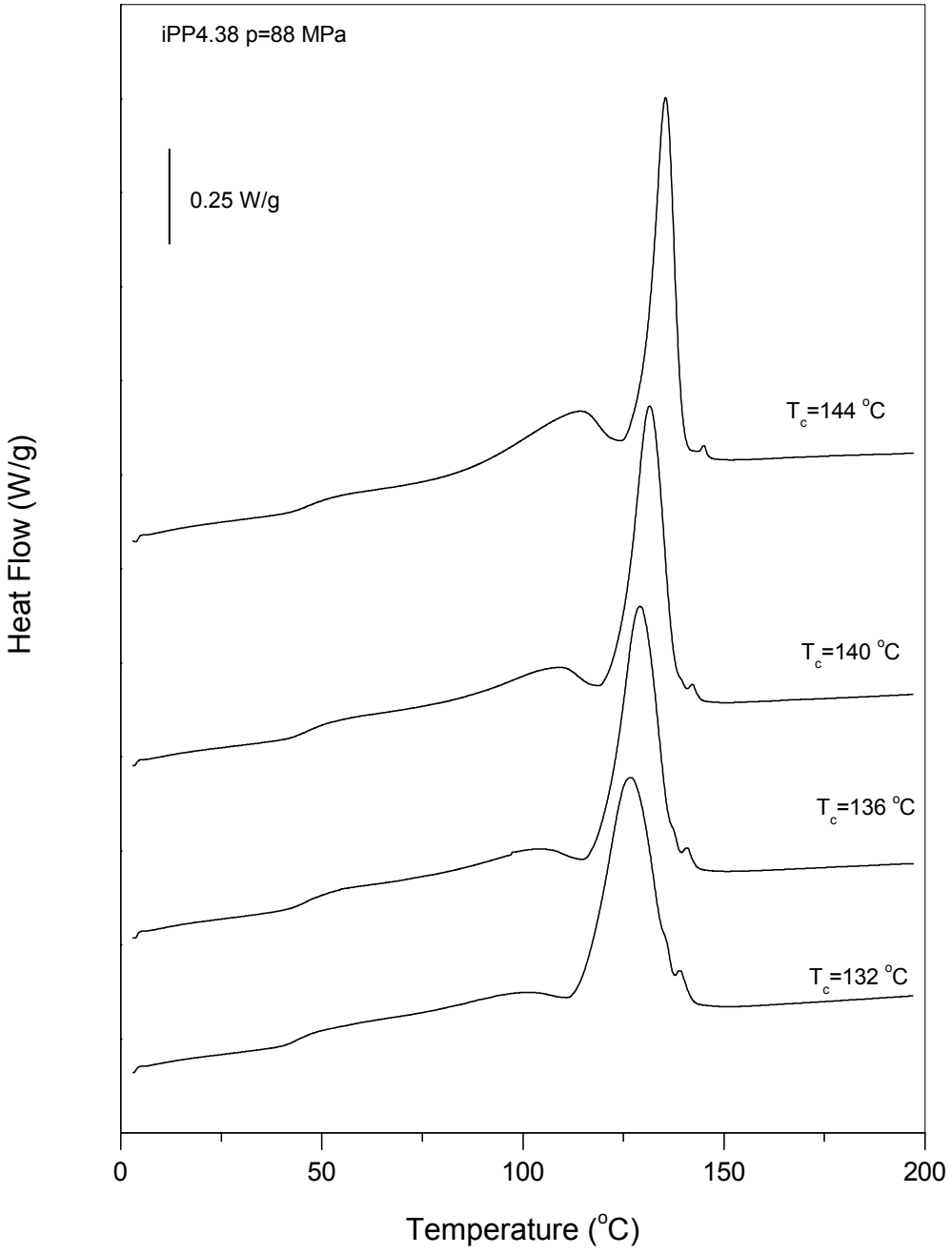

Figure 4.4.17. DSC endotherms for iPP4.38 crystallized at 88 MPa as a function of isothermal crystallization temperature.

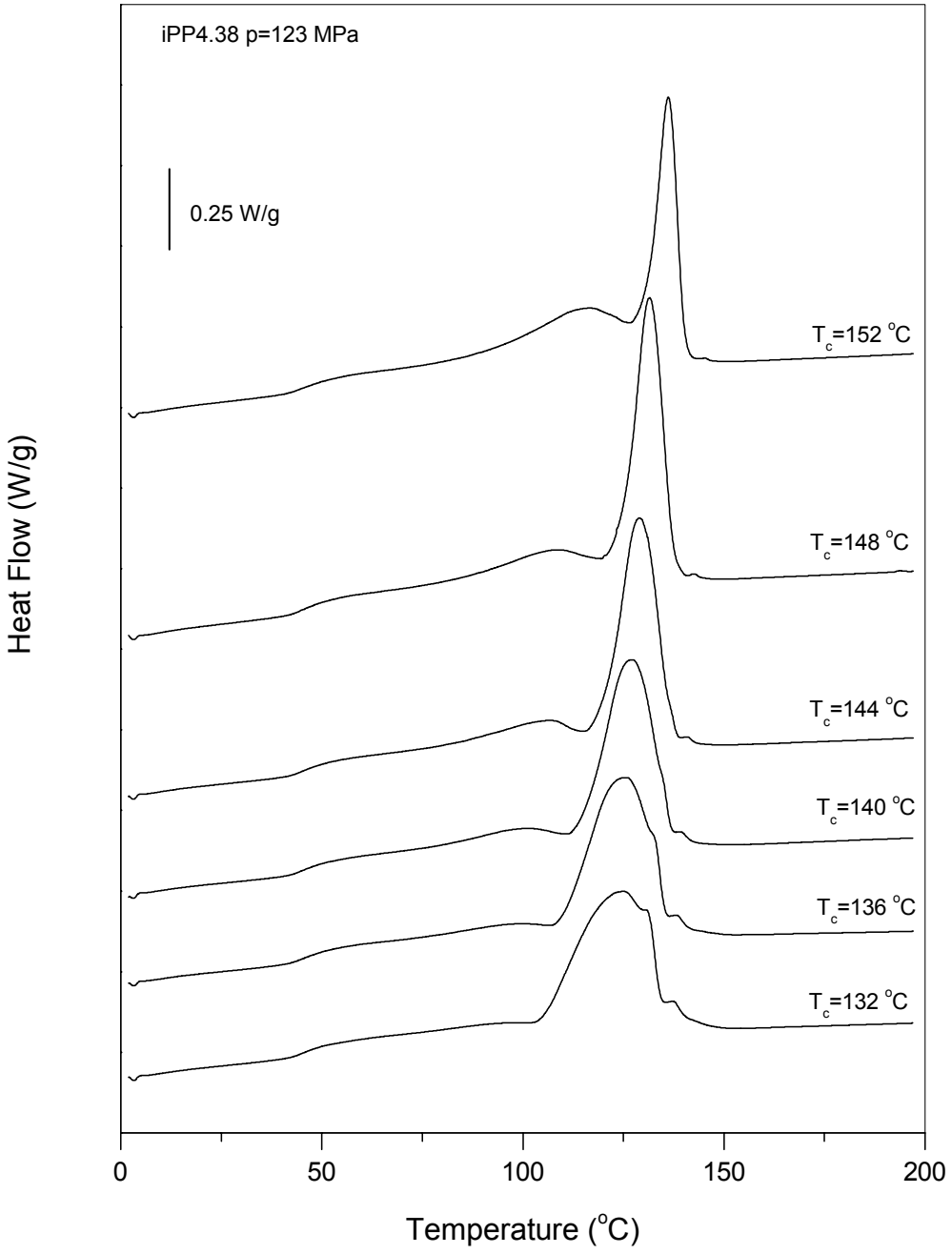

Figure 4.4.18. DSC endotherms for iPP4.38 crystallized at 123 MPa as a function of isothermal crystallization temperature.

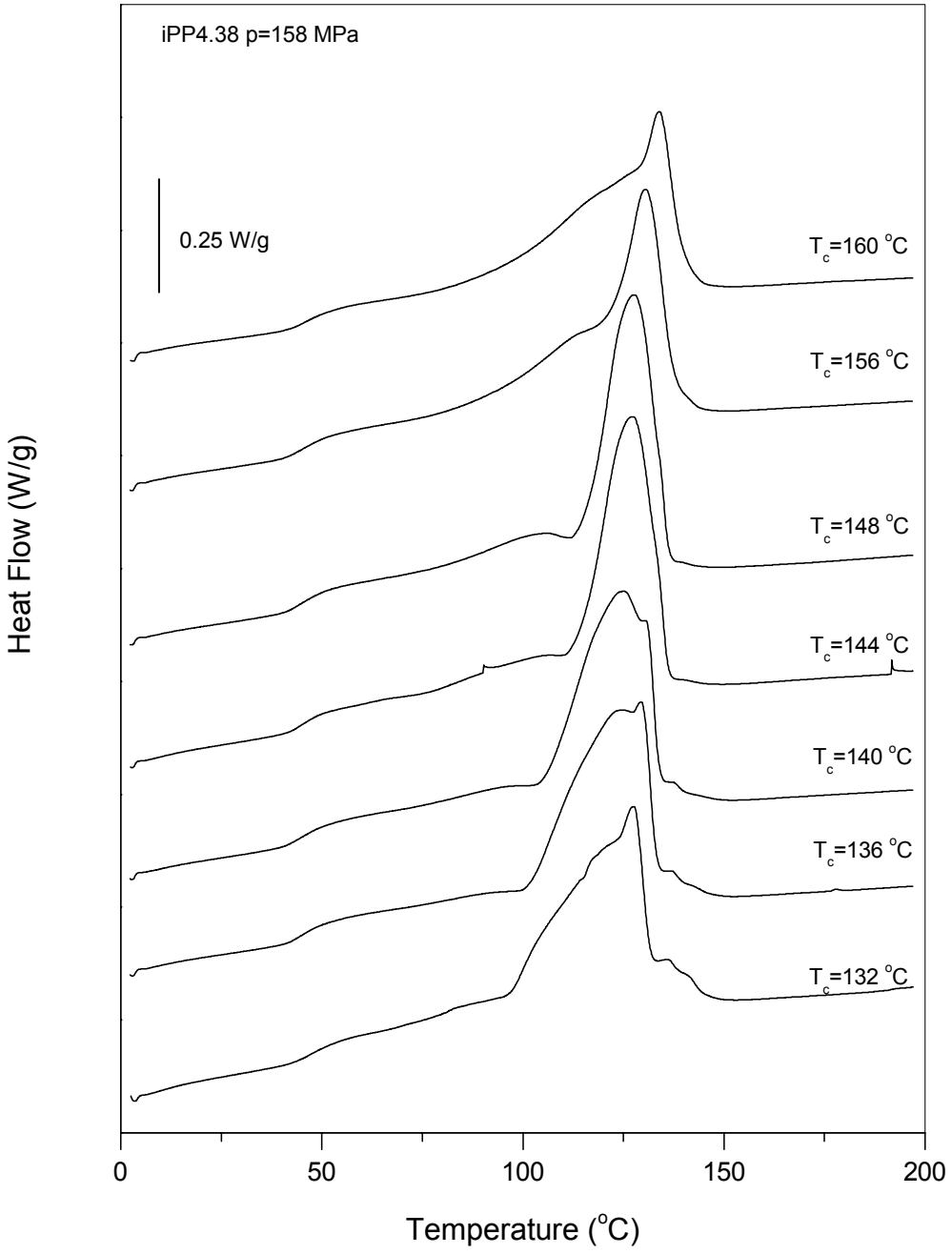

Figure 4.4.19. DSC endotherms for iPP4.38 crystallized at 158 MPa as a function of isothermal crystallization temperature.

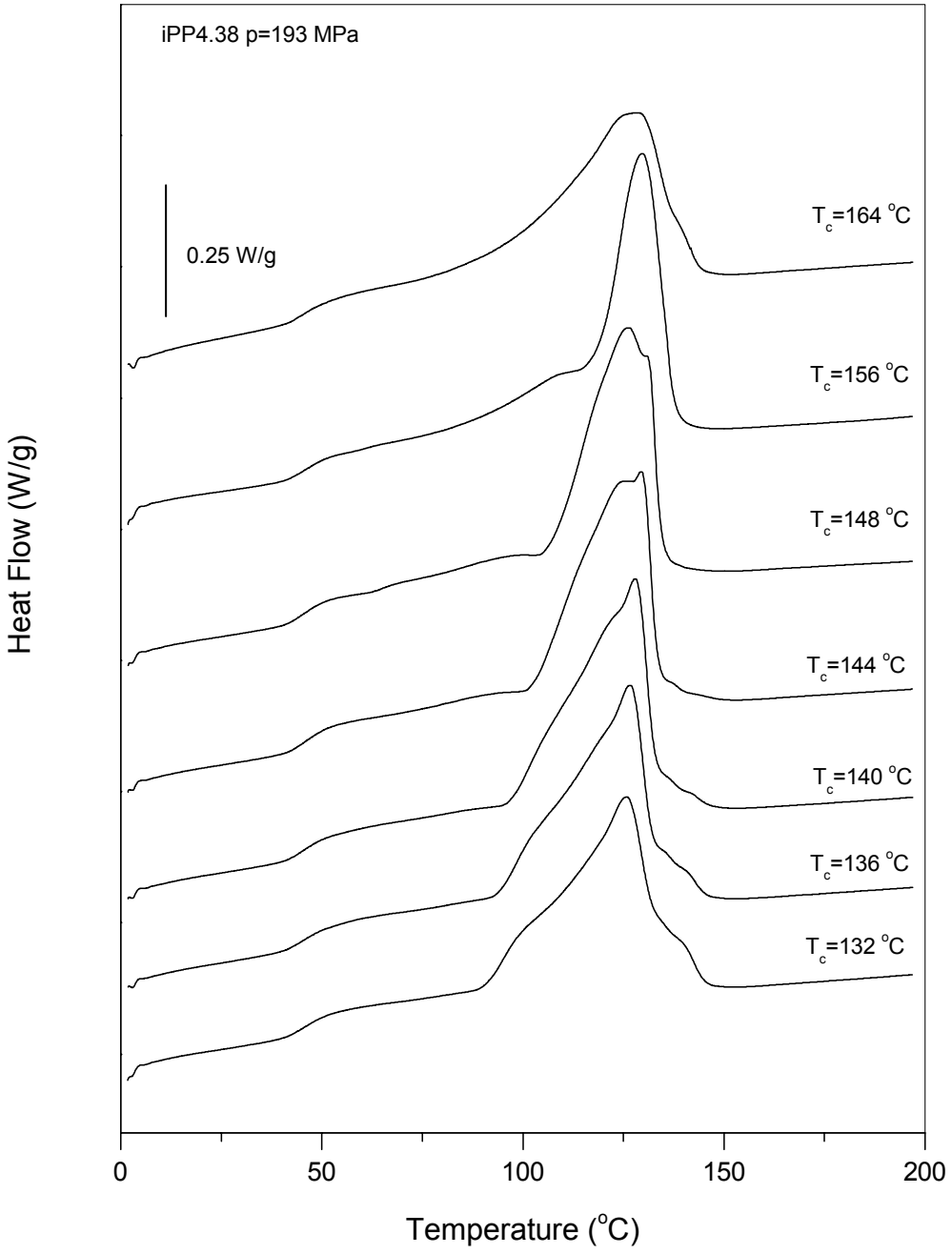

Figure 4.4.20. DSC endotherms for iPP4.38 crystallized at 193 MPa as a function of isothermal crystallization temperature.

Figure 4.4.13 displays the melting endotherms of copolymer iPP2.62 crystallized at a pressure of 88 MPa and several crystallization temperatures. Melting curves exhibit two endotherms, with the higher–temperature endotherm being much smaller than the lower–temperature endotherm. As expected, both peak temperatures increase with increasing crystallization temperature at constant pressure. Similar to the copolymer crystallized at atmospheric pressure, melting curves have a small 'hump' that appears at temperatures below their corresponding crystallization temperatures. As the crystallization temperature is increased the 'hump' becomes larger and better defined. WAXD analysis of these samples at room temperature presented in section 4.3.2 showed that all of them contain both α– and γ– phase crystals.

DSC curves of the copolymer iPP2.62 samples crystallized at pressures of 123, 158 and 193 MPa are shown in Figures 4.4.14 – 4.4.16. For all crystallization temperatures, melting endotherms exhibit one or two small peaks above the main melting peak. WAXD analysis of the copolymer iPP2.62 crystallized at p_c = 193 MPa and temperatures above 162 ^{o}C detected 100 % γ–phase, as seen in Figure 4.3.9, while DSC scans show very small peak. Analysis of the peak area showed that the area of this peak is less than 1 % of the total area.

In contrast with copolymer iPP2.62, iPP4.38 samples crystallized at the highest crystallization temperatures and pressures of 158 and 193 MPa do not exhibit the small melting peak above the main melting peak, as seen in Figures 4.4.19 and 4.4.20.

4.5. High Temperature WAXD of copolymers crystallized at atmospheric pressure

High temperature WAXD experiments were carried out on copolymer samples crystallized at atmospheric pressure in order to determine the concentration of α– and γ–phases as a function of temperature. This method was used to test the hypothesis that

the multiple endotherms in the DSC melting curves discussed in section 4.4.2 are due to the melting of different crystalline phases, namely α– and γ–phase crystals. For this purpose three samples were used, iPP2.62 crystallized at 126 ^{o}C, iPP4.38 crystallized at 120 ^{o}C, and iPP15.57 crystallized at 94 ^{o}C. Experiments were performed at peak temperatures and temperatures bellow and above peak temperatures, that were determined from DSC experiments. This way, the possible disappearance of one of the phases can be followed as the temperature is increased. It is expected that at temperatures below the lowest melting peak both phases will be present. If this hypothesis is valid, with increasing temperature the intensity of the characteristic peak of one of the phases will start to decrease and eventually disappear at a temperature just below the highest melting temperature. In addition, whether any crystal reorganization on heating has occurred can be observed by comparing the WAXD pattern obtained at room temperature and the pattern obtained at temperatures before any significant melting occurred.

It should be pointed out that an increase in the temperature will lead to an increase in the thermal vibration of atoms in the crystalline lattices of the samples. This will affect the diffraction pattern by decreasing the intensities of the diffraction peaks and increasing the intensity of the background scattering. Additionally, the unit cell expands which causes changes in the planar spacing and is manifested as a shift in 2θ positions of diffraction peaks.

Figure 4.5.1 shows the three–dimensional plot of the WAXD intensities as a function of temperature for copolymer iPP2.62 crystallized at 126 ^{o}C and atmospheric pressure. The diffraction patterns were recorded at temperatures indicated by arrows in the endotherm insert in Figure 4.5.1, and are arranged in the main figure from back to front according to increasing temperature.

The room temperature scan shows six strong Bragg reflections, including the two characteristic reflections of the α– and γ–crystals that are of interest, indicated by arrows. As the temperature was increased from 25 ^{o}C to 100 ^{o}C, which is close to the peak of the lowest endotherm, the height of the (117) reflection started to decrease considerably. This

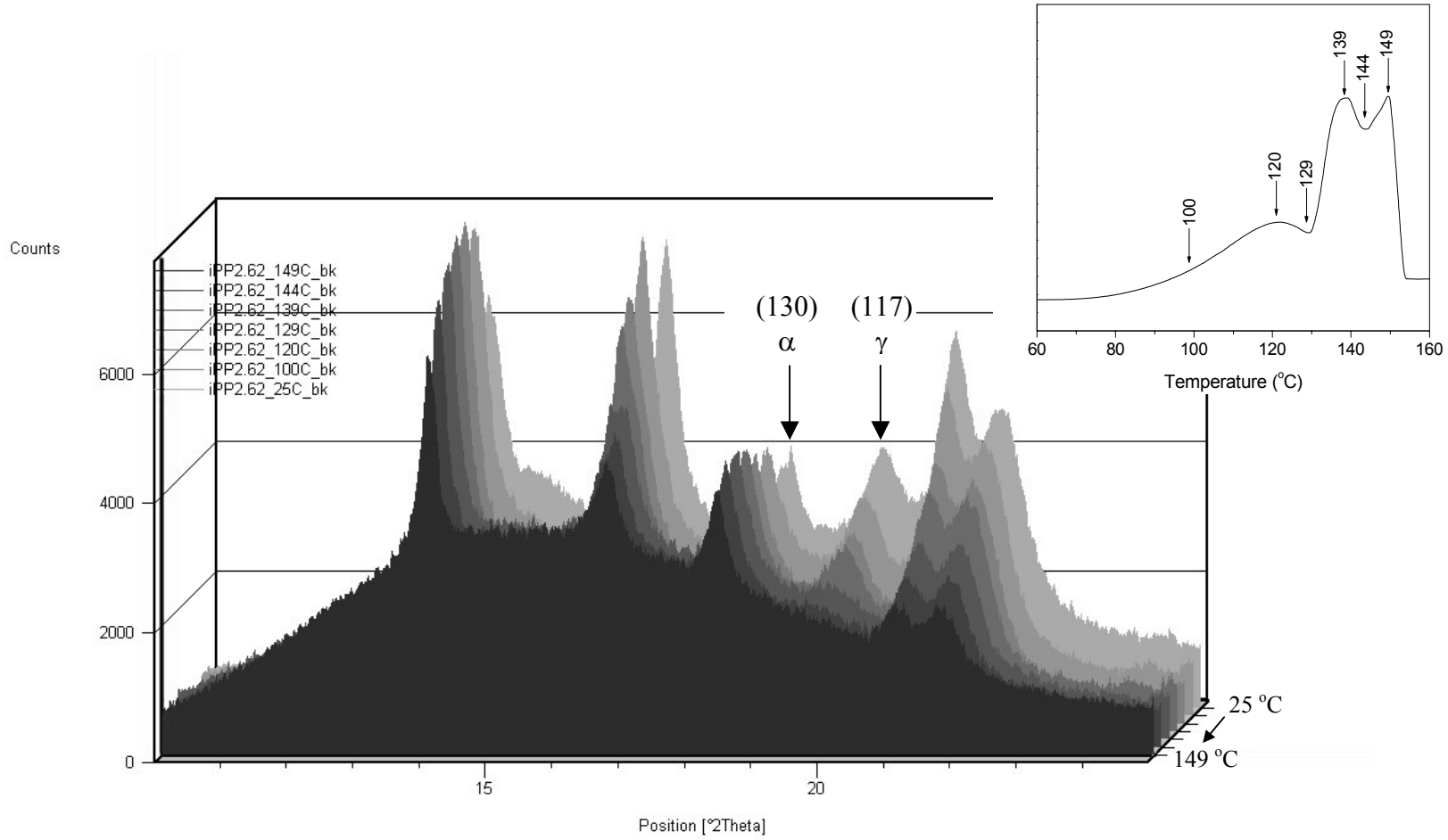

Figure 4.5.1. High Temperature WAXD of copolymer iPP2.62 crystallized at T_c = 126 °C at temperatures indicated in the inset.

indicates that γ–crystals started to melt at lower temperatures than α–crystals. At the same time there was a slight increase in the height of the (130) reflection, which could be an indication of a possible melting–recrystallization process during the heating. The melting of the thinner γ–crystals formed on quenching and their recrystallization into α–crystals on heating can be explained with the low heating rate of 5 ^{o}C/min used in this experiment. With the further increasing of the temperature up to 139 ^{o}C, the (117) reflection has almost disappeared while the height of (130) reflection did not change. Only in the temperature range of 144–149 ^{o}C, which corresponds to the highest endotherm, the height of the (130) reflection and the α–crystals content started to decrease, while the γ–crystals have completely disappeared. From these results it is evident that γ–crystals melt at lower temperatures compared with α–crystals. Accordingly, the lower two endotherms in the DSC melting curves are due to the melting of γ–crystals, while the highest endotherm is due to the melting of α–crystals.

Similar three–dimensional plots for copolymers iPP4.38 and iPP15.57 in their corresponding temperature ranges are shown in Figures 4.5.2 and 4.5.3. Same conclusions can be drawn about the melting of the different crystalline phases in these copolymer samples analogous to the copolymer iPP2.62. It should be emphasized that for the copolymer iPP15.57 it was difficult to discern the changes in the (130) reflection at the highest temperatures. That sample had very high γ–phase content (73 %) and the (130) characteristic peak of the α–phase was very weak even at room temperature measurement. In the high temperature WAXD experiment, the amorphous halo increased considerably with increasing temperature and to some extent overlapped with the (130) reflection.

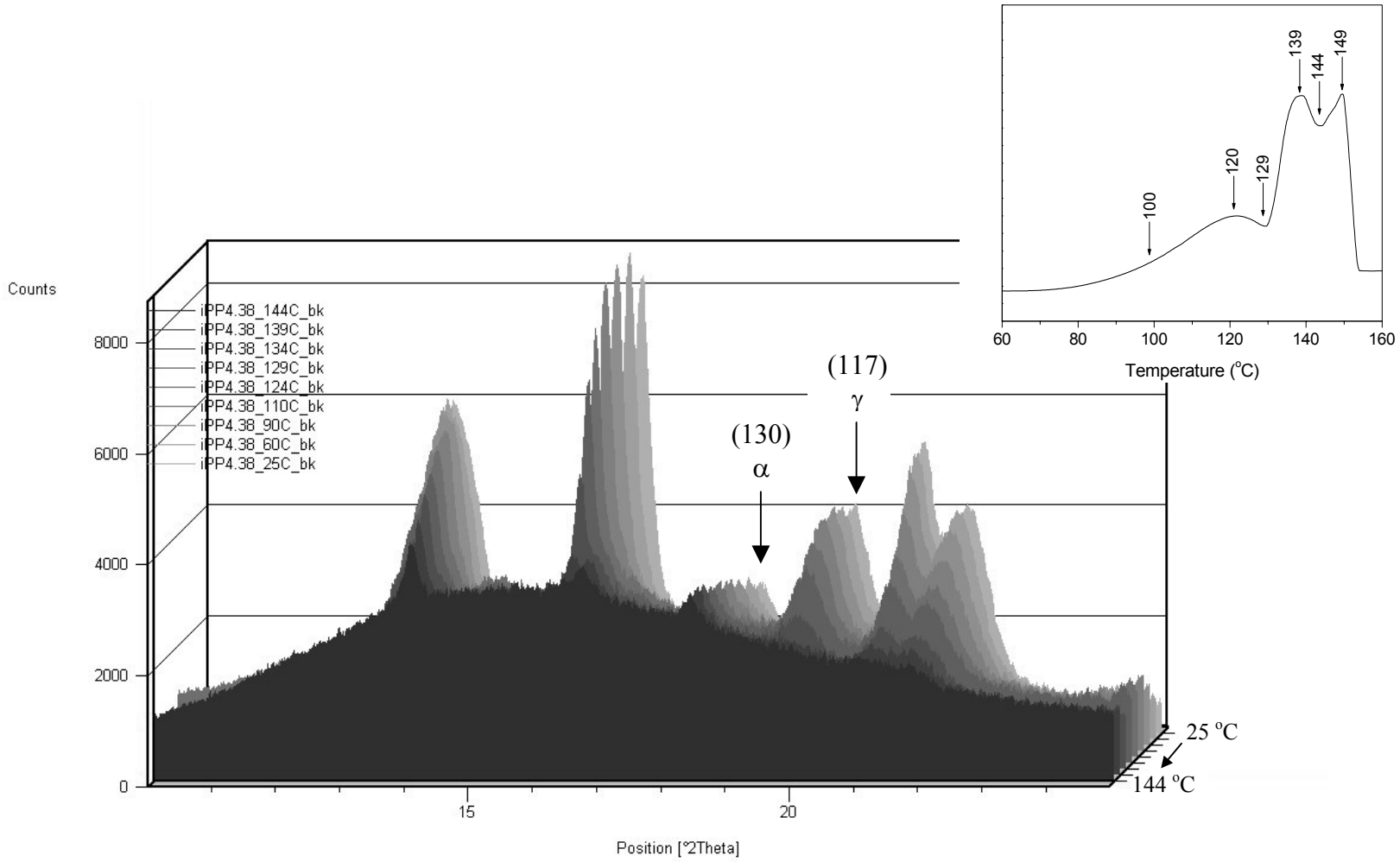

Figure 4.5.2. High Temperature WAXD of copolymer iPP4.38 crystallized at T_c = 120 °C at temperatures indicated in the inset.

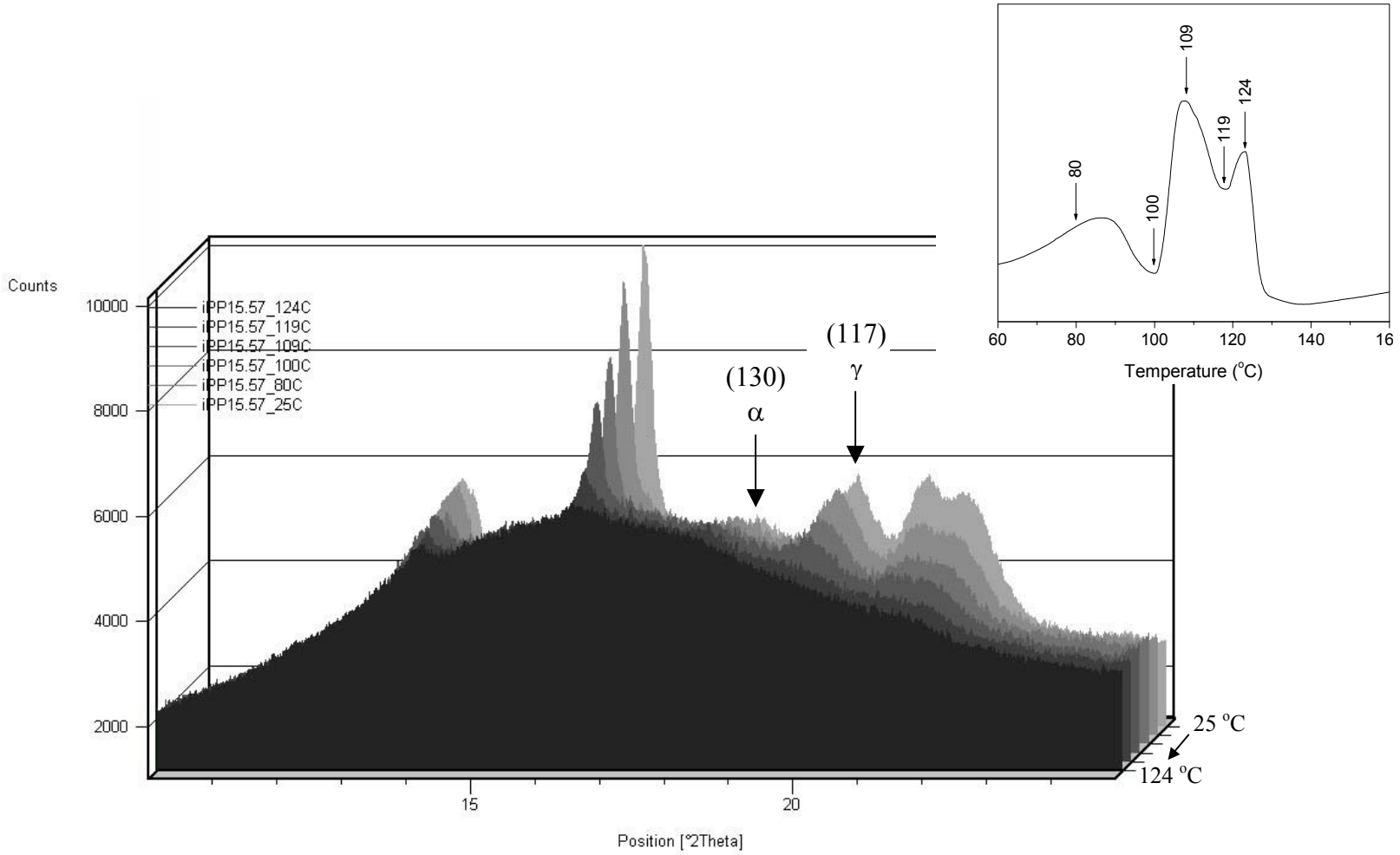

Figure 4.5.3. High Temperature WAXD of copolymer iPP15.57 crystallized at T_c = 94 °C at temperatures indicated in the inset.

4.6. Small Angle X–ray Scattering

SAXS intensity patterns and the derived correlation functions are commonly used for characterization of the polymer morphology. In this study the one–dimensional (1D) correlation function, $K_1(x)$, for the case of a semi–crystalline polymer system was applied to the random propylene–ethylene copolymers.

The focus of the first part of this section are the processing parameters of the original SAXS intensity data, prior to the evaluation of the 1D correlation function. Care has to be taken to avoid introducing artifacts due to the data processing. In the second and third part the experimental SAXS curves and the results from the 1D correlation function analysis are presented. These include the crystalline, amorphous and transition layer thickness, as well as the degree of crystallinity obtained from SAXS as a function of defect content and crystallization conditions (temperature and pressure).

4.6.1. Thermal Fluctuations Correction and Interface Determination

Semi–crystalline polymers can be described in terms of an ideal two–phase model of densely packed, isotropically distributed stacks of parallel crystalline and amorphous layers. In that case the long period can be calculated from the maximum peak position of the Lorentz corrected SAXS intensity patterns using the equation (2.8.3). For the ideal two–phase system with sharp phase boundaries the long period represents a sum of the thickness of the crystalline (ℓ_c) and amorphous phase (ℓ_a). However, the pseudo-two-phase model with diffuse phase boundary is more realistic representation of polymer systems. According to this model the expression for the long period becomes:

$$L = \ell_c + \ell_a + \ell_{tl} \qquad (4.6.1)$$

where ℓ_{tl} is the diffuse transition (or interfacial) layer thickness from the crystalline to the amorphous phase. This transition layer thickness can be determined from SAXS experiments.

In general, there are two approaches for calculating ℓ_{tl} from SAXS data. One is to use the 1D correlation function based on the linear gradient of electron density outlined in section 2.8.2, and the other is to use a modified Porod's law suggested by Ruland.[116,117] In the 1D correlation function approach, the displacement from the slope of the self–correlation triangle can be used to calculate the interfacial layer. However, the modified Porod's law method has been recommended for polymers.[118]

According to Porod's law, for an ideal two–phase system with sharp phase boundaries the scattered intensity decreases proportionally to the q^{-4} at the tail region of the scattering vector:

$$\lim_{q\to\infty} I_{\mathrm{p}}(q) = \frac{K_{\mathrm{p}}^{'}}{q^4} \tag{4.6.2}$$

where $K_{\mathrm{p}}' = (2\pi)^2 \times K_{\mathrm{p}}$, and K_{p} is the so–called Porod's law constant. Porod's law predicts that $I_{\mathrm{p}}(q)\times q^4$ reaches a constant for large values of the scattering vector.

This law provides a means of extrapolation of the scattered intensity to large scattering angles where experimental measurement of the intensity becomes impractical. Polymers often exhibit deviations from Porod's law, which means that the product $I_{\mathrm{p}}(q)\times q^4$ does not reach a constant value. This behavior can be explained by the variations in the microstructure of the polymer. Positive deviation from Porod's law may be due to the presence of thermal density fluctuations or mixing within the phases that results in increased scattering at high angles. It can cause underestimation of the transition layer thickness and overestimation of the invariant. On the other hand, the presence of a diffuse phase boundary causes a reduction of the high–angle scattering resulting in a negative deviation. Ruland[116] has shown that Porod's law may be modified to include the effects of

these deviations and has proposed methods to determine the density fluctuations and the width of the diffuse transition layer.

For accurate determination of the ℓ_{tl} the scattering background due to the electron–density fluctuations within phases has to be determined and subtracted from the net corrected absolute intensity. In this study the electron–density fluctuations that are responsible for positive deviation from Porod's law were calculated using the empirical method proposed by Ruland[119] according to the following equation:

$$I_B(q) = Fl \cdot \exp(b_1 \cdot q^2) \tag{4.6.3}$$

where Fl is the thermal density fluctuation at $I_B(q=0)$, and b_1 is a constant. To determine the Fl and b_1 in this equation, the net corrected absolute intensity $I_{net}(q)$ was fitted in a region where only the $I_B(q)$ is present, that is for $q \to \infty$ (tail region). Values of Fl and b_1 were estimated from the intercept and the slope of the plot of $\ln I_{net}(q)$ vs q^2. The background scattering intensity was then subtracted from the observed intensity:

$$I_{corr}(q) = I_{net}(q) - I_B(q) \tag{4.6.4}$$

The transition layer thickness can be determined depending on the model that describes the electron density profile across the interface layer. In this study the linear–gradient and sigmoidal–gradient models were used and are shown in Figure 4.6.1.

According to the linear–gradient model, the thickness of the transition layer was determined by fitting the linear tail region in the plot of $I(q) \times q^4$ versus q^2. The value of ℓ_{tl} was calculated from the intercept and slope of the linear region using the following equation:

$$\ell_{tl} = E = \sqrt{\frac{-12 \cdot \text{slope}}{\text{intercept}}} \tag{4.6.5}$$

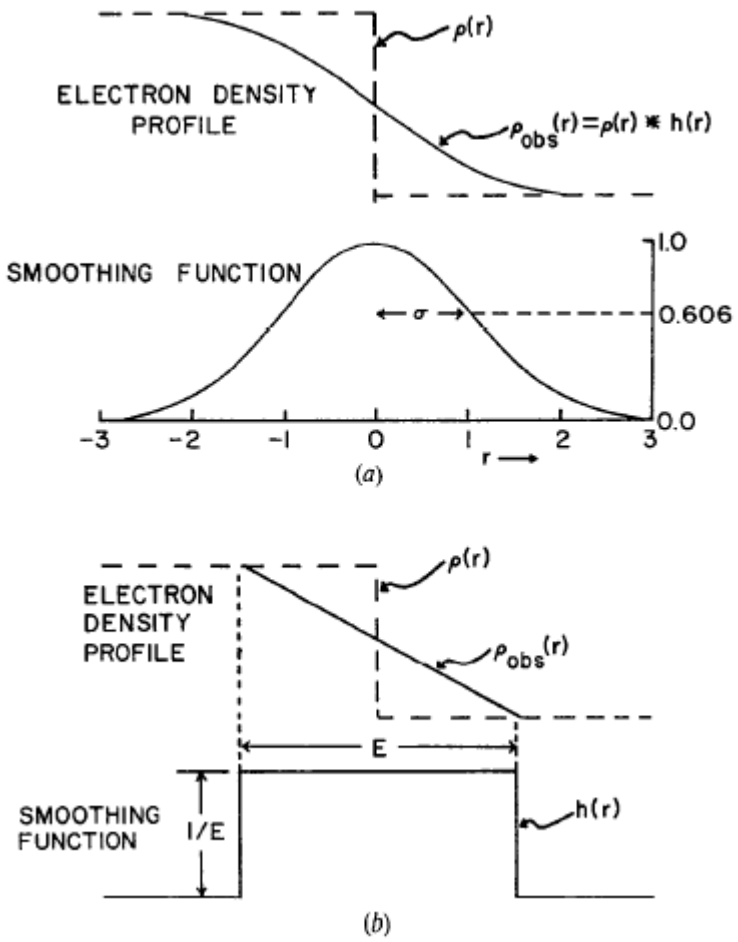

Figure 4.6.1. Electron–density profile, $\rho_{obs}(r)$, and smoothing function, $h(r)$, for (a) sigmoidal–gradient model, (b) linear–gradient model.[118]

For the sigmoidal–gradient model ℓ_{tl} was determined by fitting the linear tail region of the plot of $\ln[I(q)\times q^4]$ versus q^2, according to the following equation:

$$\ell_{tl} = \sigma = \sqrt{\frac{-\text{slope}}{\text{intercept}}} \tag{4.6.6}$$

The successful application of these equations for calculating the transition layer thickness depends on having a reliable tail intensity region. The scattering intensity in the tail region can be extrapolated to large values of the scattering vector using the Porod's or modified Porod's law. Significant errors can be introduced if there is high–scattering intensity in the tail region, or if the extrapolation is performed from a low angle region which has not reached the background. It has been shown that the type of extrapolation used does not affect the major part of the 1D correlation function, but that it affects the self–correlation triangle (Figure 2.8.2) from which the transition layer is determined.[120] Therefore, in this study if reliable tail region was obtained from the 1.5 m geometry, then the scattering data were extrapolated to the high q region. Otherwise, data from both 1.5 m and 0.5 m geometries were used for evaluation of the 1D correlation function.

4.6.2. SAXS of copolymers crystallized at atmospheric pressure

The corrected net absolute SAXS intensity as a function of the scattering vector for the copolymer iPP2.62 crystallized at several temperatures is shown in Figure 4.6.2. It can be observed that as the crystallization temperature increases from 104 ^{o}C to 116 ^{o}C, the scattering intensity increases and the position of the maximum shifts to lower scattering vectors. However, starting at T_c = 120 ^{o}C the scattering peaks are not well defined and resemble a shoulder (see curves indicated with arrows). Also, the intensity starts to decrease with increasing crystallization temperature up to 126 ^{o}C.

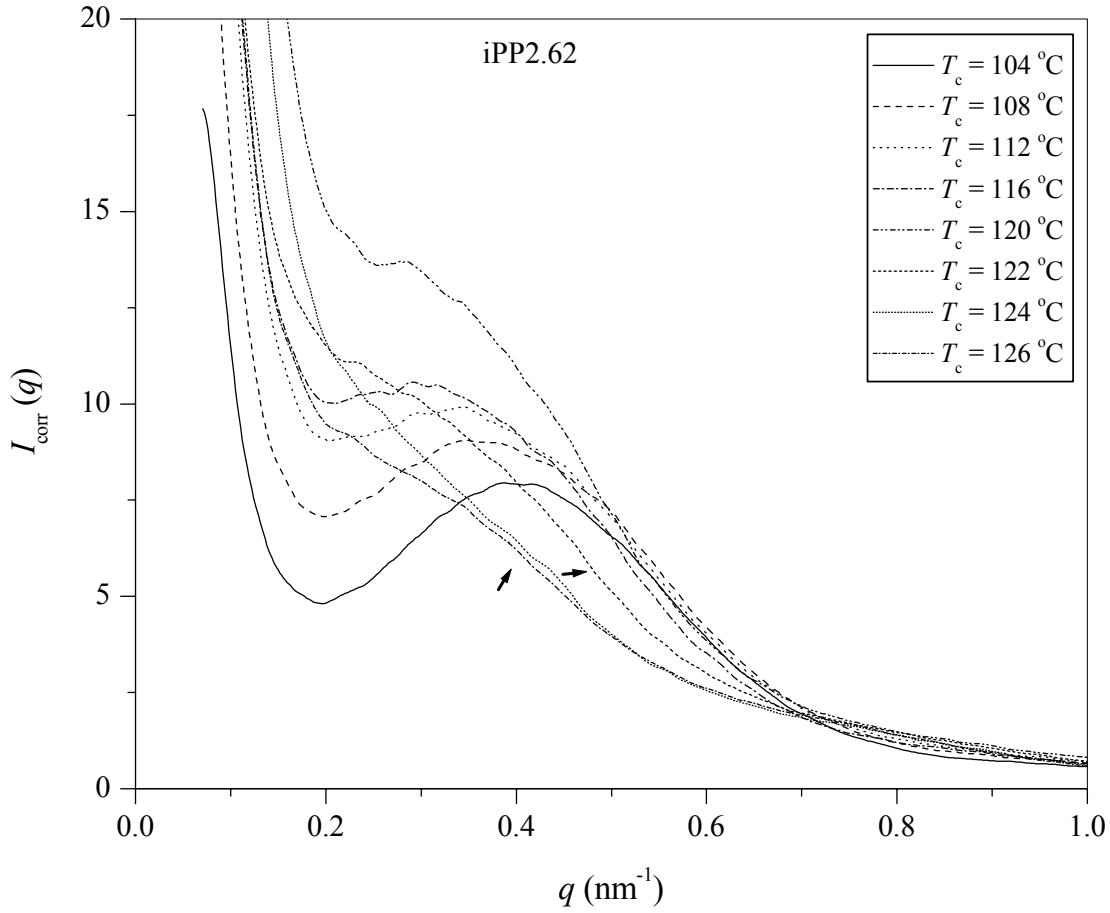

Figure 4.6.2. SAXS intensity profiles for iPP2.62 copolymer crystallized at different temperatures.

Lorentz corrected intensity profiles of these samples are shown in Figure 4.6.3. On this figure well defined peaks are visible even for the samples that did not show distinct peaks in the scattering intensity profiles. They also show second maximum indicated by arrow in Figure 4.6.3, which for some of the samples is not well defined and is shaped as a shoulder. In the studied temperature range, with increasing crystallization temperature both peaks shift to lower q–values. If the ratio of the scattering vectors at these peaks has a value of approximately 2 then the peak at the higher q–value is a second order peak that corresponds to the same periodicity. The q_2/q_1 ratio for the samples crystallized below T_c = 120 ^oC was in the range of 1.9 to 2.0. But for the samples crystallized in the temperature range of 120 – 126 ^oC, this ratio had values from 1.6 to 1.8 indicating that it is not a second order peak.

In order to better observe the occurrence of the second peak, Lorentz corrected intensities for the samples crystallized in the temperature range of 120 – 126 ^oC together with the sample crystallized at 104 ^oC are plotted in Figure 4.6.4. Curves are shifted along the y–axis for clarity. It can be observed that the intensity of the second peak increases significantly with the increase of crystallization temperature. For T_c = 104 ^oC the intensity of the second peak is 35 % of the first peak, for T_c = 122 ^oC it is 80 %, and for the T_c = 126 ^oC both peaks almost have the same height. The ratio q_2/q_1 which is less than 2 and the increased intensity of the second peak indicate that the second maximum is not a higher order diffraction peak.

The net corrected scattered intensity curves of copolymer iPP4.38 crystallized at different crystallization temperatures are shown in Figure 4.6.5. In a similar fashion as copolymer iPP2.62, the peak position shifted to lower q–values as the crystallization temperature was increased. At higher crystallization temperatures (above T_c = 120 ^oC), the shape of the curves changed, with the peak starting to resemble a shoulder and the intensity of the curves starting to decrease, as indicated with arrows.

Lorentz corrected intensity profiles of copolymer iPP4.38 crystallized at different crystallization temperatures are shown in Figure 4.6.6, shifted on y–axis for clarity. With

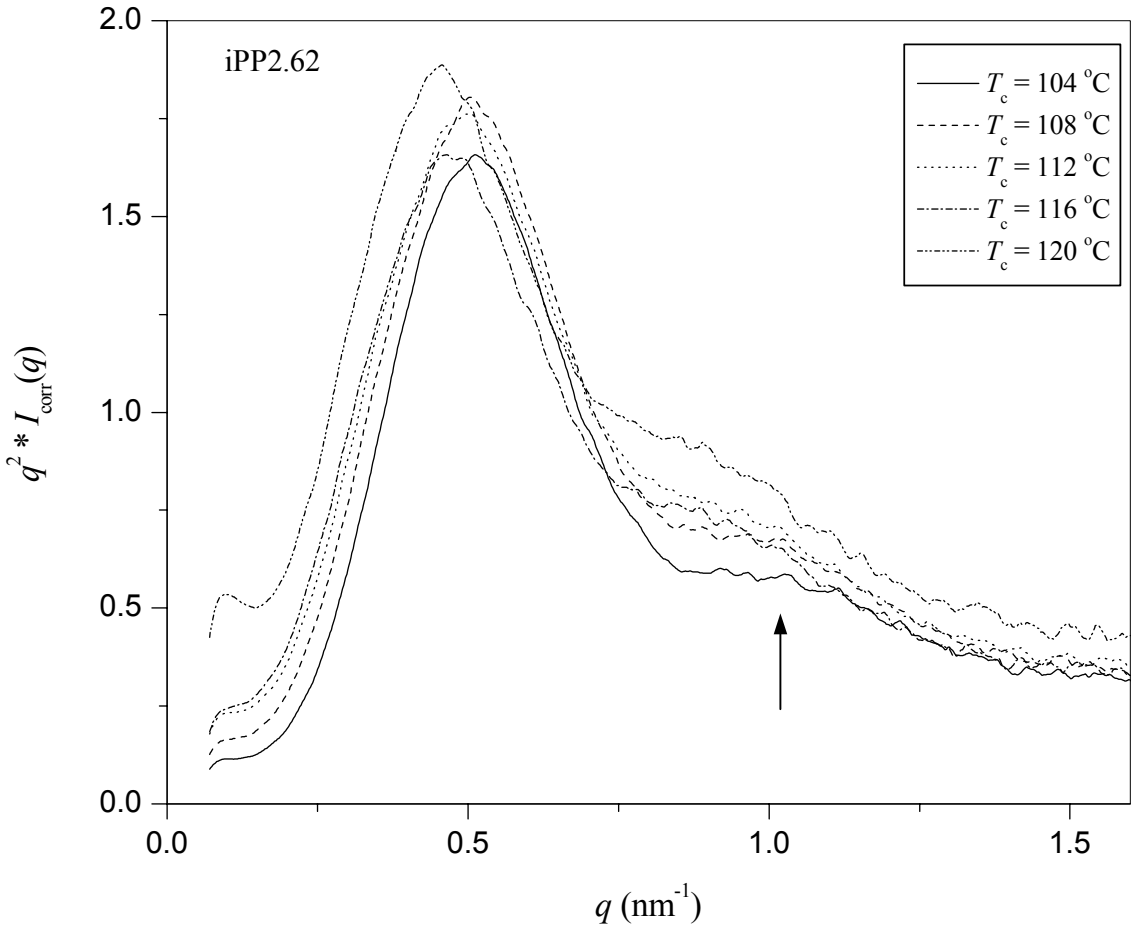

Figure 4.6.3. Lorentz corrected intensity profiles for copolymer iPP2.62 crystallized at different temperatures.

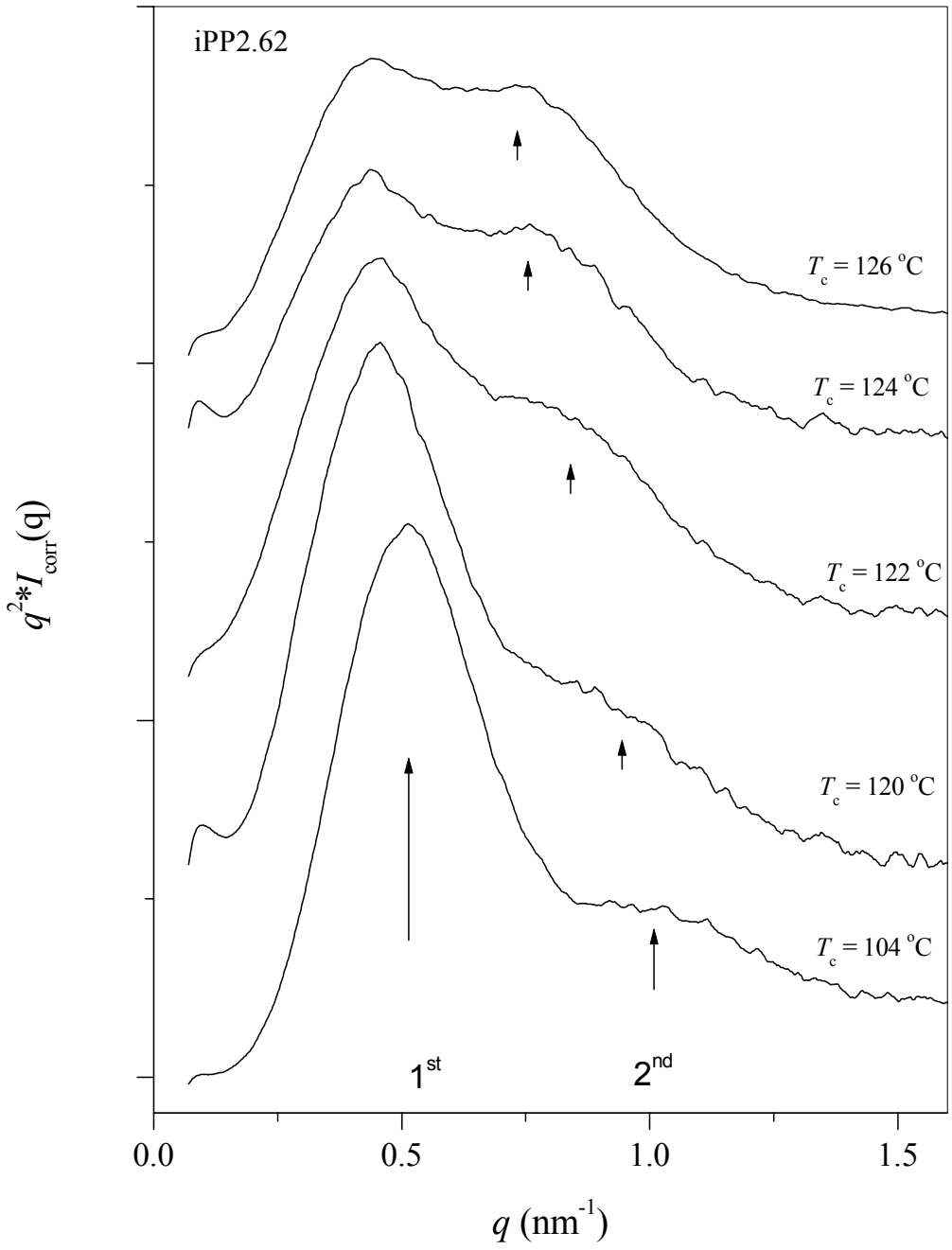

Figure 4.6.4. Lorentz corrected intensity profiles for copolymer iPP2.62 samples that exhibit unusual second maximum. Curves are shifted on y−axis for clarity.

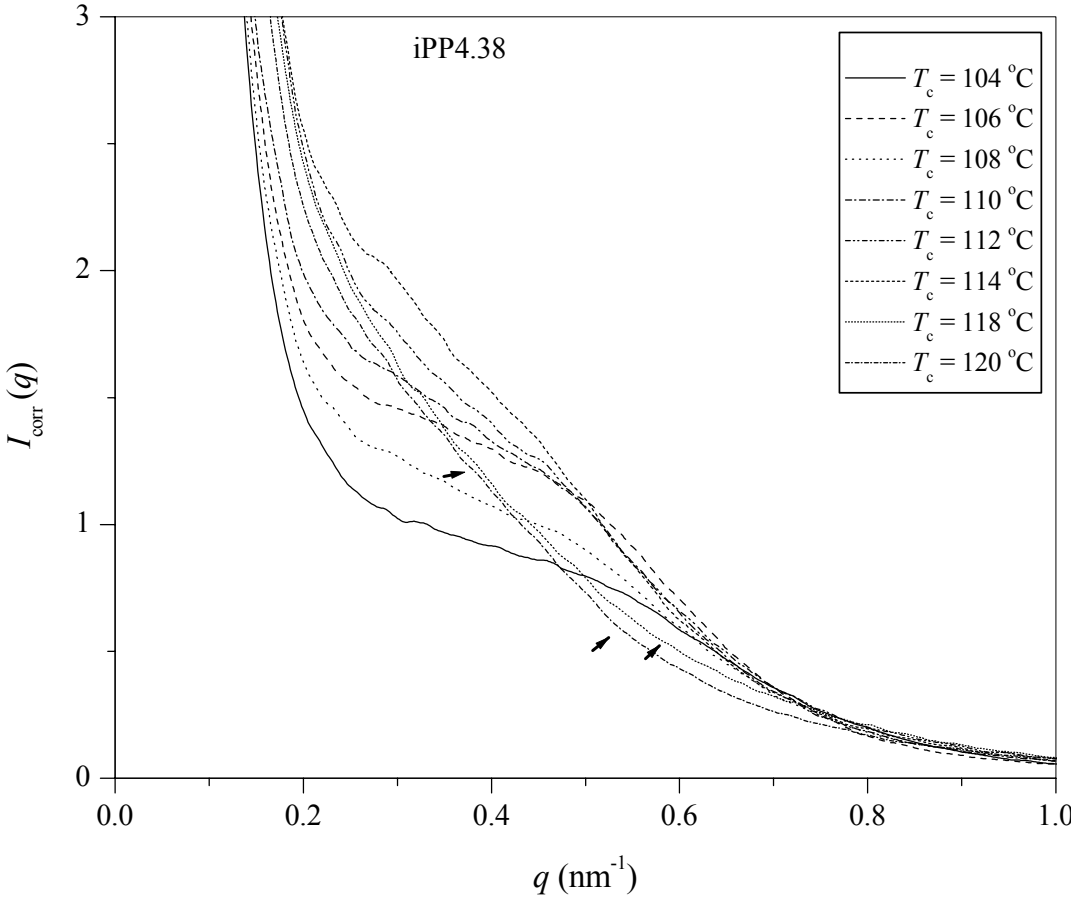

Figure 4.6.5. SAXS intensity profiles for copolymer iPP4.38 crystallized at different temperatures.

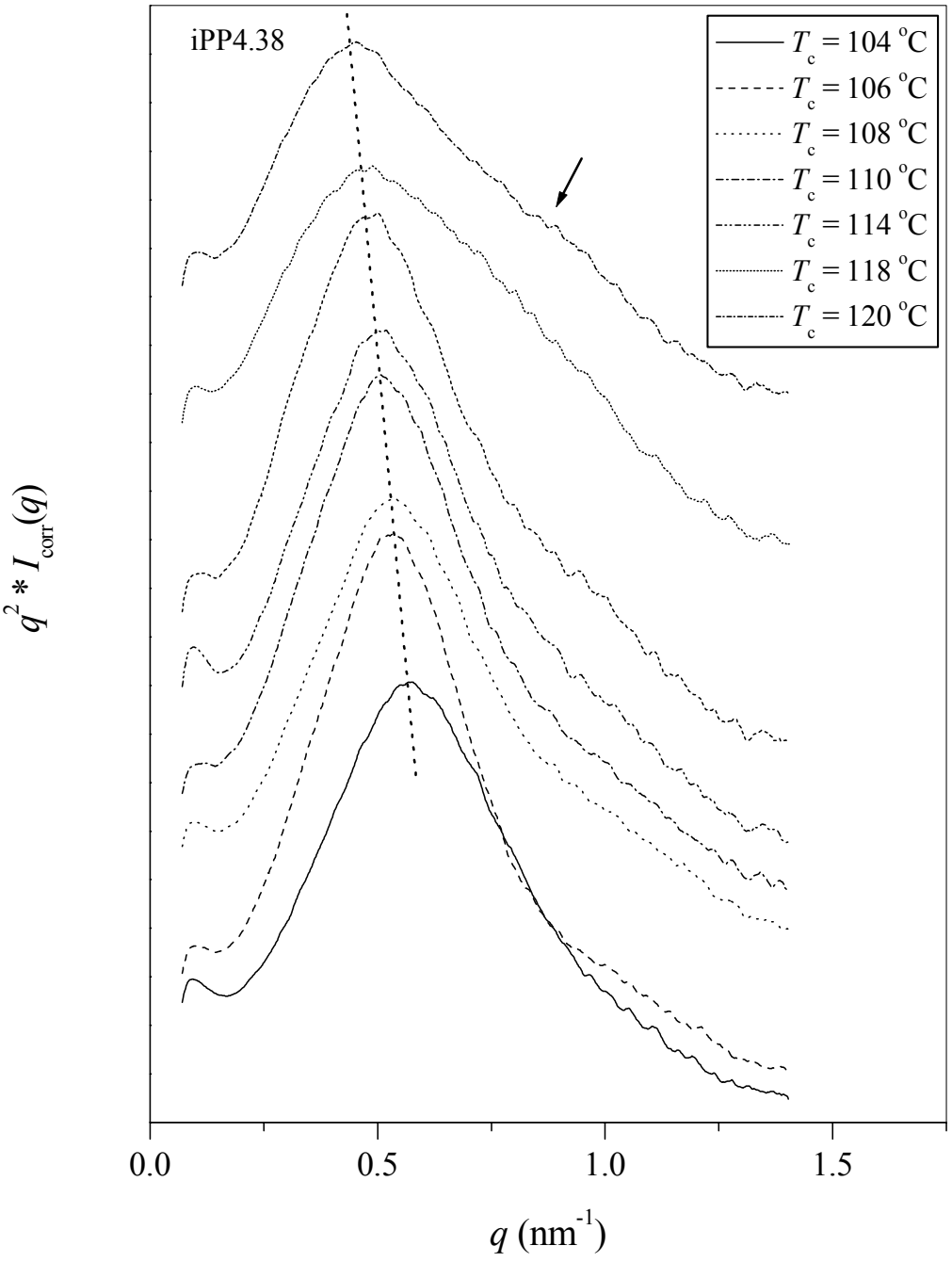

Figure 4.6.6. Lorentz corrected intensity profiles for iPP4.38 samples that exhibit unusual second maximum. Curves are shifted on y–axis for clarity.

increasing crystallization temperature peaks shift to lower values, indicating increase in the long period. For the two highest crystallization temperatures there is also an increase in the width of the peak and an increase in the second peak intensity. This peak broadening is indicated with arrow in Figure 4.6.6.

The net corrected scattering intensities of the copolymer iPP10.45 for several crystallization temperatures are shown in Figure 4.6.7. The corresponding Lorentz corrected curves, shifted along the y–axis, are shown in Figure 4.6.8. For these samples the overall scattering intensity is low and decreases with increasing crystallization temperature. Lorentz corrected data show one distinct peak, whose width increases with temperature.

The corrected net absolute SAXS intensities as a function of the scattering vector and crystallization temperature for copolymer iPP15.57 are shown in Figure 4.6.9. The corresponding Lorentz corrected curves, shifted on y–axis for clarity, are presented in Figure 4.6.10. It can be observed that with increasing crystallization temperature the intensity of the peaks increases, and the peak position shifts to lower values of the scattering vector. However, for iPP15.57 this shift is much smaller compared with the other copolymers. The width of the Lorentz corrected peaks slightly increased with increasing crystallization temperature, but the second peak was not observed.

4.6.3. One–Dimension Correlation Function Analysis

The net corrected scattered intensity of the crystallized copolymer samples was treated as described in section 4.6.1. Scattering data were corrected for the thermal density fluctuations using Ruland's method, and the thickness of the transition layer was determined for the linear-gradient and sigmoidal-gradient model. Then, the corrected

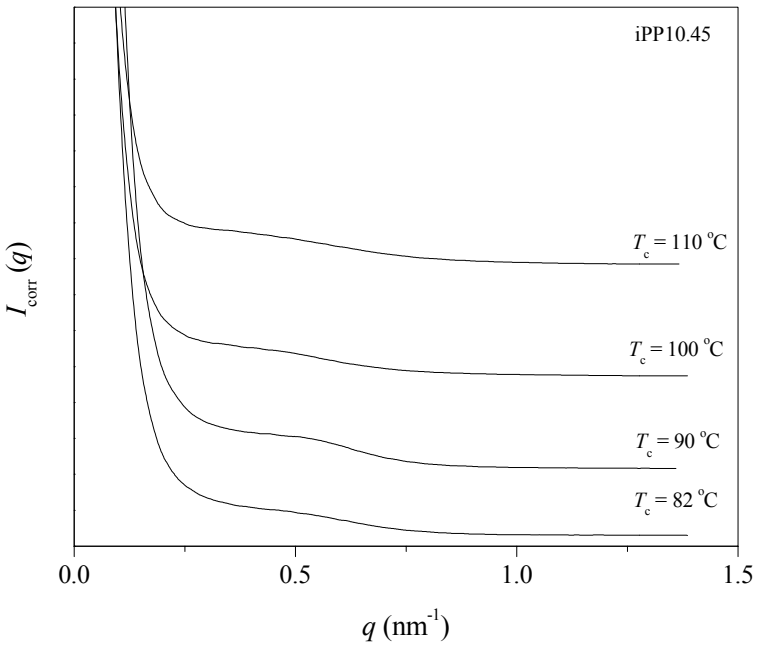

Figure 4.6.7. SAXS intensity profiles for copolymer iPP10.45 crystallized at different temperatures.

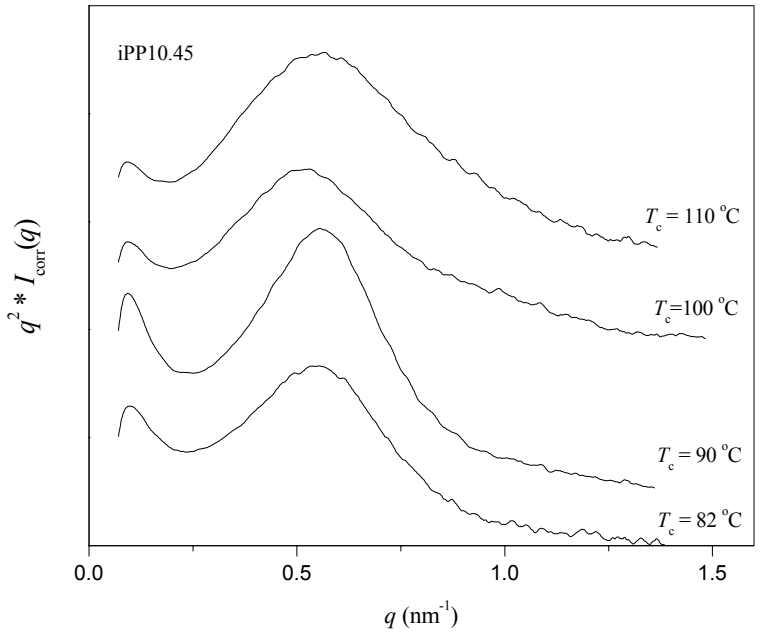

Figure 4.6.8. Lorentz corrected intensity profiles for copolymer iPP10.45 crystallized at different temperatures. Curves are shifted on y–axis for clarity.

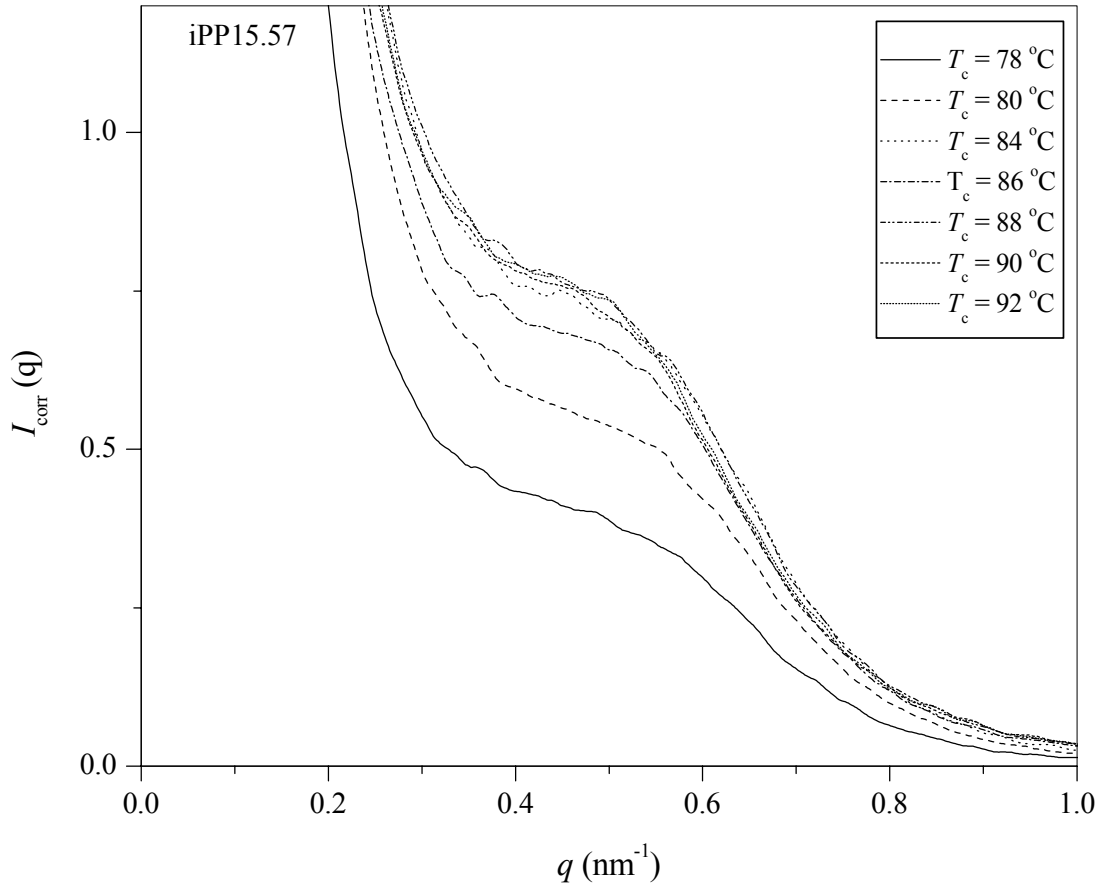

Figure 4.6.9. SAXS intensity profiles for copolymer iPP15.57 crystallized at different temperatures.

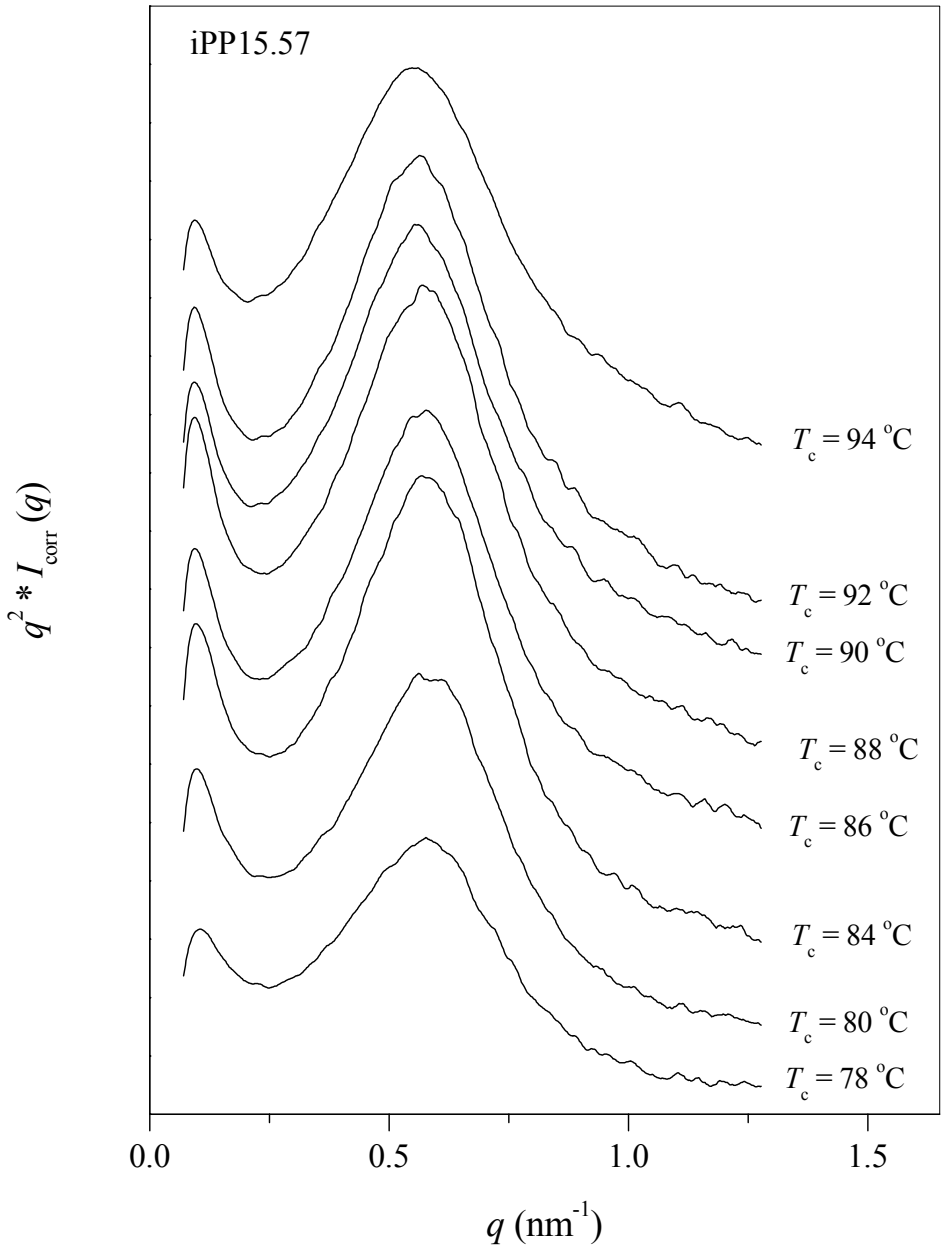

Figure 4.6.10. Lorentz corrected intensity profiles for copolymer iPP15.57 crystallized at different temperatures. Curves are shifted on y–axis for clarity.

data were extrapolated to low and high q–values using Porod–like function of the following form:

$$I_{\text{corr}} = K_{\text{p}}^{'} \cdot q^{-b} \tag{4.6.7}$$

where K_{p}' is the Porod's law constant, and $b = -4$ for ideal two–phase system with sharp boundaries. Propylene–ethylene copolymer samples used in this study exhibited negative deviation from Porod's law, and showed values close to, or less than the theoretical value of –4. Extrapolated Lorentz corrected curves were used to generate the 1D correlation functions. Normalized 1D correlation functions and the method of the self–correlation triangle, as described in section 2.8.2, were used to determine the long period, crystalline, amorphous and transition layer thickness, as well as the invariant and the electron density difference. For this procedure a MathCad routine originally written by Stein Schreiber[121] was modified for degree of crystallinity above 50 %.

Normalized 1D correlation functions $K(x)$ of the copolymer iPP2.62 as a function of crystallization temperature are shown in Figure 4.6.11. The increase of crystallization temperature is marked with arrows. In general, with increasing crystallization temperature the slope of the self–correlation triangle decreases, the position of second maximum increases, and the position of the first minimum gradually decreases. Since some of the curves overlap, for clarity they are presented individually in Figure 4.6.12.

It can be observed that with increasing crystallization temperature the shape of the 1D correlation function changes significantly. Whereas samples crystallized in the range of 104 ^{o}C to 114 ^{o}C exhibit the usual shape of the curve going through a minimum and a maximum, at 118 ^{o}C a slight skewing of the first minimum can be observed. With further increasing of the crystallization temperature the 'skewed minimum' develops into 'double–minimum'. At the same time, the position of the second maximum shifts to considerably larger values. Samples that showed an unusually high second peak in the Lorentz corrected data show this atypical 1D correlation function. The existence of a

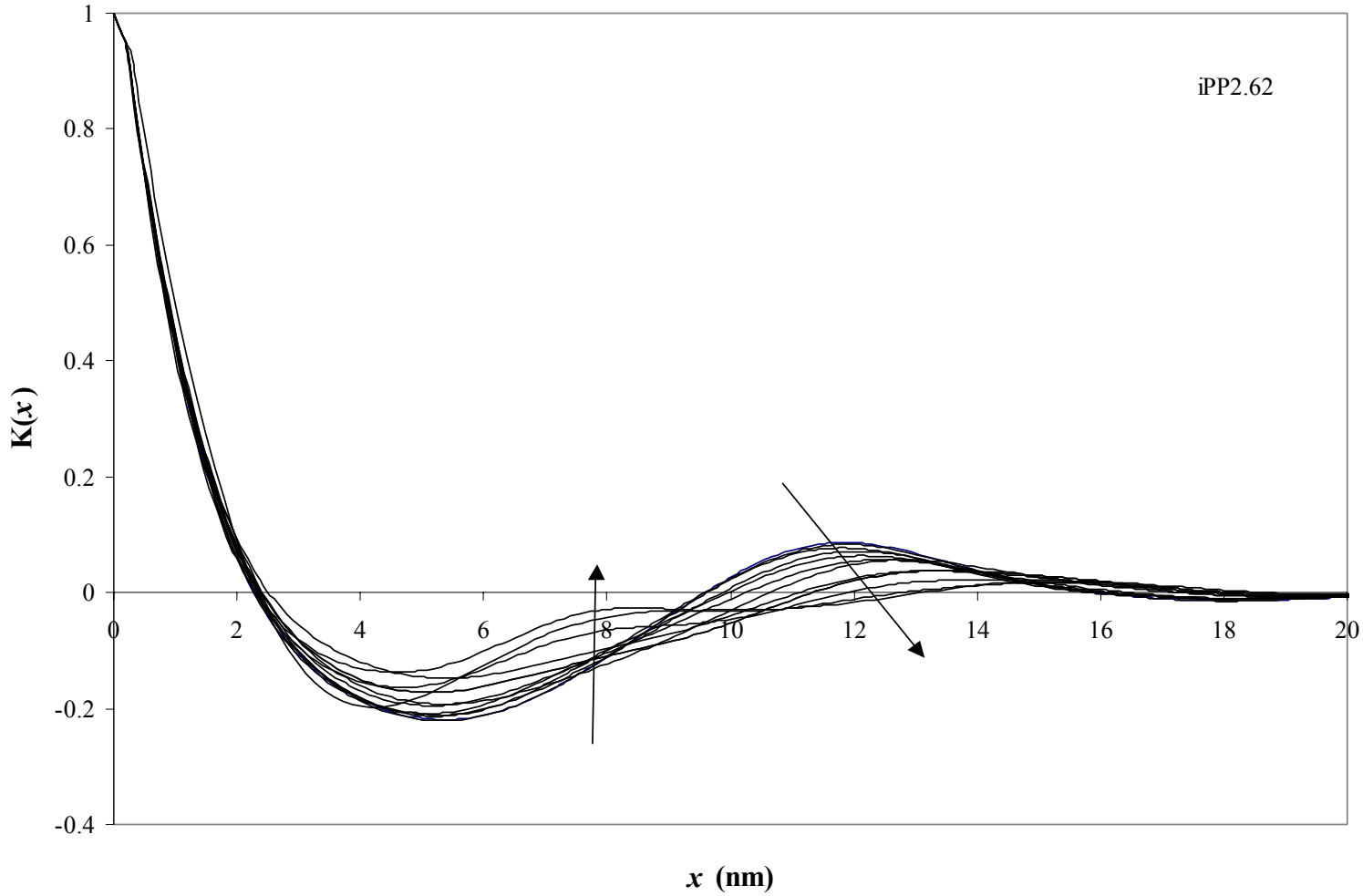

Figure 4.6.11. 1D correlation function of copolymer iPP2.62. Increasing crystallization temperature is indicated with arrows.

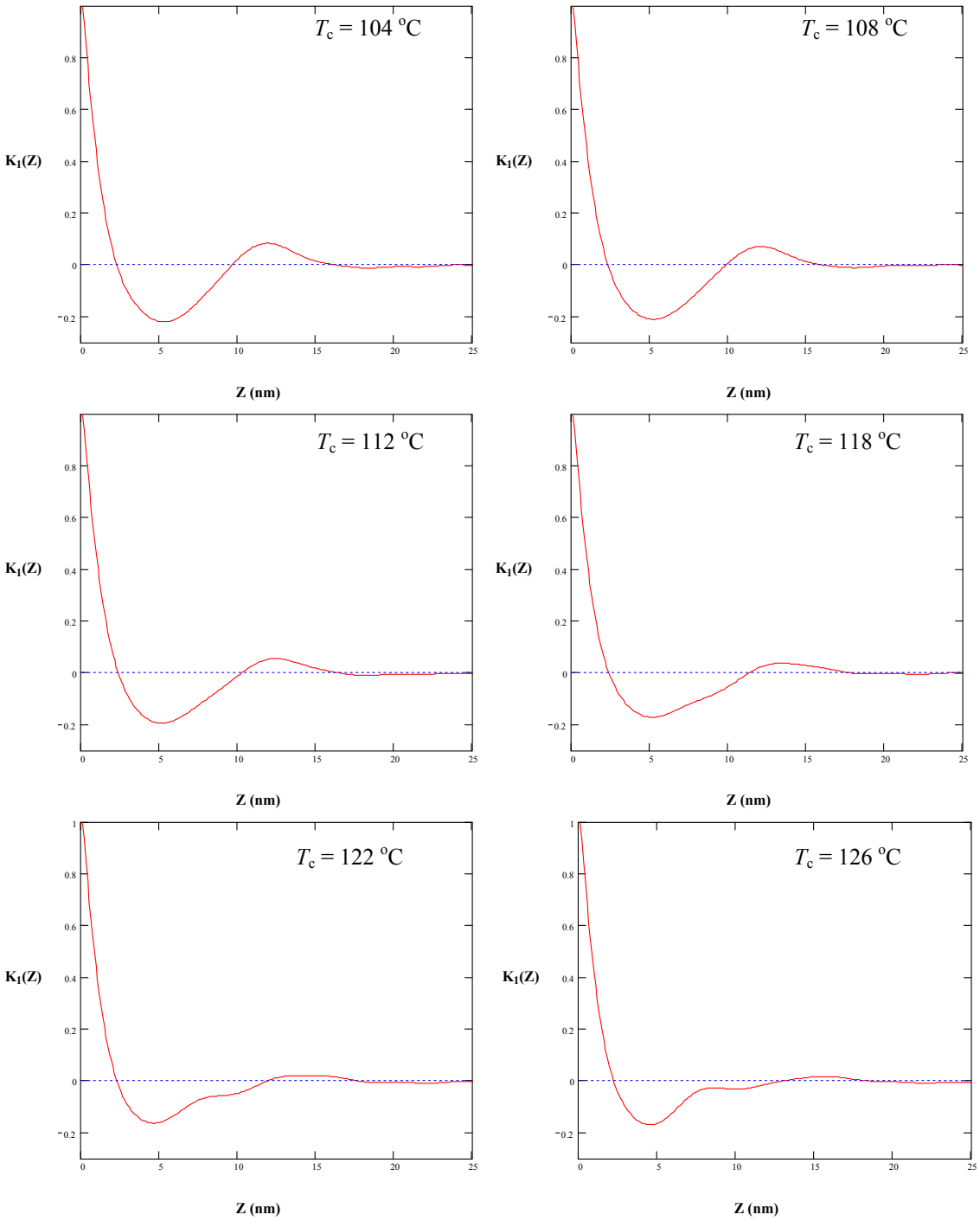

Figure 4.6.12. 1D correlation functions of copolymer iPP2.62 crystallized at indicated crystallization temperatures.

'double–minimum' can be an indication of the coexistence of two different lamellar domains. Since the iPP2.62 samples crystallized above 120 ^{o}C have two minima before the maximum in the 1D correlation function, this method cannot be used to directly extract morphological data. Firstly, some type of processing of the raw data has to be made in order to separate the contributions from the two lamellar populations, before 1D correlation function can be used. An approach for solving this problem will be discussed in section 5.2.3.4.

Figure 4.6.13 displays the normalized 1D correlation function $K(x)$ for the copolymer iPP4.38 as a function of crystallization temperature. Similar behavior to copolymer iPP2.62 is observed for the highest four crystallization temperatures, as seen from the skewing of the first minimum in the 1D correlation function. Direct application of the 1D correlation function will not be used to analyze the data of the iPP4.38 samples crystallized in the temperature range 114–120 ^{o}C.

Normalized 1D correlation functions for the copolymers iPP10.45 and iPP15.57 as a function of the crystallization temperature are shown in Figures 4.6.14 and 4.6.15. The overall shape of the curves for these copolymers is very similar, with only a slight shift in position and amplitude of the peaks.

The results from the SAXS analysis of the lamellar thickness for each of the copolymer samples as a function of crystallization temperature are shown in Tables 4.6.1–4.6.4. The lamellar thickness was determined from the self–correlation triangle method. Also in the tables are listed the calculated stem length and number of propylene monomer units traversing the crystal lamellae for both α– and γ–crystal phases. Stem length of the γ–phase was calculated for samples that exhibited large fraction of this crystal phase, typically above 50 %.

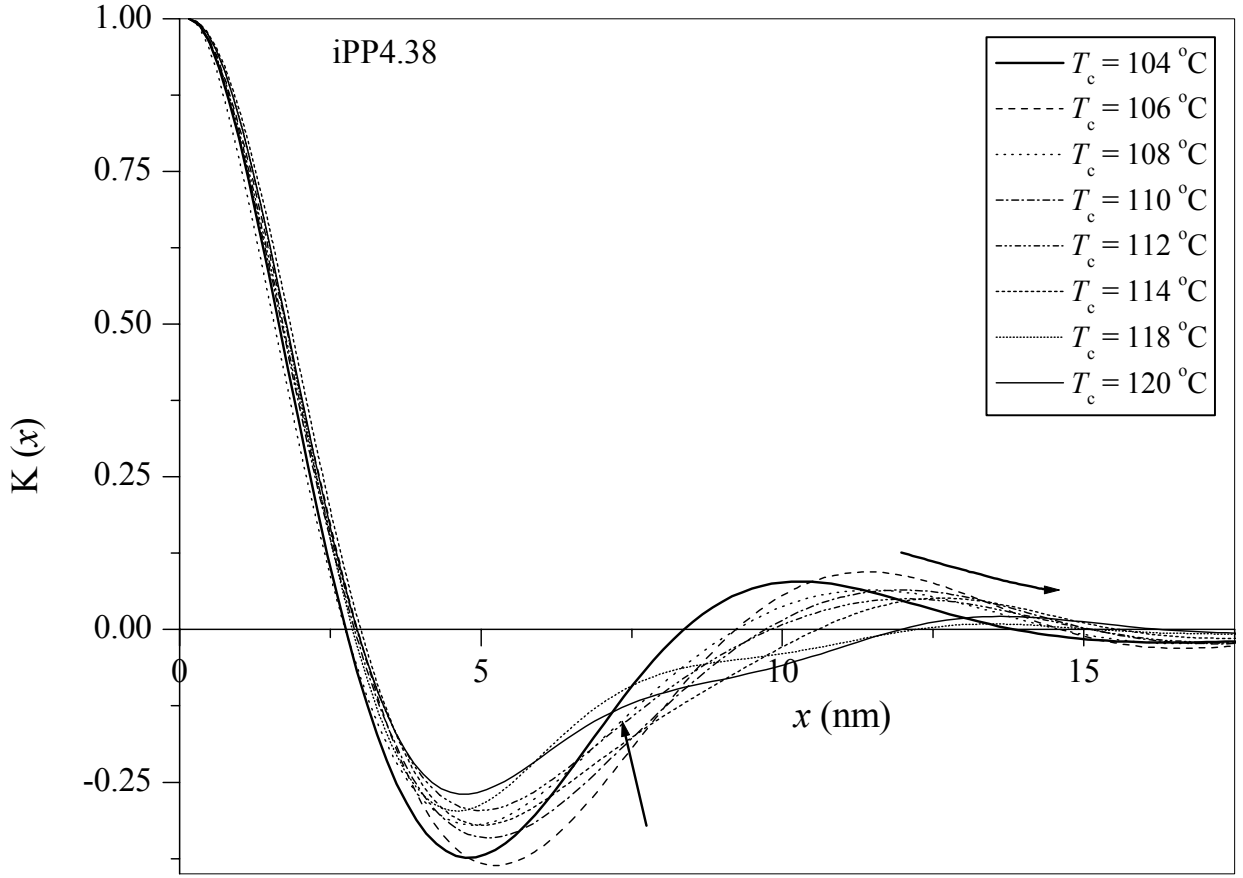

Figure 4.6.13. 1D correlation functions for iPP4.38 copolymer samples crystallized at indicated crystallization temperatures. Arrows indicate the change in shape of the curves with increasing crystallization temperature.

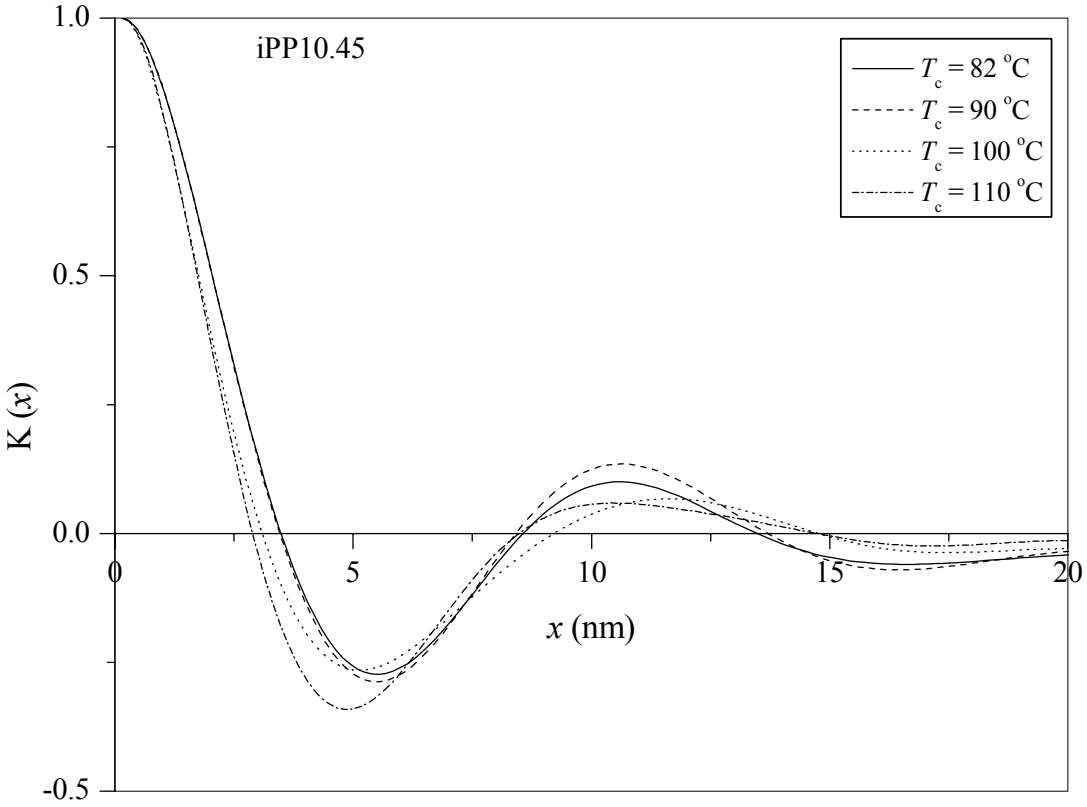

Figure 4.6.14. 1D correlation functions for copolymer iPP10.45 crystallized at indicated crystallization temperatures.

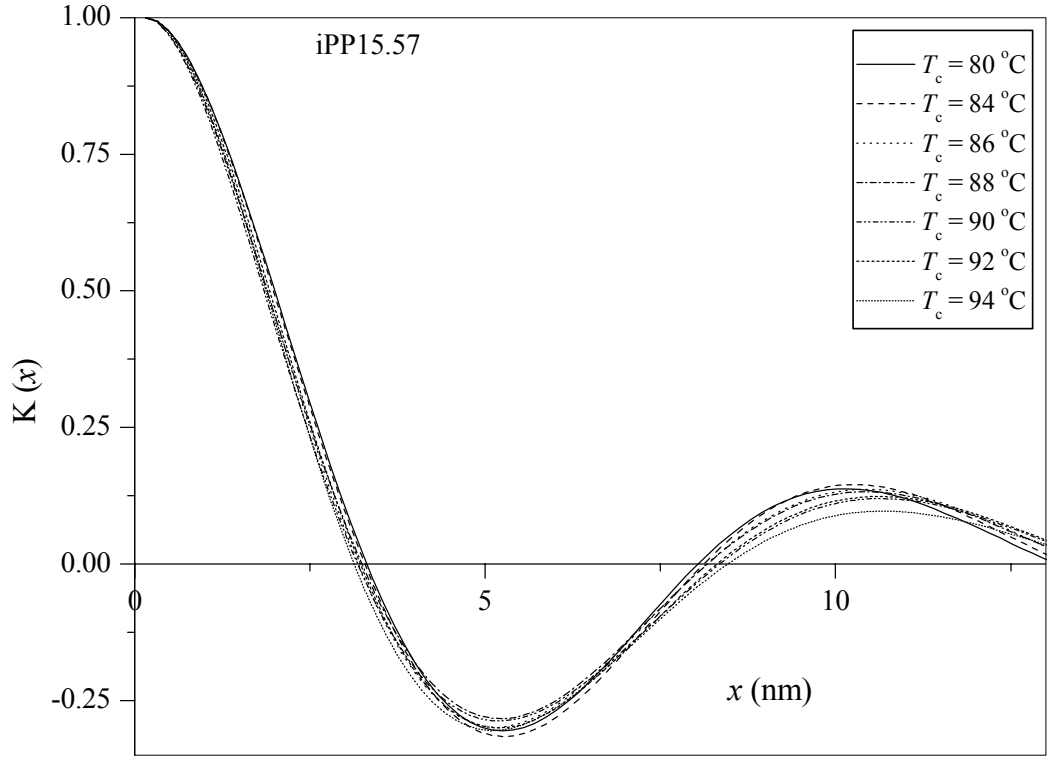

Figure 4.6.15. 1D correlation functions for copolymer iPP15.57 crystallized at indicated crystallization temperatures.

Table 4.6.1. Crystal characteristics of copolymer iPP2.62 crystallized at atmospheric pressure.

T_c (^oC)	ΔT (^oC)	w_{waxd} (%)	w_{saxs} (%)	E (nm)	Δ (nm)	LP (nm)	dn[1] (nm)	ℓ_{tl} (nm)	ℓ_a (nm)	ℓ_c (nm)	α–stem (nm)	#units	γ–stem (nm)	#units
102	68.2	70.0	65.1	3.53	2.49	12.00	4.19	1.13	3.06	7.81	7.92	36.6	–	–
104	66.2	70.4	64.2	3.29	2.33	12.05	4.32	1.00	3.32	7.73	7.84	36.2	–	–
106	64.2	71.1	67.3	2.98	2.11	11.91	3.89	1.04	2.85	8.02	8.13	37.5	–	–
108	62.2	72.0	65.2	3.19	2.26	12.17	4.23	1.01	3.22	7.94	8.05	37.2	–	–
110	60.2	72.2	65.4	2.92	2.07	12.36	4.28	1.10	3.18	8.08	8.20	37.8	–	–
112	58.2	72.7	66.5	2.84	2.00	12.73	4.27	1.10	3.17	8.46	8.58	39.6	11.13	51.3
114	56.2	73.3	66.1	3.00	2.30	12.96	4.39	0.80	3.59	8.57	8.69	40.1	11.27	52.0
116	54.2	73.2	64.4	2.97	2.12	13.27	4.73	0.45	4.28	8.54	8.66	39.9	11.23	51.8
118	52.2	73.7	67.7	2.33	1.65	13.67	4.42	0.50	3.92	9.25	9.38	43.3	12.16	56.1

1) $dn = \ell_a + \ell_{tl}$

Table 4.6.2. Crystal characteristics of copolymer iPP4.38 crystallized at atmospheric pressure.

T_c (^oC)	ΔT (^oC)	w_{waxd} (%)	w_{saxs} (%)	E (nm)	Δ (nm)	LP (nm)	dn (nm)	ℓ_{tl} (nm)	ℓ_a (nm)	ℓ_c (nm)	α–stem (nm)	#units	γ–stem (nm)	#units
104	61.1	63.6	62.8	3.00	1.84	10.31	3.83	1.4	2.43	6.48	6.57	30.3	–	–
106	59.1	65.0	64.3	2.87	2.03	11.33	4.05	1.3	2.75	7.28	7.38	34.1	–	–
108	57.1	66.1	60.9	2.16	1.53	11.43	4.47	1.0	3.47	6.96	7.06	32.6	–	–
110	55.1	67.0	65.1	2.30	1.63	11.90	4.15	1.1	3.05	7.75	7.86	36.3	10.19	47.0
112	53.1	67.9	66.8	2.28	1.61	12.06	4.00	1.0	3.00	8.06	8.17	37.7	10.60	48.9

Table 4.6.3. Crystal characteristics of copolymer iPP10.45 crystallized at atmospheric pressure.

T_c (^oC)	ΔT (^oC)	w_{waxd} (%)	w_{saxs} (%)	E (nm)	Δ (nm)	LP (nm)	dn (nm)	ℓ_{tl} (nm)	ℓ_a (nm)	ℓ_c (nm)	α–stem (nm)	#units	γ–stem (nm)	#units
82	77.5	63.2	59.3	3.30	2.33	10.53	4.29	1.81	2.48	6.24	6.33	29.2	8.21	37.9
86	73.5	64.8	60.1	3.21	2.27	10.65	4.25	1.80	2.45	6.40	6.49	29.9	8.42	38.8
90	69.5	66.4	61.1	3.39	2.40	10.64	4.14	1.67	2.47	6.50	6.59	30.4	8.55	39.4
94	65.5	66.7	61.6	3.12	2.21	10.87	4.22	1.30	2.92	6.70	6.80	31.4	8.81	40.7
98	61.5	67.8	63.6	2.89	2.05	11.00	4.60	1.45	3.15	7.00	7.10	32.8	9.21	42.5
100	59.5	68.0	63.1	2.49	1.76	11.26	4.53	1.19	3.34	7.10	7.20	33.2	9.34	43.1
110	49.5	68.5	64.0	2.41	1.71	11.45	4.12	1.00	3.12	7.33	7.43	34.3	9.64	44.5

Table 4.6.4. Crystal characteristics of copolymer iPP15.57 crystallized at atmospheric pressure.

T_c (^oC)	ΔT (^oC)	w_{waxd} (%)	w_{saxs} (%)	E (nm)	Δ (nm)	LP (nm)	dn (nm)	ℓ_{tl} (nm)	ℓ_a (nm)	ℓ_c (nm)	α–stem (nm)	#units	γ–stem (nm)	#units
72	77	60.5	58.9	3.39	2.4	10.48	4.31	2.12	2.19	6.17	6.26	28.9	–	–
74	75	60.6	60.2	3.34	2.36	10.64	4.23	1.85	2.38	6.41	6.50	30.0	–	–
76	73	61.1	58.7	3.33	2.36	10.48	4.33	1.96	2.37	6.15	6.24	28.8	–	–
78	71	61.6	58.1	3.32	2.35	10.30	4.32	1.38	2.94	5.98	6.07	28.0	7.86	36.3
80	69	62.0	58.9	3.27	2.31	10.19	4.19	1.86	2.33	6.00	6.09	28.1	7.89	36.4
84	65	63.4	59.2	3.25	2.30	10.20	4.16	1.88	2.28	6.04	6.13	28.3	7.94	36.7
86	63	62.7	60.0	3.22	2.28	10.50	4.20	1.65	2.55	6.30	6.39	29.5	8.29	38.2
88	61	63.9	59.1	3.15	2.22	10.51	4.30	1.25	3.05	6.21	6.30	29.1	8.17	37.7
90	59	64.0	58.8	3.04	2.15	10.66	4.39	1.29	3.10	6.27	6.36	29.3	8.25	38.7
92	57	64.5	63.1	3.08	2.18	10.65	3.93	1.91	2.02	6.72	6.82	31.5	8.84	40.8
94	55	64.8	63.2	2.87	2.03	10.64	3.91	1.80	2.11	6.73	6.83	31.5	8.85	40.8

4.6.4. SAXS of copolymers crystallized at elevated pressures

SAXS analysis was used to evaluate the influence of pressure on the morphology of isothermally crystallized copolymer samples iPP2.62 and iPP4.38. In the case of the *i*–PP homopolymer studies have shown that the lamellar thickness decreases with increasing crystallization pressure.[38,122]

Figure 4.6.16 shows the net corrected absolute SAXS intensities of the copolymer iPP2.62 as a function of crystallization temperature at a pressure of 123 MPa. It can be seen that with increasing crystallization temperature the scattering intensity increases and the peak maximum shifts to lower q values (larger long period). Lorentz corrected data, presented in Figure 4.6.17, show similar behavior. For the copolymer iPP2.62 crystallized isothermally at 193 MPa the scattering intensity increased less dramatically with increasing crystallization temperature, as seen in Figures 4.6.18 and 4.6.19.

Figures 4.6.20 show the SAXS intensity profiles of copolymer iPP2.62 as a function of crystallization pressure at T_c = 170 ^oC. It can be seen that with increasing pressure, the peak maximum shifts to higher scattering vectors indicating smaller long periods. Also, the scattered intensity decreases with increasing pressure.

Normalized 1D correlation functions of copolymer iPP2.62 crystallized at p_c = 123 and 193 MPa as a function of crystallization temperature are shown in Figures 4.6.21 and 4.6.22. 1D correlation functions were obtained from Lorentz corrected curves shown in Figure 4.6.17, as outlined in section 4.6.3. Figure 4.6.21 shows that for iPP2.62 crystallized at p_c = 123 MPa the position of second maximum shifts to larger values with increasing crystallization temperature, while the position of the first minimum is almost unchanged. Similar behavior for the position of the second maximum is observed for iPP2.62 crystallized at the highest pressure of 193 MPa, however the position of the first minimum also shifts to higher values. Characteristic feature of the 1D correlation function of the pressure crystallized samples was that with increasing crystallization

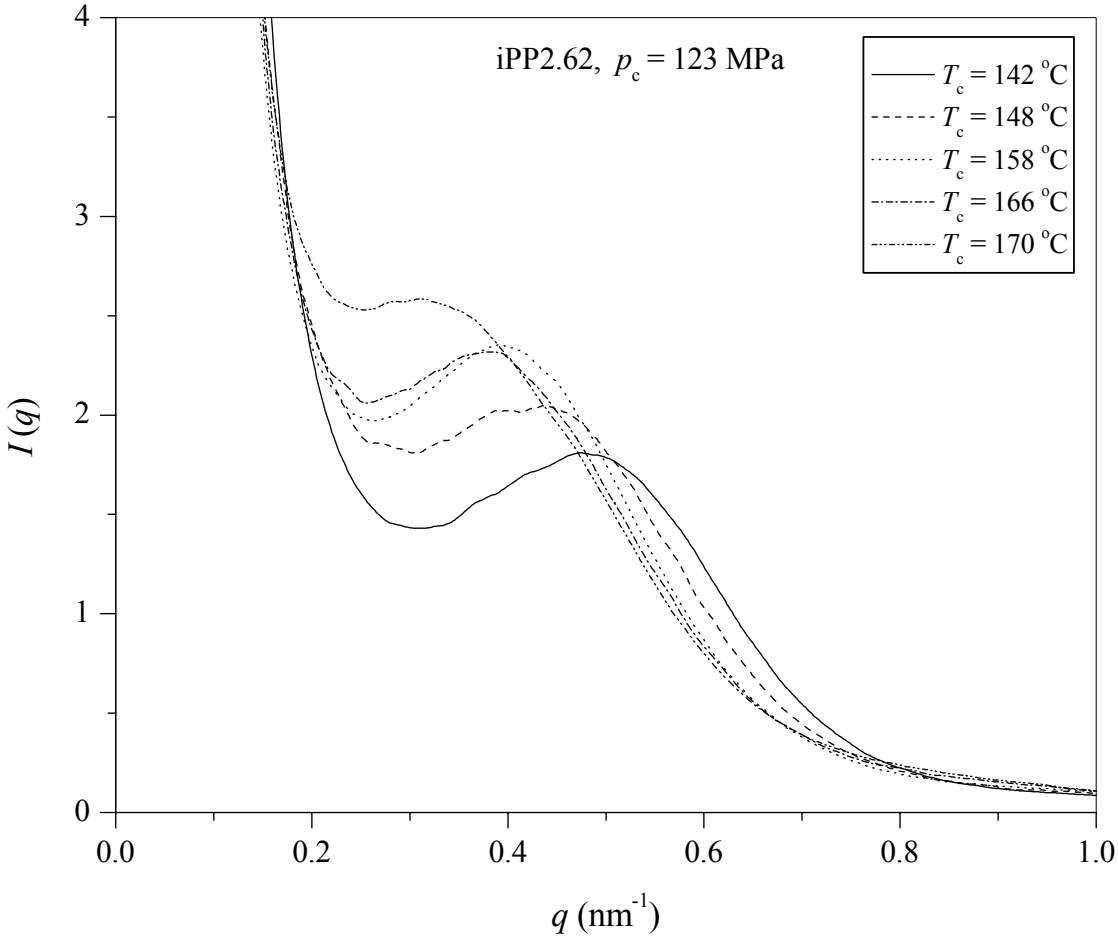

Figure 4.6.16. SAXS intensity profiles for copolymer iPP2.62 crystallized at 123 MPa.

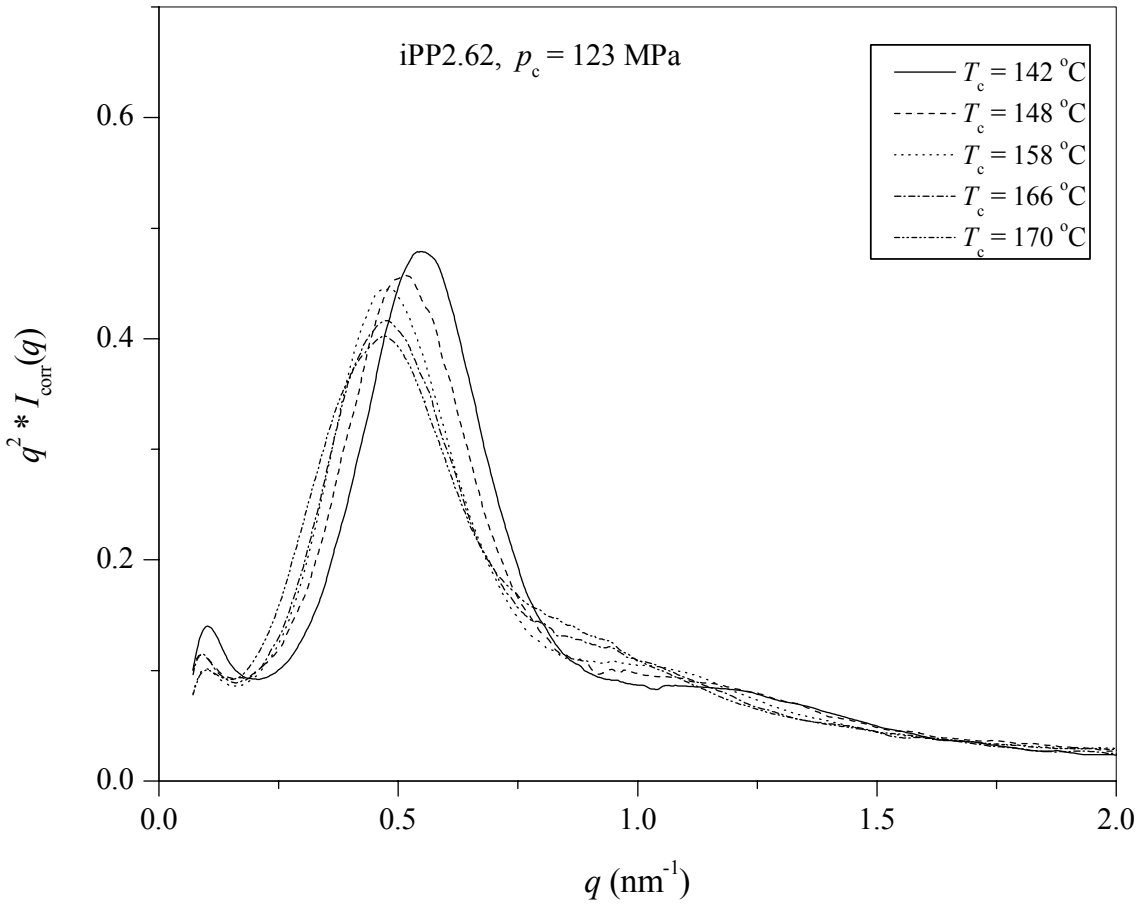

Figure 4.6.17. SAXS Lorentz corrected data of the data in Figure 4.6.16.

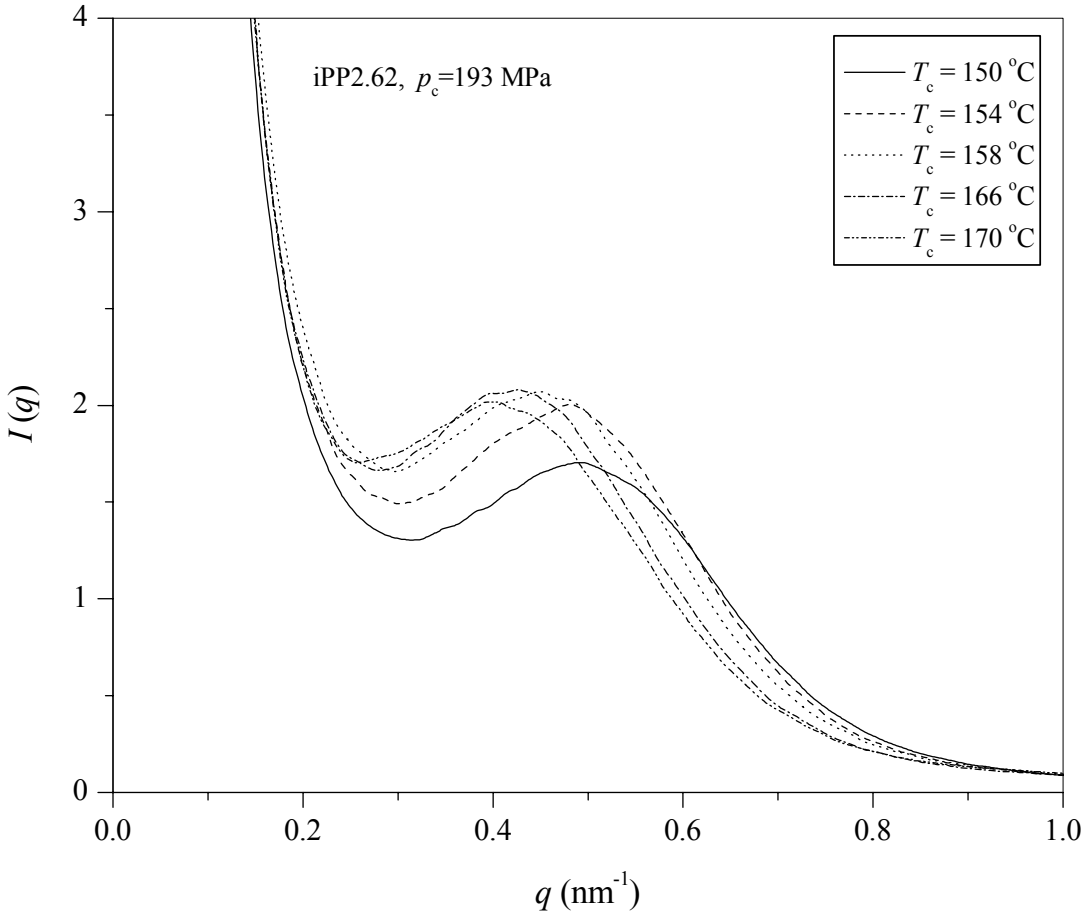

Figure 4.6.18. SAXS intensity profiles for copolymer iPP2.62 as a function of crystallization temperature at p_c = 193 MPa.

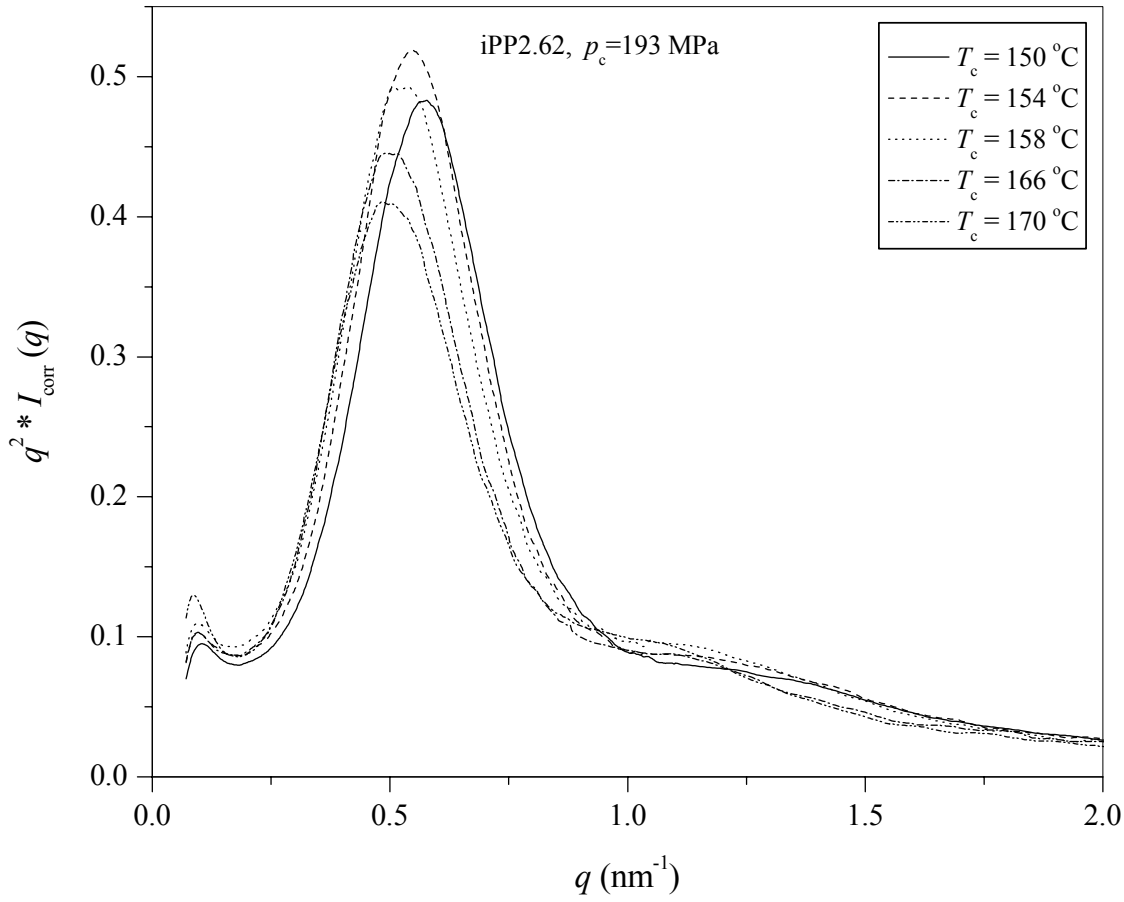

Figure 4.6.19. SAXS Lorentz corrected data of the data in Figure 4.6.18.

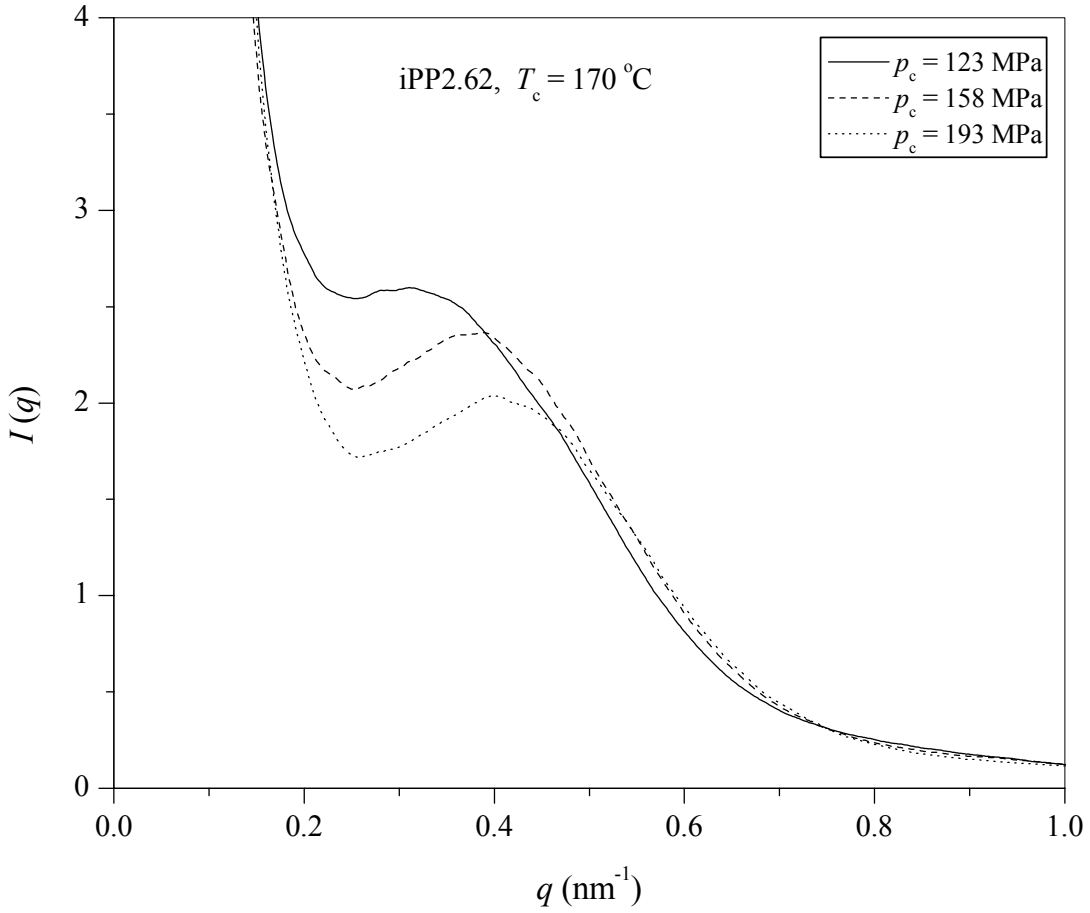

Figure 4.6.20. SAXS intensity profiles for copolymer iPP2.62 crystallized at T_c = 170 °C and three crystallization pressures.

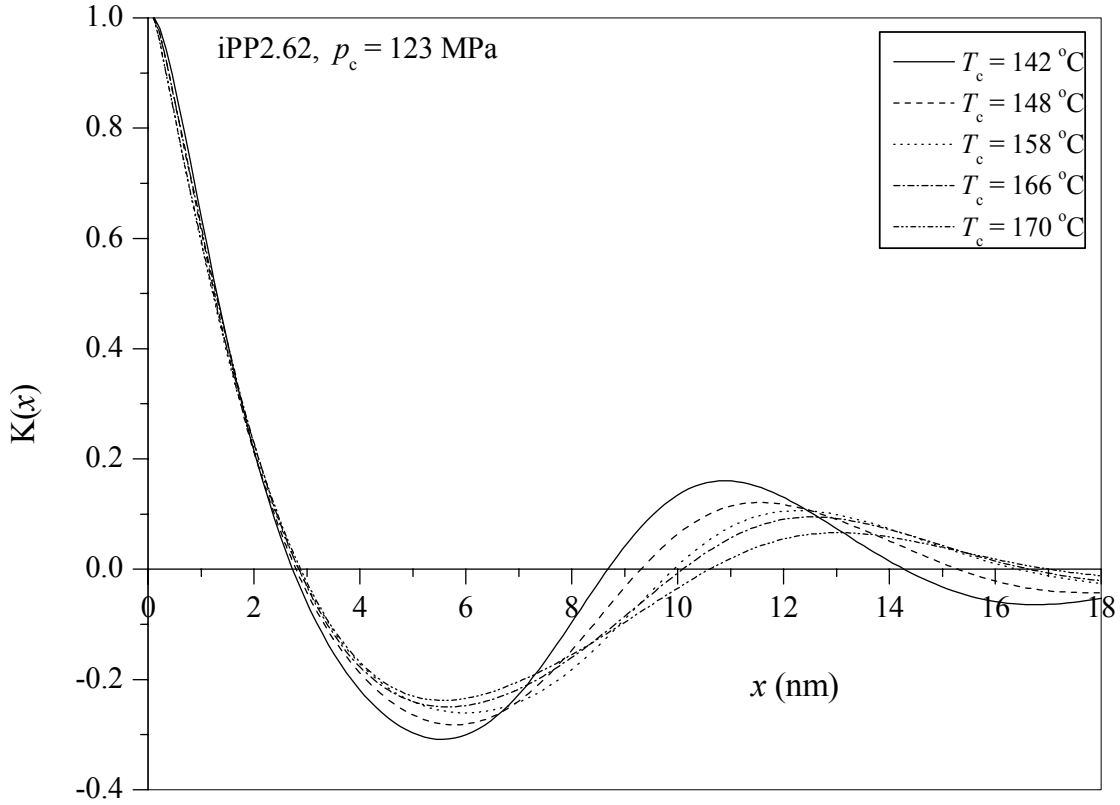

Figure 4.6.21. 1D correlation functions of copolymer iPP2.63 crystallized at 123 MPa and indicated temperatures.

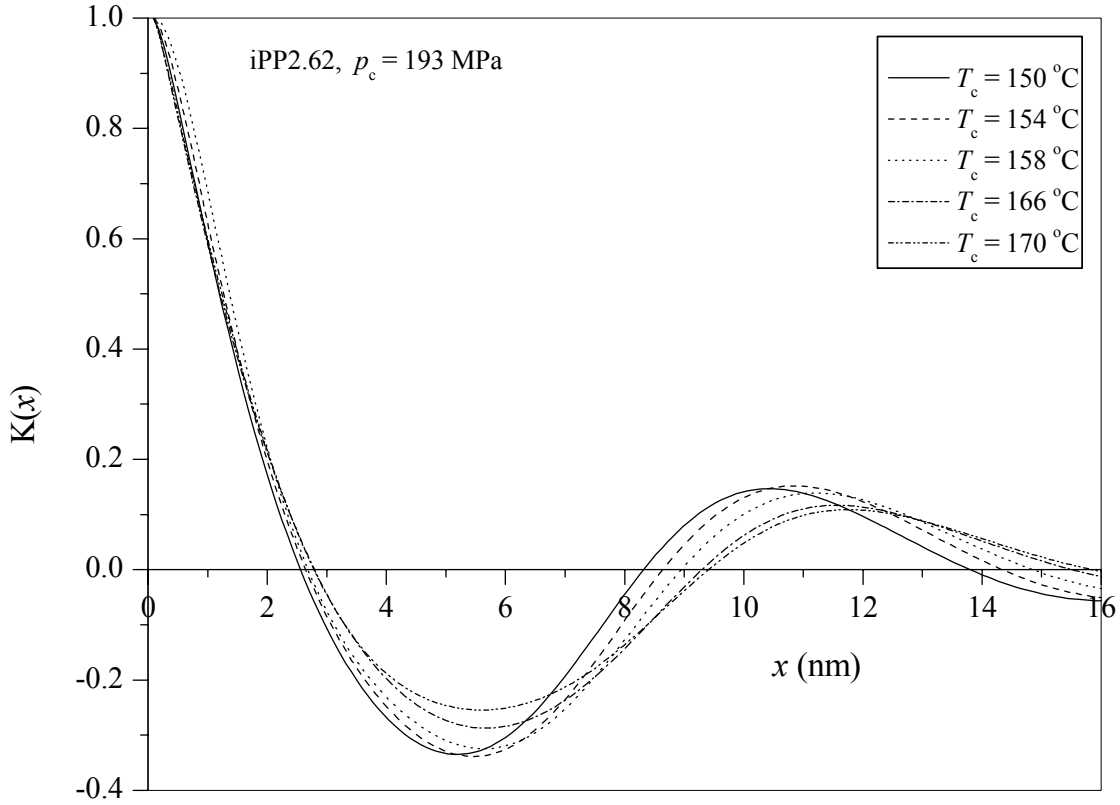

Figure 4.6.22. 1D correlation functions of copolymer iPP2.63 crystallized 193 MPa and indicated temperatures.

temperature the first minimum becomes broader and its amplitude decreases. Knowing that the lamellar thickness determined from SAXS represents a weight average thickness, this peak broadening indicates that the lamellar thickness distribution becomes wider with increasing crystallization temperature.

Figure 4.6.23 displays the 1D correlation functions of samples presented in Figure 4.6.20. This figure shows the influence of crystallization pressure on the shape of the 1D correlation function at constant crystallization temperature. It can be seen that with increasing pressure the position of the second maximum and the value of the long period shifts to smaller values. This feature is in good agreement with the findings reported for the *i*–PP homopolymer.[38,122]

The results from the SAXS analysis of the lamellar thickness for copolymers iPP2.62 and iPP4.38 as a function of crystallization temperature and pressure are shown in Tables 4.6.5–4.6.12. Tables also list calculated stem length and number of propylene monomer units traversing the crystal lamellae for γ–phase.

4.7. Crystallization kinetics at atmospheric pressure

The growth rates of the random propylene–ethylene copolymers at various isothermal crystallization temperatures were obtained by measuring the spherulite diameter as a function of time. An example of the average spherulite radius versus crystallization time for copolymer iPP2.62 at crystallization temperatures ranging from 106 ^{o}C to 132 ^{o}C is shown in Figures 4.7.1 and 4.7.2. It can be seen that the change in spherulite radii is linear with time at all temperatures up to the impingement. Linear growth rates were determined from the slopes using the least squares method.

Plots of the average linear growth rates as a function of crystallization temperature are shown in Figure 4.7.3. Growth rates for the homopolymer *i*–PP from

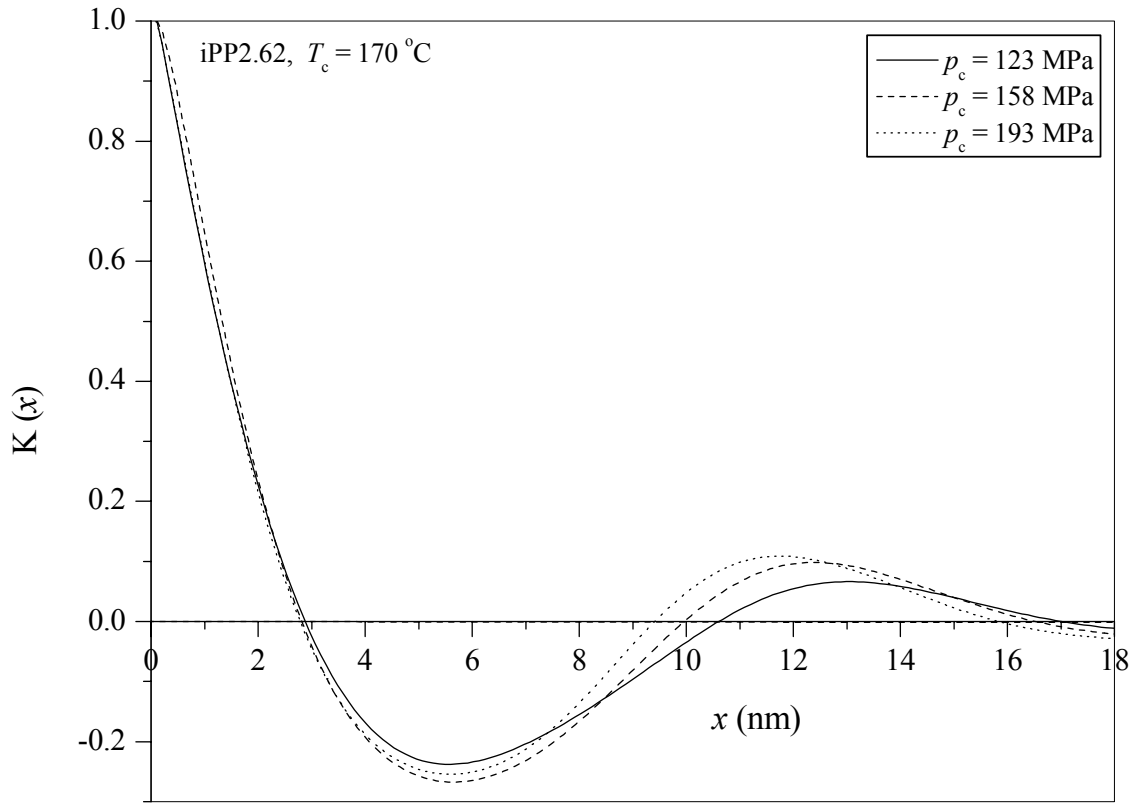

Figure 4.6.23. 1D correlation functions of copolymer iPP2.63 crystallized at 170 °C and indicated pressures.

Table 4.6.5. Crystal characteristics of copolymer iPP2.62 crystallized at MPa.

T_c (^oC)	w_{waxd} (%)	w_{saxs} (%)	E (nm)	Δ (nm)	LP (nm)	dn (nm)	ℓ_{tl} (nm)	ℓ_a (nm)	ℓ_c (nm)	γ–stem (nm)	#units
142	65.4	65.4	3.68	1.51	11.22	3.94	0.11	3.83	7.28	9.57	44.2
154	67.1	64.5	3.70	1.45	12.05	4.23	0.15	4.08	7.82	10.28	47.5
158	66.7	65.6	3.54	1.34	12.65	4.39	0.07	4.32	8.26	10.86	50.1
162	68.3	66.6	2.43	0.78	13.09	4.28	0.11	4.17	8.81	11.59	53.5
166	69.5	64.0	1.68	0.52	14.5	4.11	0.17	3.94	10.39	13.66	63.1

Table 4.6.6. Crystal characteristics of copolymer iPP2.62 crystallized at 123 MPa.

T_c (^oC)	w_{waxd} (%)	w_{saxs} (%)	E (nm)	Δ (nm)	LP (nm)	dn (nm)	ℓ_{tl} (nm)	ℓ_a (nm)	ℓ_c (nm)	γ–stem (nm)	#units
154	68.5	67.0	3.69	1.49	11.00	3.95	0.09	3.86	7.05	9.27	42.8
158	68.2	66.8	3.42	1.29	12.25	4.06	0.08	3.98	8.19	10.77	49.7
162	68.4	65.1	3.34	1.22	12.50	4.16	0.18	3.98	8.34	10.97	50.6
166	69.0	65.8	3.30	1.19	12.87	4.15	0.13	4.02	8.72	11.47	52.9
170	69.7	66.7	2.83	0.95	14.00	4.22	0.08	4.14	9.78	12.86	59.4
174	70.5	65.3	2.07	0.65	14.70	4.22	0.10	4.12	10.48	13.78	63.6

Table 4.6.7. Crystal characteristics of copolymer iPP2.62 crystallized at 158 MPa.

T_c (^oC)	w_{waxd} (%)	w_{saxs} (%)	E (nm)	Δ (nm)	LP (nm)	dn (nm)	ℓ_{tl} (nm)	ℓ_a (nm)	ℓ_c (nm)	γ–stem (nm)	#units
154	66.5	64.3	3.35	2.37	11.72	3.92	0.20	3.72	7.80	10.26	47.3
158	67.8	65.7	3.46	2.45	11.86	4.07	0.18	3.89	7.79	10.24	47.3
162	66.8	62.7	3.41	2.41	12.26	4.23	0.20	4.03	8.03	10.56	48.7
166	68.5	62.3	3.44	2.43	12.45	4.27	0.20	4.07	8.18	10.76	49.6
170	66.5	63.5	3.40	2.40	12.37	4.23	0.18	4.05	8.14	10.70	49.4
174	66.8	64.4	3.22	2.28	12.48	4.19	0.13	4.06	8.29	10.90	50.3

Table 4.6.8. Crystal characteristics of copolymer iPP2.62 crystallized at 193 MPa.

T_c (^oC)	w_{waxd} (%)	w_{saxs} (%)	E (nm)	Δ (nm)	LP (nm)	dn (nm)	ℓ_{tl} (nm)	ℓ_a (nm)	ℓ_c (nm)	γ–stem (nm)	#units
150	68	64.5	3.16	2.23	10.42	3.74	0.14	3.6	6.68	8.78	40.5
154	66.3	61.8	3.35	2.37	10.89	4.10	0.21	3.89	6.79	8.93	41.2
158	68.4	64.0	3.46	2.45	11.22	4.02	0.22	3.80	7.20	9.47	43.7
162	66.6	63.0	3.32	2.35	11.23	4.12	0.17	3.95	7.11	9.35	43.2
166	66.4	64.5	3.40	2.40	11.52	3.74	0.09	3.65	7.78	10.23	47.2
170	66.9	64.9	3.35	2.37	11.71	3.72	0.10	3.62	7.99	10.51	48.5

Table 4.6.9. Crystal characteristics of copolymer iPP4.38 crystallized at 88 MPa.

T_c (^oC)	w_{waxd} (%)	w_{saxs} (%)	E (nm)	Δ (nm)	LP (nm)	dn (nm)	ℓ_{tl} (nm)	ℓ_a (nm)	ℓ_c (nm)	γ–stem (nm)	#units
132	59.4	53.9	3.10	1.17	11.00	5.25	0.22	5.03	5.75	7.56	34.90
138	62.4	59.2	3.11	1.17	11.43	4.87	0.16	4.71	6.56	8.63	39.82
142	57.1	54.4	2.93	1.07	11.54	5.16	0.11	5.05	6.38	8.39	38.72
144	60.8	58.1	2.36	0.78	11.56	4.58	0.12	4.46	6.98	9.18	42.37

Table 4.6.10. Crystal characteristics of copolymer iPP4.38 crystallized at 123 MPa.

T_c (^oC)	w_{waxd} (%)	w_{saxs} (%)	E (nm)	Δ (nm)	LP (nm)	dn (nm)	ℓ_{tl} (nm)	ℓ_a (nm)	ℓ_c (nm)	γ–stem (nm)	#units
132	54.0	60.2	3.14	1.30	10.63	4.15	0.28	3.87	6.48	8.52	39.3
136	56.1	51.4	2.98	1.15	10.82	4.84	0.15	4.69	5.98	7.86	36.3
140	55.0	59.4	3.04	1.17	10.98	4.32	0.09	4.23	6.66	8.76	40.4
144	54.7	50.7	2.77	0.99	11.09	5.07	0.13	4.94	6.02	7.92	36.5
148	55.8	53.2	2.96	1.12	11.59	5.01	0.10	4.91	6.58	8.65	39.9
152	55.5	53.7	2.76	1.00	11.85	5.09	0.07	5.02	6.76	8.89	41.0

Table 4.6.11. Crystal characteristics of copolymer iPP4.38 crystallized at 158 MPa.

T_c (^oC)	w_{waxd} (%)	w_{saxs} (%)	E (nm)	Δ (nm)	LP (nm)	dn (nm)	ℓ_{tl} (nm)	ℓ_a (nm)	ℓ_c (nm)	γ–stem (nm)	#units
132	59.8	55.7	3.08	1.29	10.45	4.62	0.17	4.45	5.83	8.07	37.3
136	59.9	56.9	3.06	1.25	10.43	4.50	0.12	4.38	5.93	7.80	36.0
140	58.0	55.9	3.02	1.20	10.54	4.50	0.12	4.38	6.04	7.94	36.7
144	58.9	50.8	3.02	1.17	10.63	4.54	0.13	4.41	6.09	8.01	37.0
148	60.2	57.2	2.98	1.16	10.69	4.47	0.12	4.35	6.22	8.18	37.8
156	59.9	56.4	2.81	1.06	11.27	4.33	0.13	4.20	6.94	9.13	42.1
160	58.4	53.6	2.57	0.93	12.25	4.31	0.15	4.16	7.94	10.44	48.2

Table 4.6.12. Crystal characteristics of copolymer iPP4.38 crystallized at 193 MPa.

T_c (^oC)	w_{waxd} (%)	w_{saxs} (%)	E (nm)	Δ (nm)	LP (nm)	dn (nm)	ℓ_{tl} (nm)	ℓ_a (nm)	ℓ_c (nm)	γ–stem (nm)	#units
132	60.7	56.8	2.95	1.15	9.78	4.12	0.14	3.98	5.66	7.44	34.4
136	58.5	54.5	2.91	1.15	9.86	4.23	0.14	4.09	5.63	7.40	34.2
140	59	56.4	2.87	1.11	9.92	4.21	0.10	4.11	5.71	7.51	34.7
144	59.1	56.2	2.77	1.03	10.20	4.31	0.11	4.20	5.89	7.75	35.8
148	61.8	57.7	2.92	1.16	10.34	4.20	0.16	4.04	6.14	8.07	37.3
156	62.9	59.7	3.05	1.24	10.34	4.07	0.13	3.94	6.27	8.25	38.1

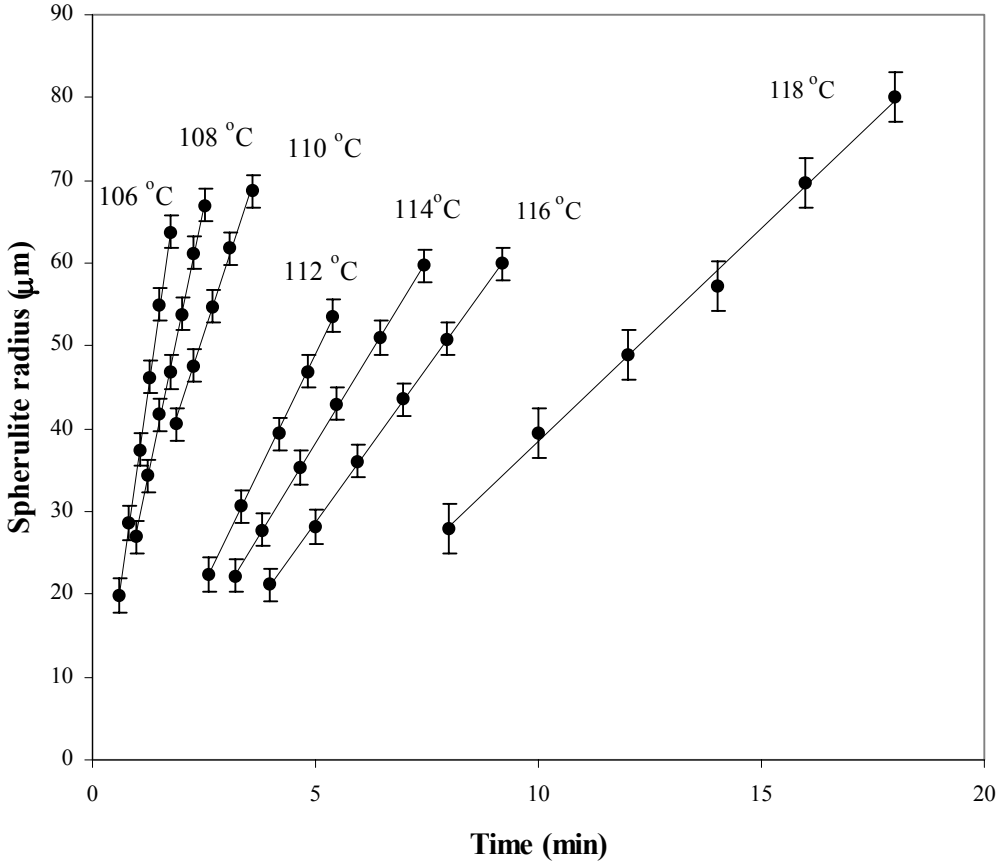

Figure 4.7.1. Spherulite radial growth of copolymer iPP2.62 isothermally crystallized at selected crystallization temperatures.

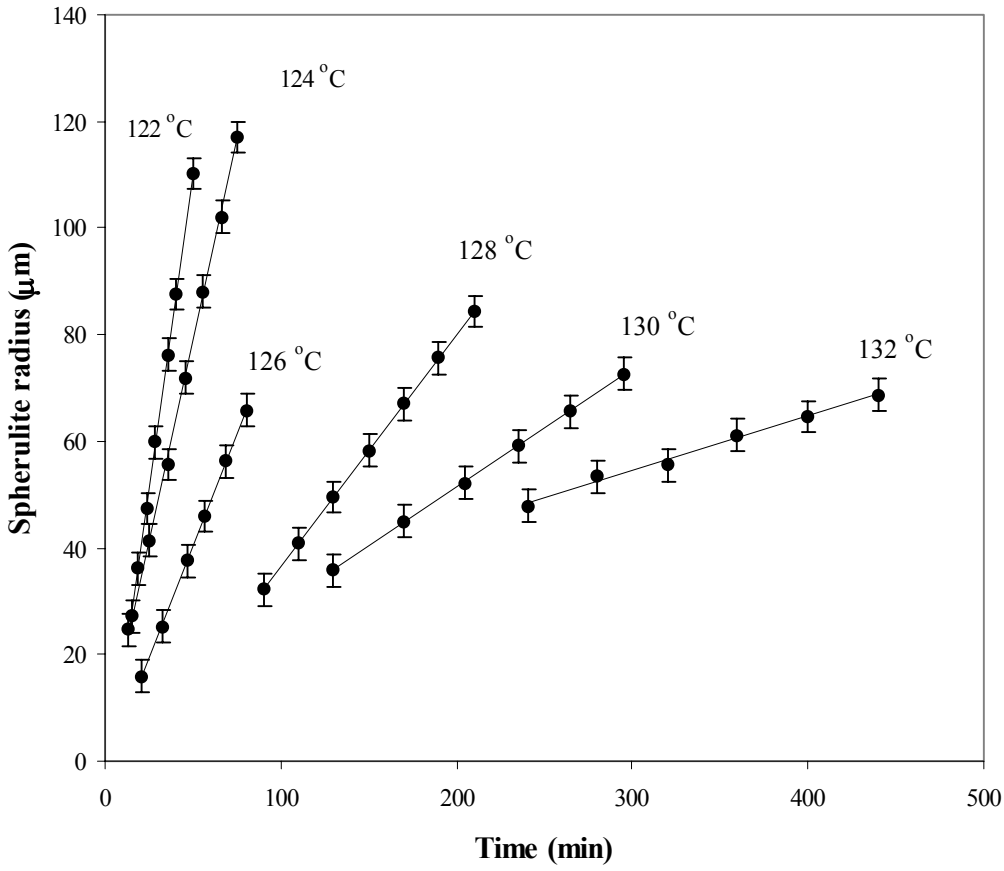

Figure 4.7.2. Spherulite growth of copolymer iPP2.62 for selected crystallization temperatures.

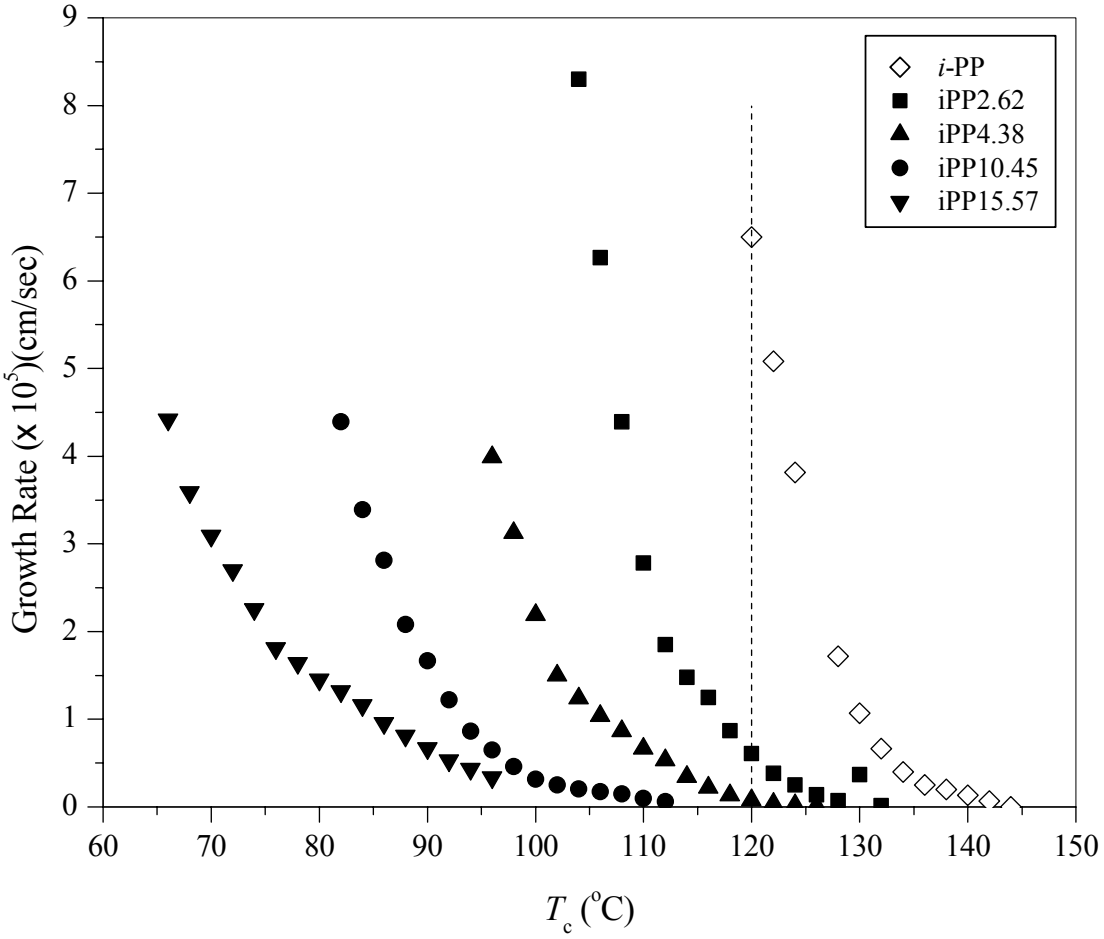

Figure 4.7.3. Linear growth rates as a function of crystallization temperature for propylene–ethylene copolymers and *i*–PP (*i*–PP data from Mezghani[6]).

Mezghani[6] are displayed in the figure for comparison. Crystallization rates decrease with increasing ethylene content at a constant crystallization temperature, as seen from the leftward shift of the curves. For instance, at T_c = 120 ^oC indicated by dashed line in Figure 4.7.3, 2.62 mol% ethylene reduces the linear growth rate by a factor of 11 compared with the homopolymer, while for the copolymer with 4.38 mol% ethylene the reduction factor is 80.

4.8. Morphology

4.8.1. Optical Microscopy

The optical microscopy study on the copolymers showed spherulitic morphologies resembling those of *i*–PP homopolymer, except that they appeared less regular both in shape and structure, showing uneven profiles and a more open texture. The latter two observations were more prominent for the two copolymers with the highest ethylene content, iPP10.45 and iPP15.57. The observed morphology was strongly dependent on the comonomer content, and in addition, it showed differences as a function of crystallization temperature. The morphological differences with increasing crystallization temperatures were (a) change in the sign of birefringence and (b) change in spherulite texture.

Typical spherulite morphology as a function of crystallization time for copolymer iPP2.62 crystallized at T_c = 120 ^oC is shown in Figure 4.8.1 (a–d). During the early stages of copolymer crystallization, two different types of morphology were observed: (1) quasi–circular and (2) elongated entities ('quadrites') as shown in Figure 4.8.1 (a). The crystallization proceeded with space filling growth that resulted in almost spherical shape of the entities that grew radially in an uniform fashion until the spherulites impinged.

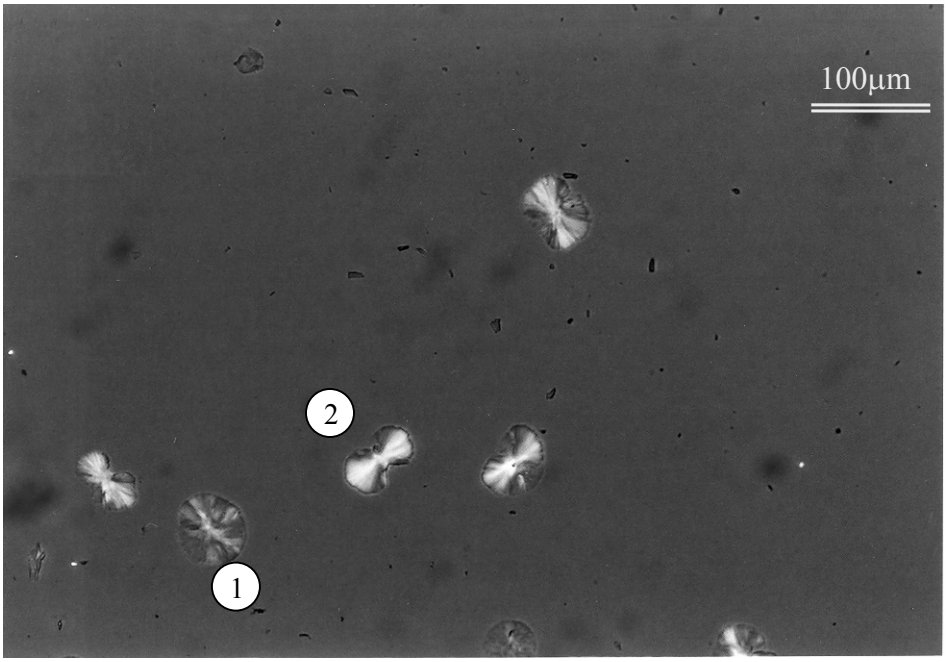

(a)

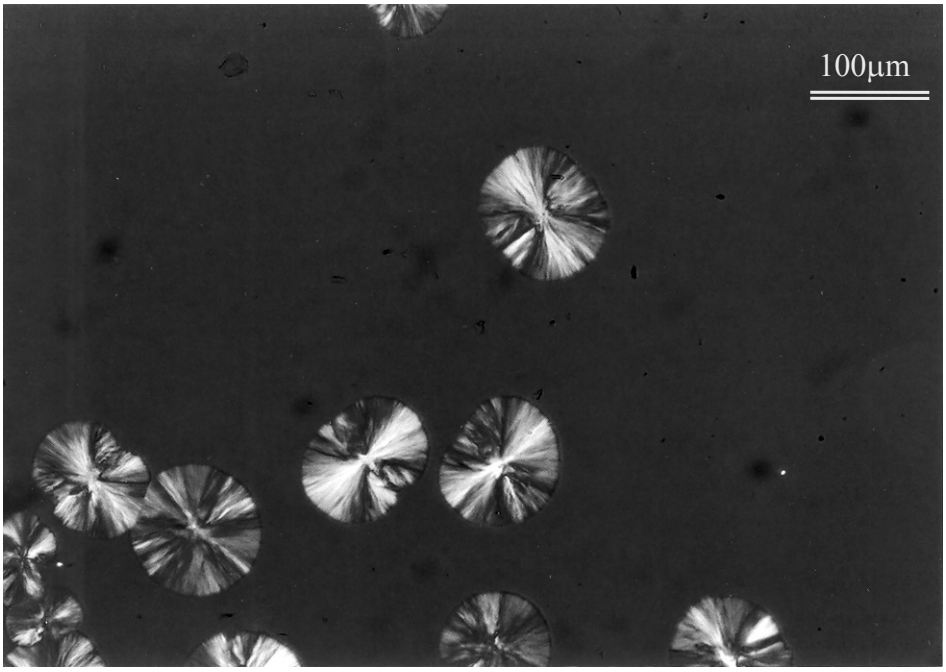

(b)

Figure 4.8.1. Optical micrographs of copolymer iPP2.62 crystallized at T_c = 120 °C as a function of crystallization time (a) 10 min, (b) 17 min, (c) 30 min, (d) after impingement.

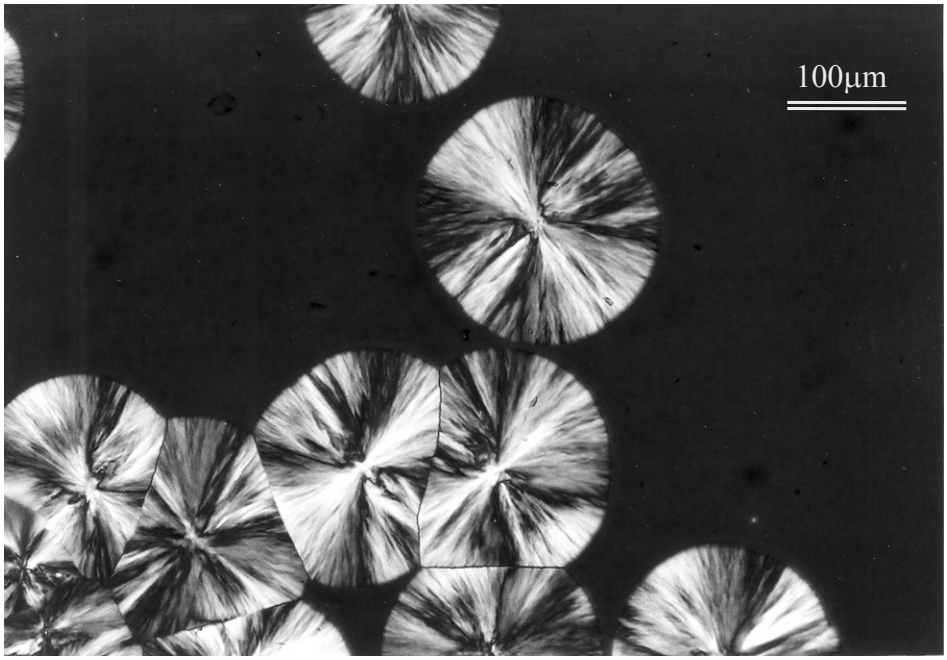

(c)

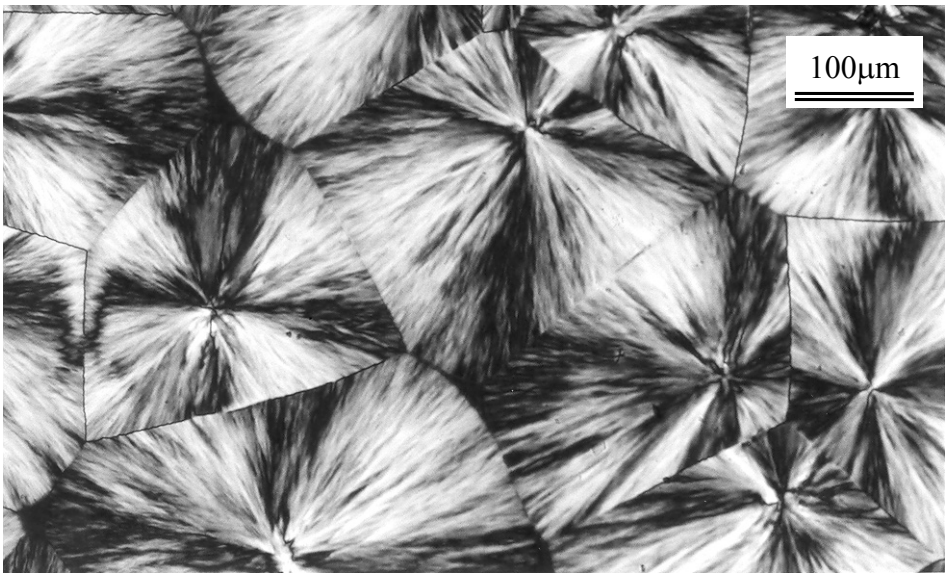

(d)

Figure 4.8.1. Continued. (c) 30 min, (d) after impingement.

In general, isothermal crystallization in the studied temperature range led to formation of predominantly positive spherulites. This behavior was more prominent at low crystallization temperatures. Crystallization at higher temperatures led to formation of both positive and mixed type spherulites. Negative spherulites were not observed in any of the samples. Figures 4.8.2 – 4.8.5 show the spherulite morphology of the four copolymer samples as a function of the degree of supercooling.

Micrographs a–c of Figure 4.8.2 show the spherulite morphology of copolymer iPP2.62 as a function of the degree of supercooling. At high degrees of supercooling the nucleation density was high and resulted in much smaller spherulites that were positive in birefringence and clearly manifested a Maltese cross. With decreasing degree of supercooling (Figure 4.8.2 (b) ΔT=54 ^{o}C) the Maltese cross pattern was still apparent, while some of the spherulites were of the mixed type. At a degree of supercooling of 50 ^{o}C and lower, the Maltese cross became less prominent, and the spherulites were mostly of the mixed type, with some of them being more negative than positive.

Similar observations can be made for the spherulite morphology of the copolymer iPP4.38 as a function of degree of supercooling, as shown in Figure 4.8.3 (a–c). The only difference compared with iPP2.62 is the more coarse texture of the spherulites obtained at higher crystallization temperatures, especially above T_c = 120 ^{o}C.

Micrographs a–c of Figure 4.8.4 show the morphologies of the copolymer iPP10.45 as a function of the degree of supercooling. The micrographs shown are taken at similar degree of supercooling as for the copolymer iPP2.62. With increasing crystallization temperature, the birefringence sign changes from positive to mixed. It can be seen that spherulites were of a more open and coarse texture, where each branch of the spherulite appeared dendritic like. The 'cross–hatched' type branching characteristic for α–crystals is absent from these samples, since the branching in these samples occurs at much smaller angles. This is particularly apparent in Figure 4.8.4 (c) for the samples crystallized at a degree of supercooling of 50 ^{o}C.

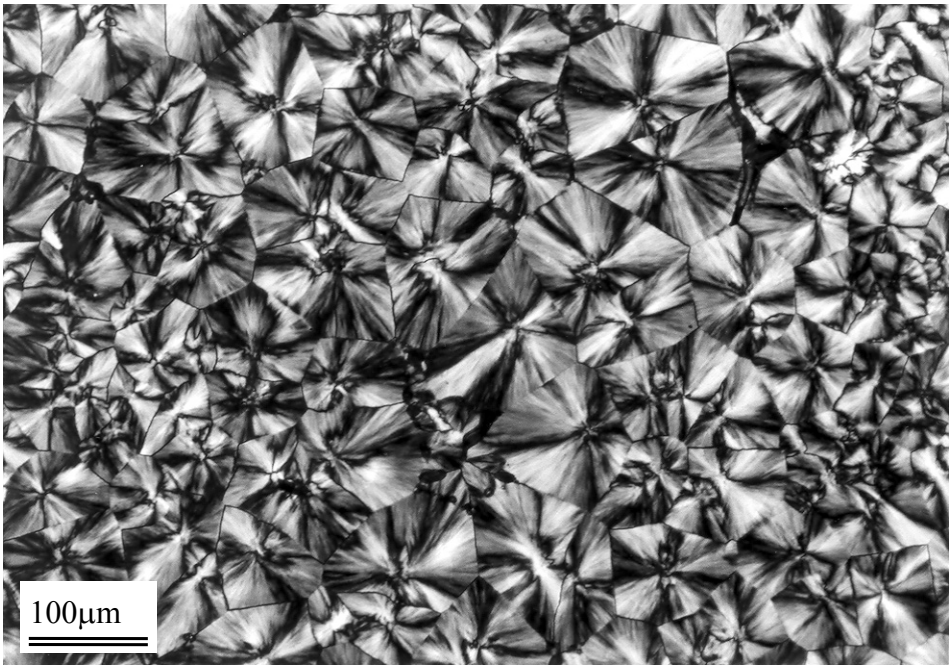

(a)

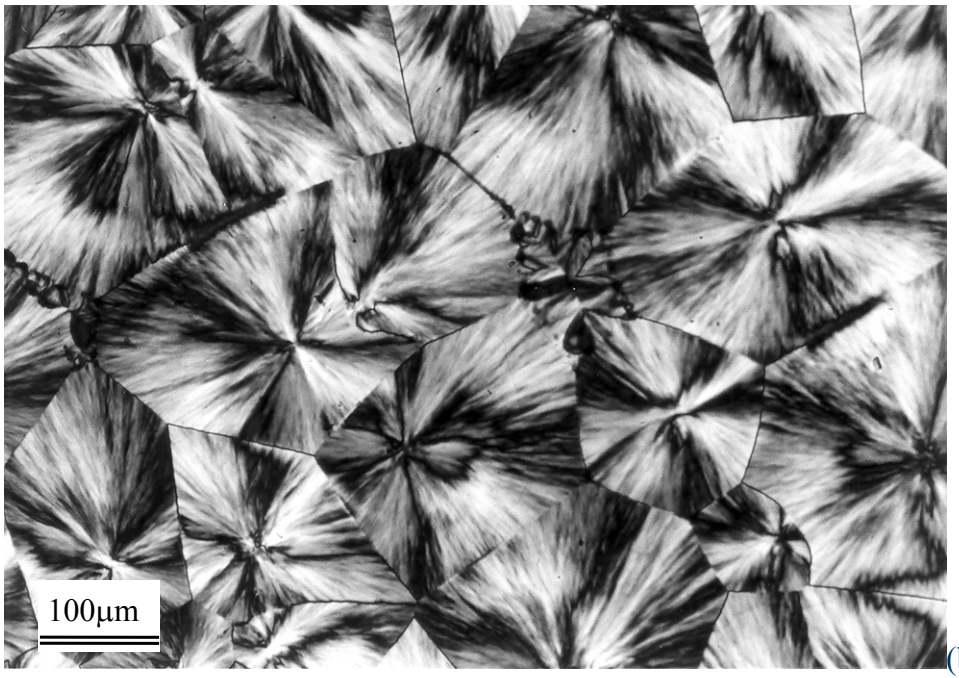

(b)

Figure 4.8.2. Optical micrographs of copolymer iPP2.62 as a function of degree of supercooling, (a) $\Delta T = 60\ ^{o}C$, (b) $\Delta T = 54\ ^{o}C$, (c) $\Delta T = 50\ ^{o}C$.

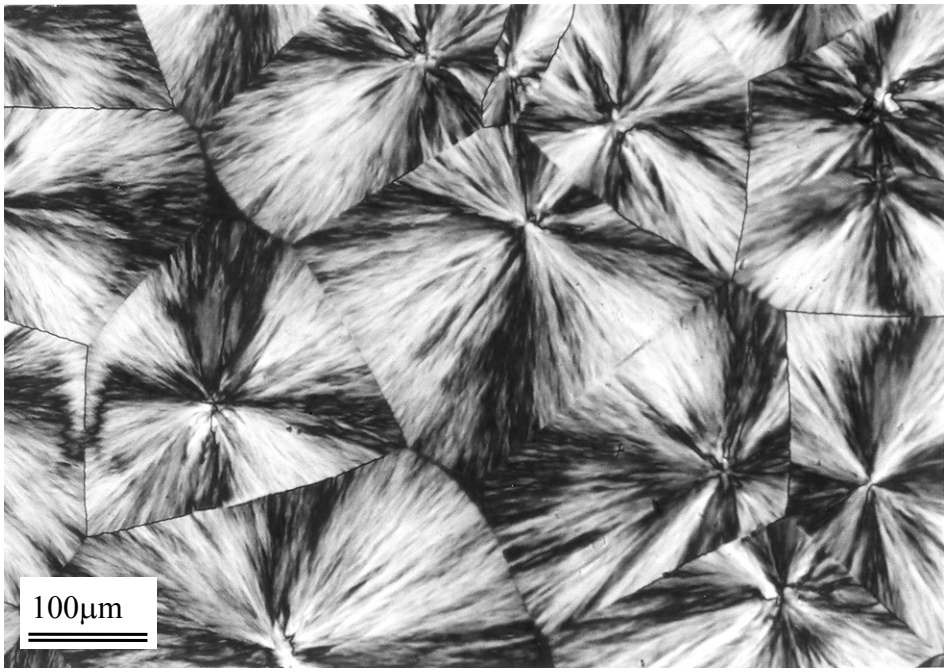

(c)

Figure 4.8.2. Continued. (c) $\Delta T = 50\ ^{o}C$.

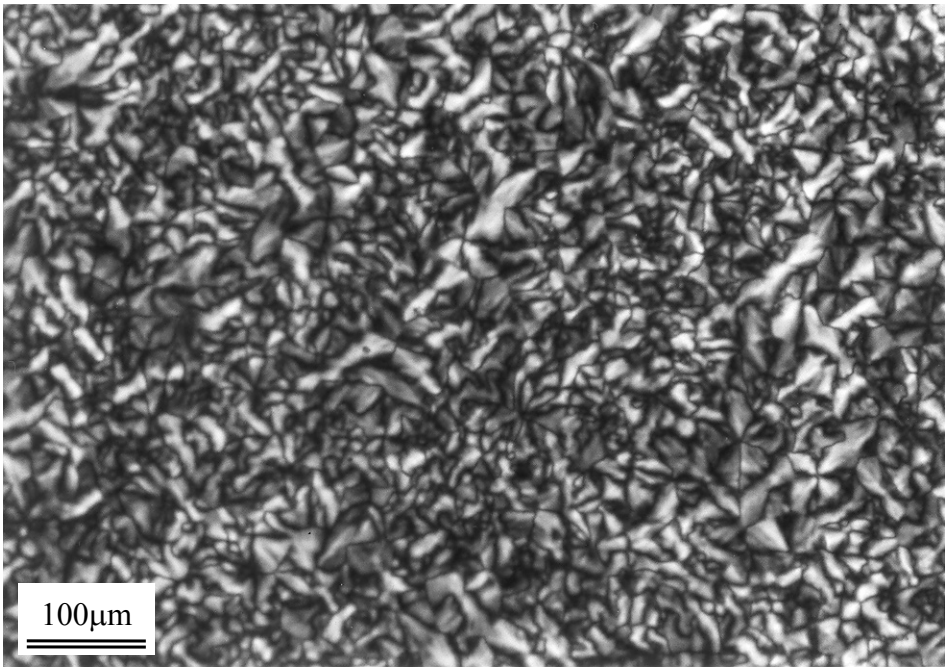

(a)

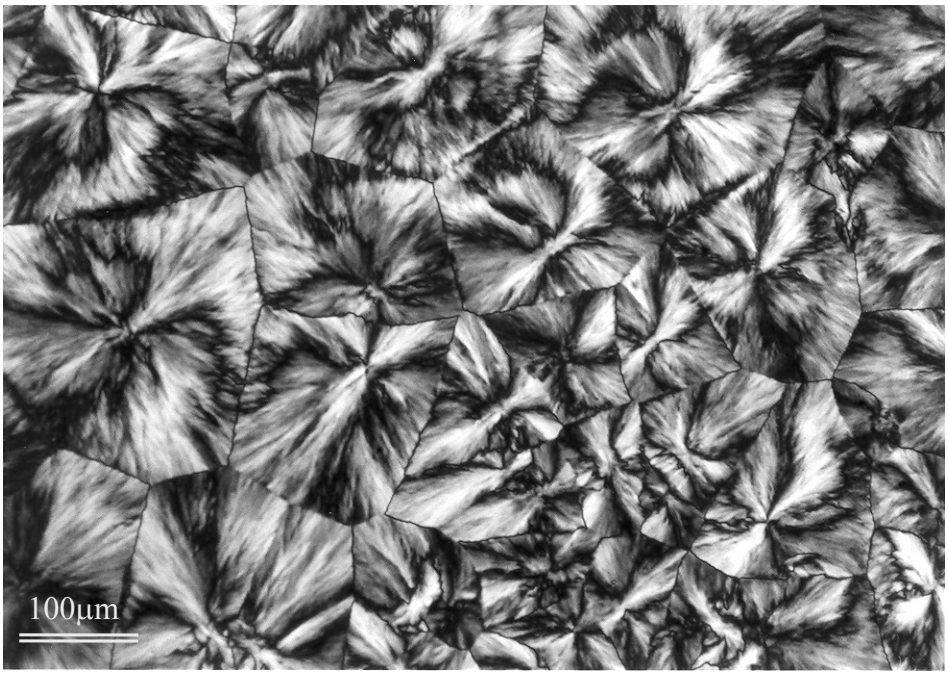

(b)

Figure 4.8.3. Optical micrographs of copolymer iPP4.38 as a function of degree of supercooling, (a) $\Delta T = 62\ ^{o}C$, (b) $\Delta T = 54\ ^{o}C$, (c) $\Delta T = 48\ ^{o}C$.

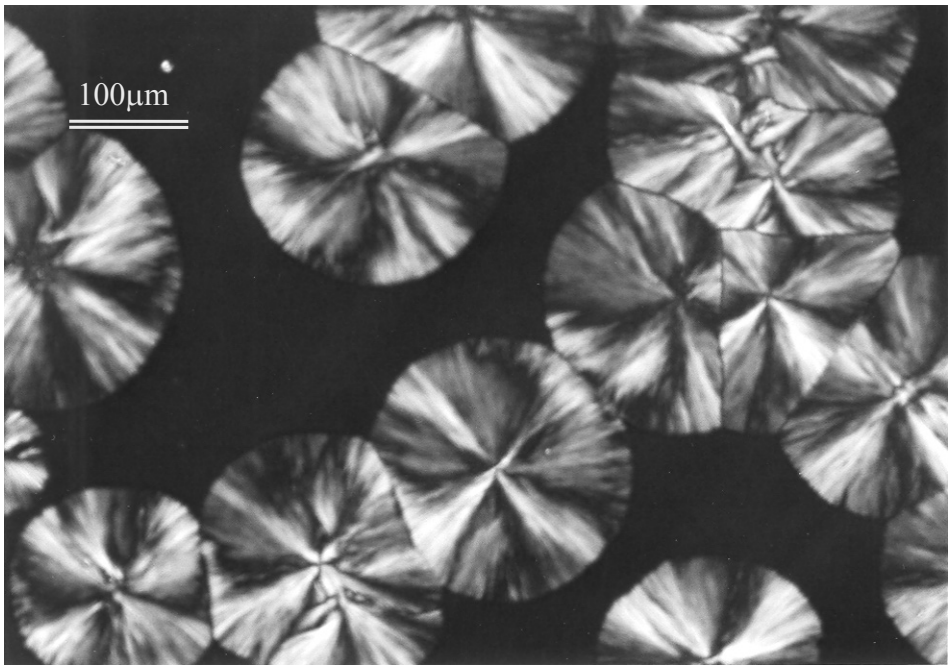

(c)

Figure 4.8.3. Continued. (c) $\Delta T = 48\ ^{o}C$.

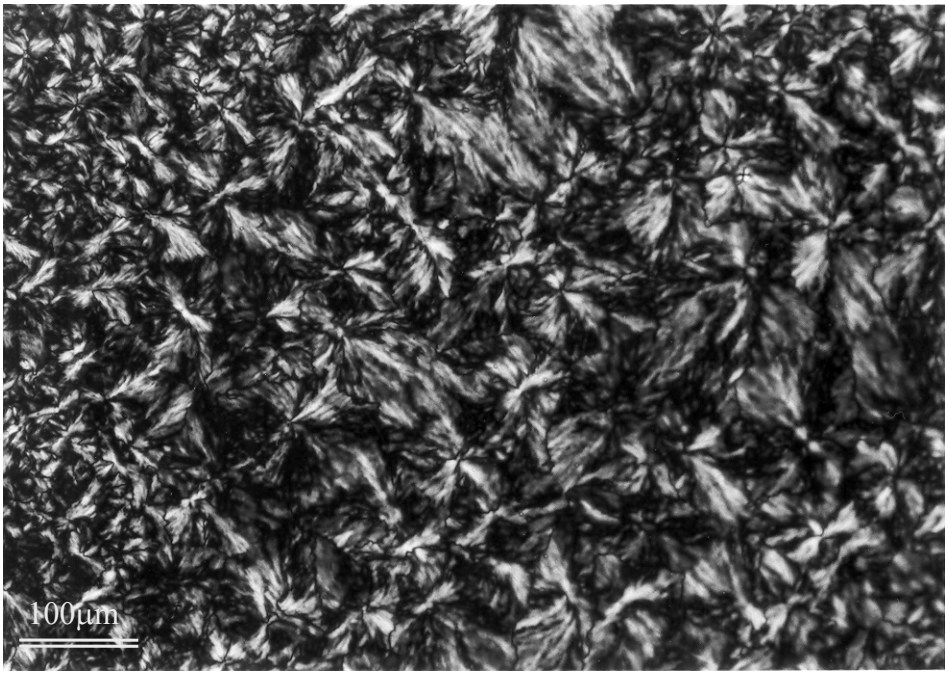

(a)

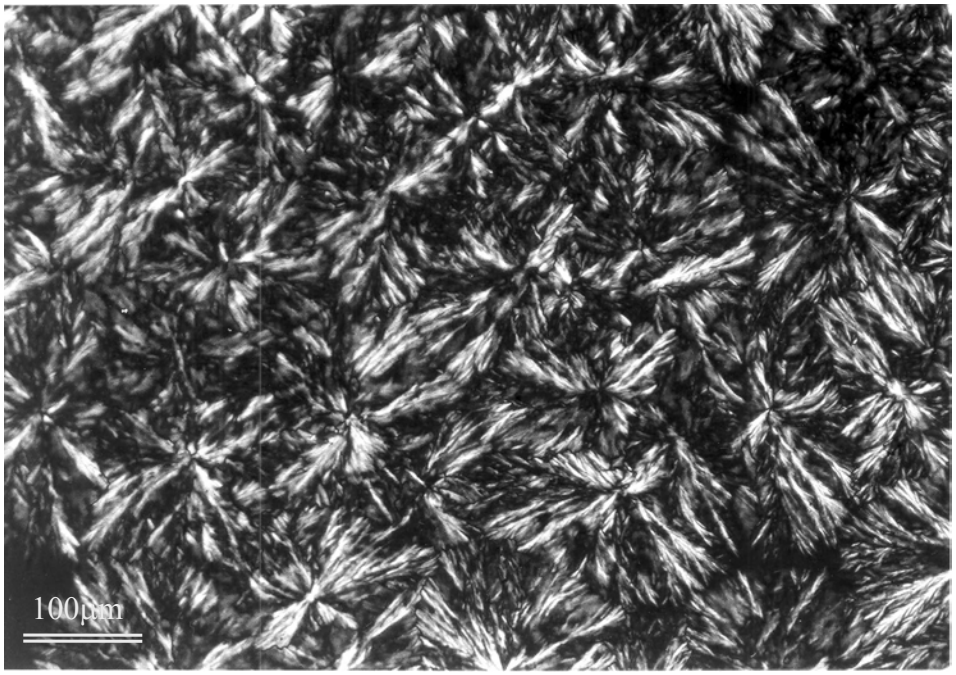

(b)

Figure 4.8.4. Optical micrographs of copolymer iPP10.45 as a function of degree of supercooling, (a) $\Delta T = 66\ ^{o}C$, (b) $\Delta T = 60\ ^{o}C$, (c) $\Delta T = 50\ ^{o}C$.

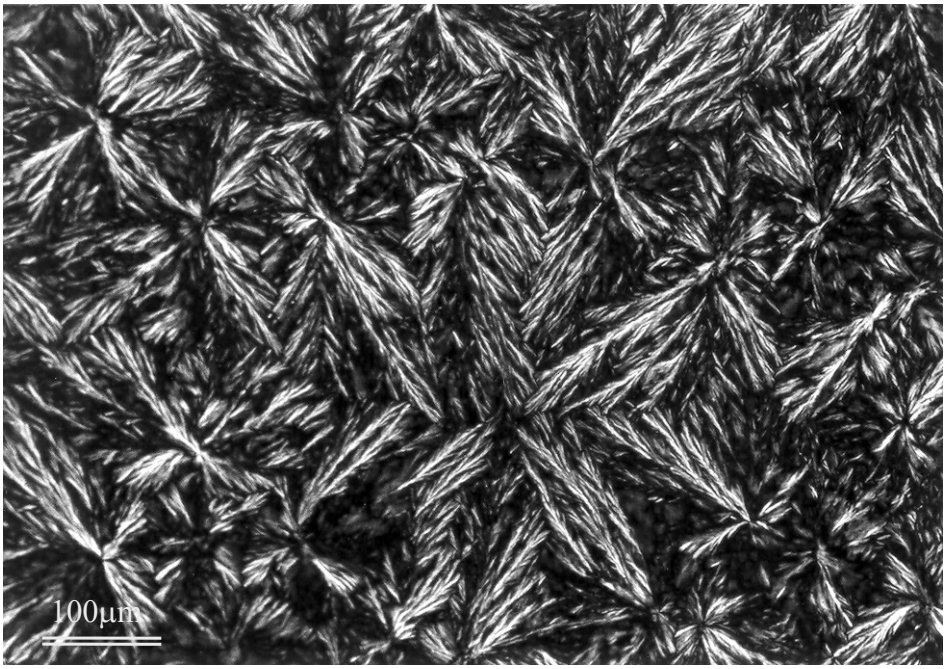

(c)

Figure 4.8.4. Continued. (c) $\Delta T = 50\ ^{o}C$.

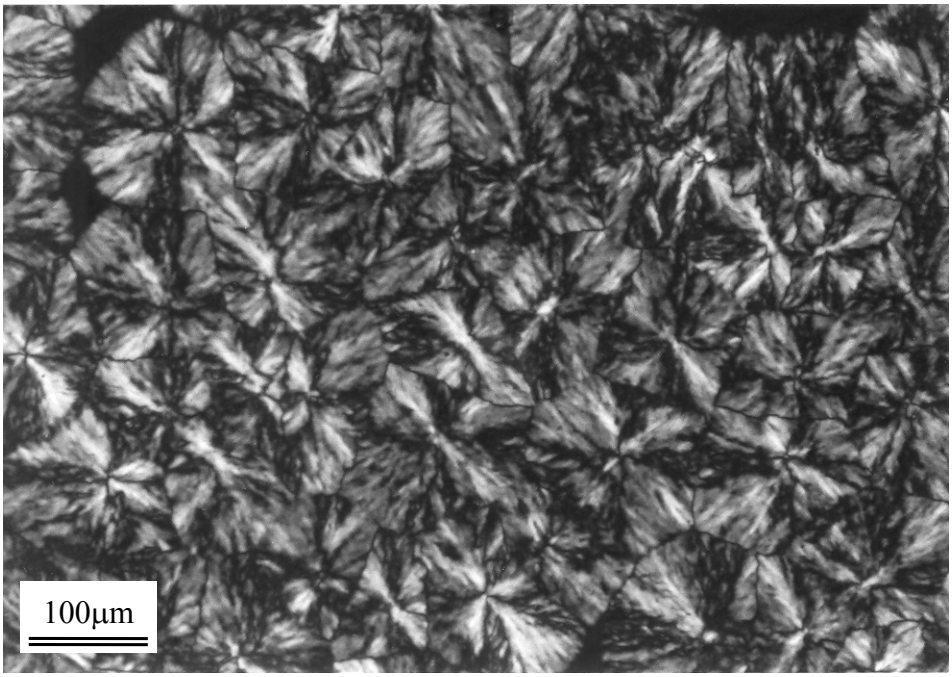

(a)

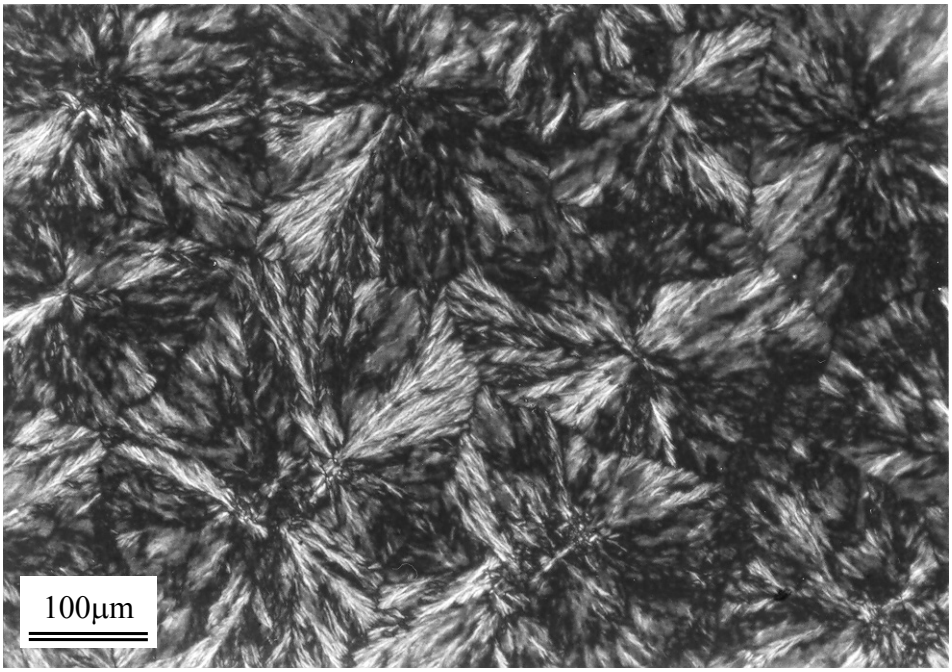

(b)

Figure 4.8.5. Optical micrographs of copolymer iPP15.57 as a function of degree of supercooling, (a) $\Delta T = 60\ ^{o}C$, (b) $\Delta T = 53\ ^{o}C$.

4.8.2. Scanning Electron Microscopy

The morphology of the random propylene–ethylene copolymers crystallized at atmospheric and high pressures was studied using the SEM technique. Samples for microscopy were prepared by permanganic etching procedure.

SEM micrographs of the iPP2.62 sample crystallized at T_c = 124 ^oC and atmospheric pressure are shown in Figures 4.8.6 and 4.8.7. This sample had approximately 57 % γ–crystal phase as determined from WAXD experiments. The small round features in the upper right side of the micrographs are believed to be due to the etching artifacts. At lower magnification (× 1000) the typical spherulitic structure was observed, dominated by radially growing lamellae with low angle branching indicated with arrows. The presence of the cross–hatched branching at 80^o from the radial lamellae that is characteristic of the α–crystal form of *i*–PP was not detected. The low angle branching can be better observed at higher magnification micrograph (× 3000) in Figure 4.8.7. Another interesting feature can be observed on these figures in the areas indicated with arrows. These features resemble the unique feather–like structure first observed by Mezghani and Phillips[39] for the pure γ–form of homopolymer *i*–PP isothermally crystallized at 200 MPa.

SEM micrographs of the iPP2.62 sample crystallized at T_c = 126 ^oC and atmospheric pressure are shown in Figures 4.8.8 – 4.8.11. This sample had 62 % γ–crystal phase. Similar to the previous sample, a feather–like structure growing approximately radially from the center of the spherulite can be observed in Figure 4.8.9. Figures 4.8.10 and 4.8.11 show the higher magnification of outlined area from Figure 4.8.9. These figures also indicate the existence of two populations of lamellae with different thickness, as indicated with arrows.

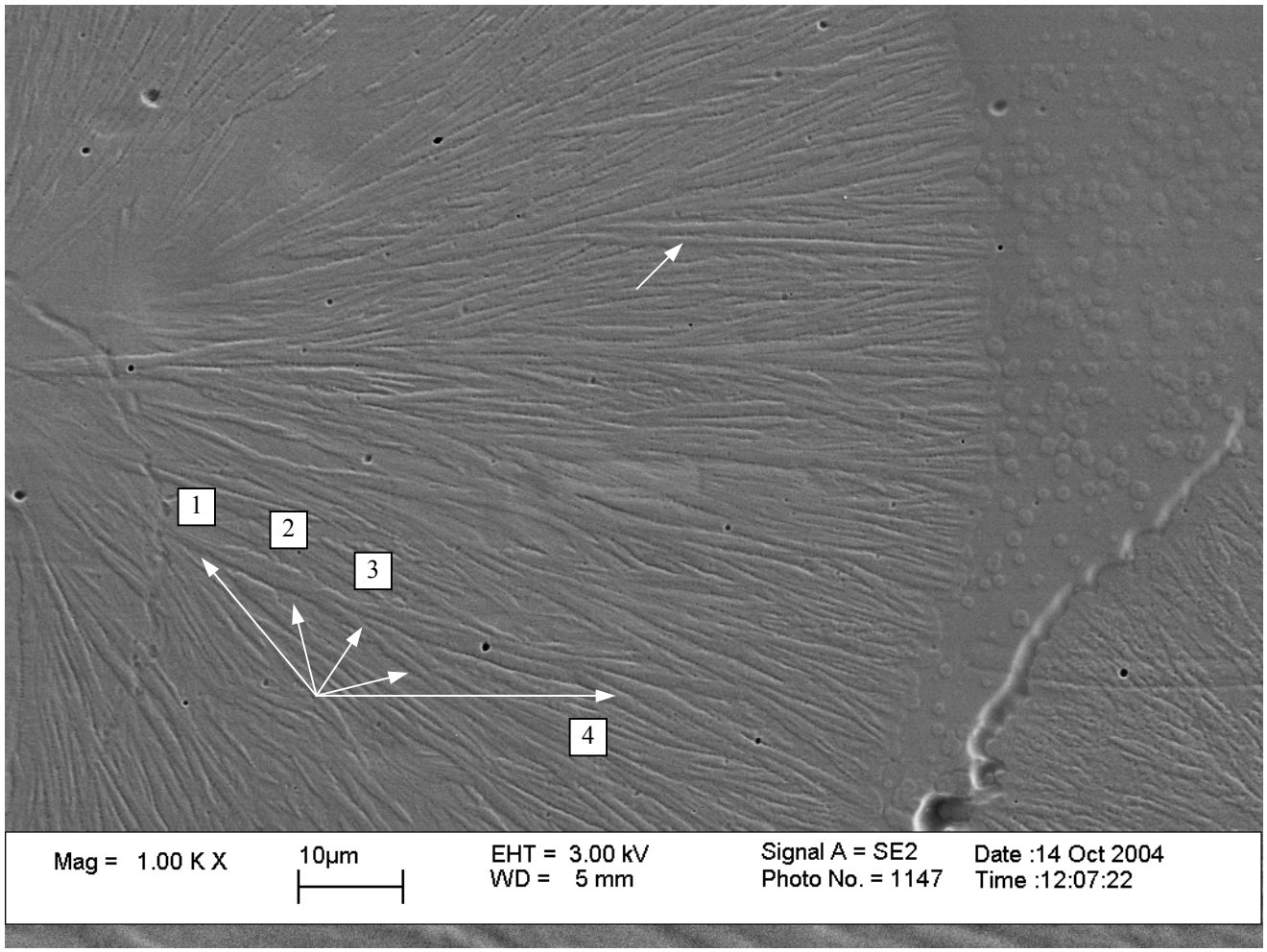

Figure 4.8.6. SEM micrograph of sample iPP2.62 crystallized at T_c = 124 ^{o}C at atmospheric pressure.

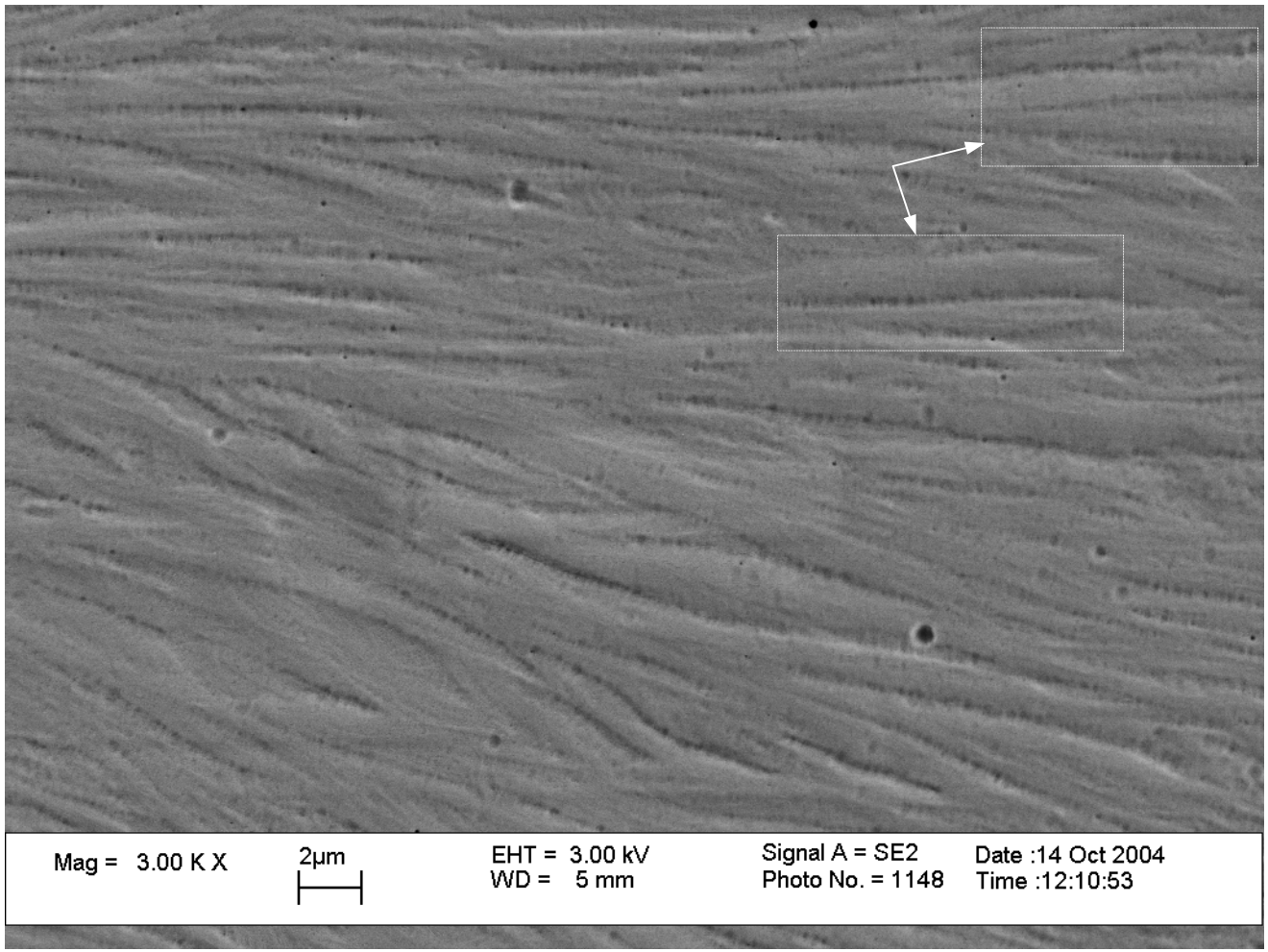

Figure 4.8.7. SEM micrograph of iPP2.62 crystallized at T_c = 124 ^{o}C at atmospheric pressure. Same sample as on Figure 4.8.6.

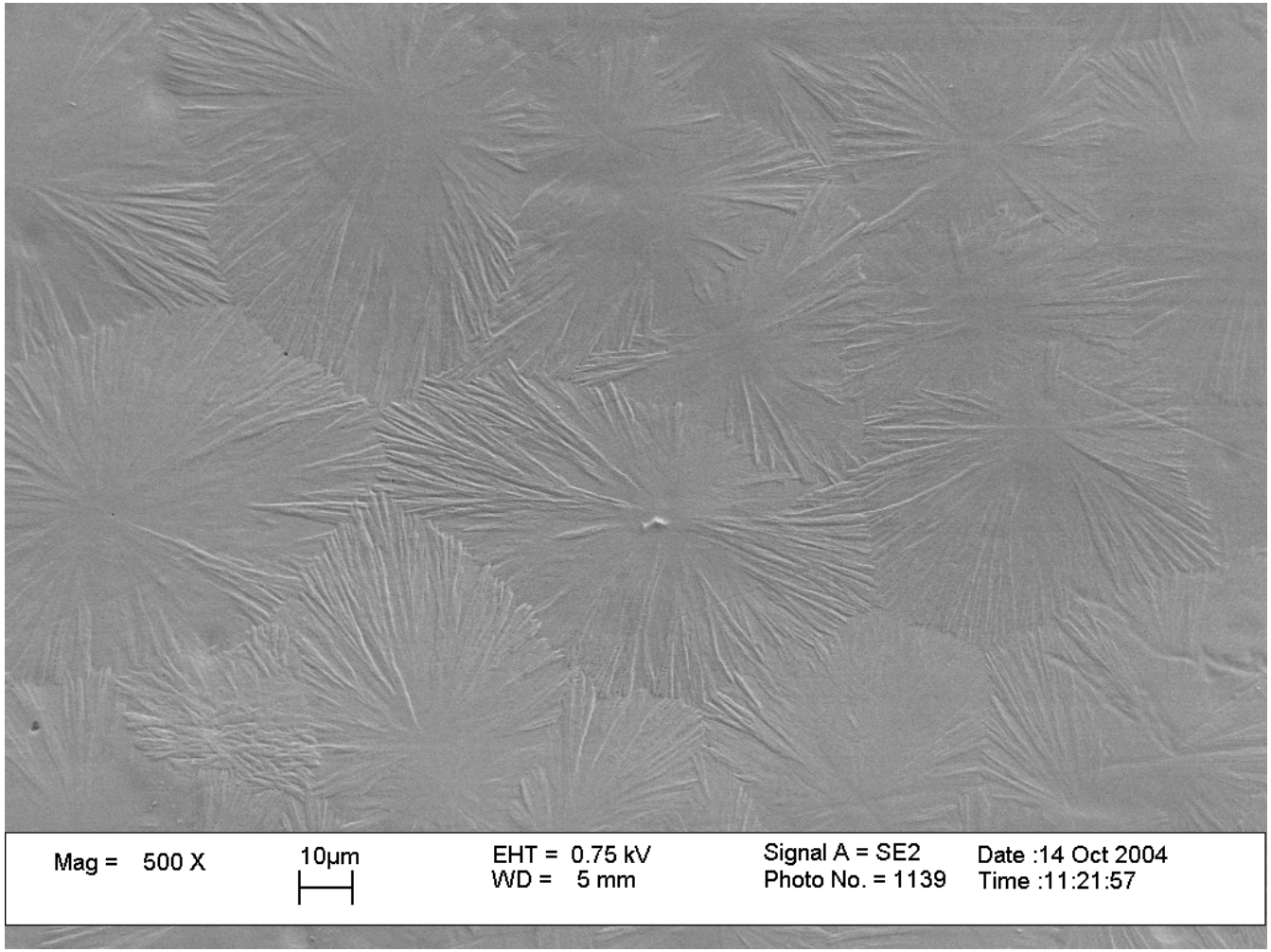

Figure 4.8.8. SEM micrograph of sample iPP2.62 crystallized at T_c = 126 ^{o}C at atmospheric pressure.

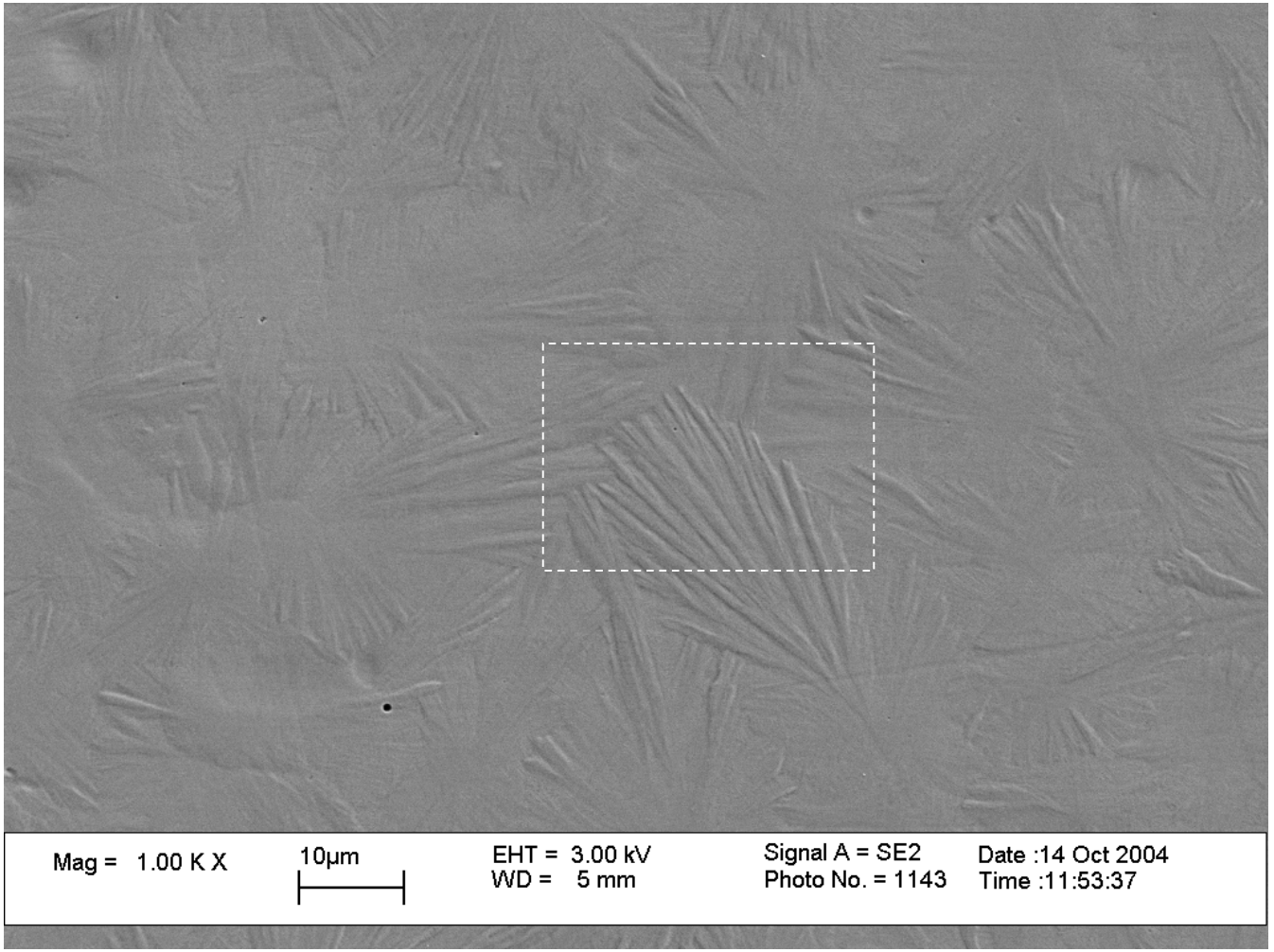

Figure 4.8.9. SEM micrograph of different area of sample iPP2.62 crystallized at T_c = 126 ^{o}C at atmospheric pressure.

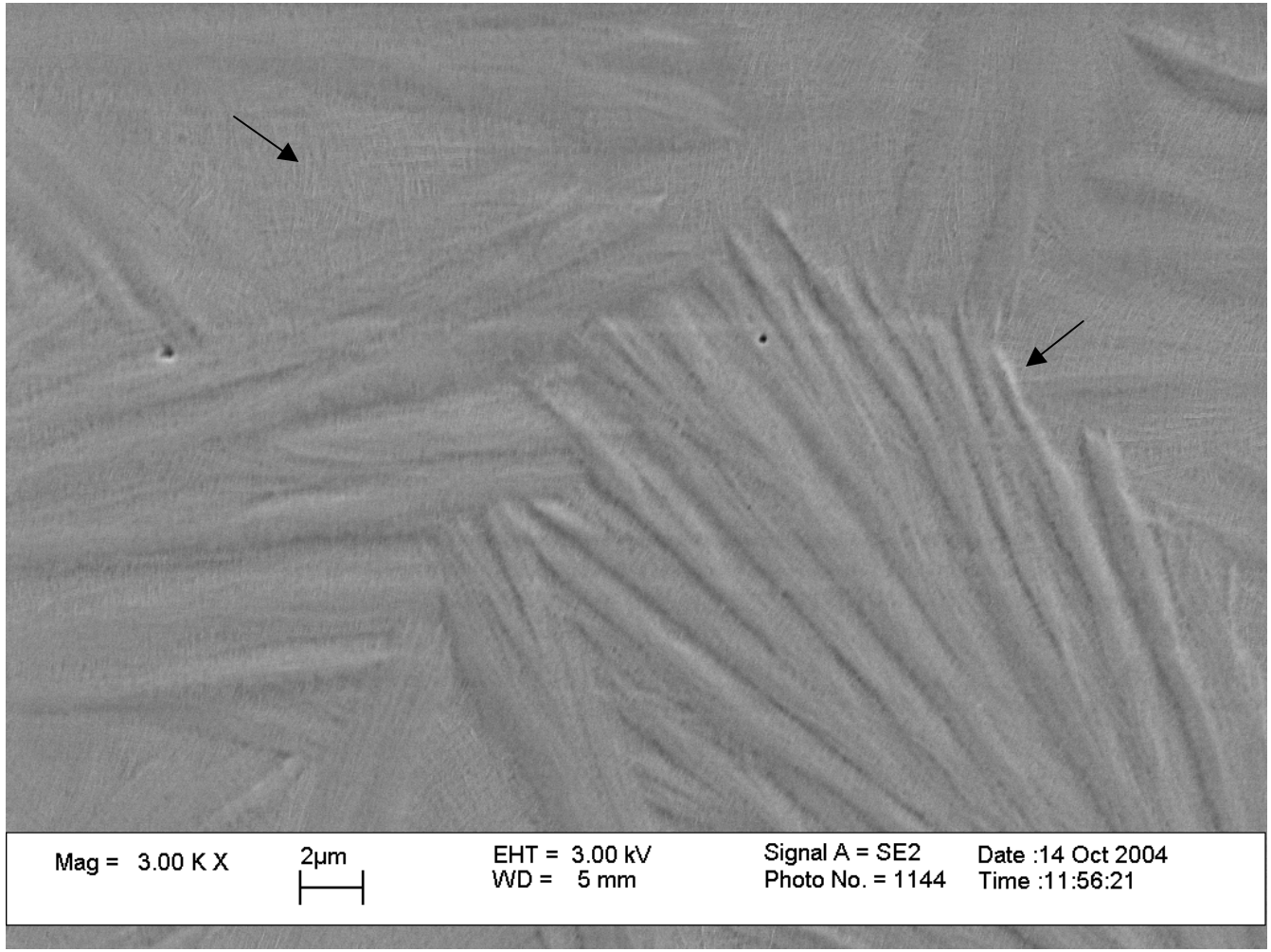

Figure 4.8.10. SEM micrograph of sample iPP2.62 crystallized at T_c = 126 ^{o}C at atmospheric pressure. Magnified area from Figure 4.8.9.

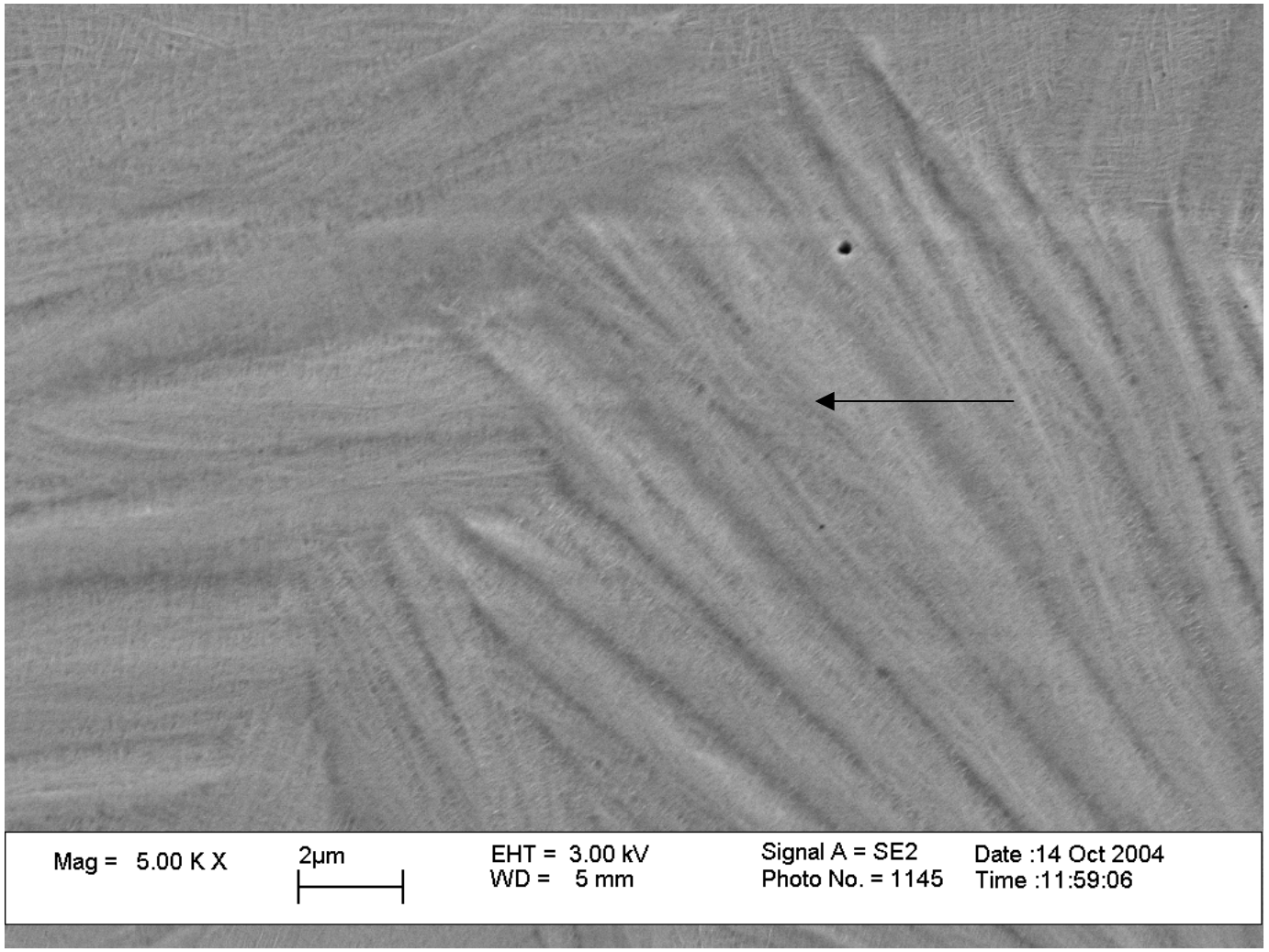

Figure 4.8.11. SEM micrograph of iPP2.62 crystallized at 126 ^{o}C at atmospheric pressure. Same sample as on Figure 4.8.9.

SEM performed on copolymer samples crystallized at high pressures revealed that there is a change in their spherulite structure with applied pressure. Figures 4.8.12–4.8.14 show the micrographs of the copolymer iPP2.62 crystallized at T_c = 170 ^oC and pressure of 193 MPa. It can be seen that there is an absence of the spherulite morphology characteristic of the copolymers crystallized at atmospheric pressure. When crystallized under high pressure these copolymers produced a 'bundle–like' structures that showed less ordered lamellar packing than that of the atmospheric crystallized samples. Similar features can be seen for the copolymer iPP4.38 crystallized at 193 MPa and 156 ^oC as shown in Figure 4.8.15. Same bundle–like structures are observed, but with dimension smaller than that of the iPP2.62 copolymer shown in Figure 4.8.13.

4.8.3. Atomic Force Microscopy

The iPP2.62 copolymer sample crystallized at T_c = 170 ^oC and p_c = 158 MPa was analyzed using atomic force microscopy (AFM). These studies were carried out on a Asylum Research MFP3D atomic force microscope using the tapping mode. The results are shown in Figures 4.8.16 and 4.8.17. Similar to SEM micrographs, these figures show the bundle-like lamellar structures. Because of the higher magnification and better resolution these micrographs enable more accurate measurement of the dimensions of the crystalline structures in the copolymer sample.

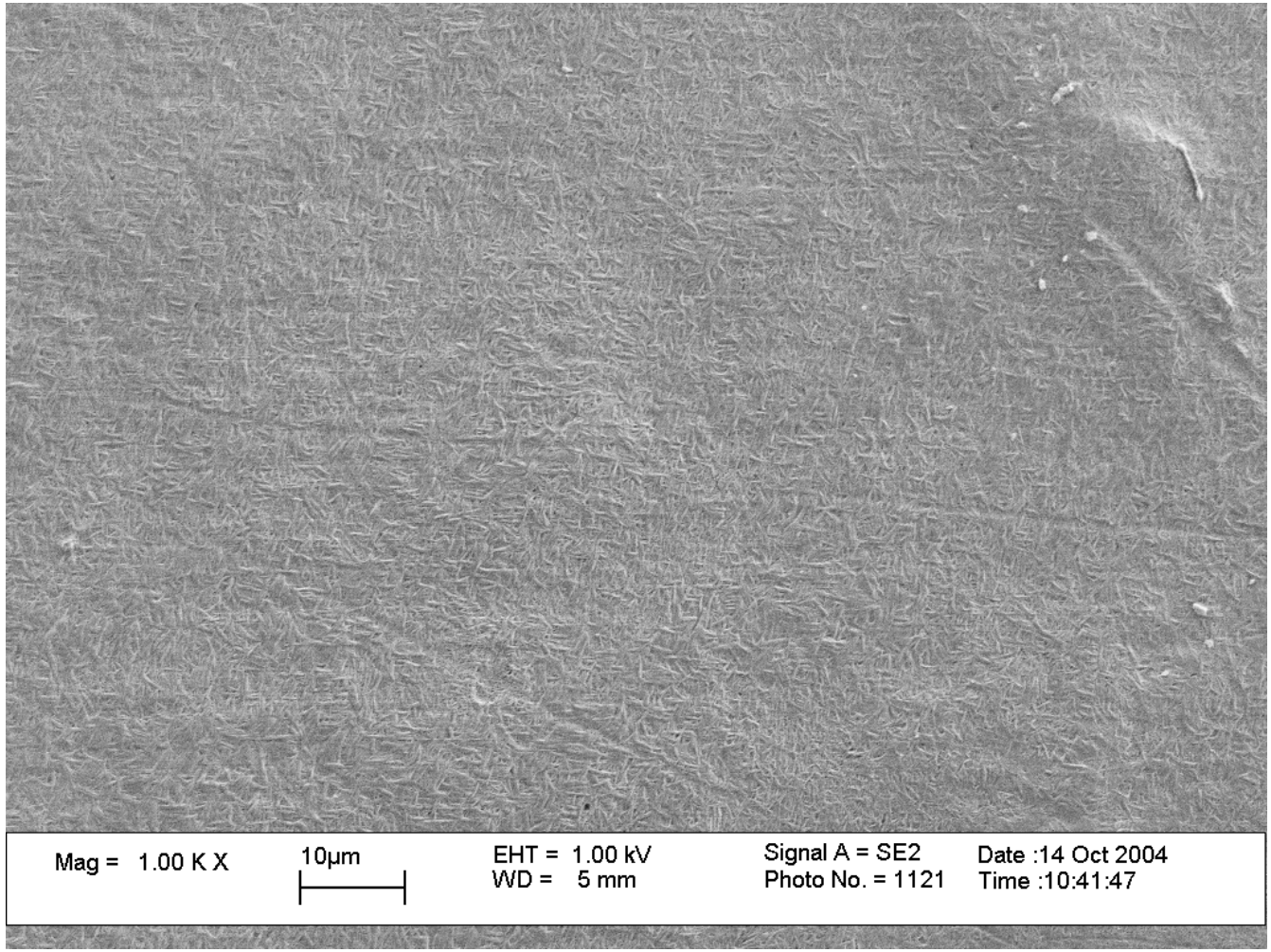

Figure 4.8.12. SEM micrograph of sample iPP2.62 crystallized at T_c = 170 ^{o}C and p_c = 158 MPa.

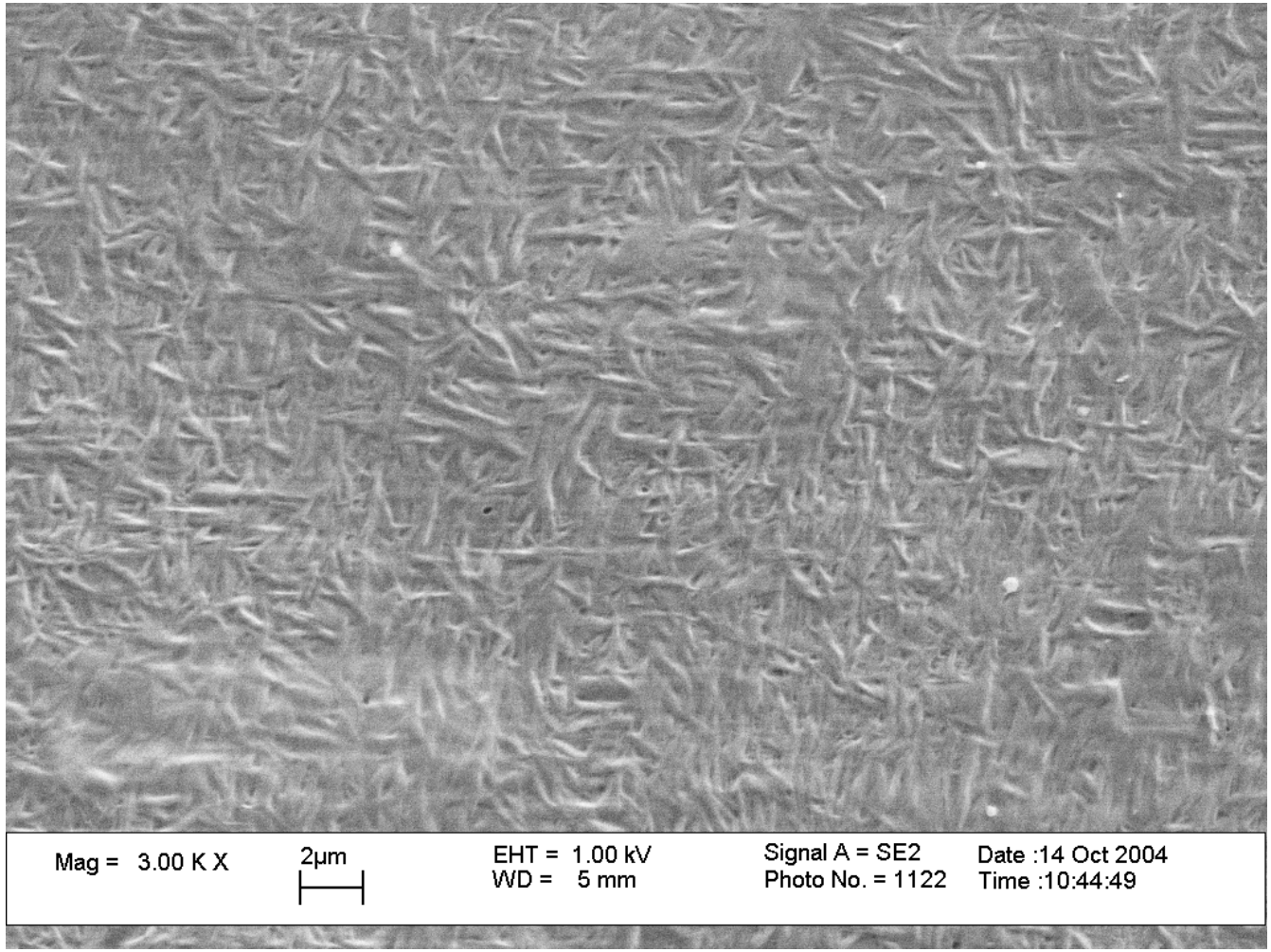

Figure 4.8.13. SEM micrograph of iPP2.62 crystallized at T_c = 170 °C and p_c = 158 MPa. Same sample as in Figure 4.8.13.

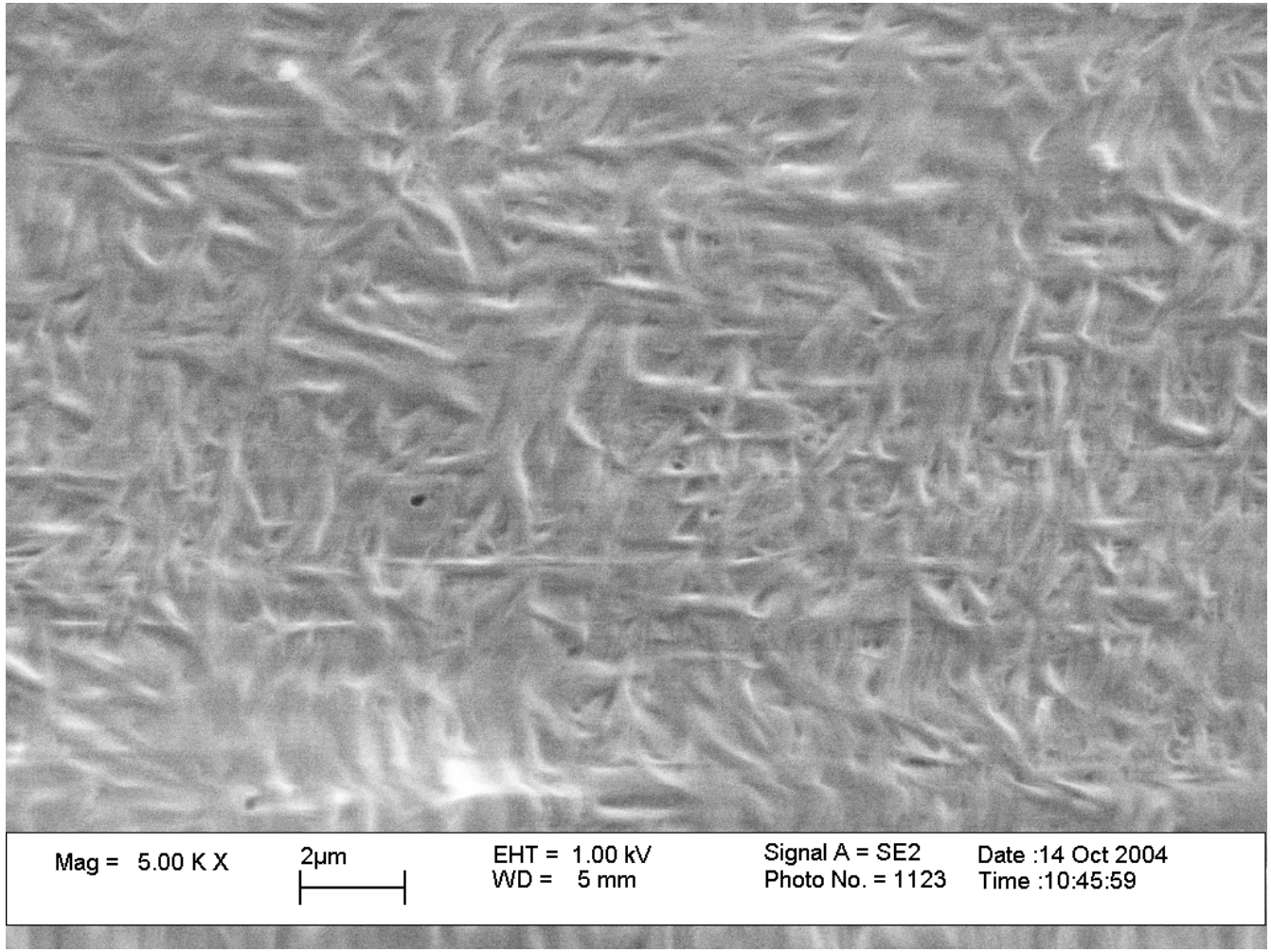

Figure 4.8.14. SEM micrograph of iPP2.62 crystallized at T_c = 170 °C and p_c = 158 MPa. Magnified are from Figure 4.8.13.

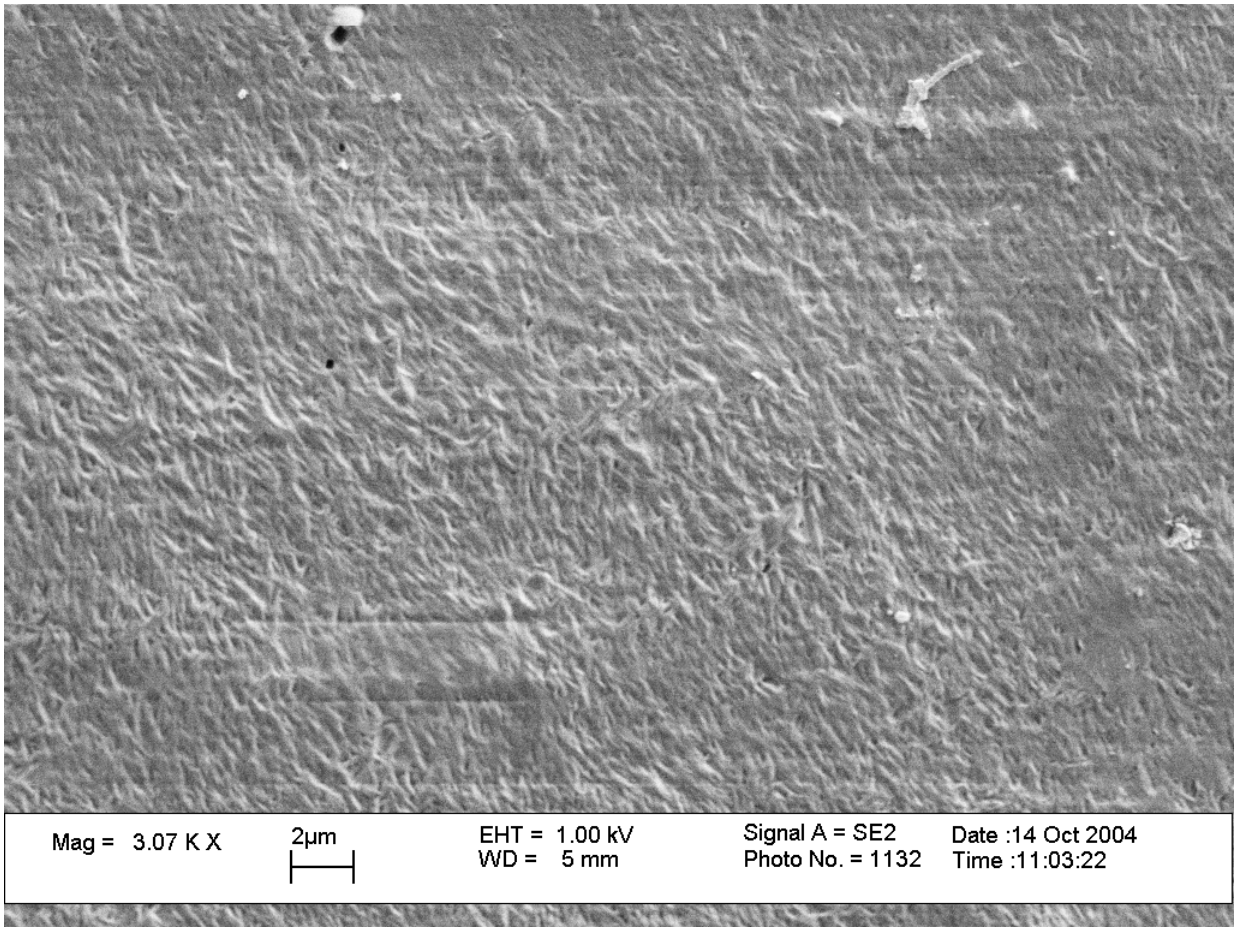

Figure 4.8.15. SEM micrograph of sample iPP4.38 crystallized at T_c = 156 °C and p_c = 193 MPa.

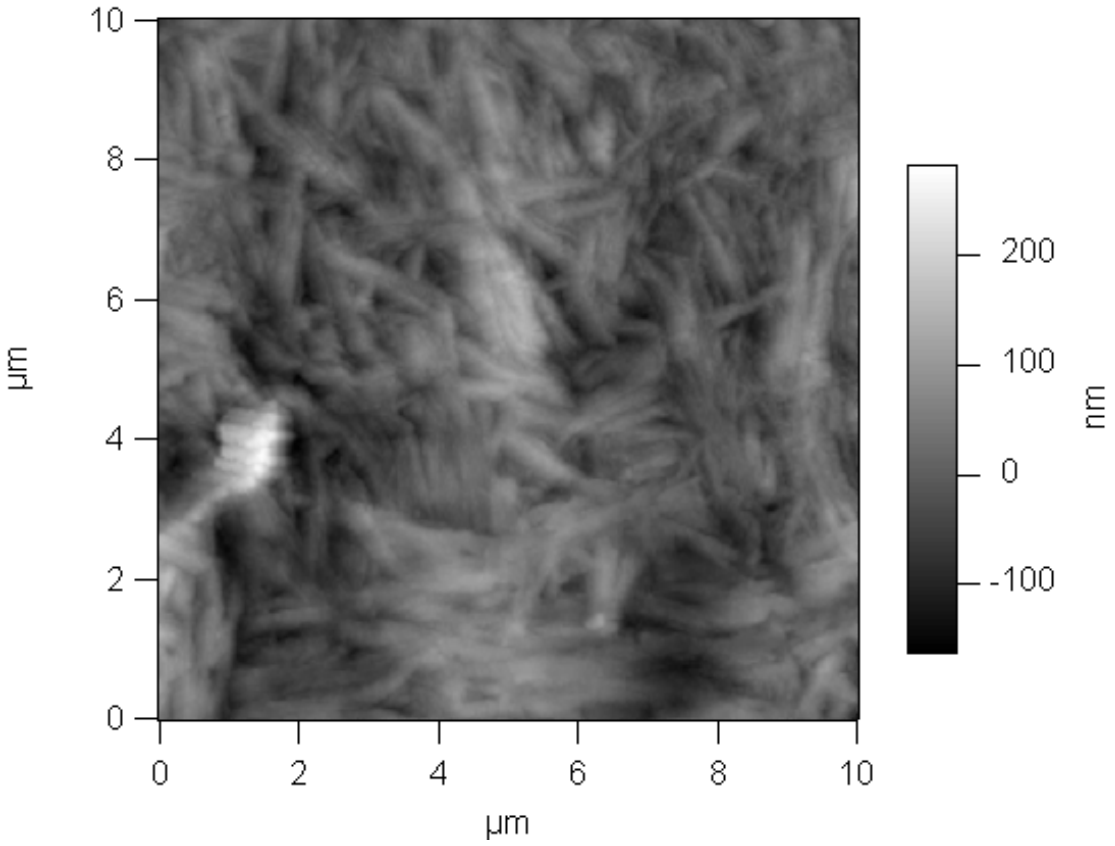

Figure 4.8.16. AFM micrograph of iPP2.62 crystallized at T_c = 170 ^oC and p_c = 158 MPa.

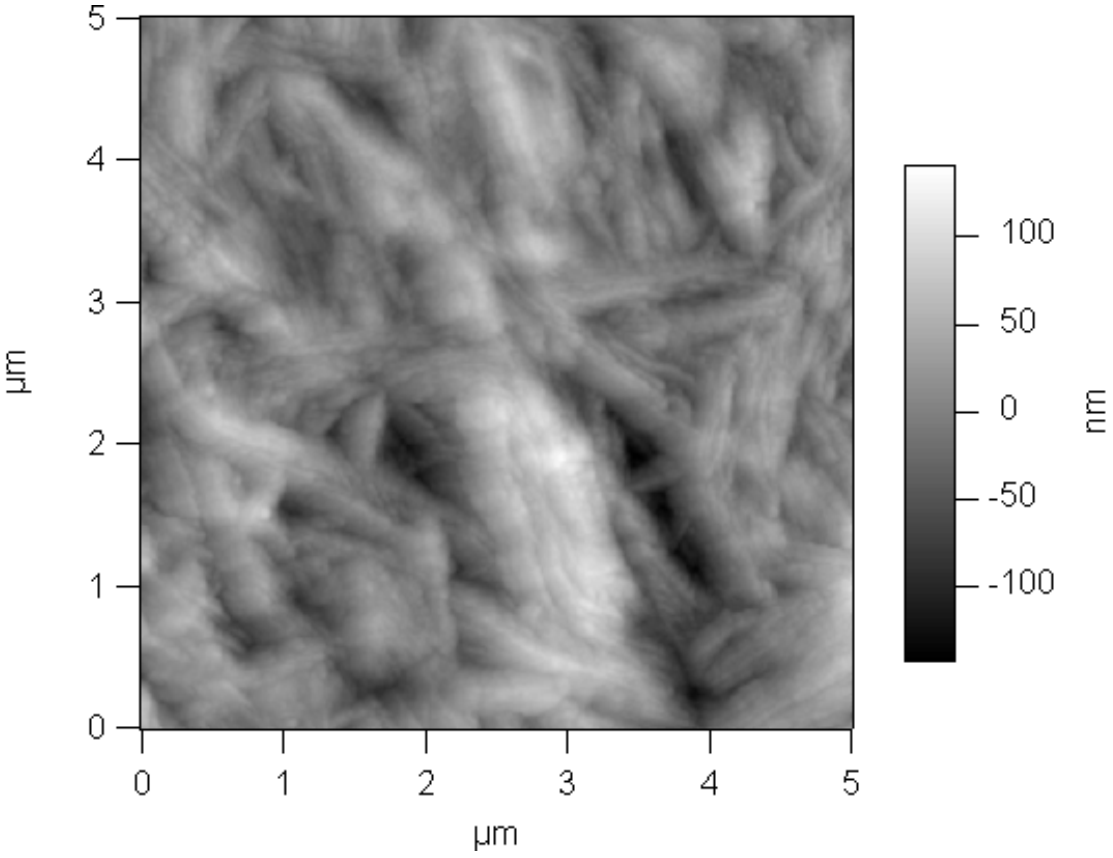

Figure 4.8.17. AFM micrograph of iPP2.62 crystallized at T_c = 170 °C and p_c = 158 MPa. Magnified area from Figure 4.8.16.

5. DISCUSSION

5.1. Microstructure Properties from ^{13}C NMR

The morphology and crystallization behavior of propylene–ethylene copolymers and their ultimate end properties are influenced by their chain microstructure. Therefore it is very important to determine their microstructure characteristics, such as ethylene concentration, propylene and ethylene number–average sequence lengths and stereoregularity. These are all properties that were determined from the ^{13}C NMR.

From Figure 4.1.1 it is evident that in the NMR spectra of the propylene–ethylene copolymers there are three sharp peaks at approximately 47 ppm, 29 ppm, and 22 ppm, which correspond to the three different carbon atoms in the propylene monomer unit, methylene, methine and methyl, respectively. No significant head–to–head and tail–to–tail structures were observed, due to the absence of the resonances arising from the inverted propylene units.[123] Since Ziegler–Natta catalysts used to synthesize these copolymers are highly regioselective in propylene insertion, it was expected that the fractionated copolymers would not contain regio–defects, at least not in the amount above the detection limit of the NMR instrument (0.1 % mol).

Results presented in Table 4.1.3 show that fractions extracted with the solvent with higher boiling point (cyclohexanes) contain less then 5 mol% ethylene, and are composed of long propylene sequences (37 for iPP2.62 and 23 for iPP4.38) with only isolated ethylene units, represented with triads such as PPE and PEP. As seen from Table 4.1.2 their spectra do no contain resonances arising from ethylene dyads ($S_{\alpha\delta}$, $S_{\gamma\gamma}$, $S_{\beta\delta}$), triads ($S_{\gamma\delta}$, $S_{\delta\delta}$) or alternating propylene–ethylene units ($T_{\delta\delta}$).

Fractions extracted with solvent with lower boiling point (hexanes) have peaks due to the sequences of two ($S_{\alpha\delta}$, $S_{\gamma\gamma}$, and $S_{\beta\delta}$) or three ($S_{\gamma\delta}$ and $S_{\delta\delta}$) ethylene units. However, their number–average ethylene sequence lengths, $\overline{n}_e$, are 1.18 and 1.29,

indicating that these fractions have only small amounts of short blocks EE and/or EEE. From Tables 4.1.2 and 4.1.3 it can be seen that copolymer fraction iPP10.45 contains some alternating sequences (EPEEP) and only ethylene dyads (PEE). Copolymer fraction with 15.57 mol% ethylene (iPP15.57) has the most complex ethylene sequences, such as sequences with three ethylene units (PEEEP) and alternating structure (EPPEPE). These types of sequences have profound impact on the crystallization and melting behavior of the copolymers. Presence of short uninterrupted propylene sequences reduces the crystallization growth rates, and changes the resulting morphology and polymorphism.

From Table 4.1.3 it can be seen that only copolymer iPP15.57 contains [EEE] triads in the concentration of 1.15 mol%. Therefore, there is no significant level of ethylene blocks in the copolymer fractions. Another way of visualizing the length of the ethylene sequences in the copolymer macromolecules is by calculating the number–average sequence length of uninterrupted methylene carbons, n_o, as defined in equation (2.7.4). The results from these calculations are shown in Table 5.1.1. Values of n_o for the fractionated copolymers are in the range 1.04 – 1.25, which further confirms the fact that there are no long ethylene sequences that are capable of crystallizing.

Starting copolymers iPPu3% and iPPu5% used for the fractionation were characterized by the manufacturer as random copolymers. It is of interest to characterize the randomness of the microstructure of the fractionated copolymers in terms of a single parameter. Such a parameter is the randomness parameter χ_R, as defined in equation (5.1.1) which can be used as a measure for randomness in the sequence distribution of the copolymer repeat units.[124]

$$\chi_R = \frac{[PE]}{2[P][E]} \tag{5.1.1}$$

Values of the parameter χ_R that correspond to different types of copolymer (random, block, of alternating) are listed in Table 5.1.2.

Table 5.1.1. Values for the number–average sequence length of uninterrupted methylene carbons, n_o, and the randomness parameter, χ_R, for studied copolymer fractions.

Sample ID	n_o	χ_R
iPP2.62	1.04	1.03
iPP4.38	1.06	1.02
iPP10.45	1.16	0.95
iPP15.57	1.25	0.92

Table 5.1.2. Values for the randomness parameter for various types of copolymers.[124]

Randomness parameter	Copolymer type
$\chi_R = 1$	random
$\chi_R > 1$	more alternating character
$\chi_R < 1$	more blocky character
$\chi_R = 2$	completely alternating
$\chi_R = 0$	completely block

Calculated values of χ_R for the copolymer fractions using the equation 5.1.1 are shown in Table 5.1.1. From the values in Table 5.1.1 it can be seen that the fractions have values for χ_R close to unity (average value is 0.98). Fractions that have higher ethylene content are characterized with more blocky character, which has been shown to be typical for the copolymers synthesized with Ziegler–Natta catalysts.[75] However, since the concentration of [EEE] triads in the fractions is either very low (in case of iPP15.57) or zero (iPP2.62, iPP4.38, and iPP10.45) and the departure from the true random comonomer distribution is very small, these fractions will be characterized as 'random copolymers'.

A decrease in tacticity with increasing comonomer content has been reported by Zannetti *et al.*[125] similar to the observations made for our fractionated copolymers. An ideal isotactic polypropylene chain consists of a series of like–handed left or right) *meso* additions described by the *meso* pentad as mmmm. Any departure from the ideal isotacticity, influenced by the type and number of inserted structural irregularities along the polymer chain will be represented by any type of pentad other than mmmm, as shown in Figure 2.7.2. Data presented in Table 4.1.4 indicate that copolymer fractions has low amount of stereo defects of the type mmmr and mrmm. Based on the presence of only one racemic addition in the chains these copolymers can be described as a stereoblock polymers of left– and right–handed *meso* additions.

As was the case for the comonomer composition, fractions iPP10.45 and iPP15.57 have the most complex stereo–sequence pentads distribution. They have stereo–defects of the type mmrr and mrrm, that indicates that copolymer chains contain single irregularities (syndiotactic unit) among a series of like–handed *meso* additions. However, they also contain mrmr defects which represent a dyad or two subsequently added irregularities. Stereo defects of the copolymer fractions (expressed as the concentration of the *racemic*, *r*, units) increases with the ethylene content at the rate of approximately 1 to 1.5 irregular units for each comonomer unit incorporated in the chain.

5.2. Atmospheric Pressure Crystallization Study

5.2.1. Formation of γ–phase

WAXD patterns of the fractionated copolymers crystallized at atmospheric pressures showed that in the studied crystallization temperature range a mixture of both α– and γ–crystal forms. This can be observed on Figures 4.3.1 – 4.3.4. The amount of γ–crystals formed as a function of the crystallization temperature for the four copolymer samples is reported in Figure 5.2.1.

It can be observed that the amount of γ–phase produced increases with the increasing crystallization temperature in all copolymers. At a fixed crystallization temperature the content of γ–phase increases with increasing ethylene and total defect content. The maximum amount of the γ–phase that was produced in these copolymers at atmospheric pressure was 74 %. Also, in all copolymers at a degree of supercooling in the range of 55–60 ^{o}C a plateau is observed in the amount of γ–phase produced.

The formation of γ–form in the case of metallocene *i*–PP homopolymer has been associated with the presence of shorter isotactic sequences. It was found that the lower the degree of isotacticity, the higher is the amount of crystallized γ–phase.[41,126] For random propylene–ethylene copolymers there are two parameters that will have an effect on the γ–phase formation: concentration of ethylene and stereo–defects. They both generate shorter crystallizable isotactic *i*–PP sequences in the macromolecular chains.

The increase in the amount of the γ–phase content with increasing crystallization temperature can be a consequence of two competing thermodynamic and kinetic processes depending on the availability of crystallizable sequences. Based on the packing energy calculations it was shown that γ–phase is slightly more stable than α–phase in the case of infinite crystals.[127] Thermodynamically, γ–crystalline form is favored because the

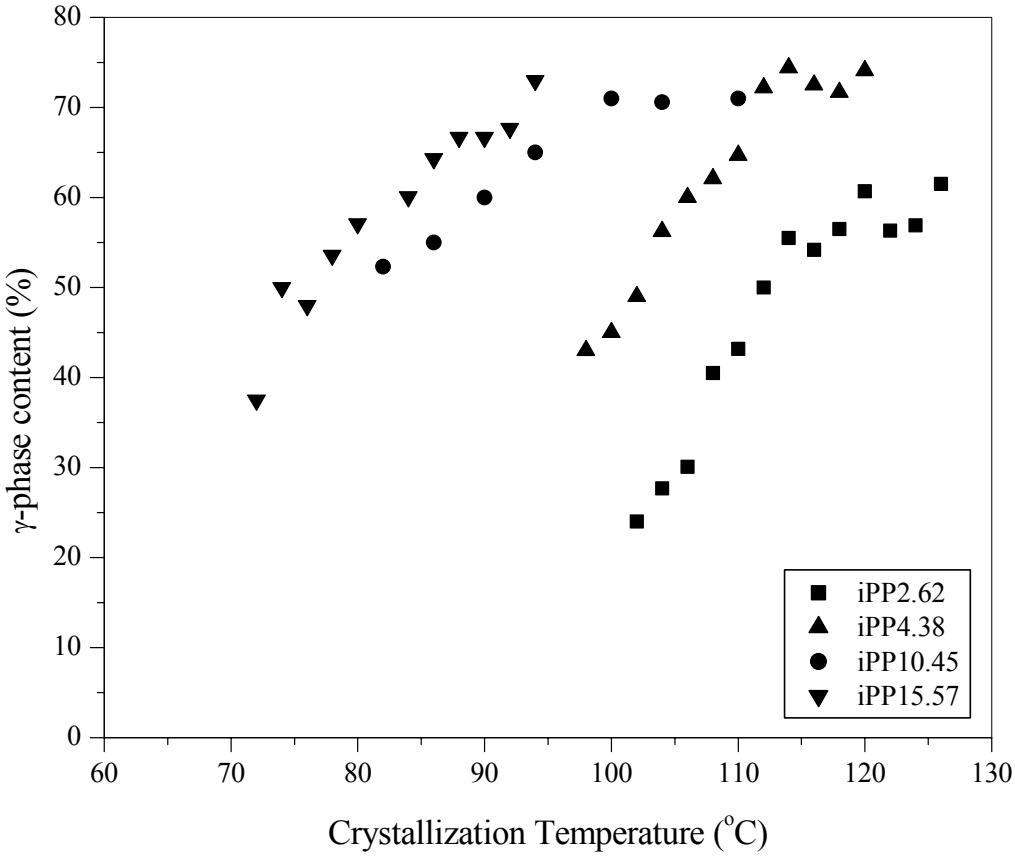

Figure 5.2.1. γ–phase content as a function of the crystallization temperature for the copolymer fractions crystallized at atmospheric pressure.

comonomer and stereo defects and the α/γ structural disorder are tolerated more in the γ–form than in the crystals of α–form.[126]

Important question that arises in the case of the propylene–ethylene copolymers is how the concentration of the crystallizable *i*–PP sequences changes with temperature. At a given temperature only sequences whose length exceeds the critical number of crystallizable units, ξ_{cr}, can participate in the crystallization process. As the crystallization temperature is increased, because of the increase in lamellar thickness with temperature, the composition and sequence distribution of the non–crystallizable portion of the system also change. To qualitatively illustrate this the approach developed for ethylene copolymers by Alamo and Mandelkern[128] was used. According to this approach, the dimension of the of the critical size nucleus ℓ_g^* for copolymer with infinite molecular weight can be determined from the equation:

$$\ell_g^* = \frac{2\sigma_e}{\Delta G + RT\ln(1-X)} \tag{5.2.1}$$

where σ_e is the fold surface free energy, $\Delta G = \Delta H_f(\Delta T/T_m^0)$, and X is the mole fraction of the defects. The critical number of crystallizable units, ξ_{cr}, determined from ℓ_g^* is plotted in Figure 5.2.2 as a function of the defect mole fraction and crystallization temperature. Parameters used to calculate ℓ_g^* in equation (5.2.1) were those of the *i*–PP homopolymer: σ_e = 62.3 erg/cm^2, ΔH_f = 209 J/g, and T_m^0 = 186.1 ^{o}C.

From Figure 5.2.2 the significant qualitative observation that can be made is that the critical number of crystallizable units changes with composition and temperature. At lower crystallization temperatures the formation of the α–phase is more favored kinetically, resulting in lower γ–phase content. For example, for copolymer sample iPP2.62 that has 5.76 mol% total defects at T_c = 80 ^{o}C ξ_{cr} = 14, meaning that sequences with 14 or more propylene units will be able to crystallize. As the crystallization temperature is increased, the number of long isotactic sequences that can crystallize by

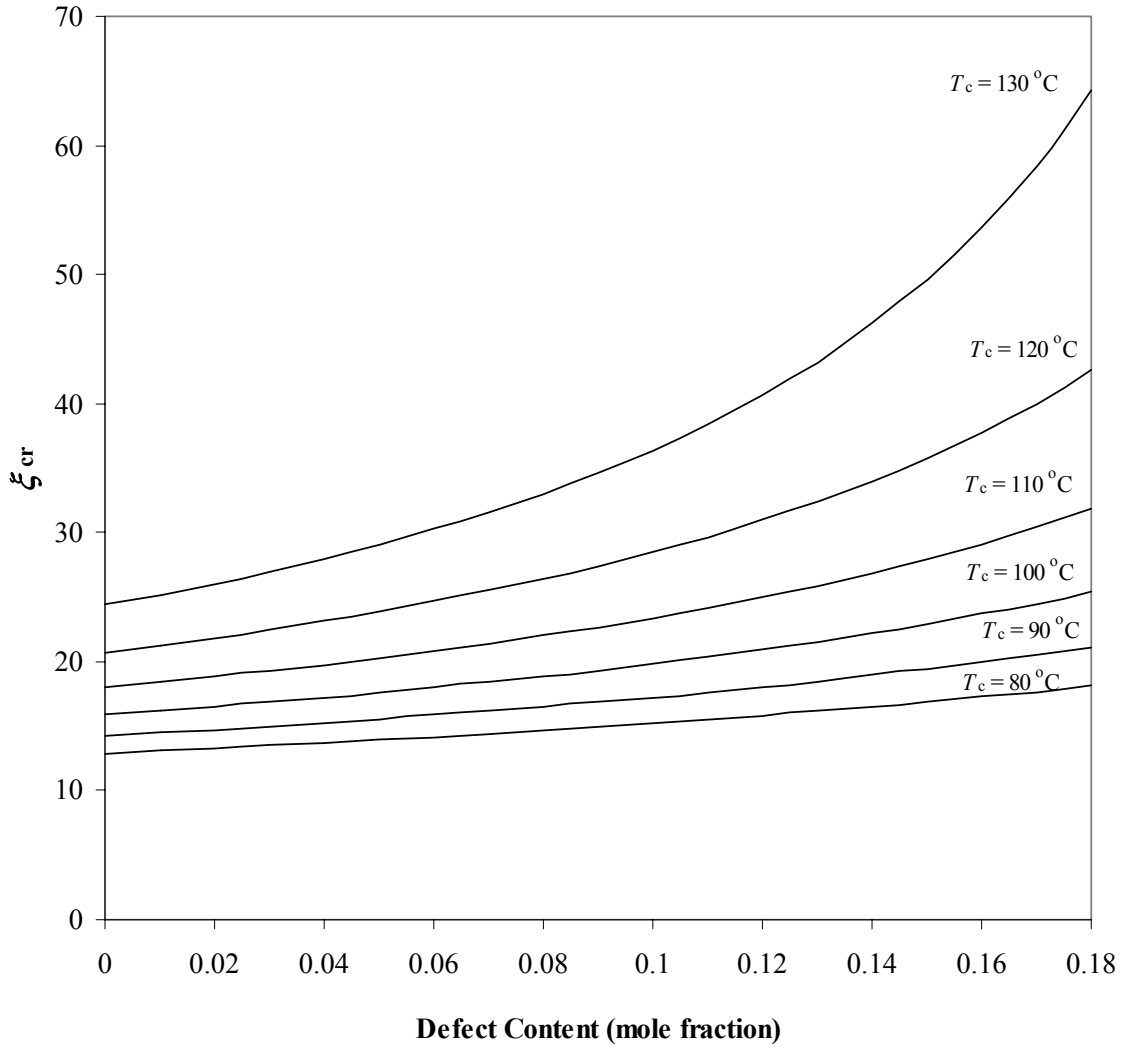

Figure 5.2.2. Calculated critical number of repeating units as a function of the defect concentration of *i*–PP for indicated crystallization temperatures.

with 14 or more propylene units will be able to crystallize. As the crystallization temperature is increased, the number of long isotactic sequences that can crystallize by chain folding into α–phase is reduced. On the other hand, the increased number of shorter sequences can be accommodated into γ–phase crystals by tilting of the chains and not necessarily by chain folding.[30,46,129] As a result, with increasing crystallization temperatures the γ–form develops during the slow crystallization process. At these temperatures only long uninterrupted isotactic sequences are capable of crystallizing in the α–form, while the shorter sequences that contain more defects produce the γ–crystals. However, when the temperature is further increased ξ_{cr} assumes very large values, and the concentration of sequences that equal or exceed this value becomes very small. At these temperatures α–phase will dominate again because only the longest sequences will crystallize by chain folding.

5.2.2. Multiple Melting in DSC

All four random propylene–ethylene copolymers used in this study exhibit complex melting behavior similar to that of the isotactic polypropylene. The existence of the two melting endotherms in the DSC scans of these samples can be explained by any of the following:

1. Melting of less stable crystals at the lower endotherm region, their recrystallization during the heating process and their subsequent remelting in the higher endotherm region.

2. Melting of γ–phase and α–phase crystals in the low and high endotherms, respectively.

3. Melting of two crystalline lamellar thickness populations which have different melting temperatures.

Another point that needs to be discussed is whether during the melting of the copolymer samples there is solid–solid transformation from γ to α–phase during the DSC experiments. It has been shown for the *i*–PP homopolymer that this transformation occurs at temperatures above 140 ^{o}C and that it is time dependent.[89,91] Also, according to Pae[91] the γ to α transformation occurs very slowly and cannot be detected in the DSC experiment during heating at a rate of 10 ^{o}C/min. Therefore, solid–solid transformation from γ to α crystals does not occur in copolymers samples during DSC melting experiments.

The first hypothesis of melting–recrystallization–remelting can be tested by an analysis of the heating rate effect on the melting behavior of the copolymer samples. For this purpose we have studied the evolution of peak melting temperatures and heat of fusion related to each endotherm with changes in heating rate for iPP2.62 sample crystallized at three isothermal crystallization temperatures. These crystallization temperatures are representative of low (T_c = 126 ^{o}C), medium (T_c = 114 ^{o}C) and high (T_c = 102 ^{o}C) degree of supercooling. Corresponding melting curves are shown in Figures 4.4.9–4.4.12.

For the sample crystallized at low degree of supercooling, shown in Figure 4.4.9 and 4.4.12, the temperature interval between the low and high melting peaks decreases with increasing heating rate, while the ratio of low to high peak heat of fusion increases. These observations can be taken as evidence for the existence of melting–recrystallization process during heating. As the heating rate is increased, there is less time for copolymer macromolecules to recrystallize above the initial low–temperature melting endotherm. Therefore, only smaller fraction of the material has time to recrystallize during the heating, hence the upper endotherm has lower melting temperature and lower heat of fusion. Another significant observation is that both the ratio of the heats of fusion associated with the high and low endotherm, and the temperature interval between the low and high endotherm level off at high heating rates (Figure 4.4.12). Also, significant recrystallization process for polymers with high

molecular weight is not expected at heating rates above 20 ^{o}C/min. In our experiments, double melting endotherms were observed even for samples melted at 40 ^{o}C/min. All these facts suggest that the melting–recrystallization–remelting process is not responsible for the occurrence of the two melting peaks, although the occurrence of non–relevant recrystallization phenomena cannot be excluded.

In the case of the samples crystallized at high and medium degrees of supercooling, a new endotherm in a form of shoulder appears just above the higher melting peak as seen in Figures 4.4.9 and 4.4.10, respectively. For iPP2.62 crystallized at 114 ^{o}C this endotherm shows only at the two lowest heating rates, while for iPP2.62 crystallized at 102 ^{o}C the shoulder disappears only at the highest heating rate of 40 ^{o}C/min. The phenomenon of partial melting and recrystallization during heating can contribute to the appearance of the high temperature shoulder, which disappears with increasing of the heating rate. This is an indication that the less perfect crystals are melting and recrystallizing when the heating rate is sufficiently slow. For the iPP2.62 samples crystallized in the temperature range of 102 – 110 ^{o}C this behavior occurs during the heating at a rate of 10 ^{o}C/min as seen in Figure 4.4.4. The fact that the shoulder temperature remains relatively constant with increasing crystallization temperature further supports the fact.

The comparison of the melting behavior of the samples crystallized at low to high degrees of supercooling points out that the effects of the melting–recrystallization phenomenon are less prominent for samples crystallized at high temperatures than samples crystallized at low crystallization temperatures. This observation is expected since crystallization at high crystallization temperature leads to thicker and more stable crystals that are less susceptible to recrystallization. On the other hand, from the DSC melting curves it was observed that the multiple melting behavior is more prominent for samples crystallized at high crystallization temperatures.

When all of these observations are taken into consideration it can be concluded that although some melting–recrystallization–remelting does occur during the heating, this phenomenon is not responsible for the multiple melting peaks of these copolymers.

The second hypothesis that the melting of γ– and α–phase crystals is responsible for the multiple melting was tested by high temperature WAXD. Using the HTWAXD the possible disappearance of one of the phases can be followed as the temperature is increased. For this purpose three samples were used: iPP2.62 crystallized at 126 ^{o}C, iPP4.38 crystallized at 120 ^{o}C, and iPP15.57 crystallized at 94 ^{o}C. The experiments were carried out at temperatures determined from DSC, such as the peak temperatures, as well as the temperatures below and above peak temperatures. The experimental procedure and the results are presented in section 4.5. If this hypothesis is valid, with increasing temperature the intensity of the characteristic peak of one of the phases will start to decrease and eventually disappear at temperature just below the highest melting temperature.

High temperature diffractograms presented in Figures 4.5.1–4.5.3 showed that with increasing temperature, the intensity of the characteristic reflection of the γ–phase starts to decrease at the onset of the melting process. At temperature of 100 ^{o}C, which is close to the peak of the lowest endotherm, the height of the (117) reflection started to decrease considerably. This indicates that γ–crystals started to melt at lower temperatures than α–crystals, thus decreasing the γ–crystals content from 51.5% to 41.3% (approximately 20%). At the same time, the intensity of the characteristic reflection of the α–phase remained constant until the temperature of the onset of the highest melting endotherm was reached. At 139 ^{o}C, the temperature that corresponds to the second endotherm, the (117) reflection has almost disappeared and the content of the γ–crystals decreased to less than 15 %, while the height of (130) reflection did not change. Only in the temperature range of 144–149 ^{o}C, which corresponds to the highest endotherm, the height of the (130) reflection and the α–crystals content started to decrease, while the γ–crystals have completely disappeared.

Therefore, with great certainty it can be postulated that the multiple melting behavior of the propylene–ethylene copolymers is due to the melting of two different polymorphic crystals, α– and γ–phase crystals. Consequently, the lower two endotherms in the DSC melting curves are assigned to the melting of the γ–crystals, while the highest endotherm is assigned to the melting of the α–crystals. The lowest broad melting endotherm that occurs at temperatures below the crystallization temperatures is due to the melting of the material which did not crystallize at these higher crystallization temperatures even for very long crystallization times, but crystallized into γ–phase crystals during the quenching.

These results are in agreement with published results for metallocene *i*–PP,[41,126] as well as for random Ziegler–Natta[74,75] and metallocene[87] propylene–ethylene copolymers that associate the lower melting endotherm with the melting of the γ–phase, and the higher–melting endotherm with the melting of the α–phase.

From Figures 4.4.4–4.4.7 it can be seen that the ratio of the area under the lower endotherm to the area under the upper endotherm increases with ethylene content and crystallization temperature. This observation is in agreement with the observed increase in the γ–phase with ethylene content and crystallization temperature from the WAXD experiments (section 4.3.1). If the above statement about the melting endotherm assignments is valid, than the γ–phase content of the copolymers can be determined from the DSC endotherms and compared with the results obtained from WAXD. This procedure involves deconvolution of DSC peaks and analysis of peak areas. γ-phase content from DSC endotherms can be calculated using the following equation:

$$\gamma_{\mathrm{DSC}} = \frac{\Delta H_{\gamma}}{\Delta H_{\mathrm{tot}}} \tag{5.2.2}$$

where ΔH_{γ} is the area of the peaks at lower melting temperatures, and ΔH_{tot} is the total heat of fusion.

An example of this procedure for copolymer iPP2.62 crystallized at 126 ^{o}C is shown in Figure 5.2.3. First two melting peaks contribute to the heat of fusion due to the melting of the γ–phase crystals ($\Delta H_{f,1} + \Delta H_{f,2}$), while the third peak represents the heat of fusion of the α–phase ($\Delta H_{f,3}$).

Equation (5.2.2) was used to calculate the γ–phase content from the DSC endotherms, and the obtained results along with the γ–phase WAXD results are shown in Figure 5.2.4. There is a good correlation between the calculated γ–phase content data from WAXD and DSC for these copolymer samples, evident from the proximity of the data to the line with slope one.

5.2.2.1. Equilibrium melting temperature – Hoffman–Weeks analysis

The equilibrium melting temperature, T_m^0, is an important parameter in describing the structure–properties relationship in polymers, and is essential in the analysis of the crystallization nucleation and kinetics. For the analysis of the crystal growth data T_m^0 is needed for defining the degree of supercooling $\Delta T = T_m^0 - T_c$. Experimental determination of T_m^0 is often difficult and there is disagreement over the values of T_m^0 even for widely studied polymers.

To determine the T_m^0 of the propylene ethylene copolymers as a function of comonomer content, both Hoffman–Weeks and Gibbs–Thompson methods were used. The construction of the Hoffman–Weeks plot is described in section 2.4.

Hoffman–Weeks plot for the iPP2.62 copolymer, with extrapolations for both α– and γ–phases is shown in Figure 5.2.5. Temperatures that correspond to the higher and lower endotherms were used as melting temperatures of α– and γ–crystals, respectively. It should be noted that experimental data for melting of γ–crystals were available only for samples with more than 50 % γ–phase. For samples with lower γ–content it was

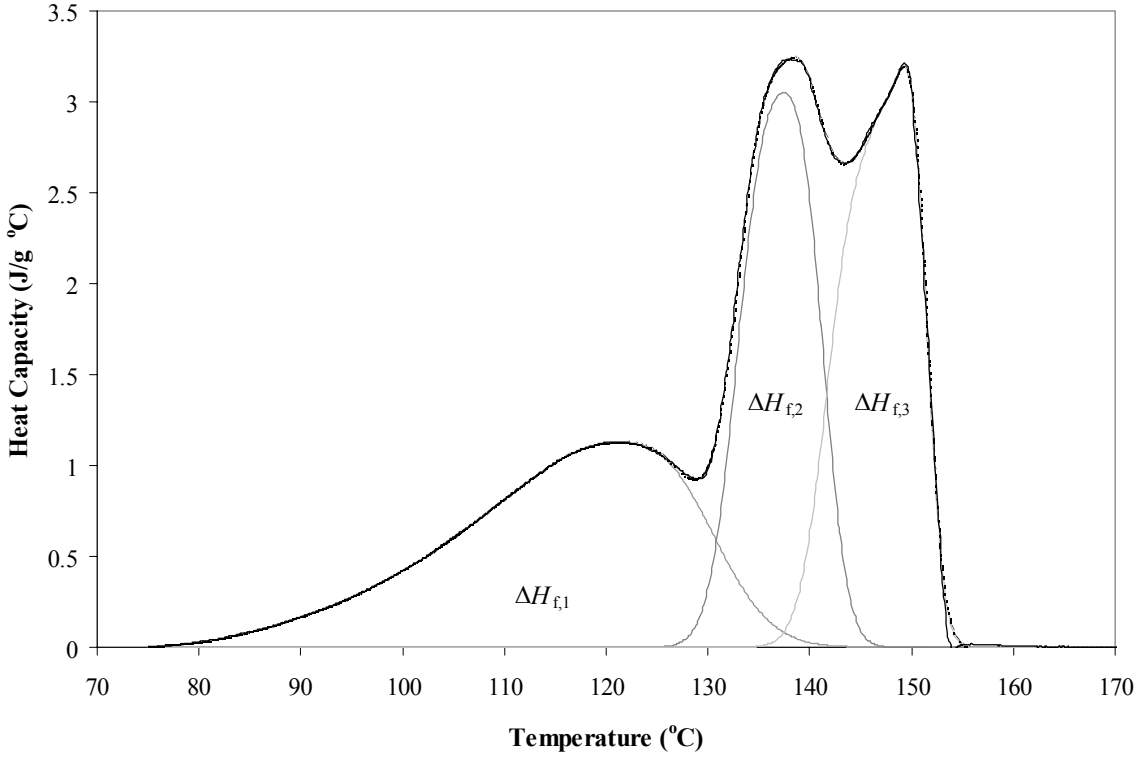

Figure 5.2.3. Peak deconvolution of the DSC melting endotherm of copolymer iPP2.62 crystallized at 126 °C and atmospheric pressure.

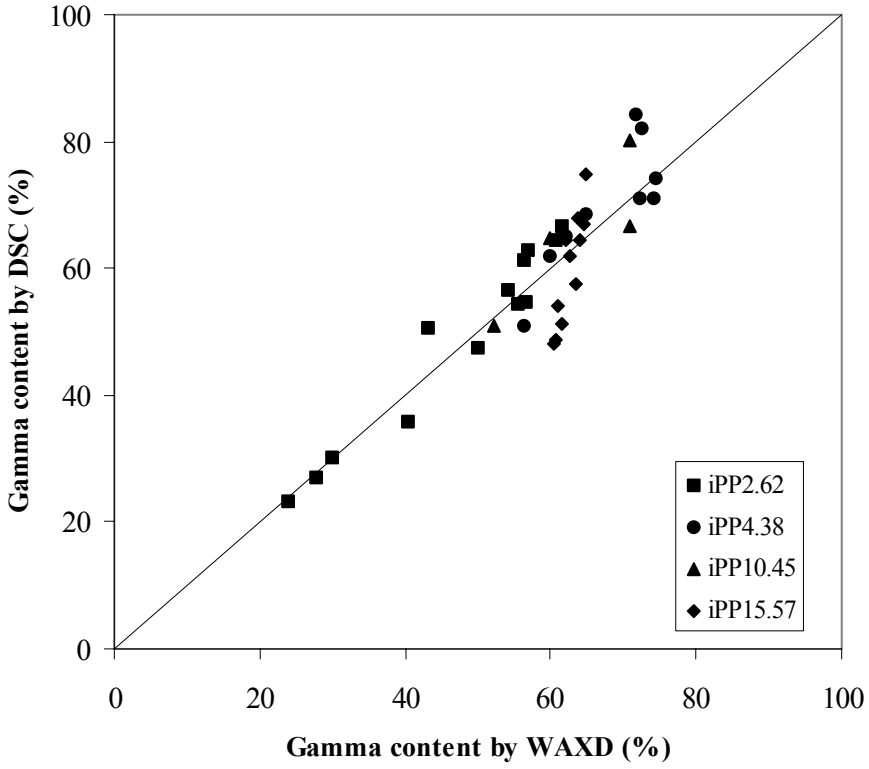

Figure 5.2.4. γ–phase content calculated from DSC versus γ–phase obtained from WAXD for the four copolymers crystallized at atmospheric pressure. The solid line corresponds to a line with the slope = 1.

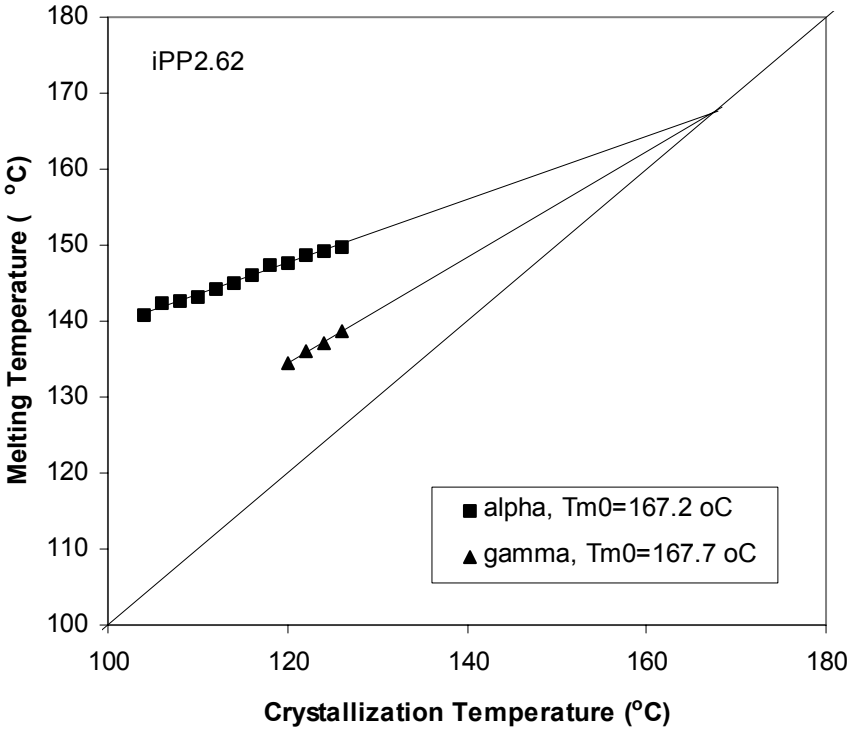

Figure 5.2.5. Hoffman–Weeks plot for α– and γ–phases of copolymer iPP2.62 crystallized at atmospheric pressure.

impossible to identify the lower melting peak temperature as seen in Figure 4.4.4. Melting data in Figure 5.2.5 exhibit an interesting tendency. When extrapolated to $T_m = T_c$, both phases give similar T_m^0, with γ–phase having slightly higher T_m^0. The value of T_m^0 for α–phase is 167.2 °C and for γ–phase is 167.7 °C. Similar phenomenon was observed by Mezghani[6] when extrapolating melting temperatures versus inverse lamellar thickness for *i*–PP.

Same type of behavior is observed for the other three copolymer fractions shown in Figures 5.2.6–5.2.8. The T_m^0 of α– and γ–phases are 166.3 °C and 165.2 °C for iPP4.38, 158.1 °C and 156.6 °C for iPP10.45, and 146.6 °C and 142.2 °C for iPP15.57, respectively. For these copolymers the extrapolation for the γ–phase led to T_m^0 lower than the T_m^0 of the α–phase.

Figure 5.2.9 displays the Hoffman–Weeks plots of the α–crystals for all four copolymers, along with the data for the *i*–PP homopolymer from Mezghani.[6] Same plots for the γ–phase are shown in the Figure 5.2.10. It can be observed that the melting temperature curves shift downward with increasing ethylene content. This behavior of the random propylene–ethylene copolymers is not unexpected, since the theories of copolymer crystallization[63-65] predict lowering of the T_m^0 with increasing comonomer content by lowering the crystal thickness or the crystal perfection.

From the slopes of the Hoffman–Weeks plots the thickening factor, γ, was calculated for both crystalline phases using the equation (2.4.2). Results are displayed in Table 5.2.1. It can be seen that the thickening decreases with increasing ethylene content. With increasing ethylene content the number of interruptions along the polymer backbone is also increasing, therefore reducing the length of crystallizable sequences and impeding the lamellar thickening. This argument should hold regardless of whether the ethylene units are excluded or included in the crystals. As suggested by Mezghani,[6] the thickening mechanism must involve 'snaking' through the crystals. Increasing defects along the polymer chains will hinder such snaking process. Additionally, for each copolymer the thickening factor of the γ–phase is always lower than the one of the

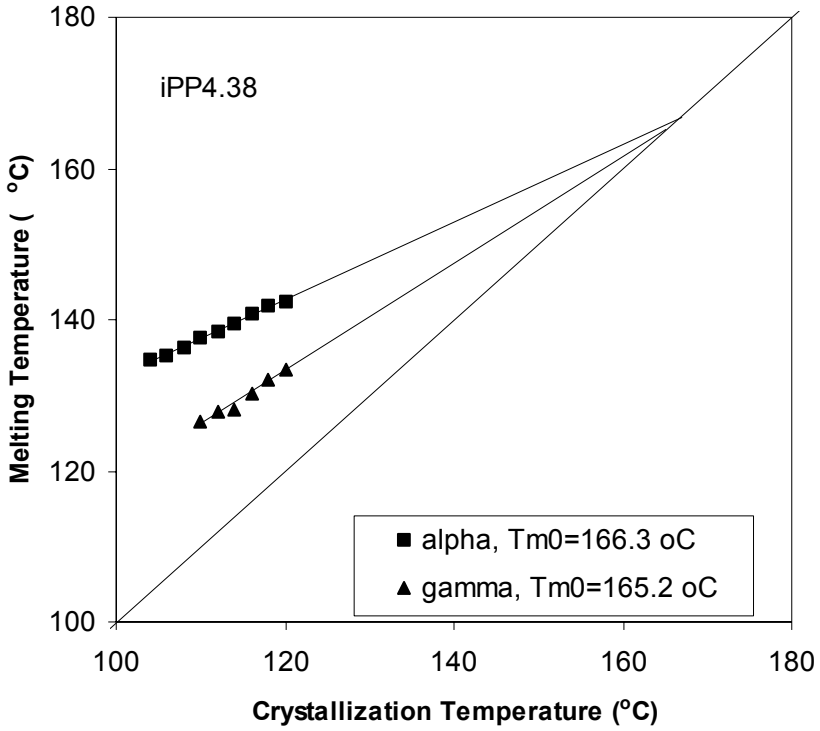

Figure 5.2.6. Hoffman–Weeks plot for α– and γ–phases of copolymer iPP4.38 crystallized at atmospheric pressure.

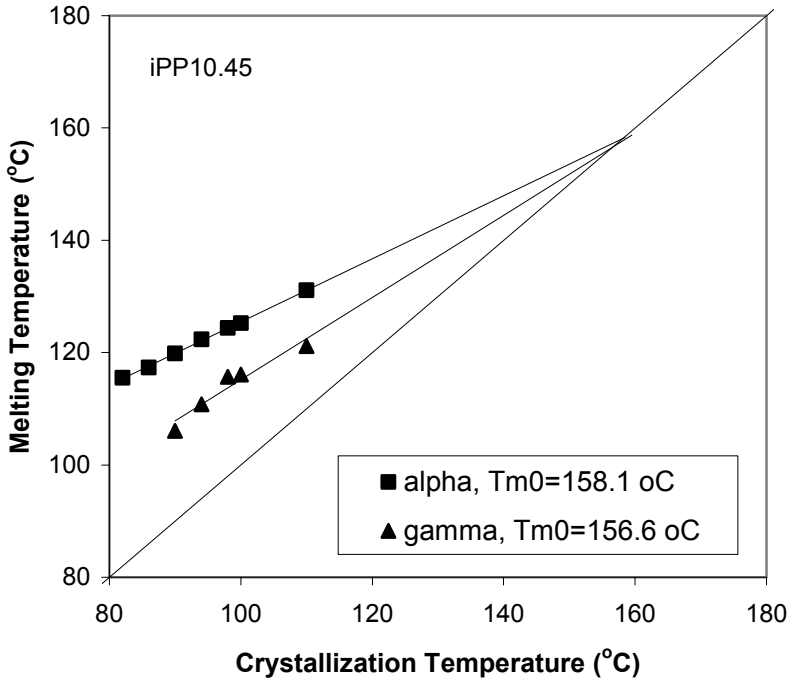

Figure 5.2.7. Hoffman–Weeks plot for α– and γ–phases of copolymer iPP10.45 crystallized at atmospheric pressure.

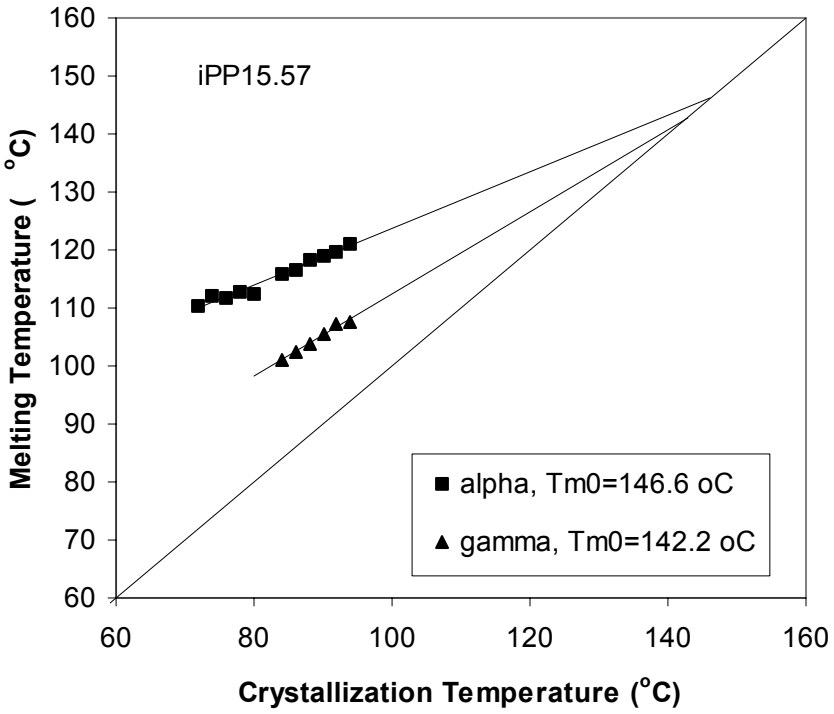

Figure 5.2.8. Hoffman–Weeks plot for α– and γ–phases of copolymer iPP15.57 crystallized at atmospheric pressure.

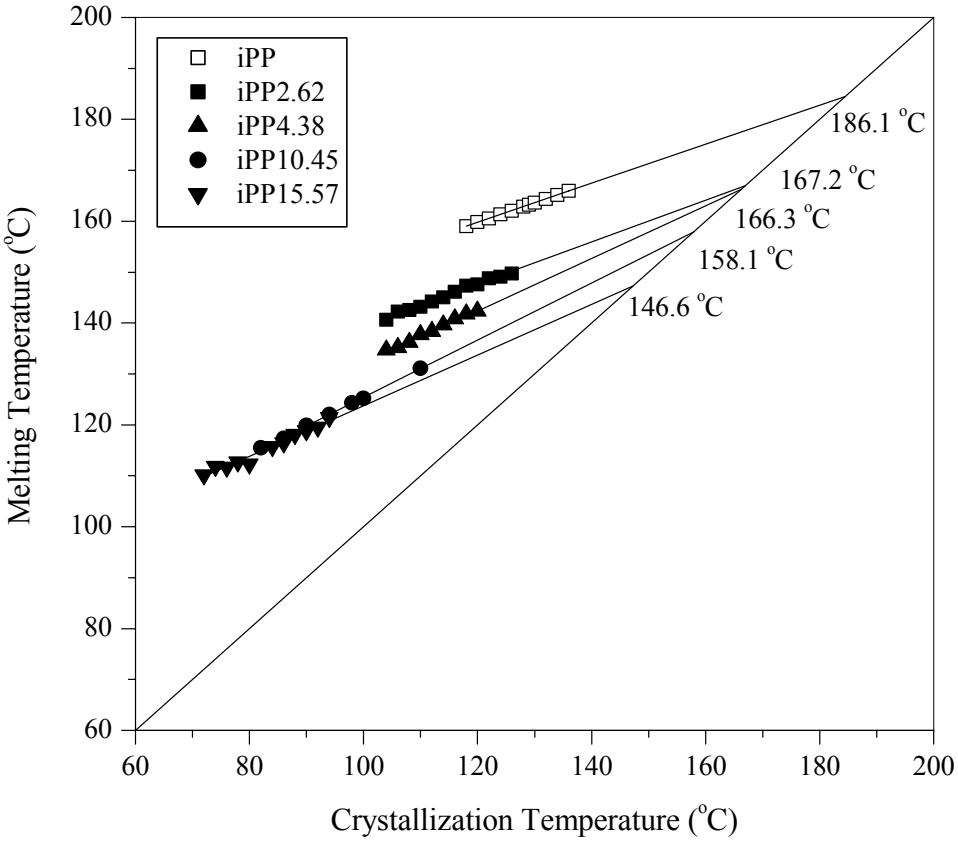

Figure 5.2.9. Hoffman–Weeks plots for α–phase of the propylene–ethylene copolymers and *i*–PP (iPP data from Mezghani[6]).

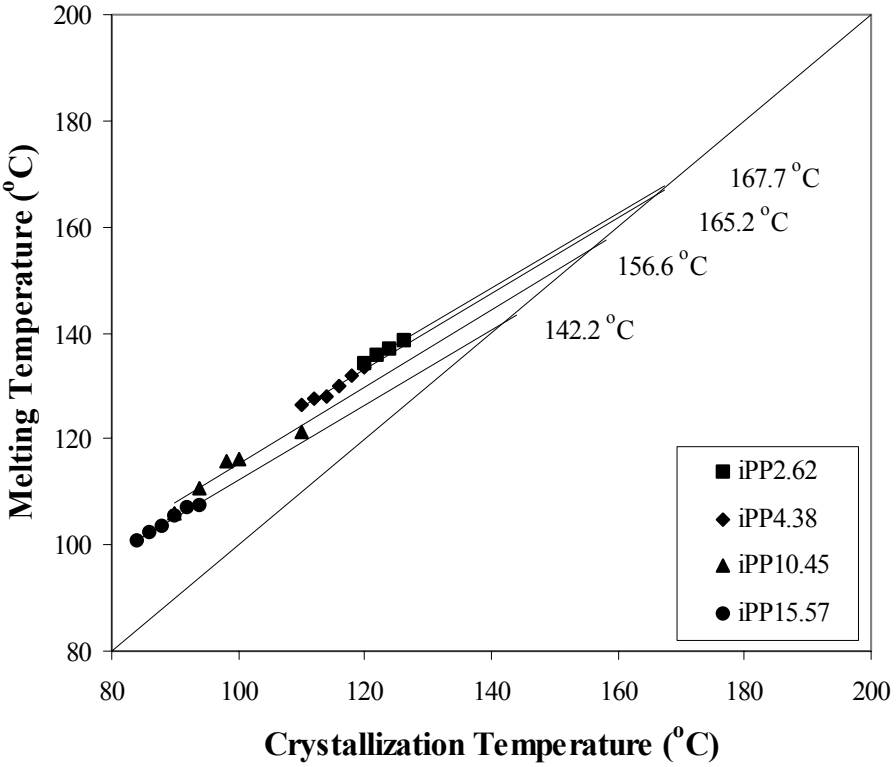

Figure 5.2.10. Hoffman–Weeks plots for γ–phase of propylene–ethylene copolymers.

Table 5.2.1. Thickening factor for propylene–ethylene copolymers.

Sample	Phase	Thickening factor
iPP2.62	alpha	2.41
	gamma	1.43
iPP4.38	alpha	1.96
	gamma	1.41
iPP10.45	alpha	1.78
	gamma	1.37
iPP15.57	alpha	2.04
	gamma	1.41

α–phase. The reason behind this behavior of the γ–phase is its unique crystal structure. Shorter isotactic sequences can crystallize into γ–crystals by arranging in layers parallel to the *ab* plane and by tilting at an angle of 40^{o} respective to the *b*–axis. This unorthodox chain arrangement can lead to γ–crystals with little on no chain folding. The absence of chain folding or the presence of non–adjacent reentry of the copolymer molecules into the γ–crystals will cause a decrease in the lamellar thickening process of the γ–crystals.

5.2.3. Morphology Studies by SAXS

Figure 5.2.11 compares the values of the long period (LP) calculated from the position of the first maximum in Lorentz corrected data and the second maximum in the 1D correlation function for copolymer iPP2.62 as a function of crystallization temperature. It can be seen that both LP have same tendency of increasing with the increase in the crystallization temperature. In general, the values of the LP calculated from the Lorentz corrected data are higher than those estimated from the 1D correlation function. The explanation behind this tendency is the assumption of sharp phase boundary between the amorphous and crystalline phases for the Lorentz corrected method. On the other hand, the 1D correlation function considers an intermediate transition phase between the amorphous and crystalline phases, which is more realistic and will be used in this study to estimate the thickness parameters of copolymers.

At the crystallization temperature of 120 ^{o}C the values of the LP estimated from both methods are almost identical, and for temperatures above 120 ^{o}C LP calculated from the 1D correlation function exceeds the LP calculated from the Lorentz corrected data. If we recall from section 4.6.2 samples crystallized at and above 120 ^{o}C exhibited an unusually prominent second peak in the Lorentz corrected data. Also, 1D correlation function curves at these temperatures displayed a 'double–minimum' as seen in Figures 4.6.11 and 4.6.12. This 'double–minimum' is an indication of a presence of two crystal

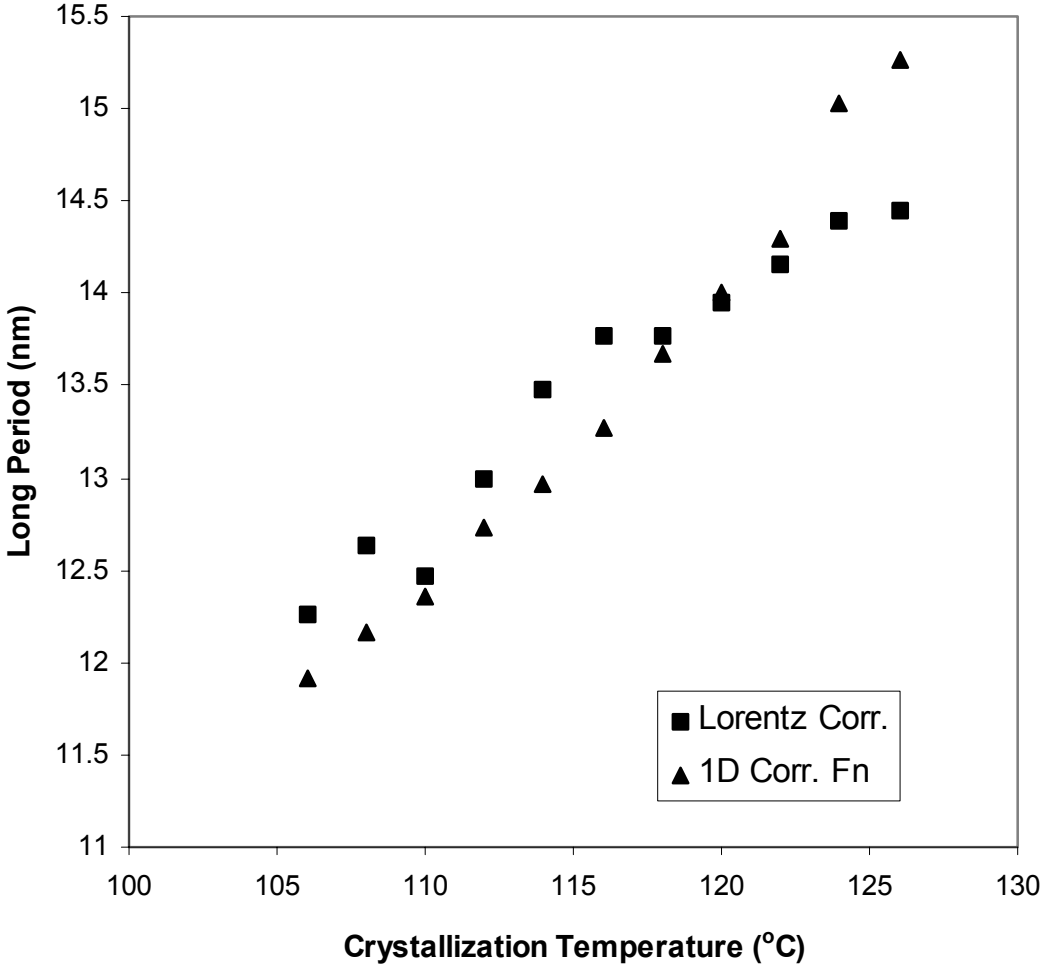

Figure 5.2.11. Long period as a function of crystallization temperature for iPP2.62 copolymer crystallized at atmospheric pressure.

thickness populations. Their overlapping in the 1D correlation function can lead to generating the second minimum and shifting the LP to unusually high values that are not the representative of the actual LP. Because of this, the scattering data collected for crystallization temperatures above 120 ^{o}C were not used in the further analysis. The typical determination of the crystal thickness from 1D correlation function from the first maximum and self–correlation triangle cannot be used in this case.

Similar behavior is observed for the copolymer iPP4.38 crystallized at temperatures at and above 114 ^{o}C, as seen in Figure 5.2.12. Figure 4.6.13 showed that the first minimum of the 1D correlation function developed a shoulder at crystallization temperatures of 114 ^{o}C. Further increase in the temperature leads to the formation of the 'second–minimum'. The possible solution for data treatment for these bimodal distribution curves will be covered in section 5.2.3.4.

Copolymers iPP4.38 and iPP15.57 do not show this behavior in the studied crystallization range. In their case, both long periods calculated from Lorentz corrected data and 1D correlation function increase proportionally with the crystallization temperature. Only for the iPP15.57 copolymers the increase in long period with temperature is less prominent, as seen in Figure 5.2.13.

The plot of the lamellar thickness determined from the self–correlation triangle of the 1D correlation function as a function of the degree of supercooling for the four copolymers is shown in Figure 5.2.14. It is obvious that the lamellar thickness increases with decreasing of the degree of supercooling. Additionally, for a given degree of supercooling the lamellar thickness decreases with ethylene content. Similar observations for the lamellar thickness as a function of the isotacticity was published for *i*–PP homopolymer considered as random stereo–copolymer.[130]

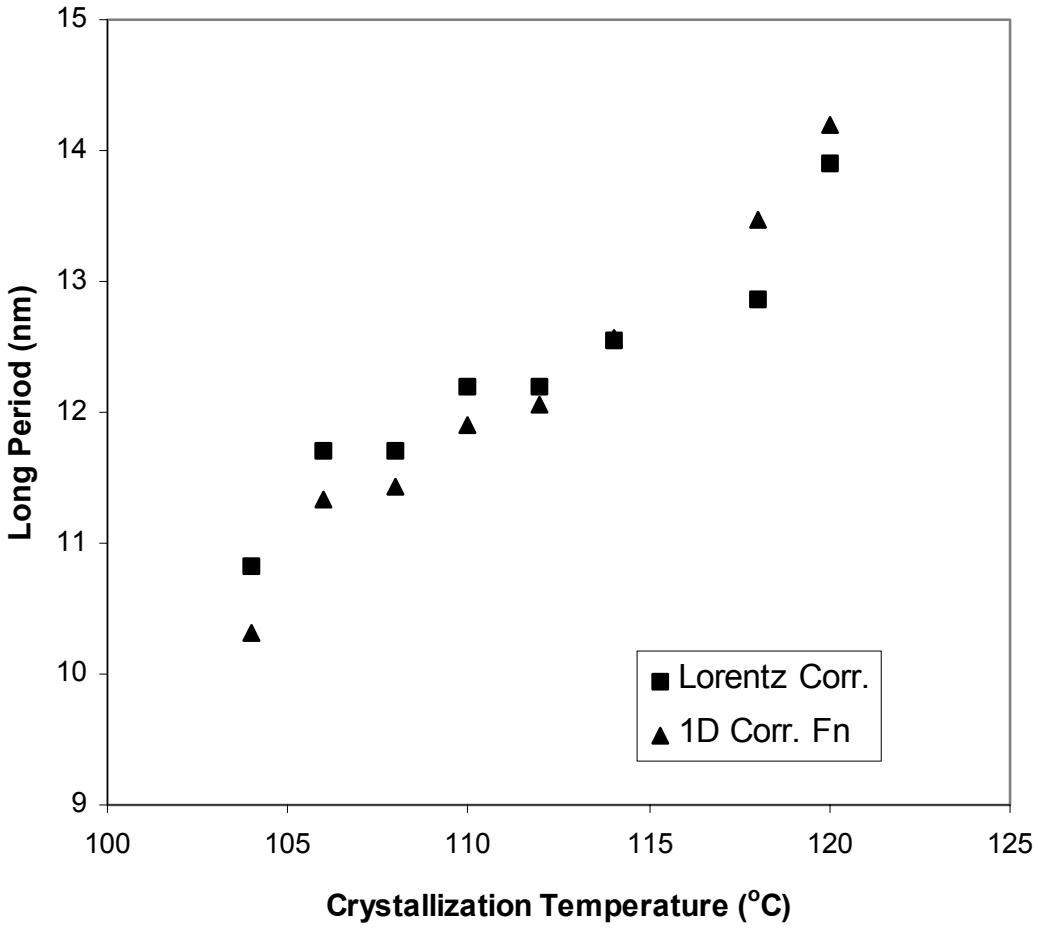

Figure 5.2.12. Long period as a function of crystallization temperature for iPP4.38 copolymer crystallized at atmospheric pressure.

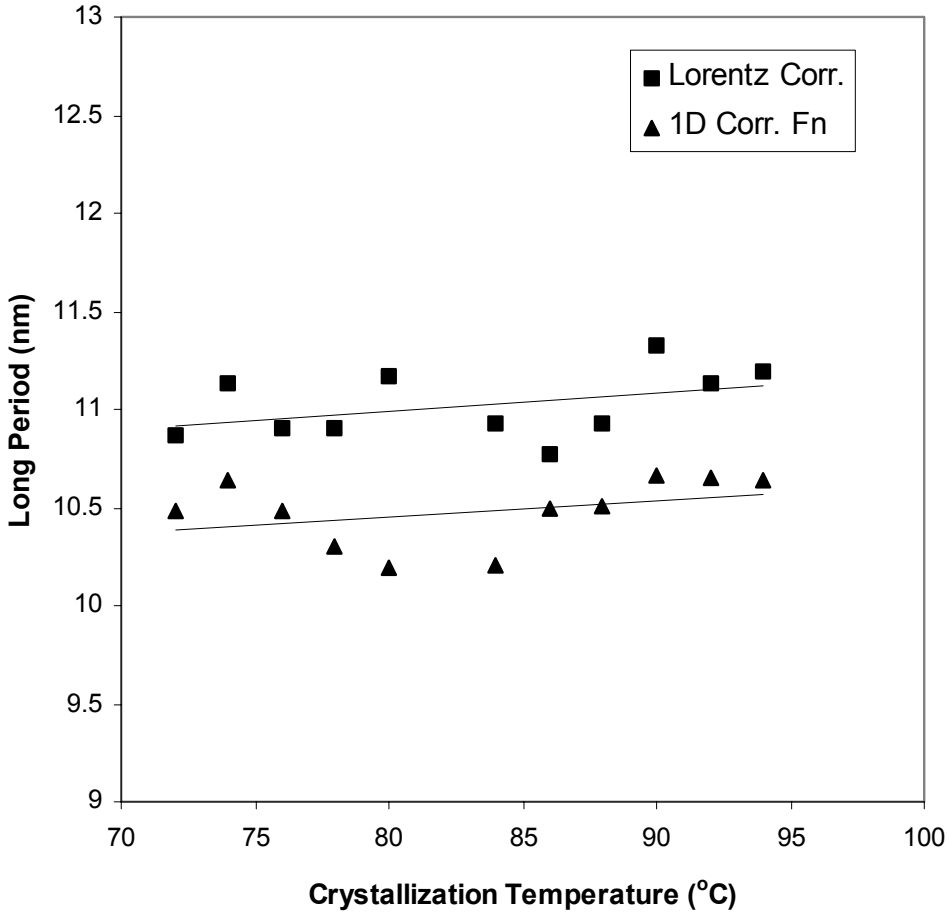

Figure 5.2.13. Long period as a function of crystallization temperature for iPP15.57 copolymer crystallized at atmospheric pressure.

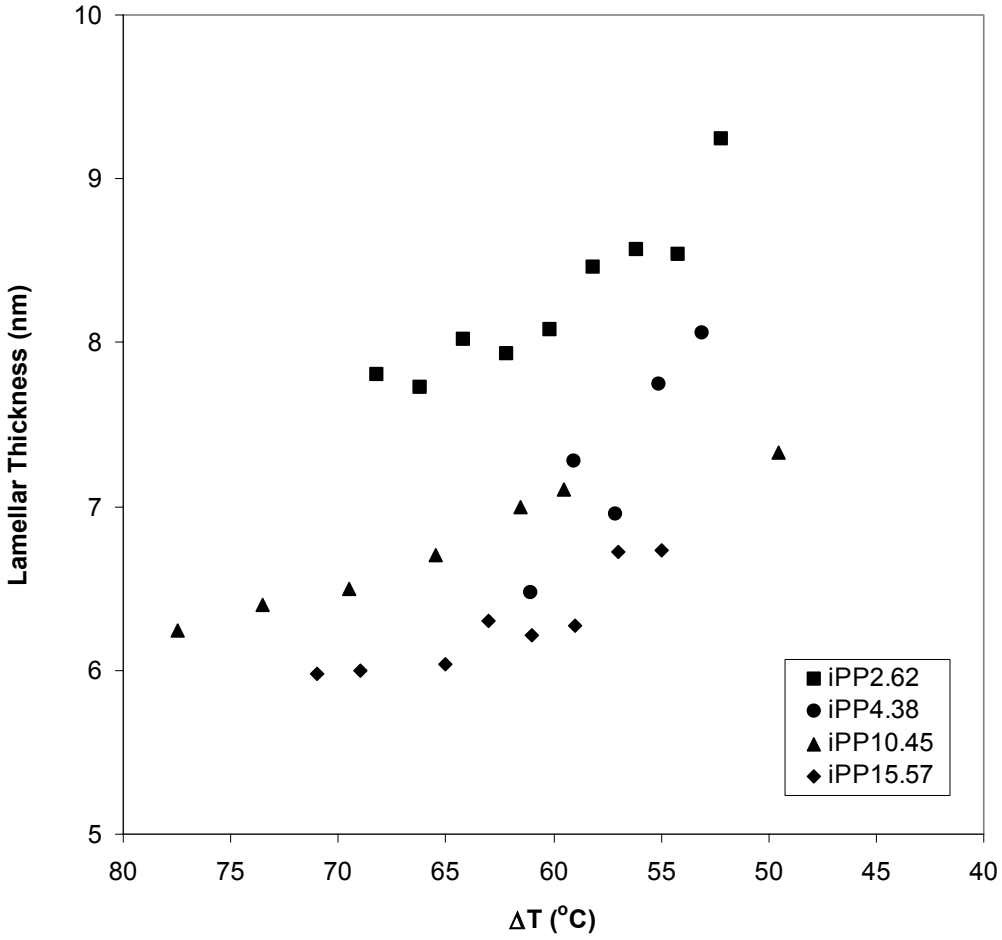

Figure 5.2.14. Lamellar thickness as a function of degree of supercooling of copolymers crystallized at atmospheric pressure.

5.2.3.1. Transition layer thickness

The possibility of the existence of the third phase in a semi–crystalline polymer system can be studied by analyzing the SAXS intensity patterns. The values of the transition layer thickness between the amorphous and crystalline phase were estimated using the linear–gradient, sigmoidal–gradient model and the self–correlation triangle method from the 1D correlation function. First two methods are based on the deviations from Porod's law, and they depend on the type of background correction used to correct the scattering data. It has been shown[131] that these methods for determining the transition layer thickness are not equivalent, since in the case of the first two methods an assumption about the profile of the electron density in the transition region has to be made (linear– or sigmoidal–gradient), which is not necessary in the third method.

The transition layer thickness as a function of crystallization temperature for the studied copolymers is shown in Figure 5.2.15 (a–d). It can be seen that the linear gradient model gives an overestimation of the transition layer thickness, while the thickness obtained from the sigmoidal–gradient model and self–correlation triangle are closer in value. For all copolymer samples the same tendency with the crystallization temperature is observed, the interfacial layer thickness decreases slightly with increasing crystallization temperature. This phenomenon could be a result of the increased crystallinity of the system, that is the crystal lamellae have better packing. In that case the increase of the lamellar thickness with increasing crystallization temperature occurs at the expense of the transition layer, causing its thickness to decrease.

Only in the case of iPP15.57 the transition layer thickness is almost independent of the crystallization temperature. The average value of the ℓ_{tl} is 1.4 ± 0.3 nm for the sigmoidal model and 1.7 ± 0.45 nm for ℓ_{tl} determined from the self–correlation triangle method. It should be mentioned that the increase in the lamellar thickness of iPP15.57 with crystallization temperature is less prominent compared with the other three copolymers, as seen in Figure 5.2.14. This copolymer has the highest amount of defects,

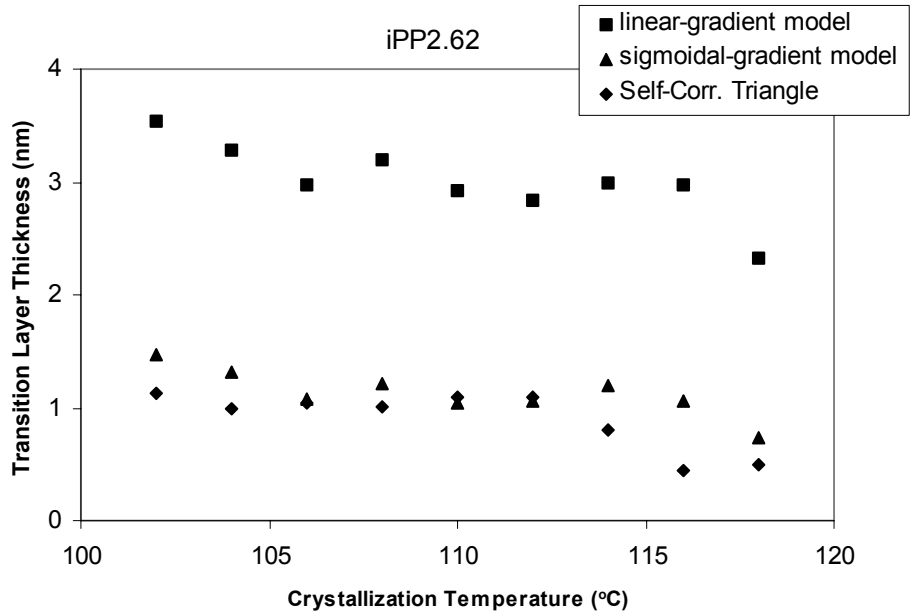

(a)

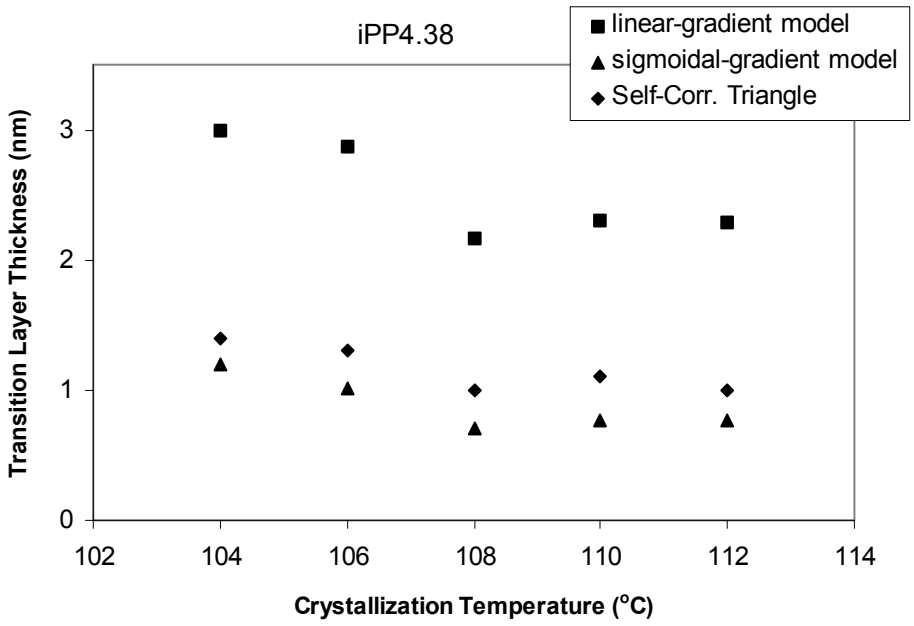

(b)

Figure 5.2.15. Transition layer thickness as a function of crystallization temperature at atmospheric pressure for (a) iPP2.62, (b) iPP4.38, (c) iPP10.45, and (d) iPP15.57.

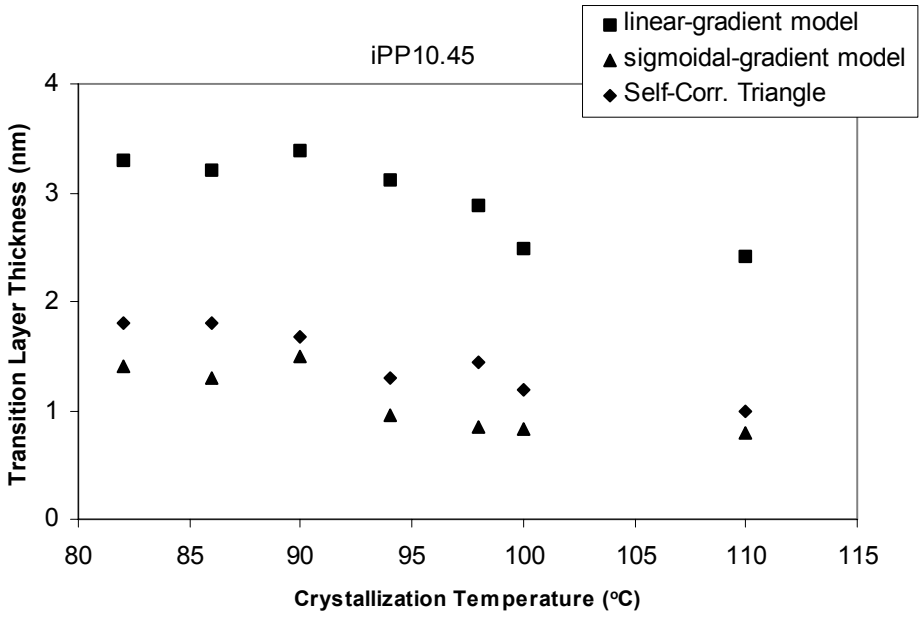

(c)

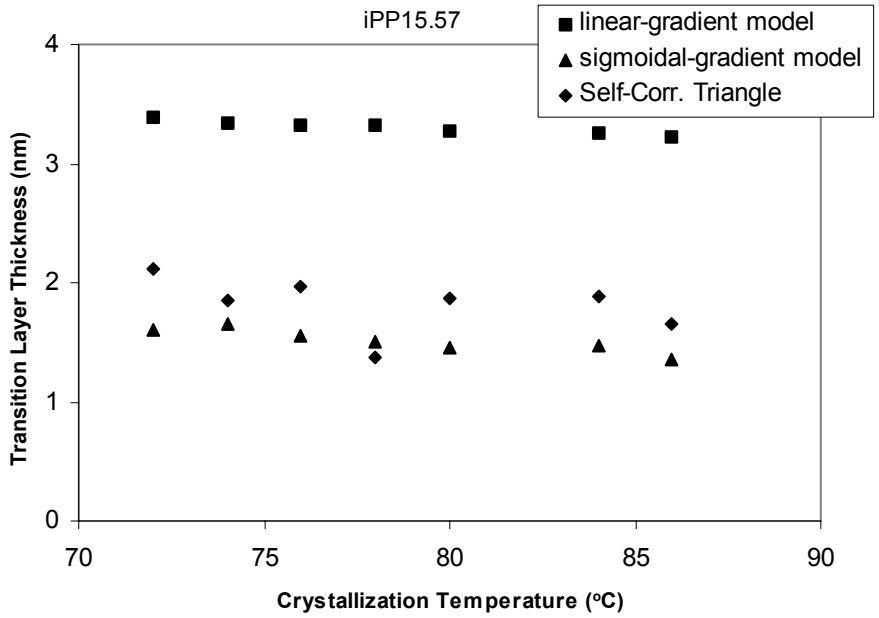

(d)

Figure 5.2.15. Continued. (c) iPP10.45, and (d) iPP15.57.

that is 15.57 mol% ethylene and 33.35 mol% total defects. This large amount of defects decreases the length of the crystallizable isotactic sequences, and effectively reduces the crystal thickness and prevents the lamellar thickening with increasing crystallization temperature.

The plot of the transition layer thickness determined from the self–correlation triangle of the 1D correlation function as a function of the degree of supercooling for the four copolymers is shown in Figure 5.2.16. Again, it can be seen that the transition layer thickness decreases with decreasing degree of supercooling. On this figure the effect of the defect content on the transition layer thickness can be observed. For a given degree of supercooling the transition layer thickness increases with increasing ethylene content. This effect can be explained by the crowding of the defects that are rejected from the crystalline phase, that produce an increase in the transition layer thickness. Similar results were published for heterogeneous ethylene–octene copolymers.[132]

5.2.3.2. Invariant and electron density difference

The total scattering power or the invariant of the copolymer samples was determined from the self–correlation triangle of the 1D correlation function, by extrapolating the slope to x = 0. This procedure was elaborated in section 2.8.2 and its graphical representation is shown in Figure 2.8.2. The values of the invariant, Q, as a function of crystallization temperature for the copolymers crystallized at atmospheric pressure are shown in Figure 5.2.17. The invariant increases with increasing crystallization temperature, however at lower degrees of supercooling it levels off. Also, at a given crystallization temperature the invariant decreases with increasing ethylene content.

The electron density difference $\Delta\eta$, between the crystalline phase, η_c, and the amorphous phase, η_a, was calculated from the invariant and the degree of crystallinity

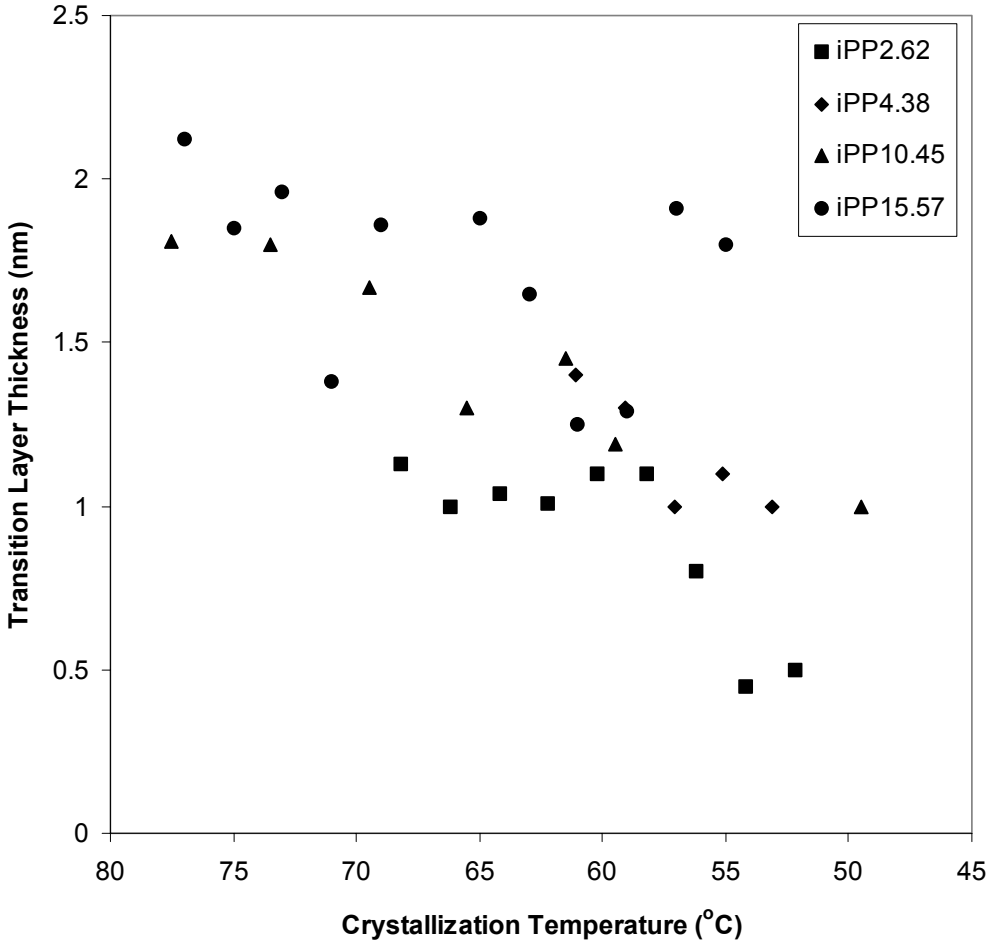

Figure 5.2.16. Transition layer thickness as a function of degree of supercooling of copolymers crystallized at atmospheric pressure.

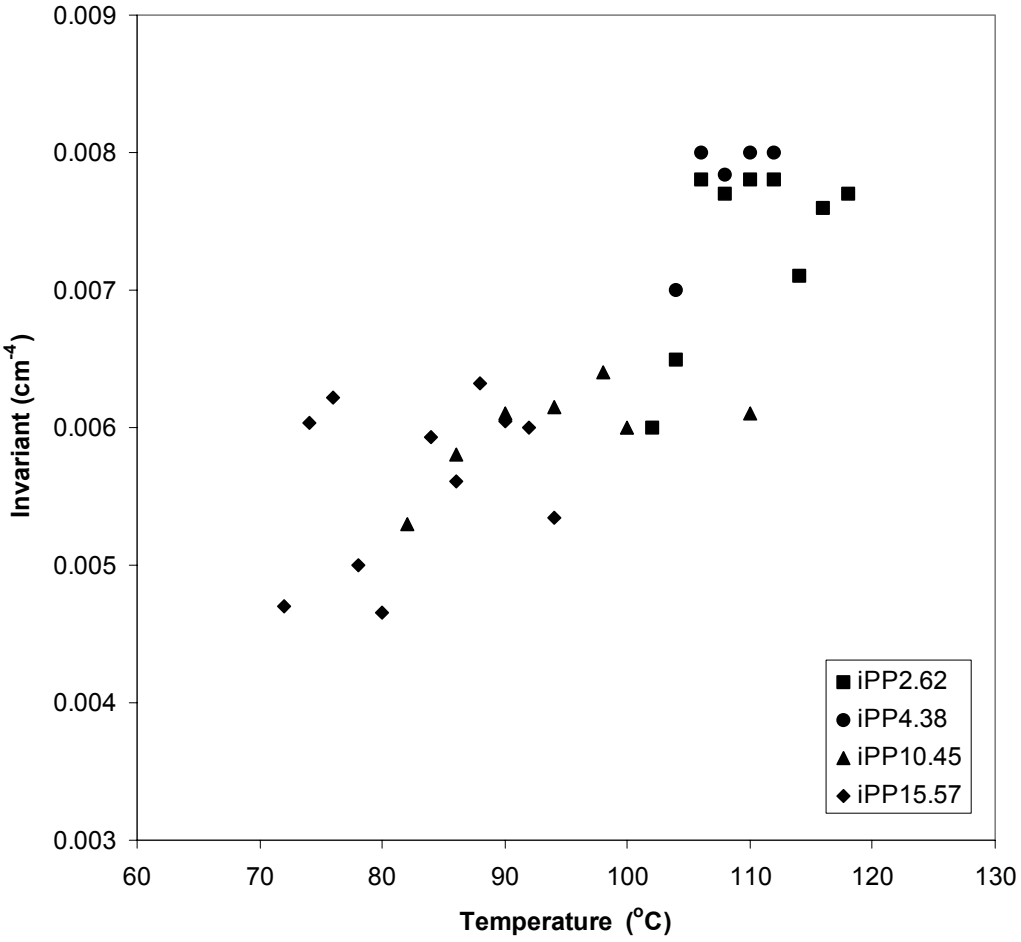

Figure 5.2.17. The invariant as a function of the crystallization temperature of copolymers crystallized at atmospheric pressure.

determined from WAXD according to equation (2.8.9) as outlined in Figure 2.8.2. In Figure 5.2.18 the electron density difference is plotted as a function of the degree of supercooling.

For all copolymers, regardless of the composition, the electron density difference increases with decreasing degree of supercooling. Crystallization of copolymers at low degrees of supercooling leads to formation of thicker and more perfect crystals. This will increase the crystalline electron density, and consequently increase the $\Delta\eta$. Also, for a given degree of supercooling, the electron density difference decreases with increasing comonomer content. Increasing defect content in the copolymers can result in incorporation of a certain degree of defects in the crystals. This in turn causes a decrease in the electron density of the crystalline phase, leading to a decrease in $\Delta\eta$.

5.2.3.3. Equilibrium melting temperature – Gibbs–Thompson plot

The equilibrium melting temperature T_m^0 can also be determined from equation (2.4.1) and the Gibbs–Thomson plot, which shows the melting temperature dependence on the lamellar thickness. From equation (2.4.1) a linear relationship is predicted in the plot of melting temperature versus inverse lamellar thickness, with the T_m^0 as an intercept in the plot. Figure 5.2.19 shows the Gibbs–Thompson plot of the melting temperature of the α–phase of the copolymers as a function of inverse lamellar thickness. The extrapolation for the α–phase is based on the measured lamellar thickness from SAXS and the high temperature endotherms from DSC. The equilibrium melting temperatures of the α–phase for the studied copolymers as determined from the intercepts are 172.6, 165.7, 159.5 and 149.3 ^oC, respectively.

In the section 5.2.2 it was established that the lower temperature endotherm in the DSC is due to the melting of the γ–phase crystals. Based on the assumption that the

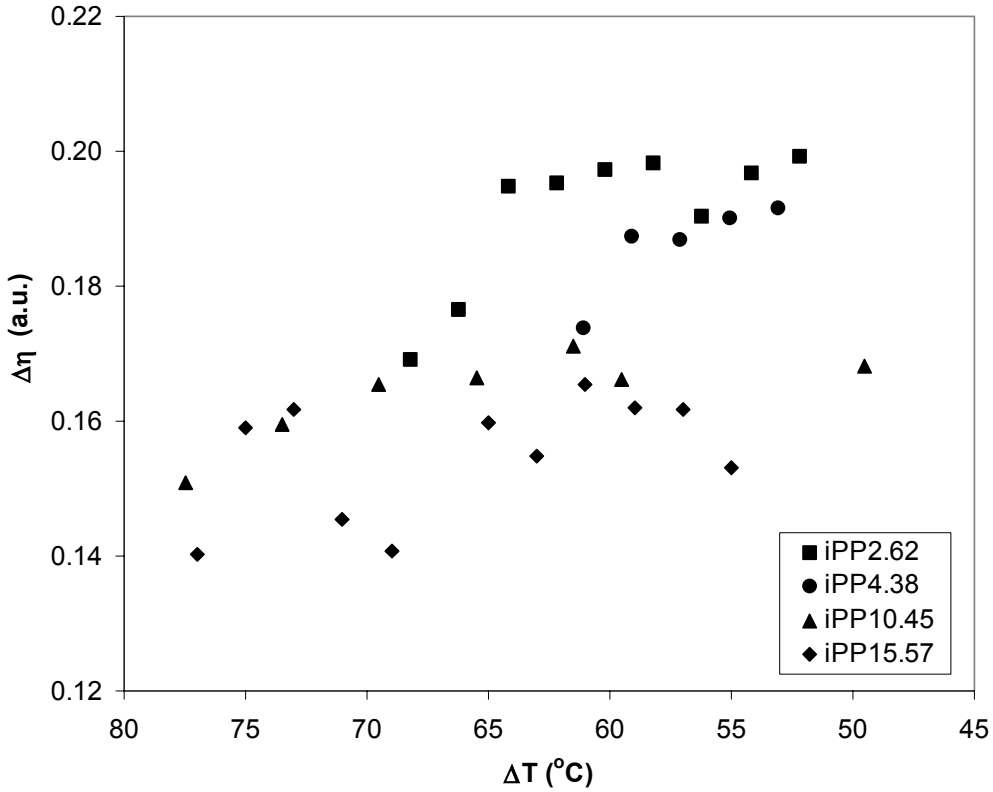

Figure 5.2.18. Electron density difference as a function of the degree of supercooling of copolymers crystallized at atmospheric pressure.

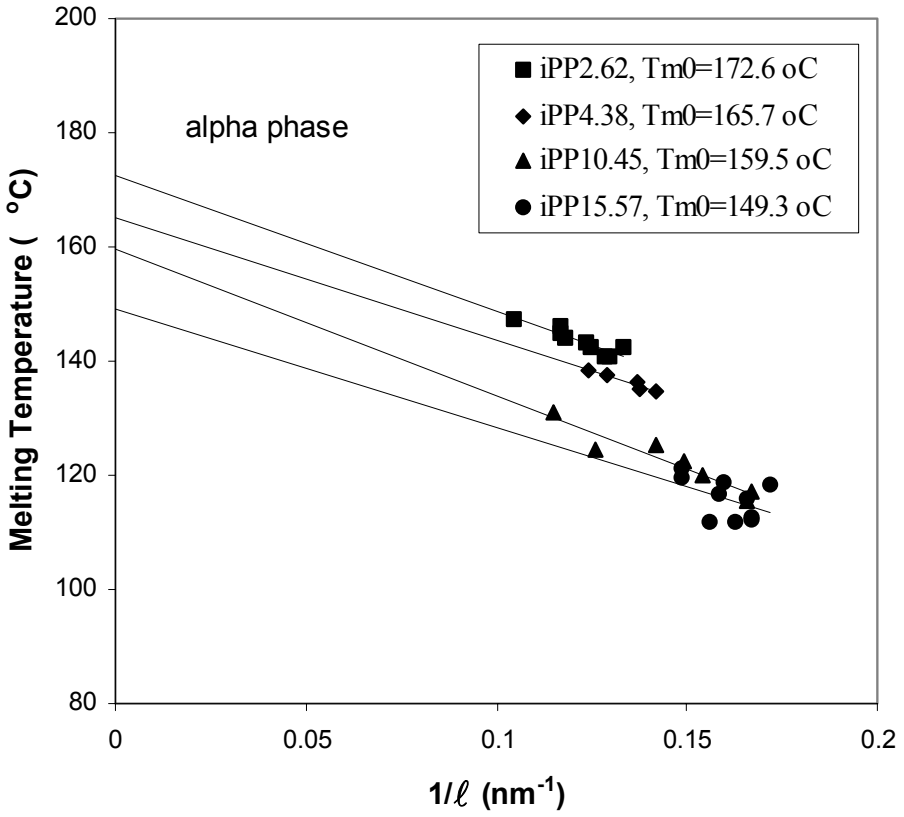

Figure 5.2.19. Gibbs–Thompson plot for the α–phase of copolymers crystallized at atmospheric pressure.

lamellar thicknesses of the γ–crystals are the same as that of the α–crystals, Gibbs–Thompson approach can be applied to determine the T_m^0 of the γ–phase. This assumption can be made only if there is no bimodal thickness distribution in the SAXS intensity profiles.

In section 4.6.3 it was shown that copolymers iPP2.62 and iPP4.38 crystallized at higher temperatures exhibited bimodal thickness distribution behavior. This was not the case for the samples iPP10.45 and iPP15.57. Therefore, Gibbs–Thompson plot for determining γ–phase T_m^0 will be used only for copolymers iPP10.45 and iPP15.57 under the assumption that both phases have same lamellar thickness. These plots are shown in Figure 5.2.20. The equilibrium melting temperatures of the γ–phase for iPP10.45 and iPP15.57 as determined from the intercepts are 157.6 and 147.8 ^oC, respectively.

The equilibrium melting temperatures of the α– and γ–phase crystals determined using the Gibbs–Thompson approach are always slightly higher than the T_m^0 determined from Hoffman–Weeks analysis. The differences in the T_m^0 stem from the different arguments on which these methods are based.

Hoffman–Weeks method was developed from combining the Gibbs–Thompson equation and the secondary nucleation theory[59,61] that relates the initial stem length with the degree of supercooling. It is based on the assumption that the difference between the crystallization and melting temperatures are due to the lamellae thickening, and that the thickening coefficient is independent of the crystallization temperature. However, the thickening process can be affected by several factors, such as the presence of non–crystallizable units in the polymer chains, high entanglement density in the interlamellar regions, as well as the type of polymer morphology. All of these factors can considerably impede the thickening of the lamellae after their formation. In contrast with the Hoffman–Weeks method, Gibbs–Thompson analysis is based entirely on the thermodynamic argument that the melting temperature of a crystal of finite size is depressed below that of a infinite crystal as a result of an increase in the free energy of the crystal with a decrease in its dimensions. Important premise for the Gibbs–Thomson

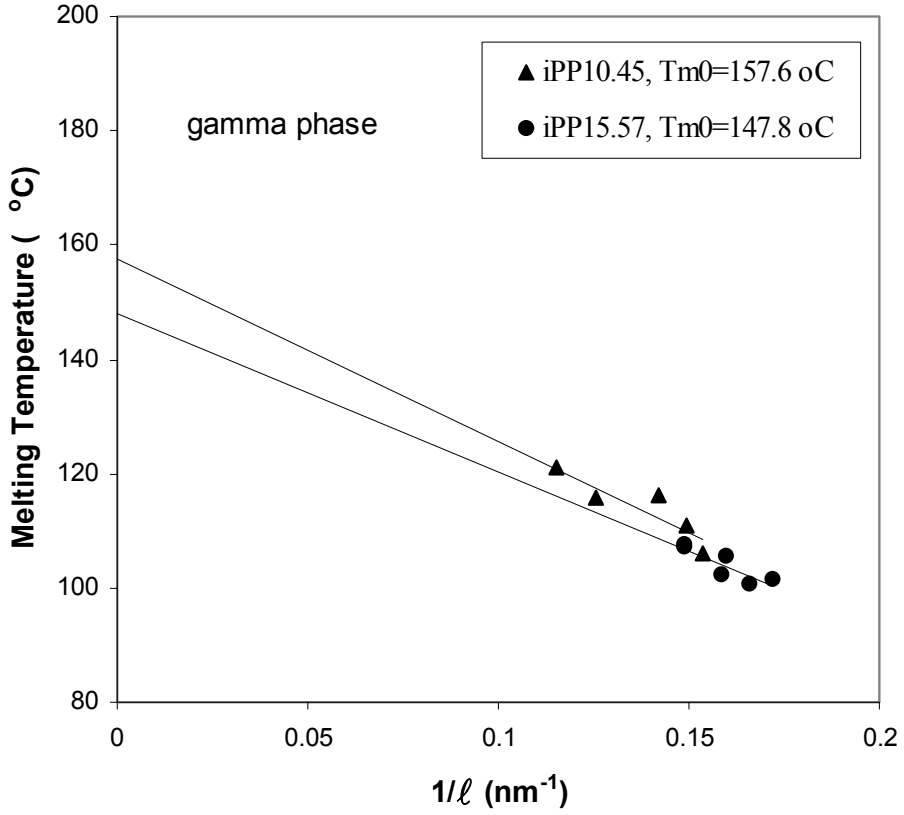

Figure 5.2.20. Gibbs–Thompson plot for the γ–phase of copolymers iPP10.45 and iPP15.57 crystallized at atmospheric pressure.

equation is that the size of the basal planes of the finite crystal are large enough for the lateral free surface energy contribution to the melting point depression to be negligible. Consequently, since Gibbs–Thompson method gives more accurate estimate of the equilibrium melting temperature, T_m^0 determined using this method will be further used in this study.

From the slopes of the linear relationships shown in Figures 5.2.19 and 5.2.20 the fold surface free energy, σ_e, can be determined using the equation (2.4.1). Table 5.2.2 lists the results for the α– and γ–phase of the four copolymers. It can be observed that for the two sets of copolymers with comparable molecular weights, iPP2.62 and iPP4.38, and iPP10.45 and iPP15.57, the fold surface free energy decreases with increasing defect content. Fold surface free energy of the propylene–ethylene copolymer crystals will be affected by factors such as whether the defects are excluded or included in the crystals, the type of folds (adjacent or non–adjacent), presence of different crystallographic structures, as well as the crystallization temperature.

In the case of ethylene units being rejected from the crystal phase they can concentrate in the folds area or interface region. Since ethylene units are sterically less hindered compared with the propylene units, their presence in the fold surface can lead to a decrease in the σ_e. Also, the decrease in σ_e with increasing defect content suggests an increase in formation of loose loops and non–adjacent reentry folding. This, in turn, would lead to an increase in the thickness of the interfacial region with increased defect content. For the four studied copolymer it has been shown that indeed the interfacial region thickness increases with increasing defect content, as seen in Figure 5.2.16.

Copolymer iPP2.62 has σ_e value of 52.51 erg/cm^2 that is close to the one reported for the homopolymer of 52.2 erg/cm^2.[6] Copolymers iPP10.45 and iPP15.57 have higher σ_e, and since they have lower molecular weight the contribution of the chain ends to the crystal–amorphous surface and σ_e cannot be neglected. In case of excluded chain ends, it seems reasonable to assume that the chain end is excluded together with several chain segments that will lead to overcrowding of the fold surface and thus increase σ_e.

Table 5.2.2. Fold surface free energy determined from Gibbs–Thompson plots.

Sample	α–phase				γ–phase		
	MW×10^{-3} (g/cm^3)	slope × 10^7 (nm)	T_m^0 (^oC)	σ_e erg/cm^2	slope × 10^7 (nm)	T_m^0 (^oC)	σ_e erg/cm^2
iPP2.62	252	238.0	172.6	52.51	–	–	–
iPP4.38	287	214.4	165.7	47.86	–	–	–
iPP10.45	86	256.0	159.5	57.86	318.2	157.6	51.86
iPP15.57	75	207.6	149.3	48.07	274.5	147.8	45.78

ΔH_f^0(α–phase) = 209 J/g
ΔH_f^0(γ–phase) = 150 J/g

These results also indicate that the γ–phase of copolymers iPP10.45 and iPP15.57 has lower value of σ_e when compared with the α–phase. This tendency was also observed for high pressure crystallized γ–phase when compared with the atmospheric crystallized α–phase of the *i*–PP homopolymer.[6] The decrease of the γ–phase σ_e can be caused by the crystal structure with non–parallel chains of the γ–phase. In this structure, polymer chains are inclined at an angle of approximately 80° relative to the fold surface plane, which can lead to partial stress relief.[133,134] For the same chain–to–chain distance in the α– and γ–lamellae, γ–form has larger distance between the chains at the lamellar surface because of the chain tilting. This leads to a reduction in the number of chains that emerge from the (010) plane in the case of γ–phase compared to the (001) plane for the α–phase.

Equilibrium melting temperature of the α– and γ–phase crystals determined from the Gibbs–Thompson method plotted as a function of the defect content is shown in Figure 5.2.21. Melting temperatures are expressed in terms of both ethylene content (closed symbols) and total defect content (open symbols). Defects reduce the equilibrium melting temperature of both phases at approximately 1–2 °C per mol% of total defects. The presence of defects in copolymer chains effectively reduces the length of the isotactic polypropylene sequences that are capable of crystallizing. This leads to reduced lamellar thickness, which is responsible for the drop in the copolymer melting temperatures and enthalpy of fusion.

5.2.3.4. SAXS data treatment for samples exhibiting bimodal thickness distributions

Lorentz corrected data of the iPP2.62 and iPP4.38 copolymer samples that exhibit unusual second peak shown in Figures 4.6.4 and 4.6.6 can be considered as composed by two partially superimposed peaks. These peaks are due to the existence of two populations of lamellar stacks, characterized by different long period. The existence of

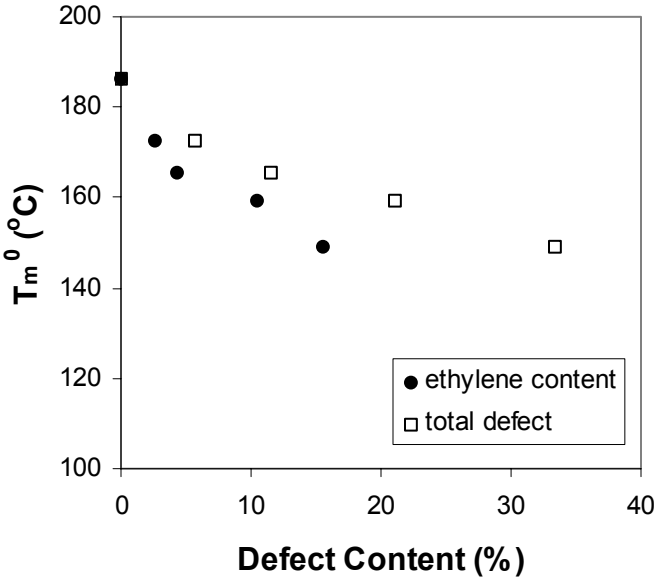

(a)

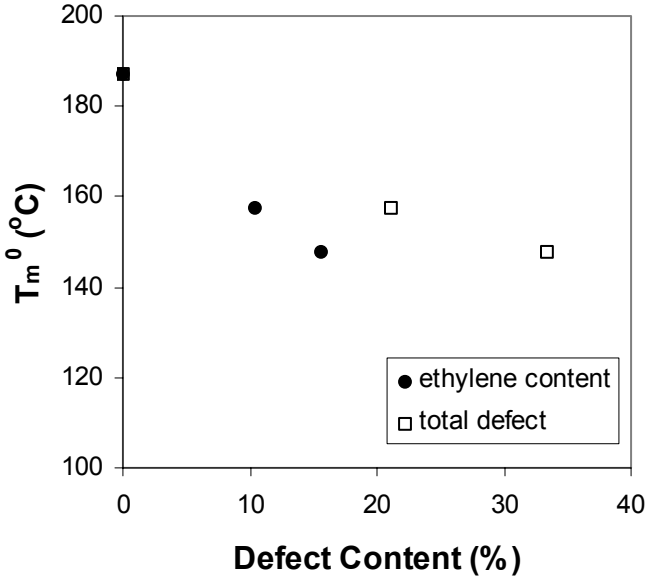

(b)

Figure 5.2.21. Equilibrium melting temperature of (a) α and (b) γ phase crystals as a function of defect content.

superimposed signals requires the use of a method for independent evaluation of the peaks and calculation of their individual contribution to the total scattering pattern.

The approach that was used in this study was developed for treatment of SAXS data of iPP–HOCP blends.[135,136] It is based on the hypothesis that the two coexisting lamellar morphologies are independent and that they do not interfere with each other. Therefore, according to this approach the scattering intensity from the two (or more) lamellar domains can be construed as linear combination of their corresponding contributions. Consequently, the Lorentz corrected (LC) data are expressed by a combination of two (or more) independent contributions, each described by a Gaussian function. The LC experimental patterns of the copolymers iPP2.62 and iPP4.38 have been fitted with two Gaussian functions in the following form:

$$q^2 I_{\text{corr}}(q) = A_1 \exp\left(-\frac{(q-q_1)^2}{2c_1^2}\right) + A_2 \exp\left(-\frac{(q-q_2)^2}{2c_2^2}\right) \qquad (5.2.1)$$

where $I_{\text{corr}}(q)$ is the intensity corrected for the thermal density fluctuation, q_i, c_i and A_i, are the center, the variance and the amplitude of the i–th Gaussian function, respectively.

It has to be mentioned that the experimental LC data of both iPP2.62 and iPP4.38 copolymer samples were fitted with two and three Gaussian functions, however the two Gaussian curves gave better fit. Figure 5.2.22 shows an example of such a fit for the copolymer iPP2.62 crystallized at 126 ^{o}C.

In Figure 5.2.22 dashed lines represent the two fitted Gaussian functions, the full line is their weighted sum, and the points are the actual experimental Lorentz corrected data. It is evident that each Gaussian function represents the peak originating from each lamellar domain. This way, the fairly complex experimental Lorentz corrected curve was separated into two independent Lorentz corrected patterns, indicated as LC1 and LC2, each containing structural information of one lamellar domain. Next, these separated Lorentz corrected patterns were treated by Fourier transform in order to generate their 1D

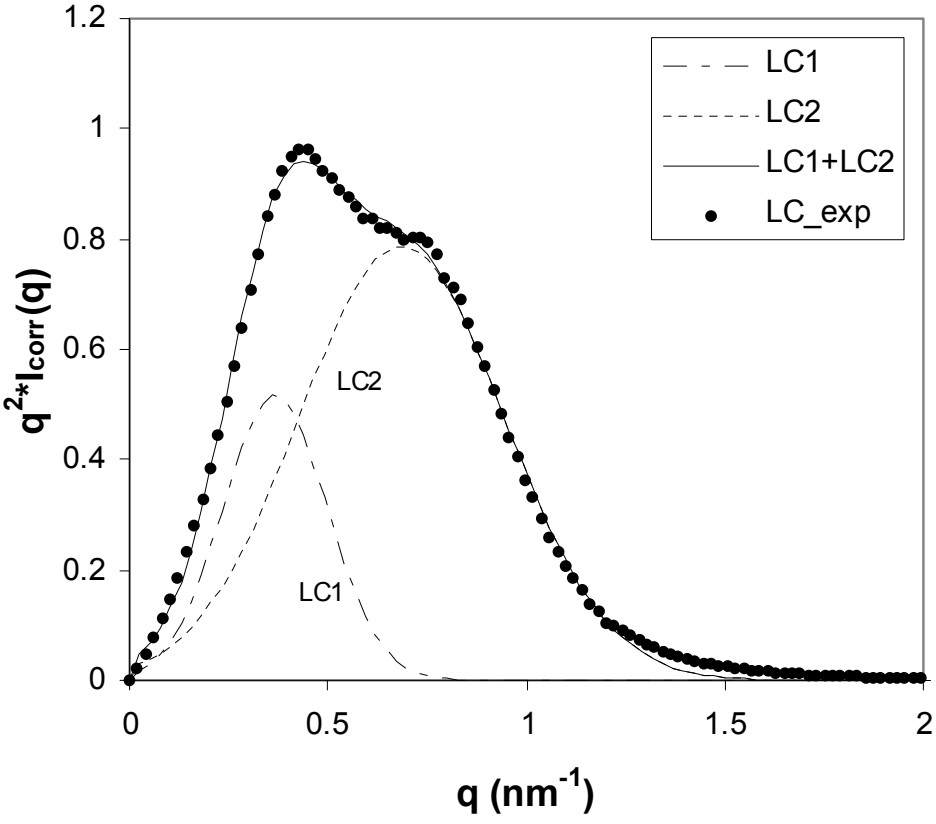

Figure 5.2.22. Lorentz corrected SAXS pattern of iPP2.62 crystallized at 126 ^{o}C fitted with two Gaussian functions, along with the experimental data.

correlation functions, K1 and K2. For the 1D correlation function analysis the same procedure was used as described in section 4.6.3. Then, the weighted sum of the K1 and K2 was compared with the experimental Kexp, as shown in Figure 5.2.23.

In Figure 5.2.23 the dashed lines represent the 1D correlation functions of the two fitted Gaussian functions, the full line is their weighted sum, and the points are the experimental 1D correlation function. From the overlapping of the experimental data and the fitting results we concluded that there is good agreement between the experiment and the fitting method. For all other samples similar fits were accomplished. The results from the fitting procedure are shown in Table 5.2.3. Self–correlation triangle method was used for lamellar thickness determination.

From these results we conclude that iPP2.62 samples crystallized at temperatures above 120 ^{o}C have bimodal lamellar thickness, with the larger lamellar domain in the range of 7.61–9.09 nm, and smaller lamellar domain with thickness considerably lower and in the range of 3.82–4.96 nm. Samples of iPP4.38 crystallized at temperatures 114 ^{o}C show the same tendency, with the thicker lamellae being 6.97–8.35 nm, and the thinner lamellae 3.65–4.08 nm.

The important question that needs to be answered is what is the reason behind the occurrence of the two thickness populations in these copolymers. Two thickness populations as detected in SAXS, can be due to the different thickness of the two crystalline phases present (α– and γ–crystals) or to the existence of two lamellae populations, one formed during the isothermal crystallization, and the other generated during the quenching from the crystallization temperature.

Marigo and coworkers[137] studied the bimodal distribution of two lamellae populations in the case of metallocene *i*–PP using the distribution functions of both the crystalline and the amorphous thicknesses. The applied fitting procedure involved optimizing parameters such as the average lamellar thickness, the standard deviation of the lamellar thickness and the number of the lamellae in the stack. Based on their results

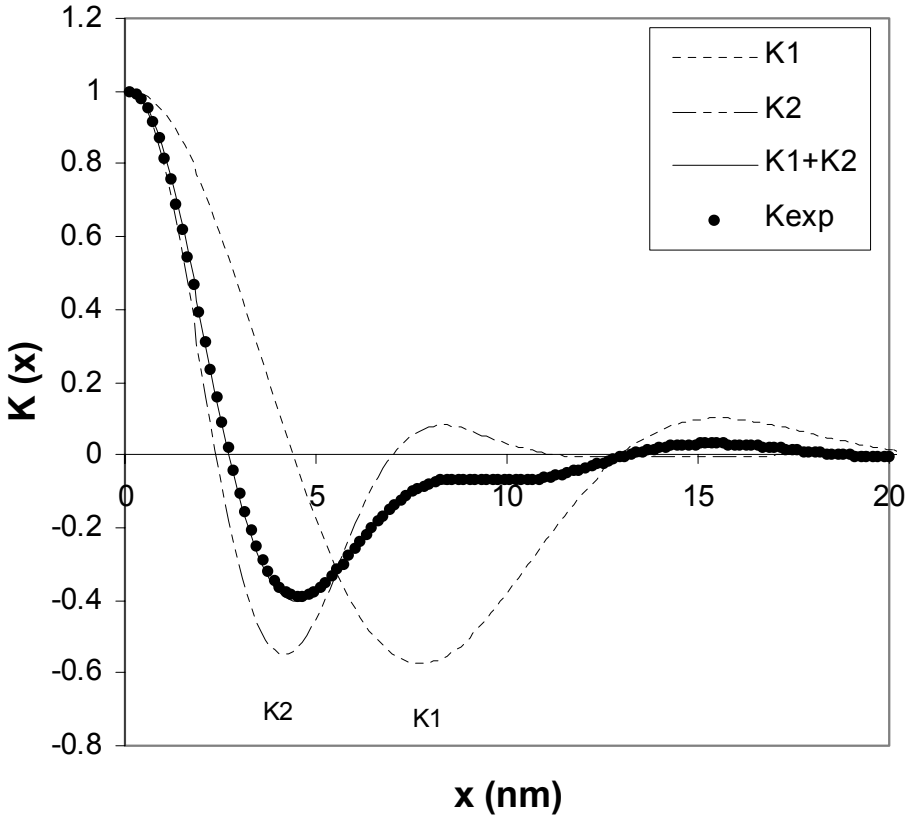

Figure 5.2.23. 1–D correlation functions of the Gaussian functions and the experimental data, as reported in Figure 5.2.22.

Table 5.2.3. Results from the bimodal thickness population fitting procedure.

Sample	T_c	Gauss#1				Gauss#2			
		LP	ℓ_c	ℓ_a	ℓ_{tl}	LP	ℓ_c	ℓ_a	ℓ_{tl}
	(^oC)	(nm)	(nm)	(nm)	(nm)	(nm)	(nm)	(nm)	(nm)
iPP2.62	120	12.68	7.61	3.01	2.06	6.64	3.82	1.57	1.25
	122	12.80	7.64	3.05	2.11	7.23	4.21	1.67	1.35
	124	14.93	9.0	3.63	2.3	7.82	4.62	1.78	1.42
	126	15.29	9.09	3.73	2.47	8.3	4.96	1.88	1.46
iPP4.38	114	11.50	6.97	2.76	1.77	6.28	3.65	1.60	1.12
	118	12.68	8.02	2.85	1.81	7.11	4.18	1.70	1.23
	120	13.27	8.35	2.90	2.02	6.99	4.08	1.87	1.04

authors have concluded that the occurrence of the two thickness populations is due to the existence of two crystalline phases, α– and γ–phase, that have different thickness distribution. In their study, samples that had more than 80 % γ–phase exhibited only one thickness population, and they argued that the single distribution model is probably due to the high percentage of the γ–phase that prevents the distinguishing of the two populations. In the case when the γ–phase content was in the 25–35% range they observed the bimodal distribution. They concluded that the two crystalline structures give rise to lamellar stacks characterized by a different periodicity.

In the case of linear polyethylene Stribeck and coworkers[138] used two Gaussian distribution function to fit the interface distribution function, which is very similar to our procedure. They hypothesized that the minor component of the bimodal fit is due to the presence of thin crystals that formed after quenching. They supported this theory with results from DSC, by comparing the weight fraction of the minor component with the fraction of the quenched crystals that was identified in the DSC endotherms.

With the aim of determining the origin of the two lamellar thickness populations, we analyzed the DSC results more in detail. These copolymer samples gave DSC endotherms that exhibited three melting peaks, as seen in Figures 4.4.4. and 4.4.5. The melting peak assignment was performed in section 5.2.2. The lowest endotherm ($\Delta H_{f,1}$) was assigned to the melting of γ–crystals formed during quenching, while the second ($\Delta H_{f,2}$) and the third peak ($\Delta H_{f,3}$) were assigned to the melting of the γ– and α– crystals, correspondingly, that are formed during the isothermal crystallization. An example of the performed peak deconvolution is shown in Figure 5.2.2. The results from both SAXS peak fitting and DSC peak deconvolution are presented in Table 5.2.4 for comparison.

In Table 5.2.4 w(LC1) and w(LC2) are the weight percentages of the lamellae population 1 with larger average lamellar thickness and population 2 with smaller average lamellar thickness, correspondingly. $w\%(\Delta H_{f,1})$ and $w\%(\Delta H_{f,2}+\Delta H_{f,3})$ are the percentage of crystals formed on quenching and during isothermal crystallization,

Table 5.2.4. Comparison of SAXS results with DSC results.

		Results from SAXS		Results from DSC			
Sample	T_c, (^oC)	*w*(LC1)	*w*(LC2)	$w\%(\Delta H_{f,1})$	$w\%(\Delta H_{f,2}+\Delta H_{f,3})$	γ%	α%
iPP2.62	120	70.1	29.9	24.9	75.1	64.5	35.5
	122	66.0	34.0	29.7	70.3	61.2	38.8
	124	42.2	57.8	32.9	67.1	62.9	37.1
	126	31.1	68.9	36.2	63.8	66.5	33.5
iPP4.38	114	84.1	15.9	21.5	78.5	74.3	25.7
	118	62.7	37.3	37.6	62.4	84.2	15.8
	120	61.2	38.8	39.7	60.3	71.0	29.0

respectively. By comparing the data from SAXS fitting procedure and DSC we can estimate the source of the two lamellar populations.

From the DSC results of copolymer iPP4.38 crystallized at 114, 118 and 120 ^{o}C it can be seen that 21.5 %, 37.6 % and 39.7 % of the heat of fusion comes from melting of thin γ–crystals formed on quenching. This agrees well with the percentage of the minor component (LC2) of the bimodal fit, which for those samples gave 15.9 %, 37.3 %, and 38.8 %. The comparison of the percentage of the major component (LC1) with the total γ–phase or α–phase content does not give as good match. Therefore, for iPP4.38 copolymer the bimodal thickness population is due to the presence of thin γ–crystals formed on quenching and thicker α– and γ–crystals formed during isothermal crystallization.

In the case of copolymer iPP2.62 the situation is more complicated. It can be seen that there is no consistent agreement between SAXS and DSC parameters for all crystallization temperatures. For the lower two crystallization temperatures, 120 and 122 ^{o}C, the percentage of the minor component is equivalent to the crystals formed on quenching, while the major component is equivalent to the crystals developed isothermally. On the other hand, for the two highest crystallization temperatures, 124 and 126 ^{o}C, the minor lamellar population matches better the total γ–content. But, it should be noted that in the case of iPP2.62, there is a larger error between the compared parameters in both cases. Reason for this may be the experimental errors in both SAXS and DSC experiments. Also, it is possible that the use of different mathematical function to model the SAXS scattering data will make these percentages closer.

Nevertheless, an important conclusion from this analysis is that it allowed an independent evaluation of the contributions of the different families of lamellae to the SAXS pattern.

5.2.4. Cocrystallization Model

In section 2.3.2 it was shown that the semi–crystalline state of a random copolymer can be described by two extremes: the comonomer units are either rejected from the crystal, or the comonomer units take part in the crystallization and are uniformly included in the copolymer crystal. In the former case, crystals consist only of homopolymer sequences and all comonomer units are located in the amorphous phase. In both cases the Gibbs free energy of the crystals will increase, and the melting temperature will decrease. In section 5.2.3.3 it was confirmed that ethylene comonomer units reduce the equilibrium melting temperature of the propylene copolymers. Although the cases of total defect inclusion and exclusion occur frequently in the crystallization models, in most real copolymer systems an intermediate model of partial inclusion is more applicable.

There are numerous studies in the literature that deal with the question whether the comonomer units are included[72,75,79,80,82] or excluded[42,77,78] from the propylene-ethylene copolymer crystals, consequently reducing the melting temperature. When addressing this issue for the case of propylene–ethylene copolymers the presence of two crystalline phases with different melting temperatures and heat of fusion represent an additional difficulty. However, it has been reported[92] that for *i*–PP homopolymer α– and γ–phases have similar equilibrium melting temperatures, that is 186.1 and 187.2 ^{o}C, respectively. In addition to this, two ΔH_f ranges are reported for both phases, 209 and 167 J/g for α–phase, and 196 and 150 J/g for γ–phase, with the higher and lower ΔH_f being close in value. Based on this, the cocrystallization models of the propylene–ethylene copolymers were analyzed only for the α–phase of these copolymers.

In the case of random propylene–ethylene copolymers two types of defects can influence their crystallization, i.e. the ethylene content and stereo defects. Previously, by means of ^{13}C NMR analysis in section 5.1 it was established that copolymers used in this study do not contain regio defects. Therefore, the exclusion and partial inclusion models

will be evaluated for ethylene, stereo and total defect content. Additionally, the copolymers were separated into two groups because of their different molecular weights, as seen from Table 4.2.1. Copolymers iPP2.62 and iPP4.38 with molecular weight in the range of 250,000–290,000 g/mol were analyzed separately from iPP10.45 and iPP15.57 with molecular weight in the range of 75,000–86,000 g/mol.

Firstly, the applicability of Flory's total exclusion model was tested by plotting the experimental α–phase equilibrium melting temperature of the copolymers as a function of the defect content. Values of the ethylene, stereo–defects and total defect content for the studied copolymers are given in Table 4.1.5. For the homopolymer values for T_m^0 = 186.1 ^oC and heat of fusion = 209 J/g were used to calculate the equilibrium melting temperature of the copolymer as a function of defect content according to Flory's equation (2.3.9). Equilibrium melting temperatures calculated using the Flory's exclusion model were presented on the same plot for comparison. The resulting plots for two sets of copolymers are shown in Figure 5.2.24.

Figure 5.2.24 (a) shows the experimental and Flory's T_m^0 for copolymers iPP2.62 and iPP4.38 plotted as function of ethylene, stereo and total defect content. In this figure the full line is the theoretical prediction using Flory's model, while closed symbols represent ethylene defect, crosses are the stereo–defects and open symbols are the total defect content. If only ethylene or stereo–defect contents are considered, the experimental points do not fall on Flory's theoretical prediction, they are much lower than predicted. On the other hand, the experimental equilibrium melting temperatures plotted as a function of total defect content (ethylene + stereo defects) give reasonably good fit to the Flory's exclusion model, although they are slightly lower than the Flory's prediction. NMR experiments performed on these two copolymers showed that they had only stereo defects of the type mmmr+mmrm, however, they did not show peak due to the adjacent ethylene and stereo defects – mmrE. Therefore, for low ethylene content copolymers different types of defects are not adjacent and are additive.

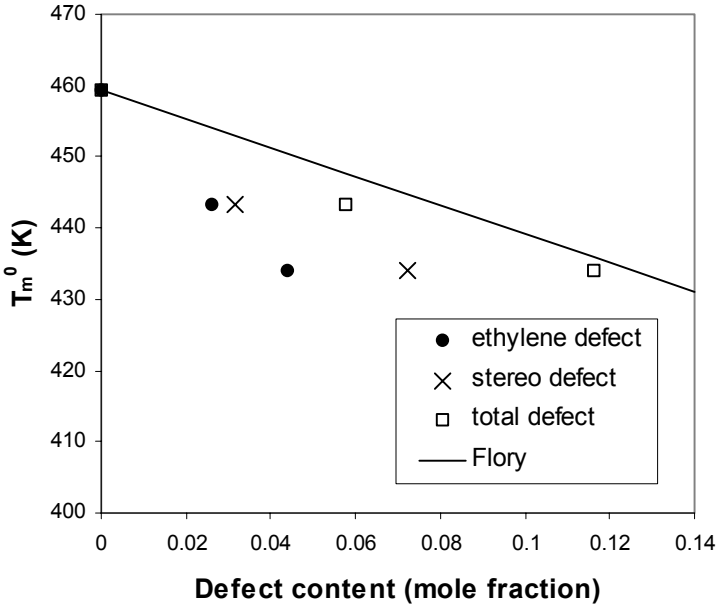

(a)

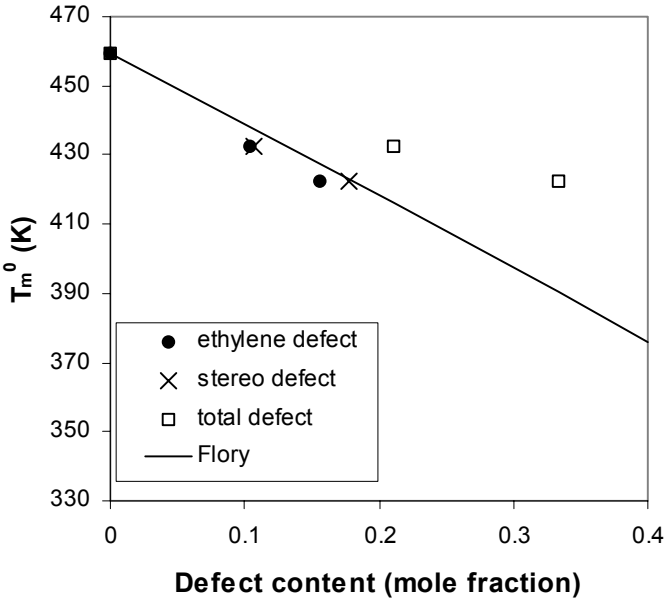

(b)

Figure 5.2.24. T_m^0 versus the mole fraction of defects for copolymers (a) iPP2.62 and iPP4.38, and (b) iPP10.45 and iPP15.57.

Same kind of plots for copolymers iPP10.45 and iPP15.57 are presented in Figure 5.2.24 (b). In this case, when the experimentally determined T_m^0 are plotted as a function of ethylene (closed symbols) and stereo (crosses) defect content, they are close to the prediction according to Flory's theory. However, experimental T_m^0 plotted versus total defect content are much larger than the theoretical predictions. These copolymers have complex types of stereo-defects, and they exhibit small peaks in the NMR spectra due to the adjacent ethylene and stereo-defects – mmrE+mrrE. This indicates that for copolymers iPP10.45 and iPP15.57 some of the ethylene and stereo defects are adjacent and therefore they are not additive in the Flory's model of copolymer crystallization.

Above observations clearly indicate that Flory's total exclusion model can not explain the reduction in the melting temperature of the studied copolymers. These results agree well with the findings of Laihonen *et al.*[72] who studied fractionated Ziegler–Natta propylene–ethylene copolymers. They concluded that the decrease of crystallinity and enthalpy of fusion, as well as the shortening in the average length of 3_1 helices with comonomer content indicates that a fraction of the ethylene units are included in the crystals. In addition, molecular mechanics calculations on model compounds suggested that the copolymer molecule with low concentration of ethylene is equivalent to *i*–PP from which a few methyl groups have been removed.[69] Therefore, isolated ethylene units can be incorporated into *i*–PP 3_1 helix and consequently the crystalline phase. According to these authors, with increasing ethylene concentration the propagation of the helix will depend on the randomness of the copolymer. The ethylene inclusion will be less likely to happen in copolymers with blocky character since the ethylene blocks will hinder the 3_1 helix of *i*–PP.

For that reason the model of partial defect inclusion was evaluated. For this, the equation (2.3.8) for the equilibrium theory of inclusion of comonomer units in the crystal was used. This equation can be rearranged to evaluate the degree of defect inclusion in the lattice by introducing the term degree of incorporation of the comonomer unit, $b = X_c/X$:[139]

$$\frac{1}{T_m^0} - \frac{1}{T_m^0(X)} = -\frac{R}{\Delta H_f^0}\left\{\frac{\varepsilon bX}{RT_m^0(X)} + (1-bX)\ln\frac{(1-bX)}{(1-X)} + bX\ln b\right\} \qquad (5.2.2)$$

where X_c is the mole fraction of the comonomer incorporated in the polymer crystal, X is the overall comonomer content, ε is the excess free energy due to the defect inclusion, $T_m{}^0(X)$ is the copolymer equilibrium melting temperature, and $T_m{}^0$ and $\Delta H_f{}^0$ are the homopolymer equilibrium melting temperature and heat of fusion, respectively.

This equation shows that there is linear relationship between the equilibrium melting point depression and mole fraction of the comonomer unit. For known copolymer equilibrium melting temperatures and value for ε, the degree of comonomer incorporation in the crystals can be determined from the plot of equilibrium melting temperature versus defect content.

The value of the excess free energy of the incorporation of the defect was determined from the decrease of the heat of fusion as a function of defect content and the equation:

$$\Delta H_f^0 = \Delta H_f^c + \varepsilon \cdot X \qquad (5.2.3)$$

where $\Delta H_f{}^0$ and $\Delta H_f{}^c$ are the heat of fusion for the homopolymer and copolymer, respectively. Values for $\Delta H_f{}^c$ were determined from the measured heat of fusion of the copolymers extrapolated to 100% crystallinity.

The excess free energy ε was determined from the slope of the $\Delta H_f{}^c$ versus defect content. For copolymers iPP2.62 and iPP4.38 the value of ε was 15.80 ± 0.5 kJ/mol when total defects were considered. For copolymers iPP10.45 and iPP15.57 ε was determined as a function of ethylene, stereo and total defect content, giving values of 27.14 ± 2.6 kJ/mol, 25.27 ± 3 kJ/mol and 13.08 ± 1.6 kJ/mol, correspondingly. These values for ε are comparable with the values published for branched polyethylenes with ranges of 18.2–37.3 kJ/mol[140] and 23–54 kJ/mol.[141] However, they are considerably larger than

values of 1.6 kJ/mol[142] and 1.9 kJ/mol[130] reported for *i*–PP considered as stereo-copolymer, 2.45 kJ/mol for the copolymers of L– and DL–lactides,[65] and 4.5 kJ/mol defect for copolymers of tetrafluoroethylene and hexafluoropropylene.[64]

With all parameters determined equation (5.2.2) was used to construct the plots shown in Figures 5.2.25 - 5.2.27 for two sets of copolymers. Figure 5.2.25 shows both the Flory's total exclusion prediction and Sanchez–Eby uniform inclusion prediction of the T_m^0. Both of these models are the boundary cases of the equation (5.2.2) for the values of $b = 0$ and 1, respectively.

The total exclusion model is shown in the plot by the full line and the uniform inclusion model is represented with dashed line. The two vertical set of data are T_m^0 of the two copolymers with total defect mole fraction of 0.0576 (iPP2.62) and 0.116 (iPP4.38) calculated from equation (5.2.2) for different values of *b*. The experimental points represented with open symbols lie lower than the Flory's theoretical line.

From the plot in Figure 5.2.25, it is possible to estimate the degree of the comonomer incorporation from the position of the experimental points on the vertical lines. The values for the *b* obtained from the plot are 0.22 for iPP2.62 and 0.10 for iPP4.38. According to these findings 10–22 % of the total defects are included in the crystals of these copolymers. Figures 5.2.26 and 5.2.27 show both the Flory's and Sanchez–Eby's prediction of the T_m^0 for copolymers iPP10.45 and iPP15.57 as a function of ethylene content for $\varepsilon = 27.14$ kJ/mol and stereo-defect content for $\varepsilon = 25.27$ kJ/mol. Using ε value obtained from total defect content did not produce meaningful results. Copolymers iPP10.45 and iPP15.57 gave lower values for *b* when using ethylene content, 0.09 and 0.07, and stereo-defect content, 0.08 and 0.09, respectively.

Values for defect incorporation obtained in this study are smaller than the results reported by Alamo *et al*.[80] (42–44%) and Hosoda *et al*.[82] (50–52%) for samples of similar composition but synthesized with metallocene catalysts. The differences in these values can be attributed to the methods by which these values were determined, as well as the

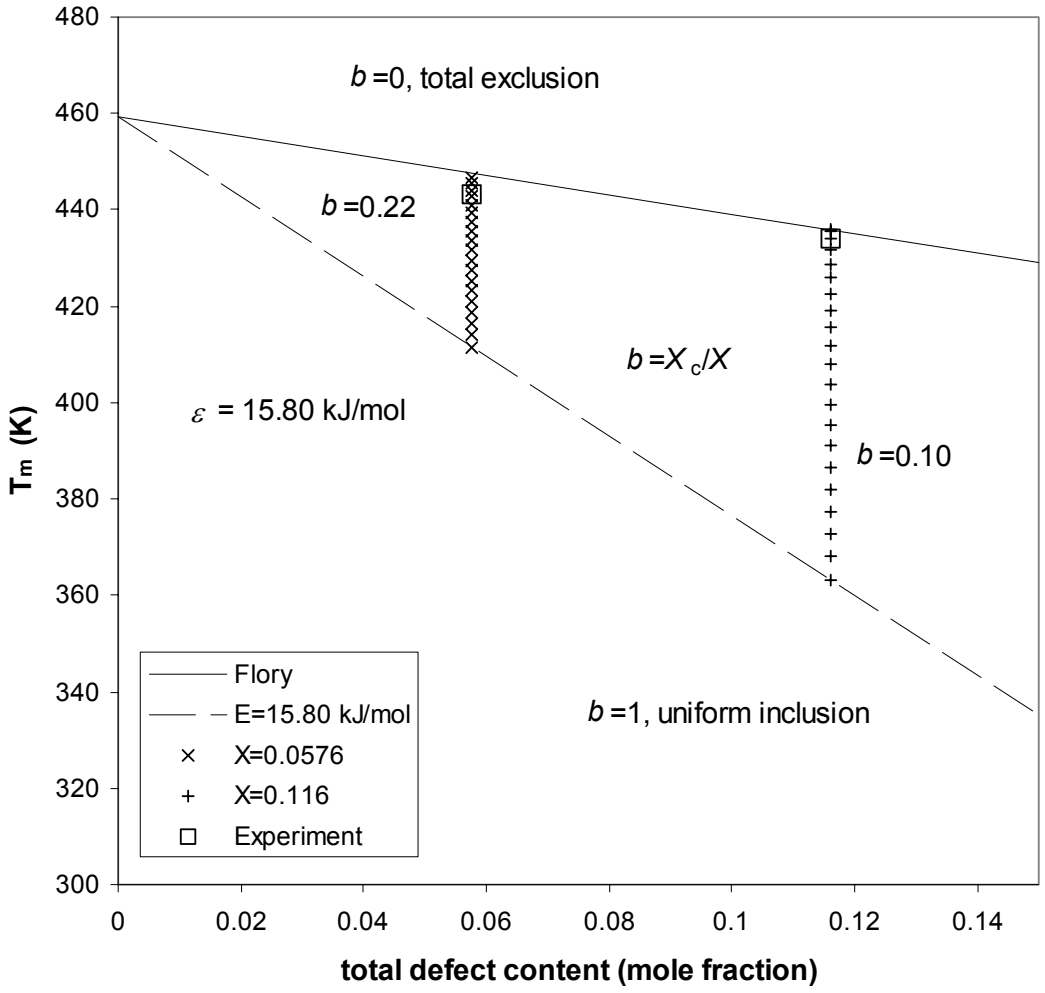

Figure 5.2.25. Equilibrium melting temperature depression as a function of total defect content for iPP2.62 and iPP4.38 (high MW samples).

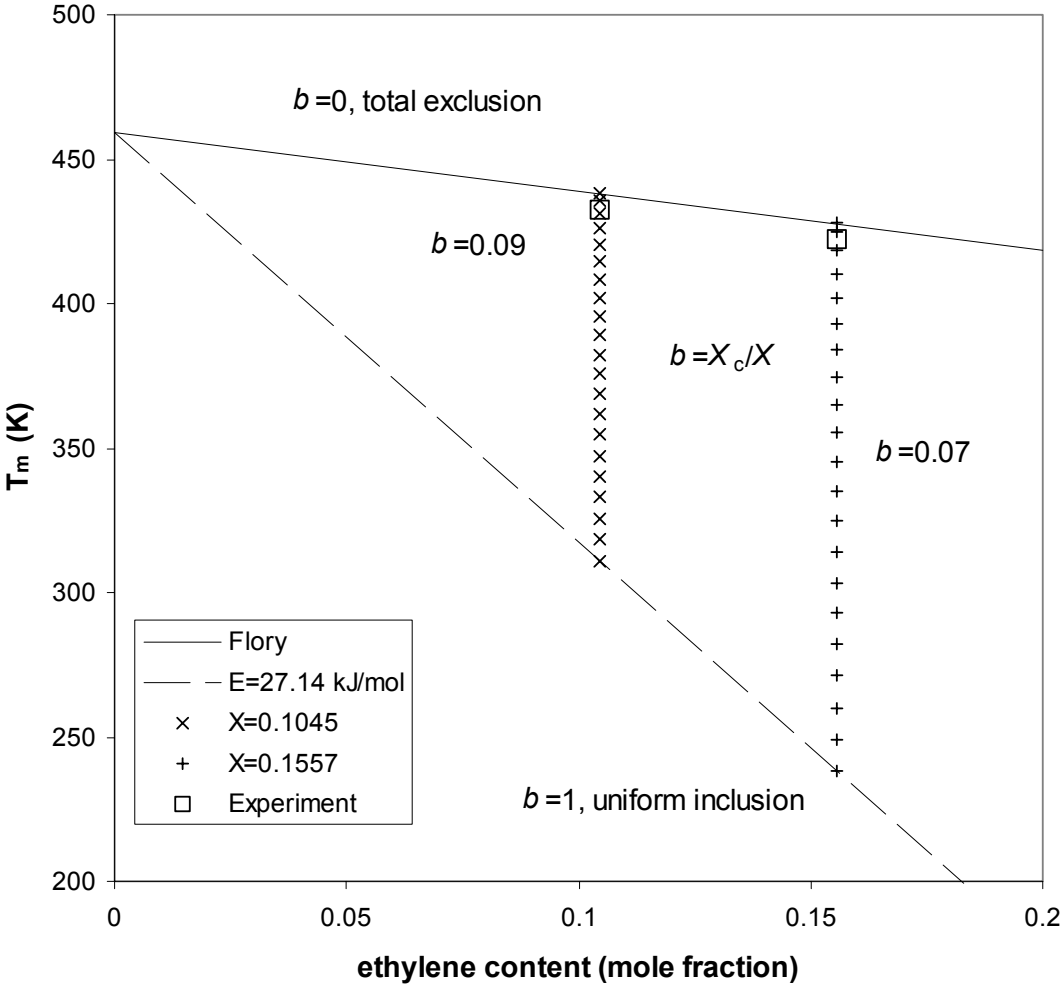

Figure 5.2.26. Equilibrium melting temperature depression as a function of ethylene content for samples iPP10.45 and iPP15.57 (low MW samples).

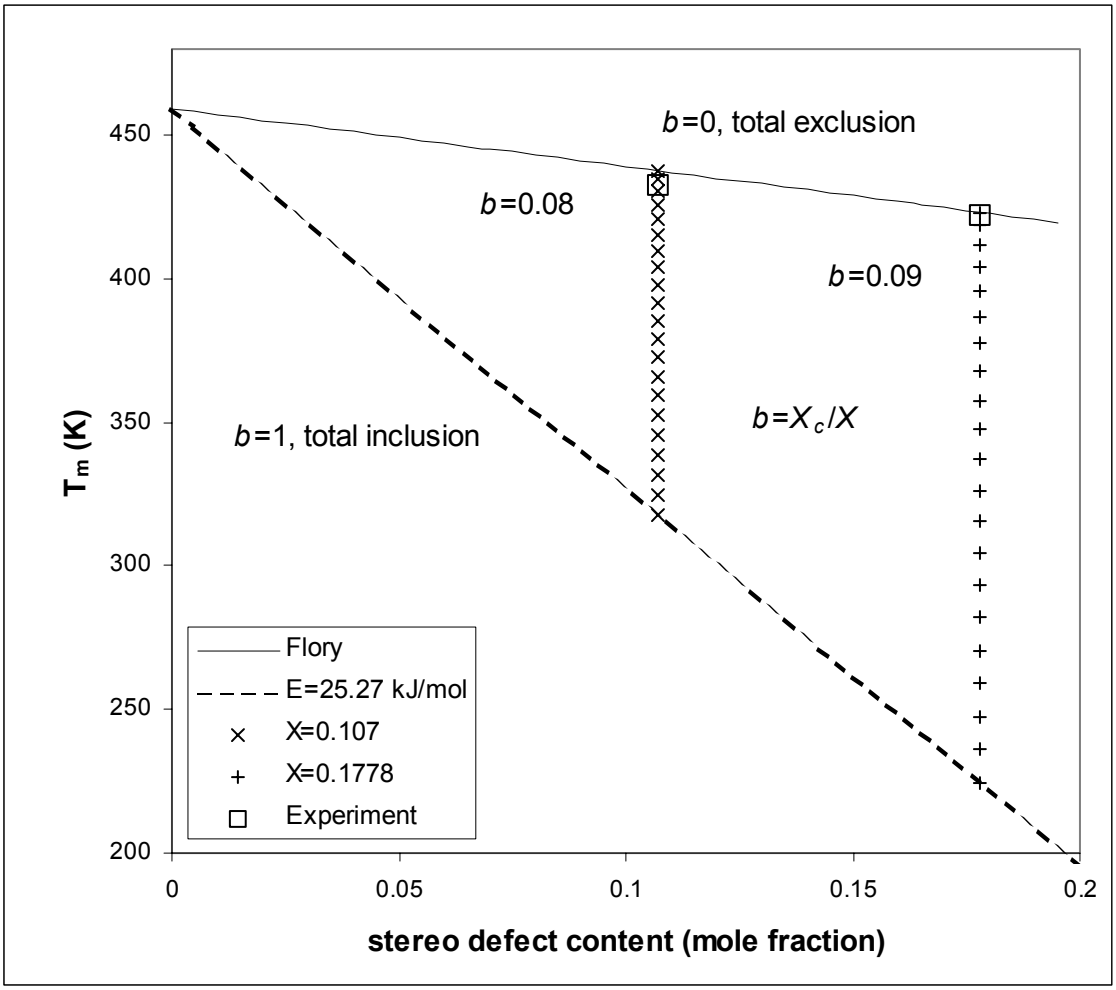

Figure 5.2.27. Equilibrium melting temperature depression as a function of stereo-defect content for samples iPP10.45 and iPP15.57 (low MW samples).

sample preparation. Alamo and coworkers used solid–state ^{13}C NMR technique to determine the partitioning of the ethylene defects within the crystals of samples that were not crystallized isothermally, but rather slowly cooled at dT/dt = 1 ^{o}C/min. The limitations of the solid–state NMR spectroscopy include the difficulties in accurate chemical shift assignments, as well as the small differences in both the chemical shifts and relaxation time between the comonomer in the crystalline phase and in the amorphous phase. Hosoda and coworkers studied the degree of comonomer inclusion in the crystal phase using the fuming nitric acid etching technique to remove amorphous component, followed by DSC and solution ^{13}C NMR measurements. This method relies on the successfully removing only the amorphous phase, and not the crystalline phase.

Nevertheless, there is a possibility that the values of ε obtained from the analysis of the observed copolymer heat of fusion as a function of defect content are not correct. These values were 15.80, 27.14 and 25.27 kJ/mol and are too large when compared with the equilibrium heat of fusion of the *i*–PP homopolymer (8.778 kJ/mol). For copolymers iPP2.62 and iPP4.38 $\varepsilon \sim 1.8 \times \Delta H_f^0$, this is unrealistic value especially considering that the defect units (ethylene and atactic propylene) have the same chemical make-up as the crystallizable units. If the values of excess free energy of defect incorporation are this large, it is unlikely that significant amount of defects will be included in the crystals. The low value of the defect incorporation *b* can be due to the incorrect overestimation of the defect energy ε as determined from the heat of fusion analysis.

Values of the calculated defect incorporation in the polymer crystals can be evaluated qualitatively by comparing the molecular characteristics of the copolymers, listed in Table 4.1.3, with the lamellar thickness results presented in Tables 4.6.1–4.6.4. The latter tables list the lamellar thickness as a function of crystallization temperature, as well as the calculated stem length and number of propylene monomer units traversing the crystal lamellae for both α– and γ–crystal phases. The length of the γ–stem was calculated for samples that crystallized in more than 50 % of γ–phase. The comparison of these characteristics is shown in Table 5.2.5.

Table 5.2.5. Average propylene sequences from NMR and lamellar thickness from SAXS for the four copolymers.

Sample	NMR	SAXS	
	$\overline{n}_p$	ℓ_{cr} (nm)	# propylene units per crystal thickness
iPP2.62	37	7.73–9.25	36–43
iPP4.38	23	6.48–8.06	30–37
iPP10.45	10	6.24–7.33	29–34
iPP15.57	7	6.15–6.73	28–32

The comparison of the number average sequence of propylene units in the copolymer ($\overline{n}_p$) that are able to crystallize with the number of propylene units that traverse the lamellae can give an insight into the amount of defects incorporation in the crystals. For the copolymer iPP2.62 values of the weight average lamellar thickness are in the range of 7.73–9.25 nm. The length of the polypropylene stems that crystallize into α–crystals that is equivalent to this range of crystal thickness is 7.8–9.4 nm, and the number of propylene units in the stems is 36–43. When this number is compared to 37, the number average sequence of propylene units, it can be concluded that although these numbers are close in value some of the defects have to be incorporated in the crystals to achieve the highest crystal thicknesses determined from SAXS.

This tendency is more prominent for copolymers with higher defect content. From Table 5.2.5 it can be seen that as the ethylene content in the copolymers increases, the average number of propylene units in the chains decreases considerably, while the crystal thickness decreases only slightly. For example, copolymer iPP15.57 with $\overline{n}_p$ = 7

achieved crystal thickness from 6 to 6.7 nm depending on the crystallization temperature. If the defects were completely excluded from the crystals, or if the defect incorporation was only 10-20% than the lamellar thickness values should have been much lower that the experimentally determined. The average propylene run in this copolymer is much lower than the length of α–stems (28–32) or γ–stems (36–41) traversing the crystals suggesting that considerable amount of the defects are included in the copolymer crystals.

In order to evaluate whether uniform inclusion model applies for copolymers used in this study, experimental T_m^0 data were fitted with Sanchez–Eby uniform inclusion model as defined by equation (2.3.10). Calculated values of the excess energy ε for the ethylene, stereo and total defect content are shown in Table 5.2.6.

It can be seen that the excess free energies due to the incorporation of defect in the polymer crystal are smaller than the equilibrium heat of fusion of the *i*–PP homopolymer, although for copolymers iPP2.62 and iPP4.38 these values are slightly larger than RT. Free energy of defect incorporation of copolymers iPP10.45 and iPP15.57 are comparable with the ones calculated for the homopolymer.[130,142,143] These relatively low values of the defect free energy lead to a conclusion that there is considerable inclusion of the comonomer and stereo–defects in the copolymer crystals.

Wendling and Suter[143] used computational thermodynamic-integration approach to calculate the local conformation and defect free energy of stereo-irregularity inclusion in *i*–PP. They found that Gibbs free energy of inclusion of isolated atactic defect is low (0.0 ± 2.1 kJ/mol defects) and enables cocrystallization according to the uniform inclusion model. Their results are in good agreement with experimental investigations that proposed an estimate of the defect free energy of 1.6 to 1.9 kJ/mol defect.[130,142] Since these values are below RT at typical crystallization temperatures (2.9–3.6 kJ/mol), the uniform inclusion model where every isolated stereo-defect can be included into the crystal can be applied for *i*–PP. On the other hand, for sequences of adjacent defects there is considerable defect free energy that makes the inclusion of atactic sequences less likely. For example, their calculations predicted that dyad and triad inclusions will lead to

Table 5.2.6. Values of the excess free energy due to the uniform incorporation of defects in the polymer crystal for propylene–ethylene copolymers.

Sample	Defect type	Defect content (mole fraction)	ε (kJ/mol)
iPP2.62	ethylene	0.0262	11.6
	stereo	0.0314	9.68
	total	0.0576	5.28
iPP4.38	ethylene	0.0438	8.9
	stereo	0.0722	5.4
	total	0.116	4.14
iPP10.45	ethylene	0.1045	4.87
	stereo	0.107	4.75
	total	0.2115	2.40
iPP15.57	ethylene	0.1557	4.52
	stereo	0.1778	3.96
	total	0.3335	2.11

defect free energy of 22.4 ± 1.7 and 11.1 ± 2.1 kJ/mol defects, respectively. When a ethylene co–unit is taken into consideration, authors argue that the space left by the missing methyl group can be occupied by other atom from the polymer chain that can move slightly towards this position, and that this occurrence is energetically favorable.

Therefore it can be concluded that even though the exclusion model fairly well describes the behavior of copolymers with lower defect content (iPP2.62 and iPP4.38) some defect inclusion has to occur to account for the lowering of their equilibrium melting temperatures. Defect inclusion increases considerably with the increase of the total defect content in the case of copolymers iPP10.45 and 1PP15.57. Also, the extent of defect incorporation will depend on the type of defect. Based on the findings from this study and published results it can be concluded that ethylene units are partially included, stereo-block defects of the type mmmr+mmrm are most probably excluded, single atactic units (mmrr+mrrm) can be totally included, while atactic diads (mrmr) are excluded from the polymer crystals.

5.2.5. Crystallization Kinetics

In this section the experimental growth rates of the copolymers measured at atmospheric pressure are analyzed using the Lauritzen–Hoffman secondary nucleation theory. The growth rate kinetics of Ziegler–Natta random propylene–ethylene copolymers with low ethylene content has not been studied extensively. This study will shed light on the effect of the comonomer content on the crystallization behavior of these copolymers.

It has been reported by Monasse *et al.*[77] that an unfractionated propylene copolymer with 4.1 mol% ethylene and M_w=450,000 g/mol exhibits a regime III to regime II transition similar to the *i*–PP homopolymer. The temperature at which the

transition between the regimes was observed was T_{tr} = 130 ^{o}C (ΔT = 54 ^{o}C) and was lower compared with the homopolymer.

Laihonen *et al.*[44] have used bulk kinetic data to perform growth rate analysis for a series of fractionated random propylene–ethylene copolymers with 2.7 – 11.0 mol% ethylene. They did not observe any break in the curve of the logarithm of the growth as a function of crystallization temperature. However, their experiments did not have data points in the low supercooling region for a change in slope to be detected. They concluded that their data fall in the regime III crystallization. Still, they observed that the growth rate of the copolymers decreases with increasing comonomer content. Similar results were published by De Carvalho *et al.*[144] on propylene copolymers with ethylene content in the range of 3–6 %. For the same reason as Laihonen they observed only the regime III behavior.

Figure 4.7.3 shows the typical crystallization behavior of polymer systems, namely the growth rate decreases with increasing crystallization temperature. Also, it can be observed that the linear growth rate depends on the copolymer composition; at a constant crystallization temperature the growth rate decreases drastically with increasing comonomer content. Similar results were found in the studies of crystallization kinetics on unfractionated[79] and fractionated propylene ethylene copolymers.[72] This is due to the fact that the critical nucleus requires a finite number of crystallizable units in a continuous sequence. This number of crystallizable units decreases with increasing comonomer, thus effectively reducing the crystal growth rate.

In order to identify regime transitions, it is best to plot the ln$G$ versus the degree of supercooling or crystallization temperature.[61] This is illustrated in Figure 5.2.28 for the four studied copolymers. Change in the slope of the curvature of this plot reveals a probable regime transition. For all samples except iPP15.57 two changes in the slope (or so-called crossover points) were detected. The first crossover point is observed as a change in the convex shape of the crystal growth rate curves, for iPP2.62 and iPP10.45 this happens at ΔT ~ 58 ^{o}C, for iPP4.38 at slightly higher ΔT ~ 62 ^{o}C, and for iPP15.57

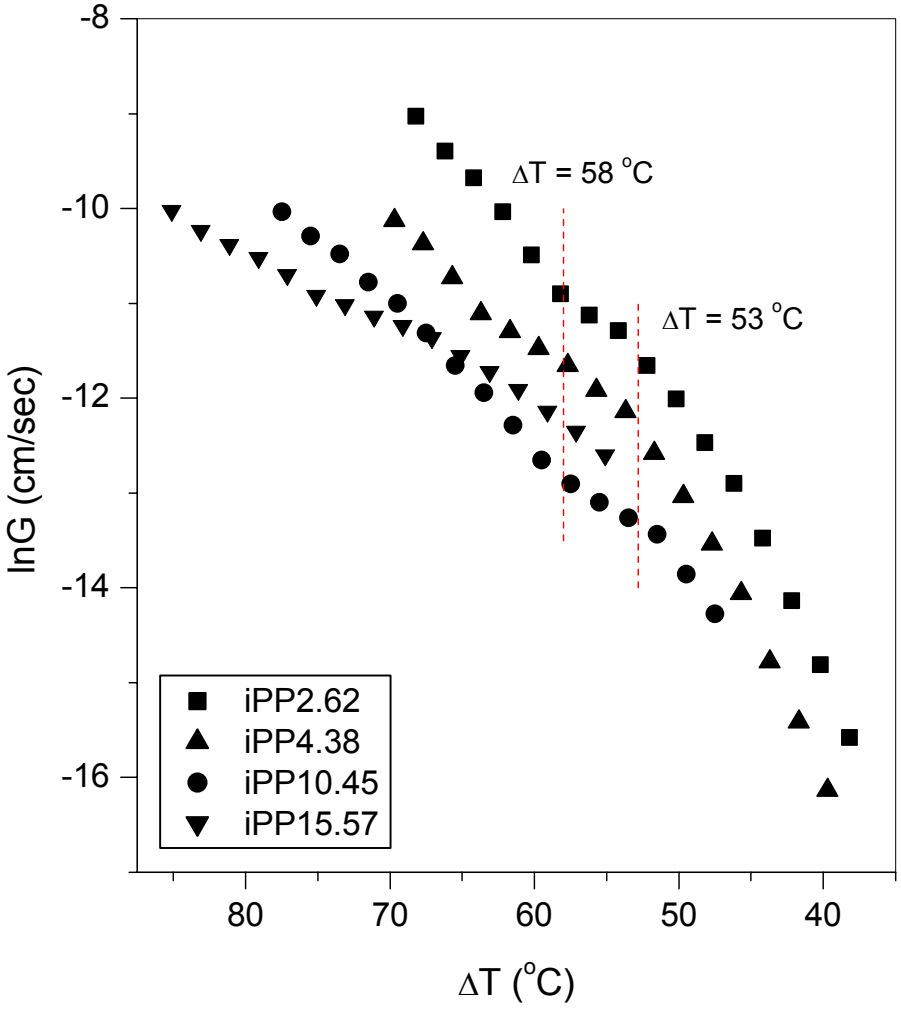

Figure 5.2.28. Logarithmic representation of the linear growth rates as a function of the degree of supercooling for the four copolymers.

$\Delta T \sim 75$ °C. The second crossover point is common for iPP2.62, iPP4.38 and iPP10.45 and is observed as a change in the slope below and above $\Delta T \sim 53$ °C.

In the context of the Lauritzen–Hoffman secondary nucleation theory, the linear growth rate of a crystalline entity for each regime is dependent on the degree of supercooling and is defined by equation (2.3.1). The test of the regimes is done through the plot of $\ln G + \Delta U^*/R(T_c - T_\infty)$. This type of plot factors out the contribution of the transport term to the growth rate, and the slope equals the negative value of the nucleation constant, K_g by using equation (2.3.3). The regime I–II transition is evident when a downward change in the slope is observed, whereas there is an upward change in the observed slope in the transition from regime II to regime III. Fold surface free energies can be calculated from the slopes of the secondary nucleation plots.

Parameters characteristic for the growth theory (e.g. σ, σ_e, and q) are sensitive to the input parameters used to calculate them (e.g. U^*, T_g, T_m^0, and ΔH_f). Consequently, an error in any of these parameters can influence the value of the fold surface free energy and the work of chain folding. Tseng[145] and Mezghani[6] have shown that for an ideal growth system changes in the values of U^* and T_g only shift the curves along the y–axis without changing its shape. In other words, the choice of U^* and T_g will not have an effect on the fold surface free energy. The only parameter that has large influence on the shape of the secondary nucleation plot is the T_m^0, but it does not alter significantly the regime transition temperatures.

The value of $U^* = 1500$ cal/mol has been used extensively in the literature in the case of *i*–PP, and it will be utilized for all copolymers. The T_g of the copolymers was calculated as depression from the homopolymer T_g by 1.6 °C per mole% ethylene.[146] In this analysis, the values of T_m^0 for the copolymers that were determined from the lamellar thickness studies were used.

Copolymers used in this study have different molecular weights; iPP2.62 and iPP4.38 have molecular weights in the range 252,000–287,000 g/mol, while this range

for iPP10.45 and iPP15.57 is 75,000–86,000 g/mol. These two groups of copolymers were analyzed separately since it has been shown that the molecular weight affects the regime transitions in *i*–PP homopolymer.[147] Additionally, because these propylene-ethylene copolymers crystallize in a mixture of α– and γ–crystalline phases, the regime analysis was performed for both phases. The linear growth rates of γ–phase were taken to be the same as those of the α–phase, since there was no change in slope in the plots of the spherulite growth rate as a function of crystallization time. If this was not the case, then discontinuities in the linear growth data at times when a transition between growth of mixed α and γ to pure γ–crystals occurs would have been observed. Also, it has been found that both polymorphs appear at the same time in the early stages of the crystallization process.[80]

Figure 5.2.29 shows the regime plots for α–crystals of copolymers iPP2.62 and iPP4.38. The dashed lines define the regions of different crystal growth behavior, and the ratios of the slopes are indicated in the plot. It can be seen that for both iPP2.62 and iPP4.38 three regimes are detected. The regime III/II transition occurs at ΔT = 58 ^{o}C for iPP2.62 and 64 ^{o}C for iPP4.38, while regime II/I takes place at ΔT = 53 ^{o}C for both copolymers. In Figure 5.2.30 the regime plots for α–crystals of copolymers iPP10.45 and iPP15.57 are displayed. iPP10.45 exhibits three regimes, with their transition at ΔT = 58 ^{o}C and 53 ^{o}C, whereas for copolymer iPP15.57 only one transition (III/II) is detectable at ΔT = 75 ^{o}C.

Figures 5.2.31 and 5.2.32 display the regime plots of the γ–crystals of the copolymers. In this case the T_m^0 of the γ–crystal phase determined from the lamellar thickness studies were used, except for the iPP2.62 and iPP4.38 for which T_m^0 from Hoffman –Weeks plots were used. From these figures it can be seen that by switching from α–crystal to γ–crystal growth only the slopes of the regimes change, while the transition temperatures remain the same.

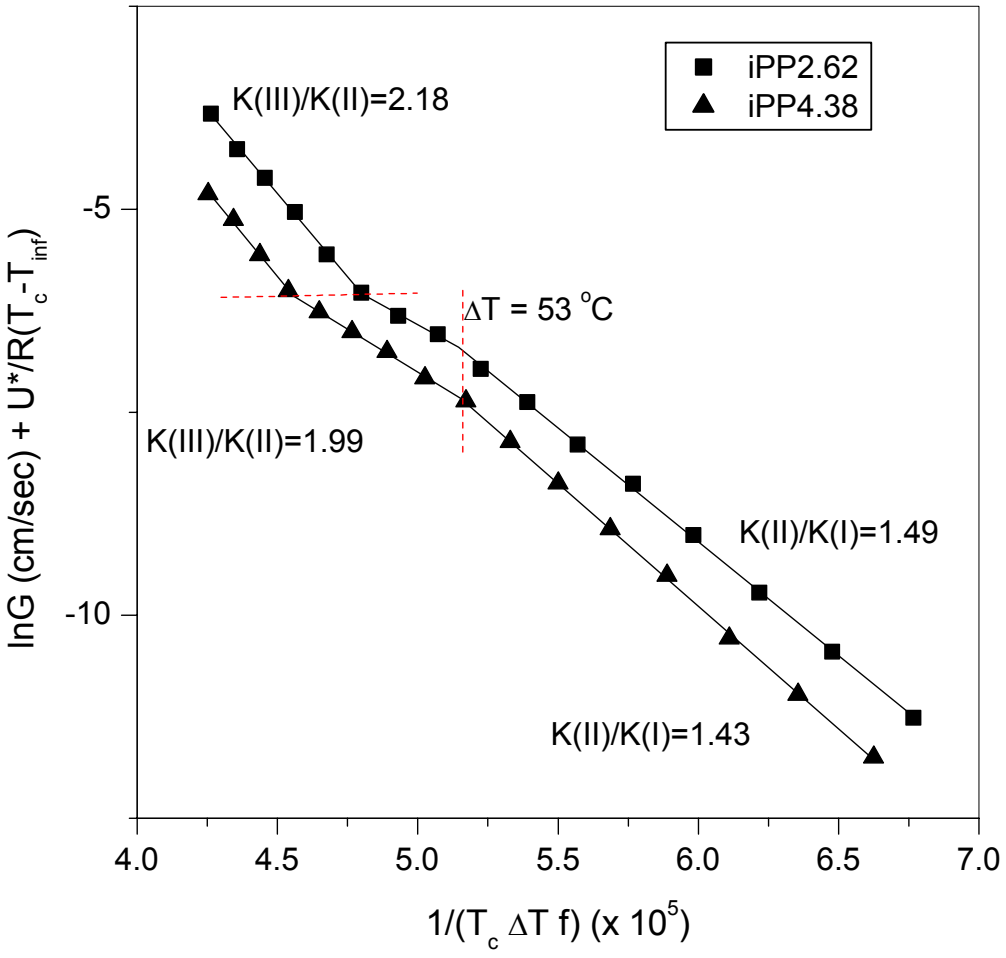

Figure 5.2.29. Regime plot for the growth of the α–crystal phase of iPP2.62 and iPP4.38 copolymers.

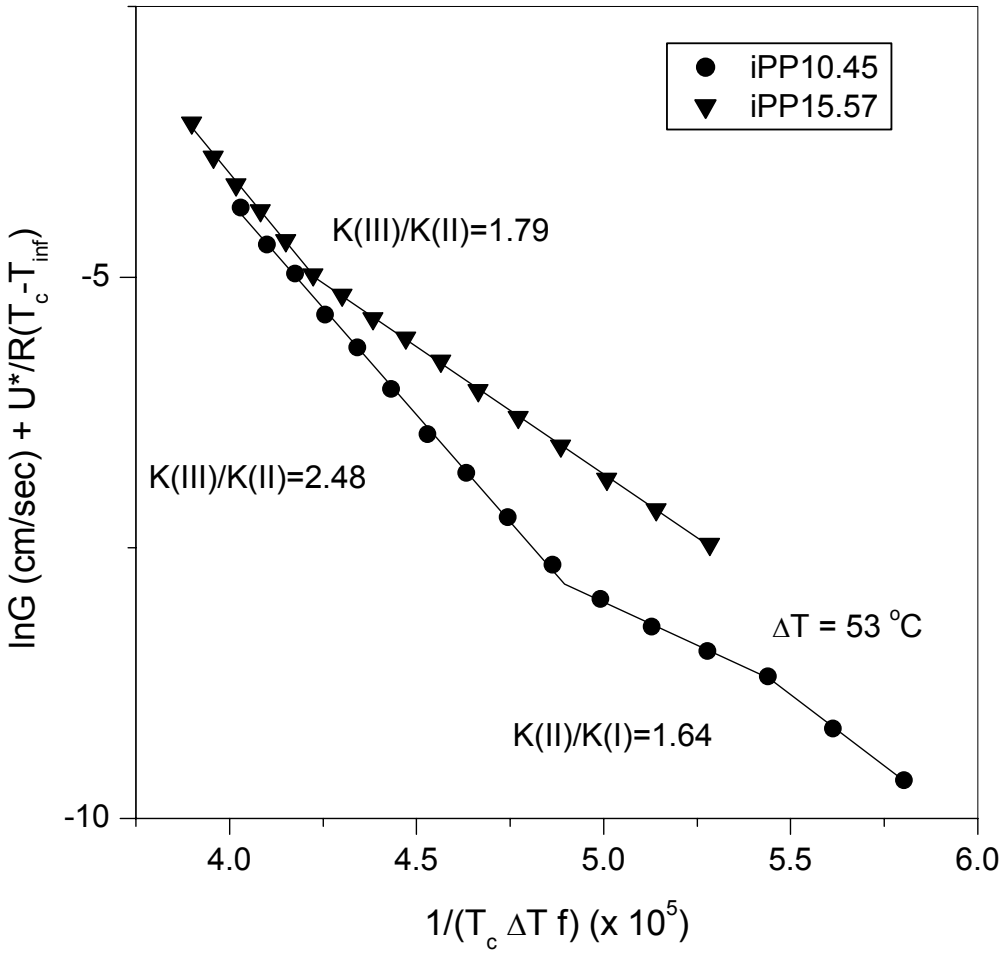

Figure 5.2.30. Regime plot for the growth of the α–crystal phase of iPP10.45 and iPP15.57 copolymers.

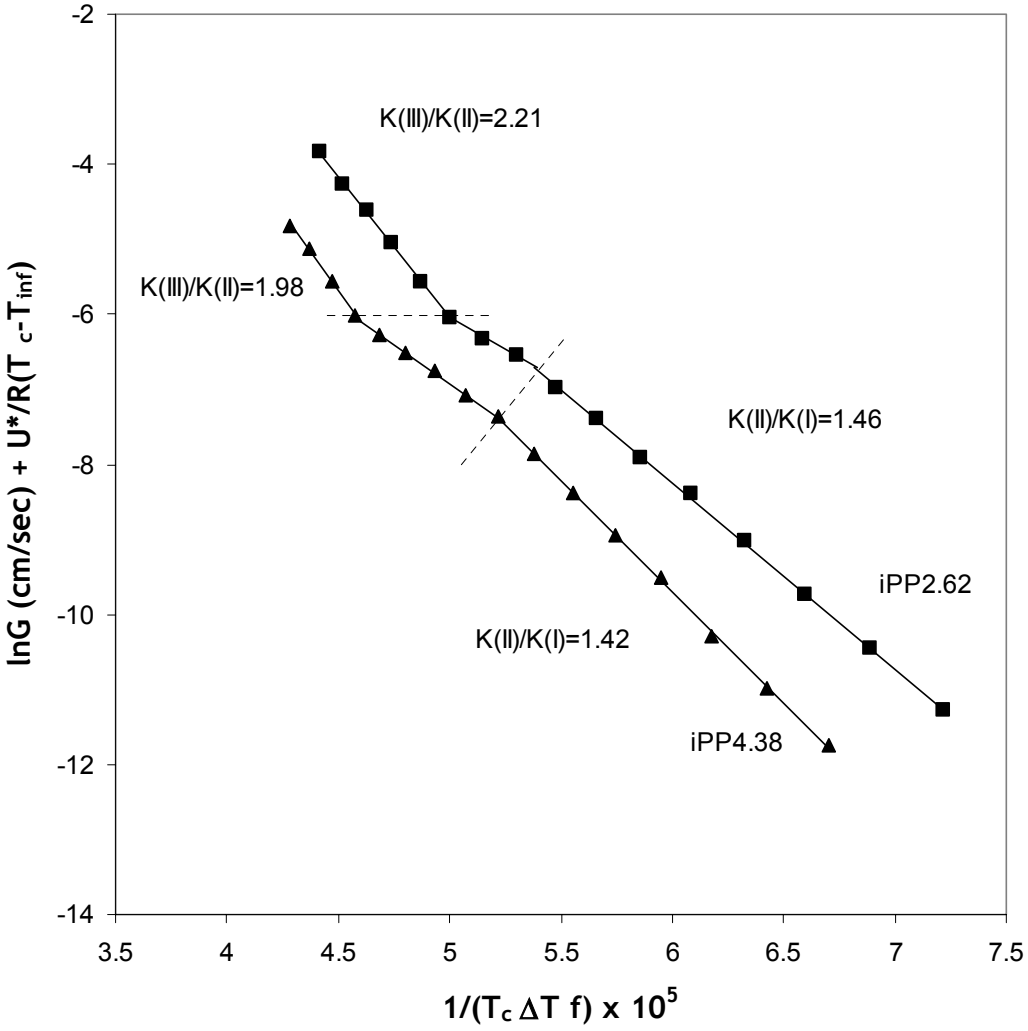

Figure 5.2.31. Regime plot for the growth of the γ–crystal phase of iPP2.62 and iPP4.38 copolymers.

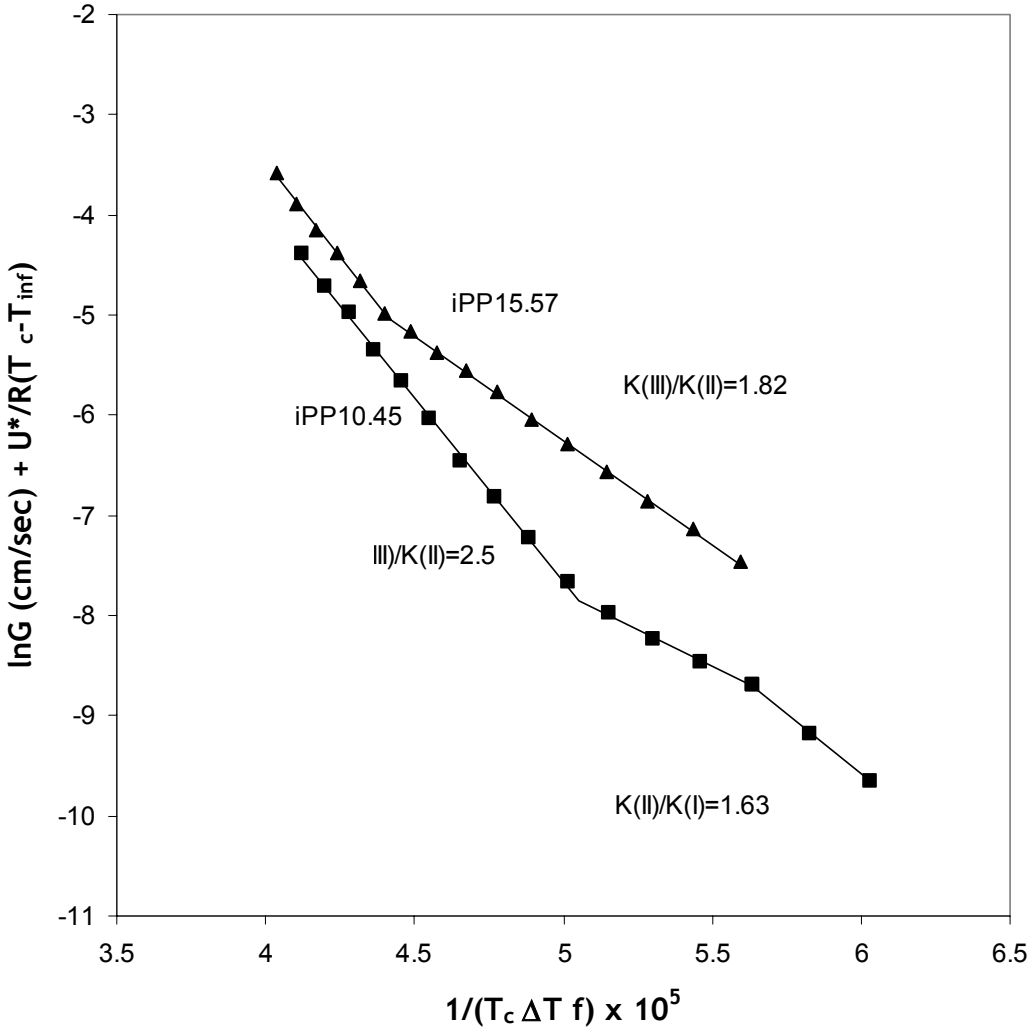

Figure 5.2.32. Regime plot for the growth of the γ–crystal phase of iPP10.45 and iPP15.57 copolymers.

The results from the kinetic analysis for the α– and γ–crystals of the propylene–ethylene copolymers are shown in Table 5.2.7. The ratios of the K_g values of the regimes III and II for all copolymers are close to 2, varying in value from 1.79 for iPP15.57 to 2.47 for iPP10.45. Values of the parameters σ and σ_e were calculated from equations (2.3.3) and (2.3.5). Based on the observations from WAXD the (110) growth plane of the α and (001) growth plane of the γ–orthorhombic crystals were used. The choice of heat of fusion does not change the value of σ_e, since according to Thomas–Stavely equation (2.3.5) heat of fusion only affects the lateral surface free energy, σ.

From the results in Table 5.2.7 it can be observed that values of σ_e are quite different for each of the crystallization regimes. For example, sample iPP2.62 for regime I has σ_e = 59.6 erg/cm^2, while the ones for regimes III and II are on average 83.6 erg/cm^2. The main reason for this difference is the deviation of the ratios of the slopes K_g(III)/K_g (II) and K_g(I)/K_g(II) from the ideal value of 2. Also, the σ_e determined for the regime I is considerably lower than the σ_e for regime III and II.

When the values of σ_e are compared to the ones determined from lamellar thickness studies listed in Table 5.2.2, a considerable difference can be observed. σ_e values determined from regime theory are always higher than the ones from the SAXS analysis. σ_e determined from the regimes III and II are nearly double, while the σ_e values from regime I are close the σ_e determined from Gibbs–Thompson plot. Regime I which occurs at very low degrees of supercooling is expected to have more adjacent re–entry folds than regimes II and III, and therefore it fits better the assumptions of the secondary nucleation model. However, σ_e results from the regime theory indicate that the γ–phase has higher value of σ_e when compared with the α–phase. This contradicts the results from the lamellar thickness analysis, which showed decrease in σ_e values when changing from α– to γ–crystal growth.

Table 5.2.7. Crystal growth kinetic data for studied random propylene–ethylene copolymers.

Sample	α–(110) growth plane							γ–(001) growth plane						
	$K_g \times 10^5$ (K^2)	regime	ΔT (^oC)	ratio	$\sigma\sigma_e$ erg^2/cm^4	σ_e erg/cm^2	q kJ/mol	$K_g \times 10^5$ (K^2)	regime	ΔT (^oC)	ratio	$\sigma\sigma_e$ erg^2/cm^4	σ_e erg/cm^2	q kJ/mol
iPP2.62	2.808	I	53	1.49	683	59.6	24.7	2.478	I	51	1.46	513	62.5	25.8
	1.883	II	58	2.19	916	79.9	33.1	1.702	II	56	2.21	705	85.8	35.5
	4.115	III			1001	87.3	36.1	3.758	III			779	94.8	39.2
iPP4.38	3.024	I	53	1.43	743	64.8	26.8	2.960	I	53	1.42	617	75.1	31.0
	2.113	II	64	1.99	1039	90.6	37.5	2.091	II	62	1.98	871	106.1	43.8
	4.211	III			1035	90.2	37.4	4.138	III			862	105.0	43.4
iPP10.45	2.621	I	53	1.64	654	57.0	23.6	2.406	I	50	1.63	510	62.1	25.7
	1.595	II	58	2.47	795	69.3	28.7	1.474	II	57	2.50	625	76.1	31.4
	3.935	III			981	85.6	35.4	3.683	III			781	95.1	39.3
iPP15.57	2.353	II	75	1.79	1202	104.8	43.4	2.081	II	71	1.82	903	109.9	45.4
	4.205	III			1074	93.6	38.8	3.790	III			822	100.1	41.4

$\Delta H_{f,\alpha} = 209$ J/g, $\sigma = 11.5$ erg/cm^2
$\Delta H_{f,\gamma} = 150$ J/g, $\sigma = 8.2$ erg/cm^2

Since the location of the regime transitions is controlled by the relative rates of secondary nucleation and surface spreading, any factor which affects either of these rates will alter the temperature at which the particular transition occurs. For the studied copolymers the change in the growth regime can be due to the change in growth phase or morphology change. Figure 5.2.1 shows the γ–phase content as a function of crystallization temperature. The degrees of supercooling that correspond to the regime III/II transition for all four copolymers coincide with the degrees of supercooling at which the γ–crystal content exceeds 50 %. Therefore, the regime III/II transition can be due to the change in the crystal growth front, from α–crystal (110) growth plane to (001) growth plane of the γ–orthorhombic crystal. The degree of supercooling at which regime III/II transition occurs increases with increasing defect content for both sets of copolymers.

For samples that exhibit regime I (iPP2.62, iPP4.38 and iPP10.45), the regime II/I transition was dependent on the degree of supercooling temperature irrespective of the copolymer characteristics. The regime II/I transition was always observed at degree of supercooling of 53 ^{o}C. Observations using polarized light microscopy (Figures 4.8.2–4.8.5) indicated that there were changes in the spherulite morphology with decreasing degree of supercooling. For these three copolymers at $\Delta T \leq 53$ ^{o}C the mostly positive spherulites became mixed, and their texture became more open and coarse.

5.3. High Pressure Crystallization Study

Extensive research on the effects of crystallization pressure on the morphology and melting of the pure γ–crystalline phase of high molecular weight *i*–PP has been conducted by Mezghani.[6] It was confirmed that both elevated crystallization pressures and low degrees of supercooling enhanced the formation of the pure γ–form. Also, based

on the Gibbs free energy approach, a temperature–pressure phase diagram shown in Figure 2.6.2 was constructed for the *i*–PP homopolymer.

In the present study, the influence of the crystallization pressure on the development of α– and γ–phases was investigated. One of the goals of this research was to apply the results from high pressure crystallization of copolymers for further expanding the phase diagram of the *i*–PP homopolymer to include the defect content. The *i*–PP homopolymer sample used in the original study was material with high isotacticity and similar molecular weight (257,000 g/mol) as fractionated copolymers used in this study. ^{13}C NMR spectroscopy showed that the *i*–PP homopolymer had isotactic pentad content of 90.7 %, with 1.26% of structural irregularities. Therefore, the *i*–PP homopolymer can be considered as stereo–copolymer with 1.26 mol% defects.

5.3.1. Formation of γ–phase

In the present study two copolymer fractions iPP2.62 (2.62 mol% ethylene; 5.76 mol% total defects) and iPP4.38 (4.38 mol% ethylene; 11.6 mol% total defects) were used for crystallization at high pressures. The aim of the research was to study the effect of the pressure on the polymorphism of these copolymers. Since it was shown that these random copolymer at atmospheric pressure crystallize in a mixture of α– and γ–phases, it was of interest to investigate whether the pressure will further promote the γ–crystalline phase, as it was the case for the homopolymer.

From the WAXD patterns displayed in section 4.3.2 it is clear that for these copolymers crystallization pressure leads to an increase in the γ–phase formation, and that at low degrees of supercooling pure γ–phase is obtained. Also, for the iPP4.38 copolymer with total defect content of 11.6 mol% pure γ–form was observed even at the lowest crystallization pressure. For this copolymer crystallization at pressures above 88

MPa and temperatures above 140 ^{o}C leads to pure γ–form regardless of the crystallization pressure. This can be seen more clearly in the plot of the γ–phase content as a function of crystallization pressure shown in Figure 5.3.1 (a) and (b). Therefore, increasing ethylene content shifts the onset of pure γ–phase formation in these propylene–ethylene copolymers to lower values of the temperature.

The effect of the total chain defects on the stability of α– and γ–forms of the random propylene–ethylene copolymers can be examined by the Gibbs free energy approach. This analysis requires calculation of Gibbs free energies for both phases with the following equation:

$$\Delta G = \Delta H_{\mathrm{f}} - T\Delta S \tag{5.3.1}$$

From the equation (5.3.1) it is evident that two parameters are needed for calculating the ΔG as a function of temperature, that is the change in the heat of fusion, ΔH_{f}, and the change of entropy, ΔS. The entropy change can be calculated from the equilibrium condition, where $\Delta G = 0$ and $T = T_{\mathrm{m}}^{\,0}$, as follows:

$$\Delta S = \frac{\Delta H_{\mathrm{f}}}{T_{\mathrm{m}}^{0}} \tag{5.3.2}$$

In the Gibbs free energy analysis, the phase with the lower free energy at a given crystallization pressure is more stable. Consequently, for the copolymers the equilibrium melting temperatures and heat of fusion of both phases as a function of crystallization pressure and total defect content have to be evaluated. The $T_{\mathrm{m}}^{\,0}$ of the α–phase of these copolymers crystallized at atmospheric pressure was discussed in section 5.2.3.3. In the following sections the $T_{\mathrm{m}}^{\,0}$ of the γ–form as a function of crystallization pressure will be estimated. Also, the ΔH_{f} of both phases as a function of crystallization pressure and defect content will be determined using the Clapeyron equation.

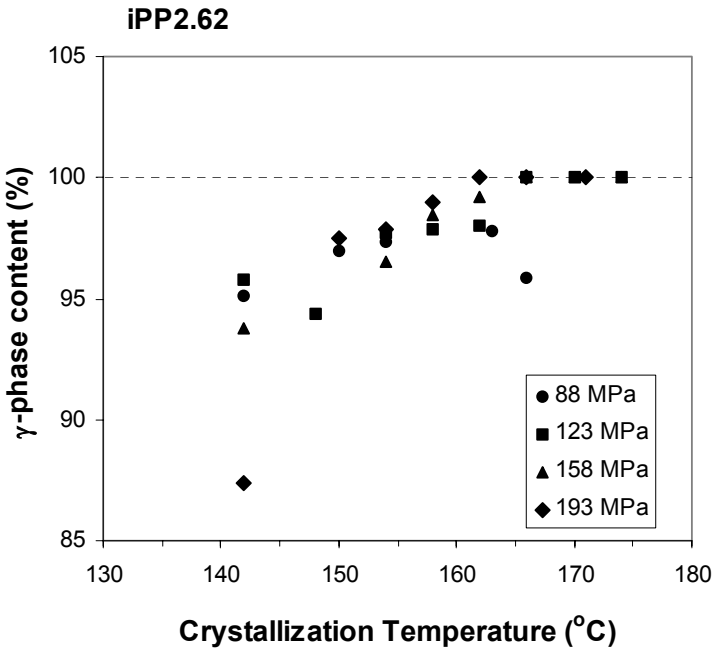

(a)

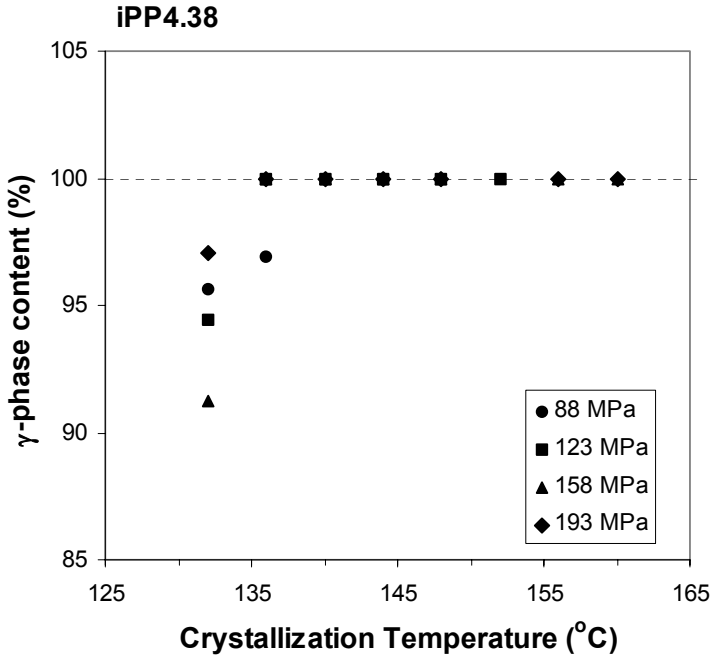

(b)

Figure 5.3.1. Content of the γ–phase of (a) iPP2.62 and (b) iPP4.38 as a function of the crystallization temperature and pressure.

5.3.2. Morphology of γ–phase from SAXS

Crystal characteristics of the copolymers iPP2.62 and iPP4.38 calculated using the self–correlation triangle method of the 1D correlation function are listed in Tables 4.6.5–4.6.12. In addition, their lamellar thickness is plotted in Figures 5.3.2 and 5.3.3 as a function of crystallization temperature and pressure. It can be observed that at constant crystallization pressure the lamellar thickness increases with crystallization temperature. Moreover, at constant crystallization temperature the lamellar thickness decreases with increasing crystallization pressure.

The introduction of pressure at constant crystallization temperature behaves similarly to increasing the degree of supercooling. This is expected to result in lower degree of crystallinity. The change in the degree of crystallinity with crystallization pressure and temperature for the two copolymers is shown in Figures 4.3.19 and 4.3.20. It can be observed that for given copolymer sample the crystallinity does not change significantly with increasing crystallization temperature.

For copolymer iPP2.62 crystallinity decreases slightly with crystallization temperature (Figure 4.3.19). On the other hand, for copolymer iPP4.38 the degree of crystallinity at first drops with increasing crystallization temperature, but at higher crystallization temperatures it levels off (Figure 4.3.20). The drop in the crystallinity corresponds to the decrease in α–phase content and increase in γ–phase content, with the crystallinity leveling off at the onset of the pure γ–crystal formation.

Since the γ–crystals content increases with increasing crystallization pressure, the decrease in the lamellar thickness with increasing pressure can be attributed to the differences in the crystallographic characteristics of the α– and γ–forms. For identical lamellar thickness the length of the α–phase stem is 0.77 of the γ–phase stem length, because α–stems form an angle of 9^o with the lamellar surface, while for the γ–stems this angle is 40^o. Therefore, for a fixed crystallization temperature and average length of the

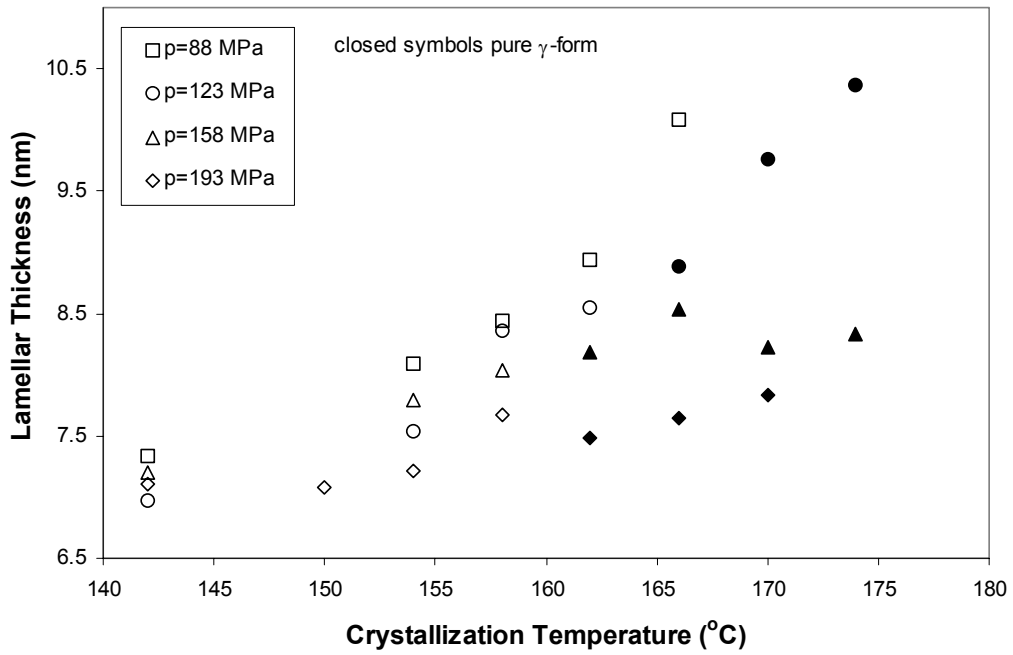

Figure 5.3.2. Lamellar thickness of copolymer iPP2.62 as a function of crystallization temperature and pressure.

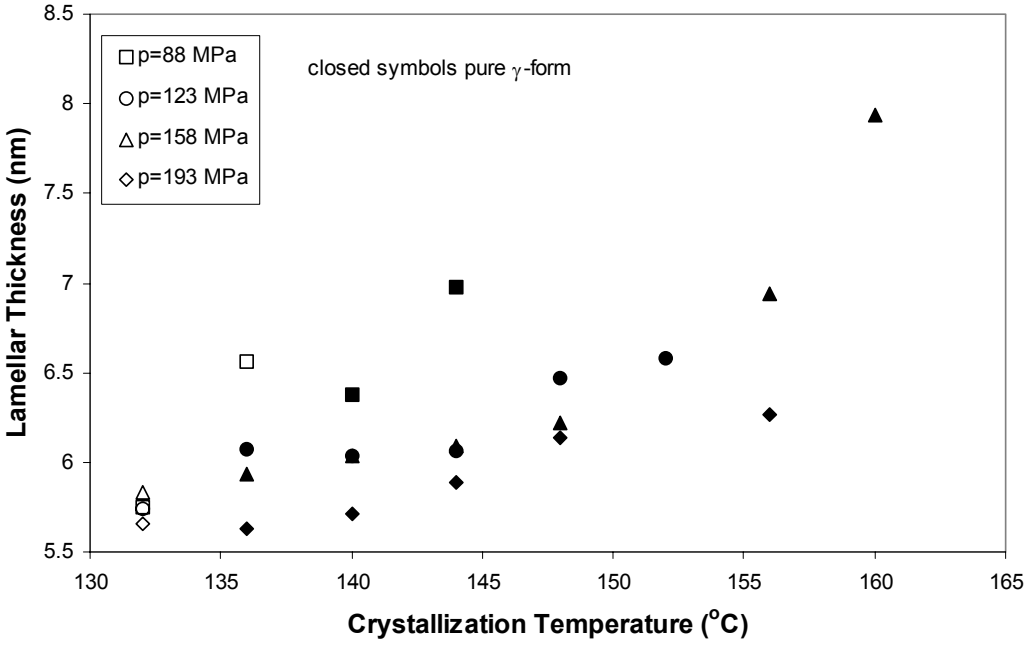

Figure 5.3.3. Lamellar thickness of copolymer iPP4.38 as a function of crystallization temperature and pressure.

angle is 40°. Therefore, for a fixed crystallization temperature and average length of the crystallizable sequences, γ–phase crystals will have lower lamellar thickness compared with α–crystals. This can be observed for copolymer iPP2.62 crystallized at p_c= 193 MPa. With increasing crystallization temperature, lamellar thickness increases until there is a drop at T_c = 162 °C, temperature at which WAXD analysis shows pure γ–form. With further increasing of the temperature lamellar thickness of the pure γ–form again starts to increase.

Figures 5.3.4 and 5.3.5 show the change in transition layer thickness of the copolymers as a function of crystallization temperature and pressure. The thickness of the transition layer for both copolymers decreases with increasing crystallization temperature, similar to the samples crystallized at atmospheric pressure. The increase of the lamellar thickness with increasing crystallization temperature occurs at the expense of the transition layer, causing its thickness to decrease.

The electron density difference $\Delta\eta$, between the crystalline phase, η_c, and the amorphous phase, η_a, was calculated from the invariant as outlined in section 2.8.2. In Figures 5.3.6 and 5.3.7 the electron density difference of the copolymers is plotted as a function of the crystallization temperature and pressure. It can be seen that for the copolymers regardless of the composition the electron density difference does not change significantly with crystallization temperature. On the other hand, for a given copolymer applied crystallization pressure led to an increase in $\Delta\eta$. Crystallization under high pressure increases the density of the crystalline phase, hence increasing the $\Delta\eta$. Also, on average copolymer iPP2.62 had higher $\Delta\eta$ compared with the copolymer iPP4.38.

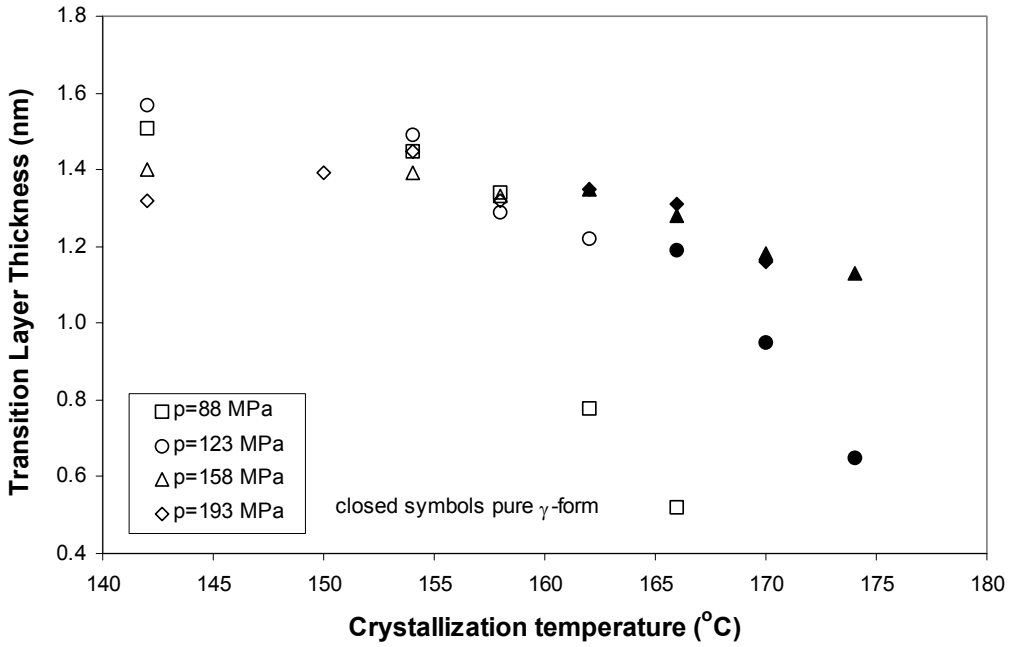

Figure 5.3.4. Transition layer thickness of iPP2.62 as a function of crystallization temperature and pressure.

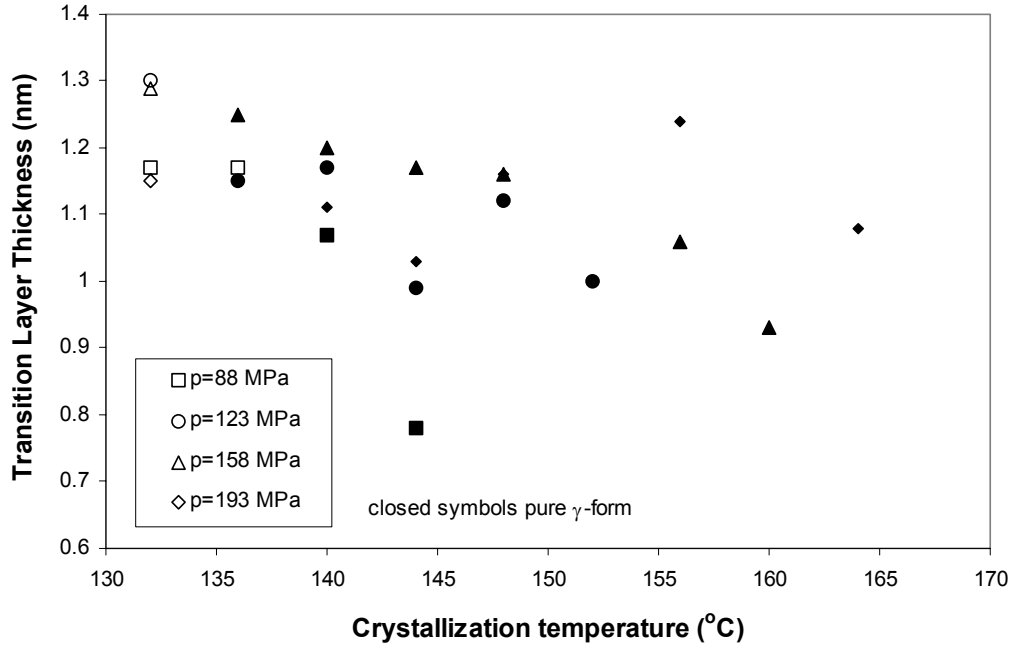

Figure 5.3.5. Transition layer thickness of iPP4.38 as a function of crystallization temperature and pressure.

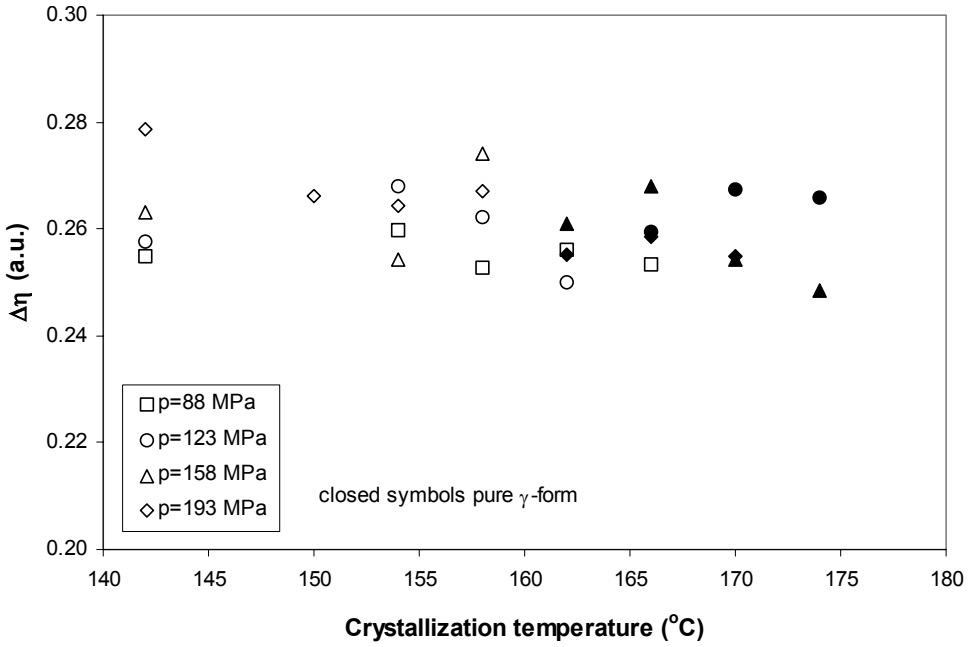

Figure 5.3.6 Electron density difference of iPP2.62 samples as function of the crystallization temperature and pressure.

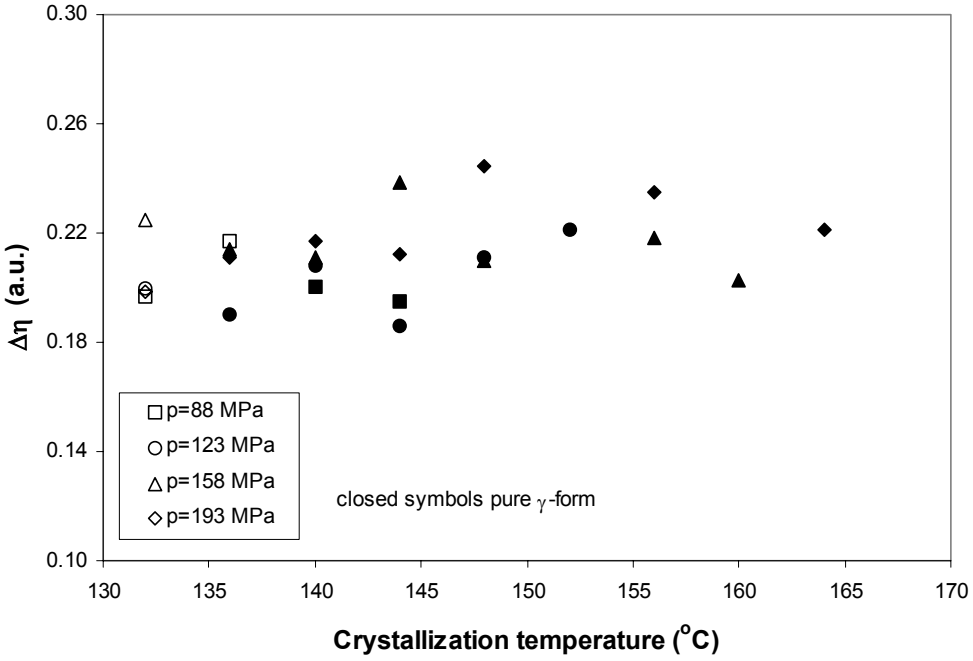

Figure 5.3.7. Electron density difference of iPP4.38 samples as function of the crystallization temperature and pressure.

5.3.3. Morphology of the copolymer samples from SEM

Random propylene–ethylene copolymer samples crystallized at atmospheric pressure generated mixture of α– and γ–crystals, as determined from WAXD studies. As outlined in the section 2.2.2, α–form is the most common crystal phase of *i*–PP with monoclinic crystal unit cell. On a morphological level, α–form lamellae exhibit an unique lamellar branching characterized by a constant angle of 80^{o} between the radial (parent) lamellae and the tangential (daughter) lamellae. γ–crystal phase was first identified as triclinic with unit cell similar to that of the α–form.[40] Bruckner and Meille[46] reevaluated the triclinic unit cell and noted that it is a sub–cell of a larger face–centered orthorhombic unit cell. The proposed new unit cell consists of bilayers of parallel molecules with chain axes inclined at 80^{o} between the bilayers. It has been shown that γ–crystal form has an epitaxial relationship with the α–form such that either can grow onto lamellae of the other phase.[49,50] In general, α–form is observed to grow first, followed by epitaxial growth of the γ–form at an angle of 40^{o}. Possible self–epitaxial growth of the γ–lamellae was observed for 100% γ–phase *i*–PP crystallized at 200 MPa.[39]

SEM micrographs of the copolymer iPP2.62 crystallized at atmospheric pressure and crystallization temperatures 124 and 126 ^{o}C showed the typical polymer spherulitic structure as seen in Figures 4.8.6 and 4.8.8. The long and radially oriented lamellae that radiate from the spherulite center are attributed to the growth of the α–crystals, while the low angle branches are consistent with the epitaxial growth of γ on α–crystals. The absence of the cross–hatching (α–α branching) is in good agreement with the findings reported by Campbell and Phillips[38] that showed no cross–hatching in *i*–PP samples with more than 60 % γ–crystals.

For these copolymer samples both the 'parent' and the 'daughter' lamellae exhibit similar thicknesses. This observation supports the findings from the SAXS experiments that showed that α– and γ–phase lamellae that crystallize isothermally contribute to one

lamellar thickness distribution (section 5.2.3.4). Although α– and γ–lamellae have different average thicknesses, the overlapping of their crystal thickness distributions does not generate bimodal SAXS pattern. Figure 4.8.10 shows another, much thinner lamellae population that according to SAXS and high temperature WAXD experiments has formed during the quenching.

The most interesting feature on the Figures 4.8.6–4.8.11 is the feather–like structure that was first reported by Mezghani and Phillips[39] for the pure γ–form of homopolymer *i*–PP isothermally crystallized at 200 MPa. Authors proposed that the growth of these structures can occur by branching of γ–lamellae on a radially grown γ or α–lamella, or by a self–epitaxial growth of γ–lamellae, as shown in Figure 5.3.8. This is the first time that this structure has been observed for propylene–ethylene copolymers and in samples with less than 100 % γ–phase. However, unlike for the homopolymer, the feather–like features in the copolymers are not dominant structures in the spherulite morphology. For the copolymer sample iPP2.62 the average width of the feathers is 1 to 2 μm, which is considerably lower than 5-6 μm found for the homopolymer. Also, feathers do not originate from the spherulite center, but rather form by epitaxial growth on the radial lamellae.

The manner in which the feathers develop in the copolymer samples is illustrated in Figure 4.8.6 as indicated with the numbers and arrows. At first the parent α or γ–phase lamella labeled as '1' grows radially from the center of the spherulite. At the point 2 the 'daughter' feather–like structure grows epitaxially on the radial lamellae. The growth of this feather is interrupted in point 3 where it splays out and new complete feather–like structure grows from each side of the 'daughter' feather, hence this indicated a possible γ–γ epitaxial growth. At the point labeled 4 there is further growth and propagation of the new 2 sets of feathers. Therefore, it has been shown that both α–γ and γ–γ epitaxial lamellar growth occurs during crystallization of propylene–ethylene copolymers.

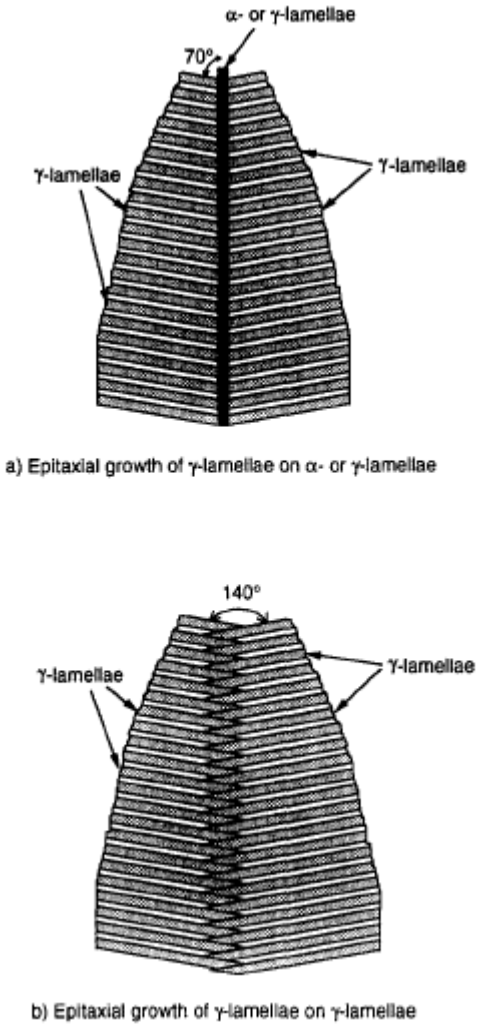

Figure 5.3.8. Schematic representation of the potential growth mechanism of the feather–like structure (from Mezghani and Phillips[39]).

SEM micrographs of copolymer samples crystallized into 100 % γ–phase at the highest pressure of 193 MPa revealed that there is a change in spherulite structure of propylene–ethylene copolymer samples with increasing crystallization pressure. Low magnification micrographs showed that the spherulite morphology of the copolymers observed at atmospheric pressure is absent for high pressure crystallized samples. This is observed for both copolymer iPP2.62 and iPP4.38 in Figures 4.8.12 and 4.8.15, respectively. High pressure crystallization of these copolymer samples produced elongated ellipsoidal structures that did not grow radially, although they did periodically branch. Their orientation in the sample is mainly in two directions, and WAXD experiments showed that there is some orientation in the (001) direction. Similar thick cigar-shaped structures have been reported for *cis*-polyisoprene crystallized at pressures above 3 kbar.[148]

Spherulitic morphology has been observed for 100 % γ–crystals obtained by crystallization of low molecular weight homopolymer[48] and for high molecular weight *i*–PP crystallized at high pressure.[39] This indicates that the development of pure γ–phase or the application of the crystallization pressure alone are not responsible for the lack of spherulitic morphology of the propylene–ethylene copolymers crystallized at high pressures. Therefore, the combination of the chain defects and crystallization pressure profoundly affects the morphology of the copolymers. Increasing the crystallization pressure elevates the melting point of the copolymers, which in turn can affect crystallization kinetics and morphology by increasing the degree of supercooling at a given crystallization temperature.

AFM micrographs shown in Figures 4.8.16 and 4.8.17 were used to measure the thickness of these lenticular or cigar-shaped crystal structures, as well as the angles between the branches. The average thickness of these species varies between 100 and 200 nm, however, there are crystals with thickness between 600 and 700 nm. These crystal structures branch at angles of ~ 15, 80 and 115^{o}.

The absence of spherulitic structures and the occurrence of the thick single crystal–like can be explained by the uniqueness of the γ–orthorhombic crystal phase, and the γ–γ orthorhombic phase homoepitaxial branching in the absence of α-crystal phase. Epitaxial growth of *i*-PP chains can occur at angles of 80^o and 100^o relative to each other, as reported by Lotz and Wittman.[30] The contact plane is the growth face that has pattern of methyl groups that allows deposition of a layer of isohiral chains at this specific angle.

Figure 5.3.9 shows the schematic representation of the epitaxial growth of γ on γ–phase crystals. The growth plane of the γ–orthorhombic phase is (001) plane, which is also the contact plane for the epitaxial growth and branching. γ–γ branching does not occur on the lateral surfaces, as was the case for the α–phase. From Figure 5.3.9 it can be seen that the contact angles between γ–γ branches are 80^o or 100^o, and 20^o or 160^o. These angles match well the experimentally determined angles between branches.

Since the branching can occur only on the growth plane, every epitaxial deposition of chain on the growth front will stop or retard the growth of the existing crystal and prevent the forming of the spherulitic structure. This is considerably different from the α–α or α–γ epitaxial growth where the branching occurs on the lateral surfaces, while the parent lamella continues to grow radially.

5.3.4. Equilibrium Melting Temperature of γ–phase

Copolymers iPP2.62 and iPP4.38 that were crystallized at high pressures were analyzed in DSC at atmospheric pressure (Figures 4.4.13–4.4.20). Melting endotherms exhibited multiple melting, although less prominent as samples crystallized at atmospheric pressure. For the iPP2.62 copolymer, all endotherms show very small melting peak at a temperature above the main melting peak. Based on the peak assignment performed on the samples crystallized at atmospheric pressure and using the

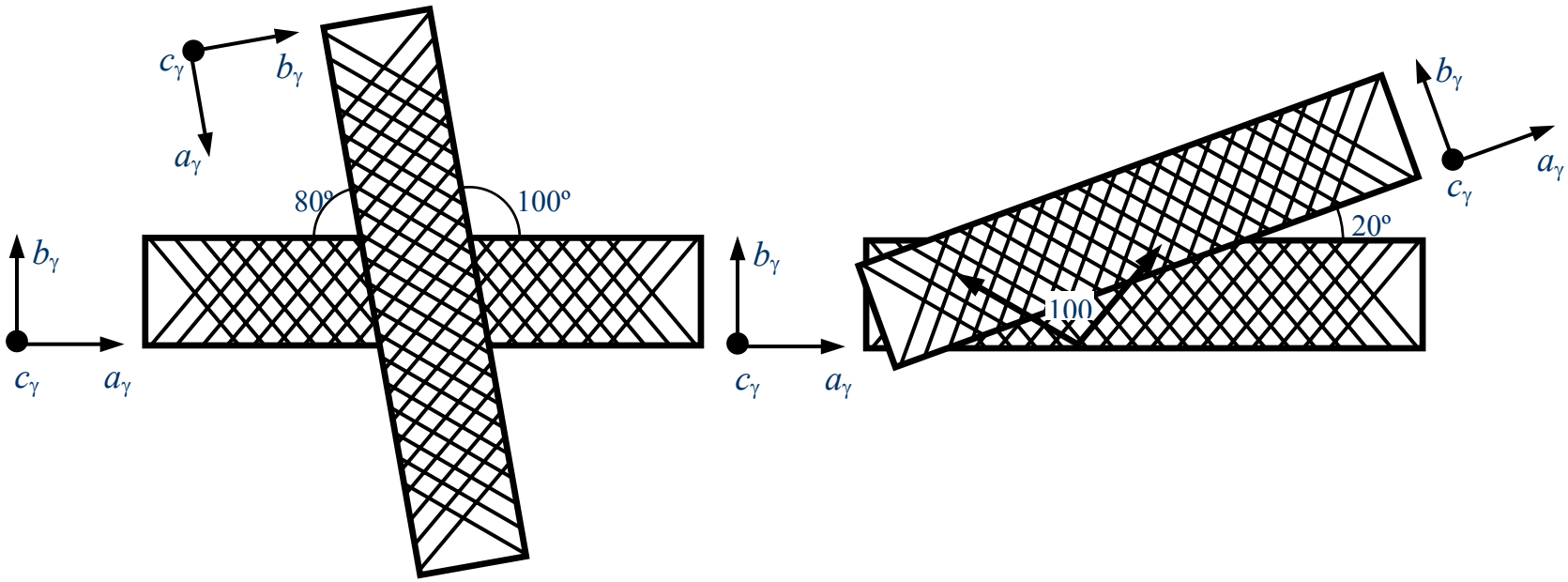

Figure 5.3.9. Schematic representation of the γ–γ orthorhombic homoepitaxial growth.

HTXRD analysis, we have assigned the main melting peak to the melting of the γ–phase, and the small high–temperature melting peak to the α–phase. This peak shows even for samples for which WAXD experiments do not show existence of α–phase. A peak deconvolution was performed for all samples showing multiple melting endotherms, and the fraction of each melting peak was calculated as shown in Figure 5.2.3. It was found, for samples that did not show α–phase peak in WAXD, that the DSC α–peak is less than 1% of the overall peak area. We conclude that the DSC instrument is sensitive enough to register the melting of small quantities of α–phase crystals that are below the detecting threshold of the WAXD. Similar DSC melting endotherms of *i*–PP samples crystallized at high pressure and melted at atmospheric pressure were reported by Mezghani,[6] and they also contained a very small high temperature peak, but the author did not comment on them. On the other hand, the iPP4.38 copolymer samples crystallized at the lowest supercoolings at pressures of 158 and 193 MPa does not show additional small endotherm above the main endotherm. This confirms well the results from WAXD analysis.

Samples crystallized at the highest temperatures regardless of the crystallization pressures exhibited broad melting endotherm at around 130 ^{o}C that increased in height with increasing crystallization temperature. This peak, in accordance with the results from the atmospheric crystallization, is due to the melting of thin crystals that are formed on quenching. The material that was not able to crystallize during the isothermal period of the crystallization crystallizes in the time frame when the crystallization temperature has been lowered to room temperature. In the high pressure experimental setup the maximum rate of cooling was 4–7 ^{o}C/min because of the bulkiness of the high pressure cell. This rate cannot be considered as quenching, and some of the material will further crystallize during the cooling. Since the pressure was attained during the whole process of cooling to room temperature, there was no melting–recrystallization transformation from γ– to α–phase during the cooling.

In order to calculate the equilibrium melting temperatures at the different crystallization pressures we need the actual melting temperatures at the corresponding pressures. DSC experiments from which melting temperatures were determined were at atmospheric pressure. To account for the change of melting temperature with pressure, all of the melting temperatures determined from DSC were corrected for the pressure. The correction was based on the experimental determination of the dependence of the melting temperature on the crystallization pressure by Zoller *et al*.[149] They have found that in the pressure range from 0 to 200 MPa the melting temperature of the isotactic polypropylene increases by 0.285 ^{o}C/MPa. These experiments were performed on *i*–PP with high isotacticity (> 96 %) and molecular weight ~300K.

Equilibrium melting temperatures of samples crystallized at high pressures were determined from Gibbs–Thompson plots of T_m versus inverse lamellar thickness. Peak temperature was chosen for the melting temperature, and for samples that had distinct α– and γ–phase melting peak, attempt has been made to use both temperatures for estimating the T_m^0 of α– and γ–phases. Gibbs–Thompson plots for the γ–phase of the iPP2.62 and iPP4.38 are shown in Figures 5.3.10 and 5.3.11. Equilibrium melting temperatures determined from Gibbs–Thompson plots for iPP2.62 copolymer γ–phase at 88, 123, 158 and 193 MPa are 203.4, 212.5, 220.2 and 229.6 ^{o}C, respectively. Equilibrium melting temperatures at the equivalent crystallization pressures for γ–phase of iPP4.38 are 192, 198.4, 211.2 and 217.1 ^{o}C, respectively. It should be mentioned that for some of the curves in these plots there were only four experimental points available for extrapolation. Although this is unfortunate, when crystallized at low pressures only limited number of samples developed pure γ-form so more experimental points could not be obtained.

Using the T_m versus inverse lamellar thickness plot for calculating T_m^0 of the α–phase in the pressure crystallized samples would assume that both phases have the same average crystal thickness. SAXS Lorentz corrected data and 1D correlation function showed only one distribution of lamellar thicknesses. The content of the α–phase in these samples was very small, with the maximum amount of 5 % detected in DSC

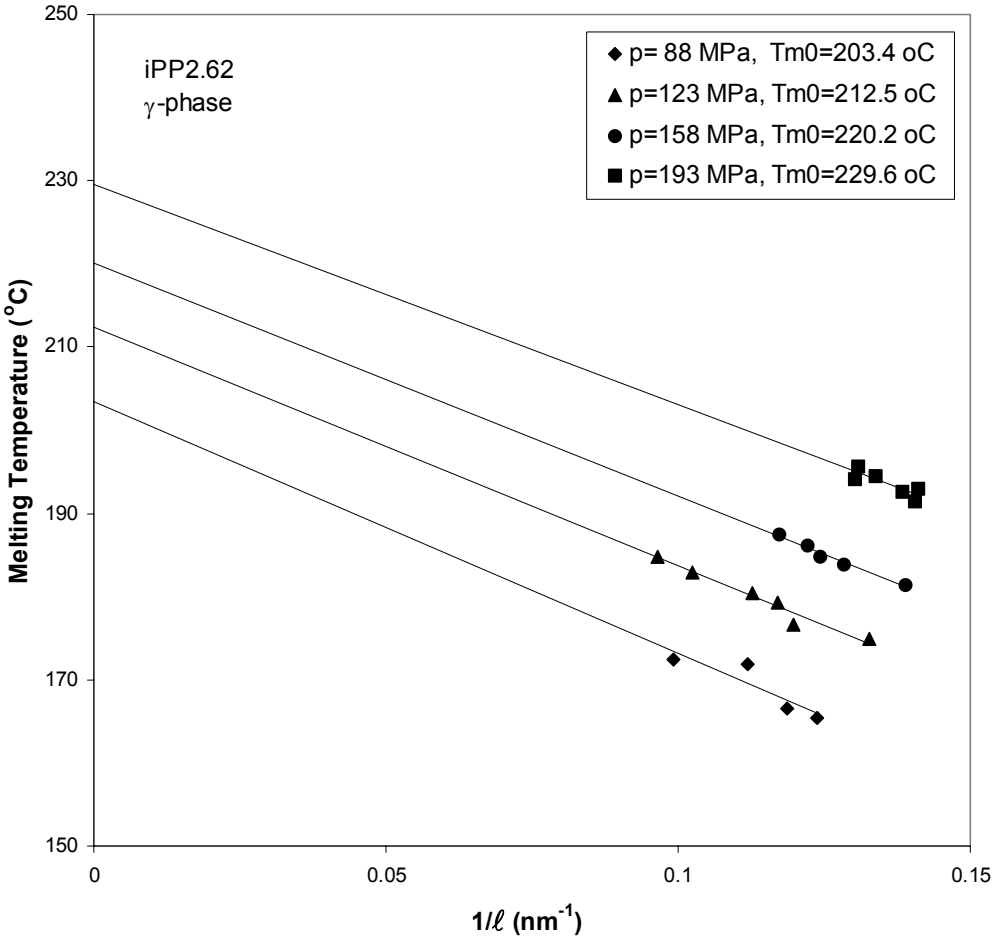

Figure 5.3.10. Gibbs–Thompson plot of melting temperature of γ–phase as a function of inverse lamellar thickness and crystallization pressure; sample iPP2.62 (total defect 5.76 mol%).

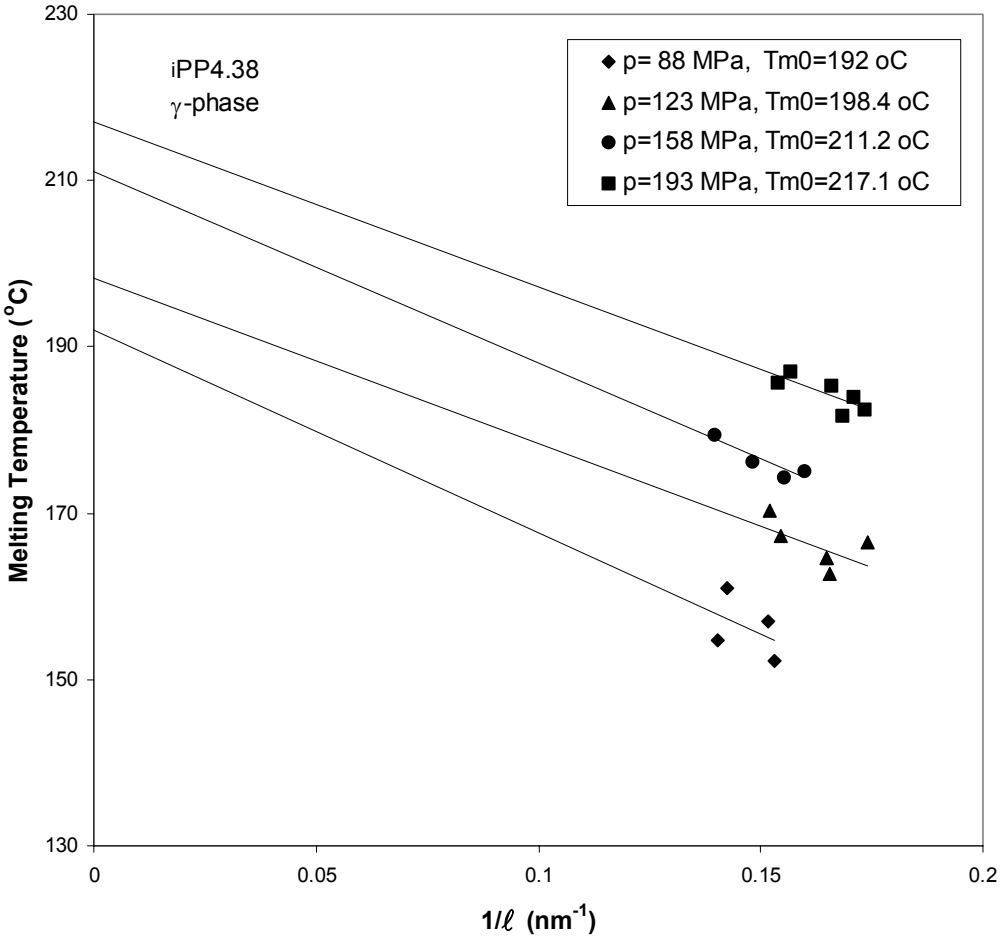

Figure 5.3.11. Gibbs–Thompson plot of melting temperature of γ–phase as a function of inverse lamellar thickness and crystallization pressure; sample iPP4.38 (total defect 11.60 mol%).

measurements. In absence of more reliable data about the α–crystal thickness, Hoffman–Weeks plot was used for determining the T_m^0 of the α–phase generated at elevated pressures. This plot for iPP2.62 samples is shown in Figure 5.3.12, and the obtained equilibrium melting temperatures at 88, 123, 158 and 193 MPa are 220.6, 209.0, 215.5 and 223.7 ^oC, respectively. In the case of the copolymer iPP4.38 there were not enough melting data points for the α–phase of the pressure crystallized samples for similar analysis to be performed.

When the melting temperatures of iPP2.62 copolymer samples crystallized at high pressure and melted at atmospheric pressure are plotted on one plot (shown in Figure 5.3.13), they extrapolate to 182 ± 1.5 ^oC. This temperature is the equilibrium melting temperature of γ–phase of the iPP2.62 copolymer at atmospheric pressure. Similar extrapolations for the iPP4.38 γ–phase are shown in Figure 5.3.14, with the result being $T_m^0 = 170.7 \pm 1.7\ ^oC$.

5.3.5. Determination of Heat of Fusion

The pressure dependence of the equilibrium melting points can be used to calculate the heat of fusion of the polymer crystals through the application of the Clapeyron equation, which defines the equilibrium between two phases:

$$\frac{dT}{dp} = \frac{T}{\Delta H_f}\left(\nu_a - \nu_c\right) \tag{5.3.1}$$

where T is the temperature at which the transformation occurs, and ν_a and ν_c are the specific volumes in cm^3/g of the melt and the crystal at the transformation point, respectively. In the case of melting of polymer crystals, T can be defined as the equilibrium melting temperature, and the specific volume changes can be related to density changes, so the above equation becomes:

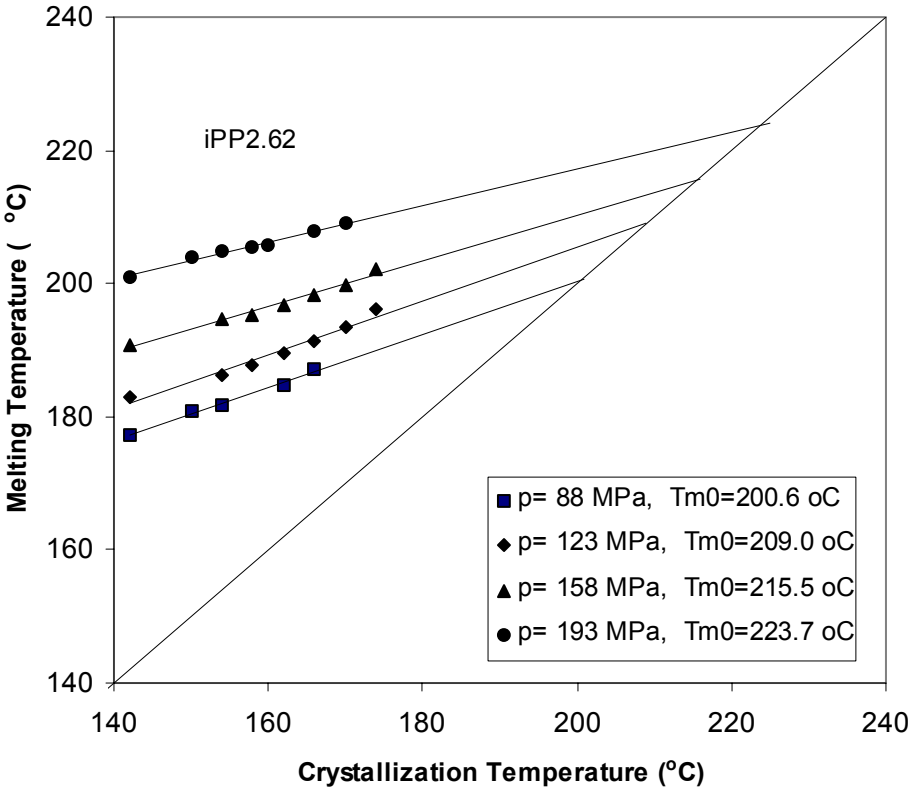

Figure 5.3.12. Hoffman–Weeks plot of melting temperature of α–phase as a function of inverse lamellar thickness and crystallization pressure; sample iPP2.62 (total defect 5.76 mol%).

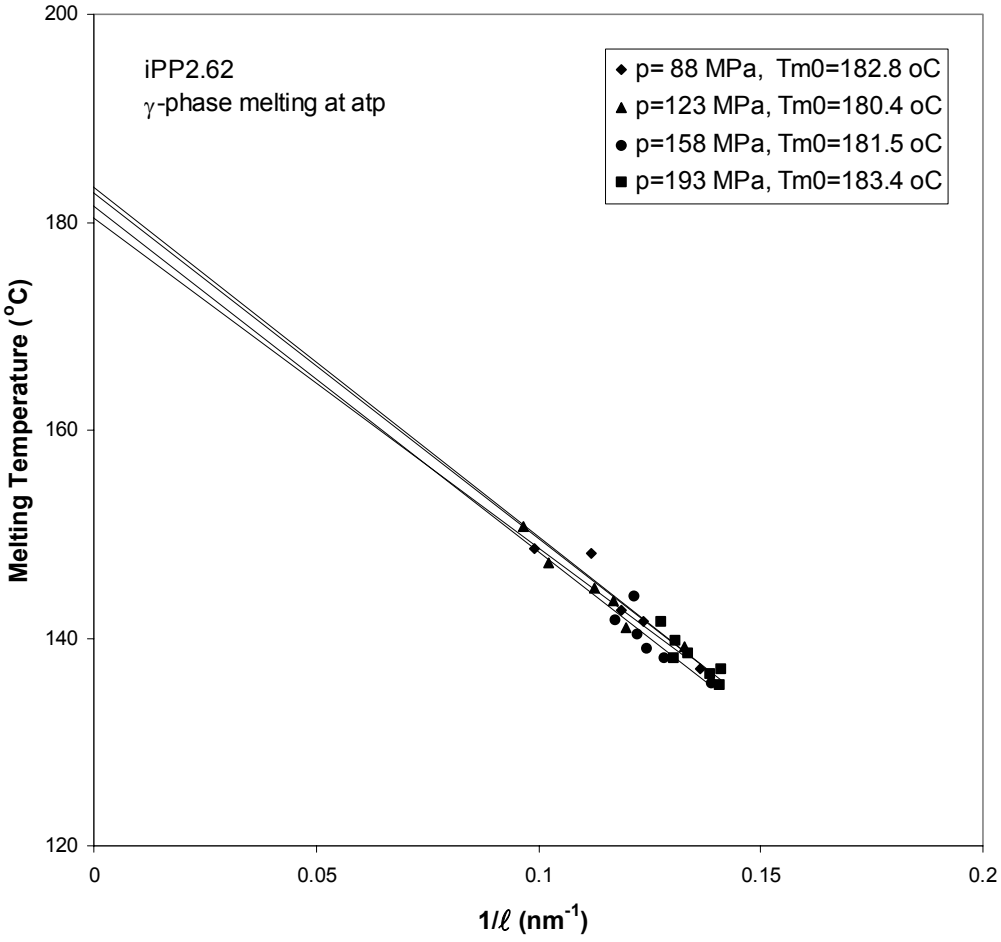

Figure 5.3.13. Gibbs–Thompson plot of melting temperature recorded at atmospheric pressure of γ–phase as a function of inverse lamellar thickness; sample iPP2.62 (total defect 5.76 mol%).

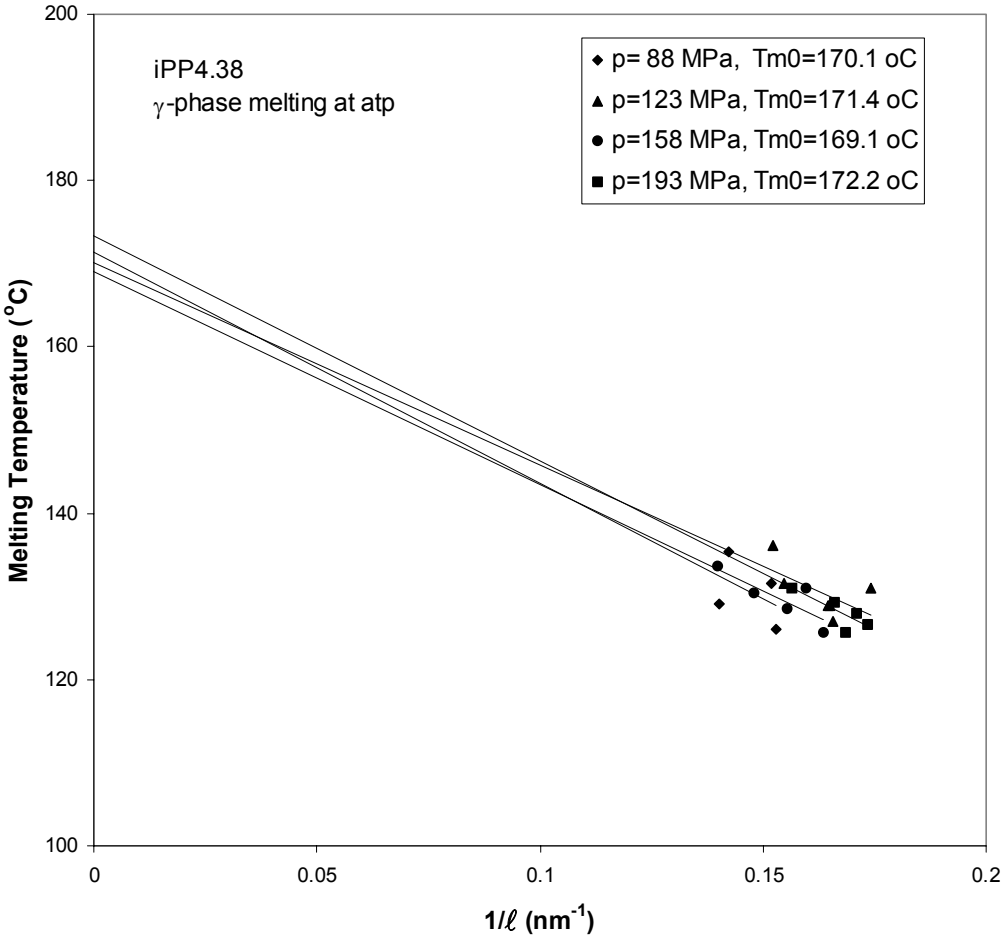

Figure 5.3.14. Gibbs–Thompson plot of melting temperature recorded at atmospheric pressure of γ–phase as a function of inverse lamellar thickness; sample iPP4.38 (total defect 11.60 mol%).

$$\frac{dT_m^o}{dp} = \frac{T_m^0}{\Delta H_f}\left(\frac{\rho_c - \rho_a}{\rho_c \rho_a}\right) \qquad (5.3.2)$$

where ρ_a and ρ_c are the melt and crystal densities (in g/cm^3), respectively.

The plot of the equilibrium melting temperature dependence on the crystallization pressure of the γ– and α–phases for the iPP2.62 copolymer is shown in Figure 5.3.15. These dependencies are linear, and the intercepts of the lines at p_c = 0 MPa are the T_m^0 of the α– (172.6 ^{o}C) and γ–form (182 ^{o}C) of the iPP2.62 sample. The data in the plots can be represented with the Clapeyron equation, therefore the slopes of the lines are related to the heat of fusion and the density change (the right side of the equation (5.3.2)).

If it is assumed that the heat of fusion does not change with the pressure, then the specific volume change can be expressed in terms of the density difference of the amorphous and crystalline phases. The value of the heat of fusion determined for the iPP2.62 α–phase is 165.0 J/g, and for the γ–phase 143 J/g. The value for the γ–phase is slightly lower than the value of 144.8 J/g[6] that was determined in the similar fashion for the homopolymer. Also, the value of 165 J/g is lower than the value of 167 J/g widely reported in the literature for the α–phase of the homopolymer.

The equivalent plot of this dependence for the γ–phase of the iPP4.38 is presented in Figure 5.3.16. Similar calculations were performed for he iPP4.38 copolymer samples, but in this case only for the γ–phase, because of the absence of the melting of the α–phase for most of the iPP4.38 samples crystallized at high pressures. The calculated value of the heat of fusion for the γ–phase of iPP4.38 was 141 J/g.

In the earlier discussion in section 5.2.4 it was established that there is partial defect incorporation in the copolymer crystals. This phenomenon leads to a reduction in the density and the heat of fusion of these copolymers. The reduction of the heat of fusion with increasing ethylene content has been reported for both unfractionated[75,79] and fractionated[72] Ziegler–Natta, as well as metallocene[80,82] propylene copolymers. These

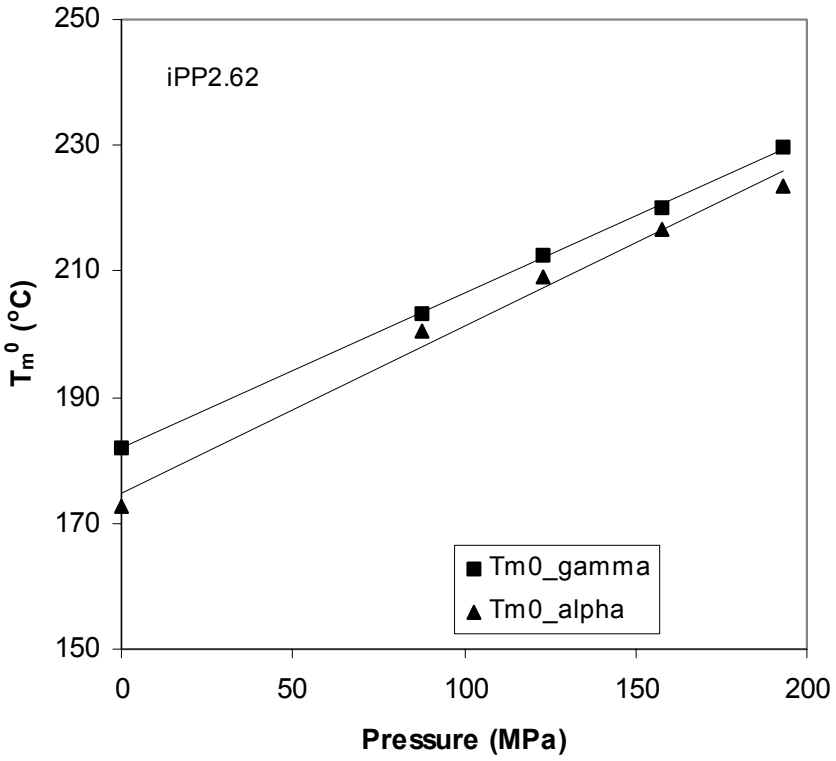

Figure 5.3.15. Equilibrium melting temperature for α– and γ–phase as function of crystallization pressure; sample iPP2.62 (total defect 5.76 mol%).

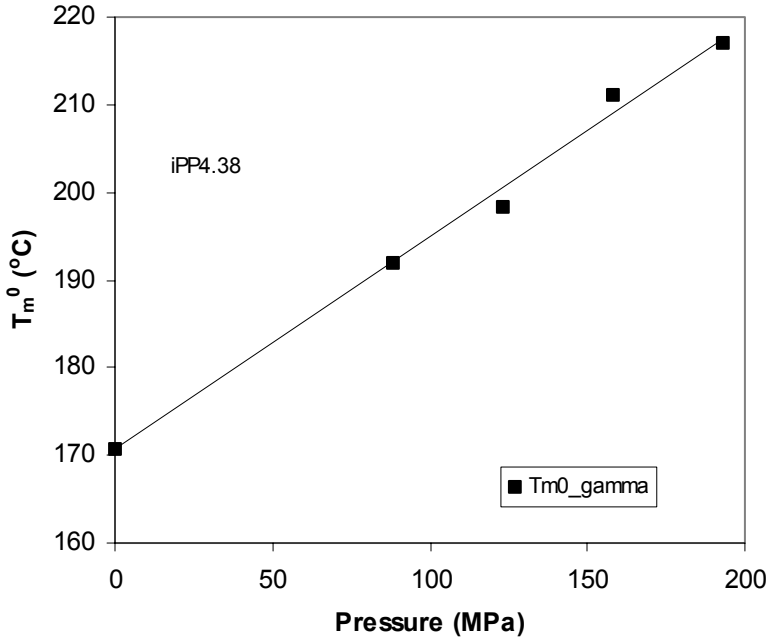

Figure 5.3.16. Equilibrium melting temperature for the γ–phase as function of crystallization pressure; sample iPP4.38 (total defect 11.60 mol%).

values for the heat of fusion are in a good agreement with the ΔH_f of the homopolymer reduced for the comonomer content.

In the earlier discussion in section 5.2.4 it was established that there is partial defect incorporation in the copolymer crystals. This phenomenon leads to a reduction in the density and the heat of fusion of these copolymers. The reduction of the heat of fusion with increasing ethylene content has been reported for both unfractionated[75,79] and fractionated[72] Ziegler–Natta, as well as metallocene[80,82] propylene copolymers. These values for the heat of fusion are in a good agreement with the ΔH_f of the homopolymer reduced for the comonomer content.

The method for determining the heat of fusion based on the Clayperon equation when the density changes with pressure is very straightforward, and has been used to describe the melting behavior of many polymers.[150-152] All parameters that are needed for the calculation of the heat of fusion are obtainable from pressure-volume–temperature (PVT) data for the corresponding polymers, except for the crystal volume at the melting point. For this, data for the degree of crystallinity close to the melting point are needed.

Since no published PVT data for random low ethylene content propylene copolymers could be found, the PVT data for the *i*–PP homopolymer that were published by Zoller *et al.*[149] were used. The previous homopolymer study[6] also used these PVT diagrams, and the same procedure will be followed here for consistent data treatment. These PVT measurements, shown in Figure 5.3.17, were performed on a highly isotactic polypropylene with $M_w \approx 300{,}000$. They were based on isothermal measurements progressing from low to high temperatures in 20 MPa pressure intervals.

Even though the melting curves shown in Figure 5.3.17 do not represent the equilibrium melting temperature, densities of the amorphous and the crystalline materials can be determined from the volume changes if the crystallinity of the samples is known. However, the crystallinity values for these samples were not available, so for this reason the crystallinity of 65 % was assumed for all samples.

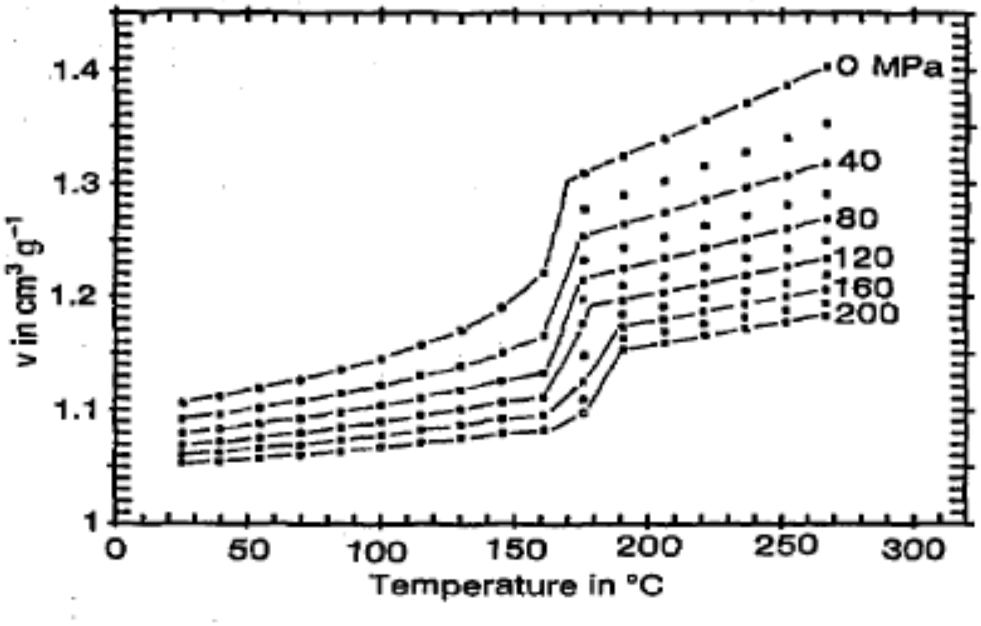

Figure 5.3.17. PVT data for *i*–PP reported by Zoller *et al*.[149]

When the changes in the densities are estimated as a function of pressure, the heat of fusion can be calculated from the Clapeyron equation. Table 5.3.1 lists the parameters needed for this analysis for several crystallization pressures. Crystal densities of the copolymers were scaled down proportionally to account for the effect of the ethylene content on the copolymer density. The heat of fusion of the α– and γ– phase was determined as the best value that generates similar equilibrium melting temperatures as the experimental T_m^0. Table 5.3.2 lists the thermodynamic parameters of the α– and γ–crystalline forms for the copolymers and *i*–PP obtained from the Clapeyron analysis.

Results of the Clapeyron analysis for sample iPP2.62 produced $\Delta H_{f,\alpha}$ = 188 J/g and $\Delta H_{f,\gamma}$ = 175 J/g, while for iPP4.38 the value of $\Delta H_{f,\gamma}$ was 164 J/g. One can make an observation that analogous to the *i*–PP homopolymer, there are two different ΔH_f values

Table 5.3.1. Specific volumes and densities for iPP2.62 copolymer

Data for homopolymer extracted from Figure 5.3.17							
Δp (MPa)	v_a (cm^3/g)	v_{tr} (cm^3/g)	v_c (cm^3/g)	ρ_a (g/cm^3)	ρ_c (g/cm^3)		
40	1.261	1.172	1.124	0.7930	0.8896		
100	1.219	1.142	1.101	0.8203	0.9086		
120	1.212	1.134	1.092	0.8251	0.9158		
160	1.195	1.115	1.072	0.8368	0.9329		
200	1.171	1.097	1.057	0.8540	0.9459		
Data for copolymer iPP2.62 with extrapolated and scaled specific volumes							
Δp (MPa)	v_a (cm^3/g)	v_{tr} (cm^3/g)	v_c (cm^3/g)	ρ_a (g/cm^3)	ρ_c (g/cm^3)	ΔT_m^0	T_m^0 (^oC)[b]
88	1.231	1.184	1.159	0.8122	0.8782	23.8	205.2
123	1.212	1.168	1.144	0.8250	0.8902	31.3	213.3
158	1.193	1.151	1.128	0.8381	0.9025	37.9	219.9
193	1.174	1.134	1.112	0.8517	0.9152	43.5	226.0

a) density values for the copolymer were scaled down by factor of 0.97.

b) determined as the best fit of equation (5.3.2) with ΔH_f = 175 J/g, and T_m^0 = 182 ^{o}C at atmospheric pressure.

Table 5.3.2. Thermodynamic parameters of the α– and γ–crystalline forms for the *i*–PP homopolymer and the copolymers.

Material	phase	T_m^0 (°C)	ΔH_f (J/g)	ρ (g/cm^3)[a]
i–PP homopolymer	α	186.1	209.0 167.0	0.936
	γ	187.2	190.0 150.0	0.933
iPP2.62	α	172.6	188.0 165.0	0.908
	γ	182.0	175.0 143.0	0.905
iPP4.38	α	165.7	170.0	0.899
	γ	170.7	164.0 141.0	0.896

a) density values were reduced to account for the effect of the ethylene content. Crystal density dependence on ethylene content was calculated from Hosoda *et al*.[82]

for these copolymers depending on the method of evaluation. For example, these values for $\Delta H_{f,\gamma}$ are 190 and 150 J/g for the homopolymer, 175 and 143 J/g for iPP2.62, and 164 and 141 J/g for the iPP4.38 copolymer. Regardless of the exact accuracy of these estimations, the most important observation is the consistent reduction of the heat of fusion with the increasing ethylene content. For the copolymer iPP4.38 there were not enough experimental data to estimate the value of $\Delta H_{f,\alpha}$. However, for this purpose, based on the observed decreasing tendency of $\Delta H_{f,\alpha}$ value of 170 J/g was suggested for copolymer iPP4.38.

5.3.6. Temperature–Pressure–Composition Phase Diagram

One of the goals of this research was to append the existing *i*–PP α–γ phase diagram to include the effect of the composition on the thermodynamic stability of the phases. For this purpose, the stability of both phases as a function of temperature and pressure was evaluated. By performing the Gibbs free energy analysis in the previous study[6] it was found that the pressure shifts the stability of the γ–phase to lower crystallization temperatures. It was predicted that at atmospheric pressure pure γ–phase is expected to form at a degree of supercooling of only ~ 10 ^{o}C, while the crystallization pressure of 200 MPa shifts this degree of supercooling to a much higher value of ~ 67 ^{o}C. An example of this analysis for the *i*–PP copolymer is shown in Figures 2.6.1 (a) and (b) for atmospheric and 200 MPa crystallization pressure.[6]

To calculate the ΔG for the copolymers two parameters, ΔH_f and T_m^0 of both phases, the latter as a function of crystallization pressure are needed. As seen in Table 5.3.2, there are two values for the heat of fusion of α– and γ– phases depending on the defect content. The higher values were the ones determined from the Clapeyron equation in case of change of specific volume with pressure. These values will be used to calculate the Gibbs free energies of the phases. The equilibrium melting points of α– and γ–

phases of iPP2.62 and γ–phase of iPP4.38 were determined from the high pressure experiments. The equilibrium melting temperatures of the iPP4.38 α–phase were calculated using the Clapeyron equation, and for 88, 123, 158 and 193 MPa these vales are 188.4, 196.0, 203.8 and 211.2 ^{o}C, respectively.

Calculated Gibbs free energies of both phases as a function of temperature at atmospheric pressure are presented in Figure 5.3.18 for sample iPP2.62 (5.76 % tot.), and in Figure 5.3.19 for the samples iPP4.38 (11.6 % tot.). Corresponding plots for these samples at crystallization pressure of 193 MPa are shown in Figures 5.3.20 and 5.3.21.

Values of the ΔG of both phases decrease with decreasing temperature, and the temperature at which these lines cross is the transition temperature at which the stability of the phases switches. From Figures 5.3.18–5.3.21 it is observed that at temperatures below the transition temperature the more stable phase is α–phase, while above this temperature γ–phase is more stable. The transition temperature can be calculated from the equilibrium condition, by equating the free energies of both phases:

$$T_{\mathrm{tr}}^{0} = \frac{T_{\mathrm{m},\alpha}^{0} T_{\mathrm{m},\gamma}^{0} \left(\Delta H_{\mathrm{f},\alpha} - \Delta H_{\mathrm{f},\gamma} \right)}{T_{\mathrm{m},\gamma}^{0} \Delta H_{\mathrm{f},\alpha} - T_{\mathrm{m},\alpha}^{0} \Delta H_{\mathrm{f},\gamma}} \tag{5.3.2}$$

Calculated transition temperatures for the atmospheric and p_{c} = 193 MPa are noted on the free energy diagrams. At atmospheric pressure 5.76 mol% defects decrease the transition temperature to 145.9 ^{o}C, while 11.6 mol% defects lower it to 137.2 ^{o}C. These values correspond to degrees of supercooling of 27 and 29 ^{o}C, correspondingly. Therefore, the degree of supercooling at which pure γ–form is expected to form is increased from the 10 ^{o}C calculated for the *i*–PP homopolymer. Same tendency is observed at the highest crystallization pressure of 193 MPa. In this case, for copolymer with 5.76 mol% defects pure γ–phase is predicted to form at a degree of supercooling of 66 ^{o}C, while for copolymer with 11.6 % defect this value is ~78 ^{o}C.

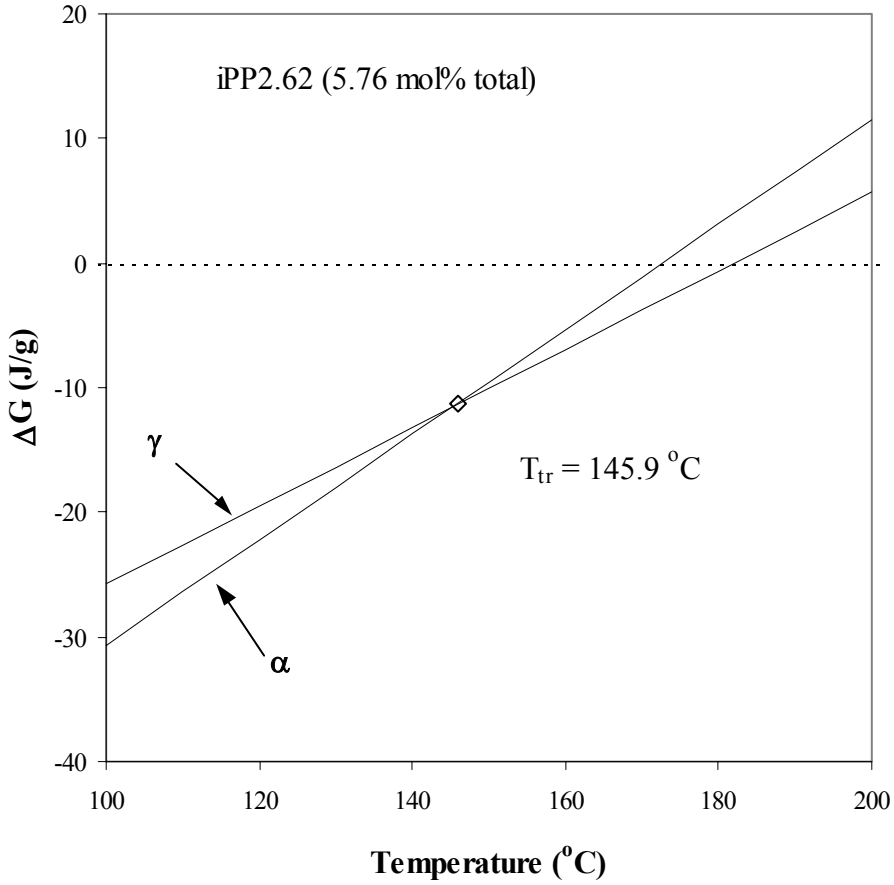

Figure 5.3.18. Gibbs free energy diagram of α– and γ–phases as a function of temperature at atmospheric pressure, for iPP2.62 copolymer with 5.76 mol% total defect content.

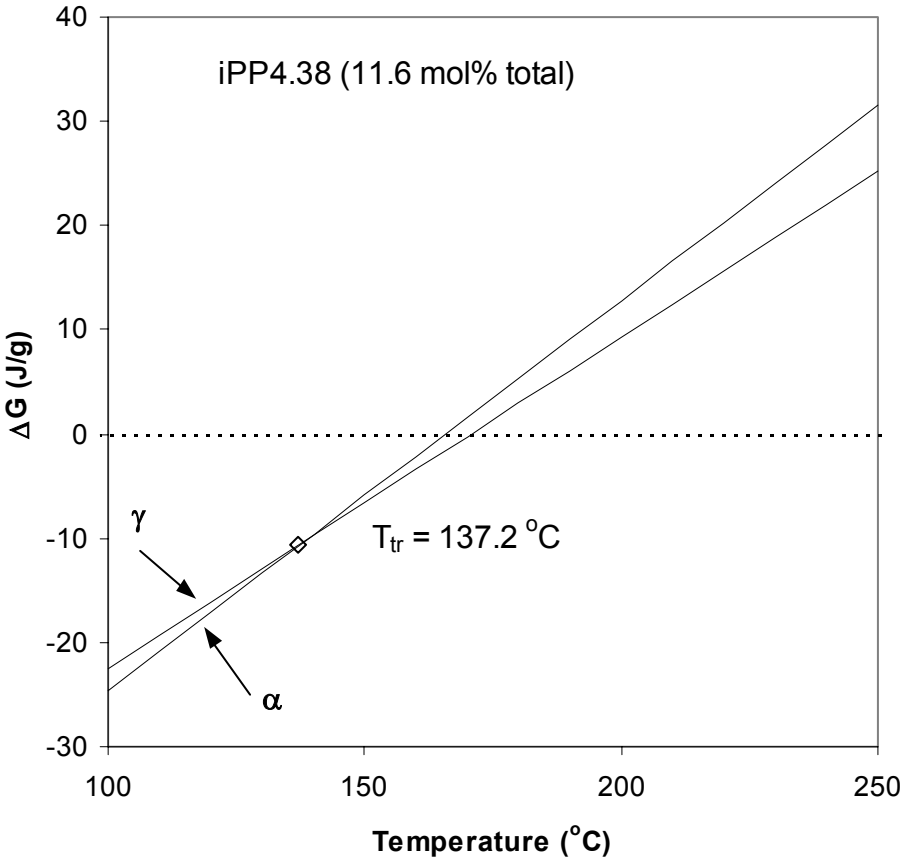

Figure 5.3.19. Gibbs free energy diagram of α– and γ–phases as a function of temperature at atmospheric pressure, for iPP4.38 copolymer with 11.60 mol% total defect content.

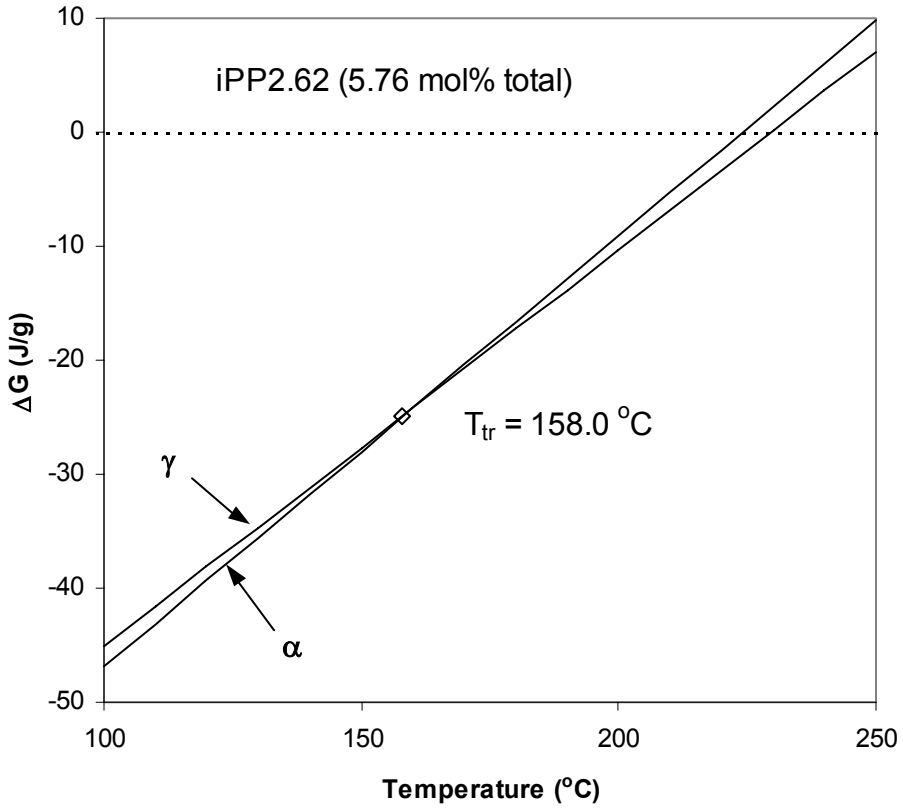

Figure 5.3.20. Gibbs free energy diagram of α– and γ–phases as a function of temperature at 193 MPa, for iPP2.62 copolymer with 5.76 mol% total defect content.

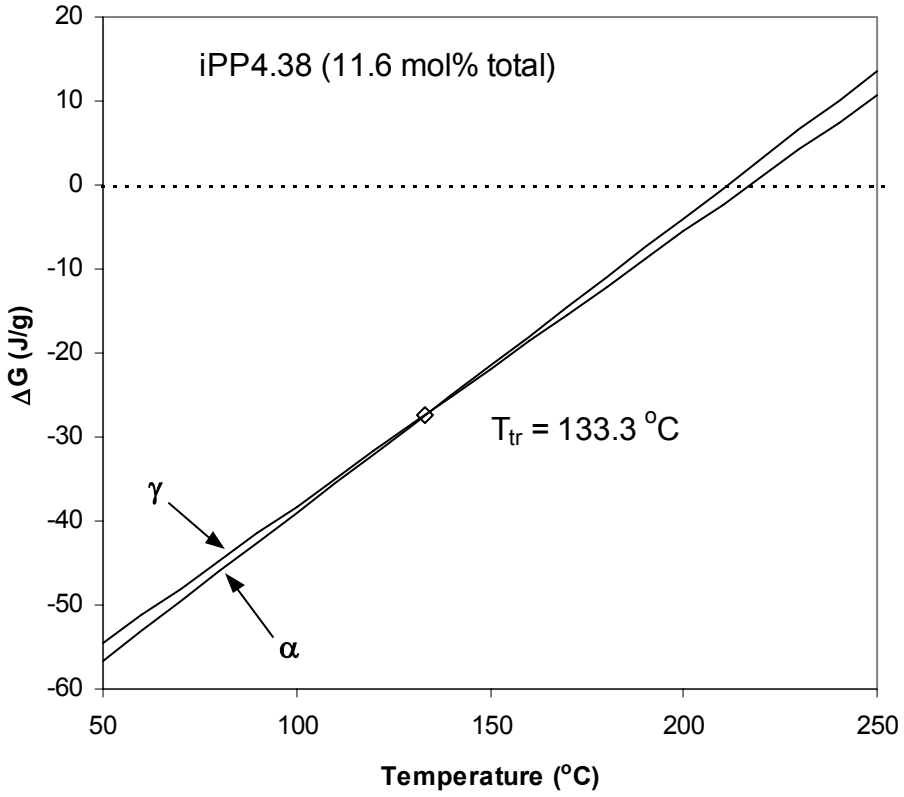

Figure 5.3.21. Gibbs free energy diagram of α– and γ–phases as a function of temperature at 193 MPa, for iPP4.38 copolymer with 11.60 mol% total defect content.

Using the T_m^0 of α– and γ– phases and calculated T_{tr}, temperature–pressure phase diagrams were constructed for both copolymer samples, shown in Figure 5.3.22 and 5.3.23. On these diagrams the lines define the regions of stability of both phases as a function of crystallization temperature and pressure, while the scattered points are the experimental data. It can be observed that there is good agreement between the experimental points and the theoretical predictions. It should be noted that below the T_{tr} more stable crystal phase is α–form, but all studied copolymers that were crystallized isothermally crystallized in a mixture of α– and γ–forms. Pure α–form was never observed in the studied crystallization temperature range.

Temperature–pressure phase diagrams of *i*–PP (1.26 mol% stereo defects), iPP2.62 (5.76 mol% total defect) and iPP4.38 (11.6 mol% total defect) were used to construct the three dimensional (3D) phase diagram of *i*–PP with composition (total defect content) as an added parameter. The resulting 3D phase diagram is shown in Figure 5.3.24, where the scattered points are the experimental data. The planes of the equilibrium melting temperatures of the γ– and α– phases are defined by the solid blue and magenta lines, correspondingly, while the solid red lines outline the plane of the theoretical transition temperatures between the α– and γ–phases. These planes were extrapolated to zero defect content in order to evaluate the equilibrium parameters for defect–free *i*–PP, which are listed in Table 5.3.3.

From the results in Table 5.3.3 it can be observed that at atmospheric pressure the equilibrium melting temperature of the α– and γ–phase for defect free *i*-PP have higher values of 186.9 and 189.9 ^oC, respectively. Also, the transition temperature at which γ–phase becomes more stable than the α–phase increases to 184.7 ^oC, which is very close in value to the equilibrium melting temperature of the α-phase. Therefore, γ–phase of defect free *i*-PP cannot be expected to form on crystallization at atmospheric pressure.

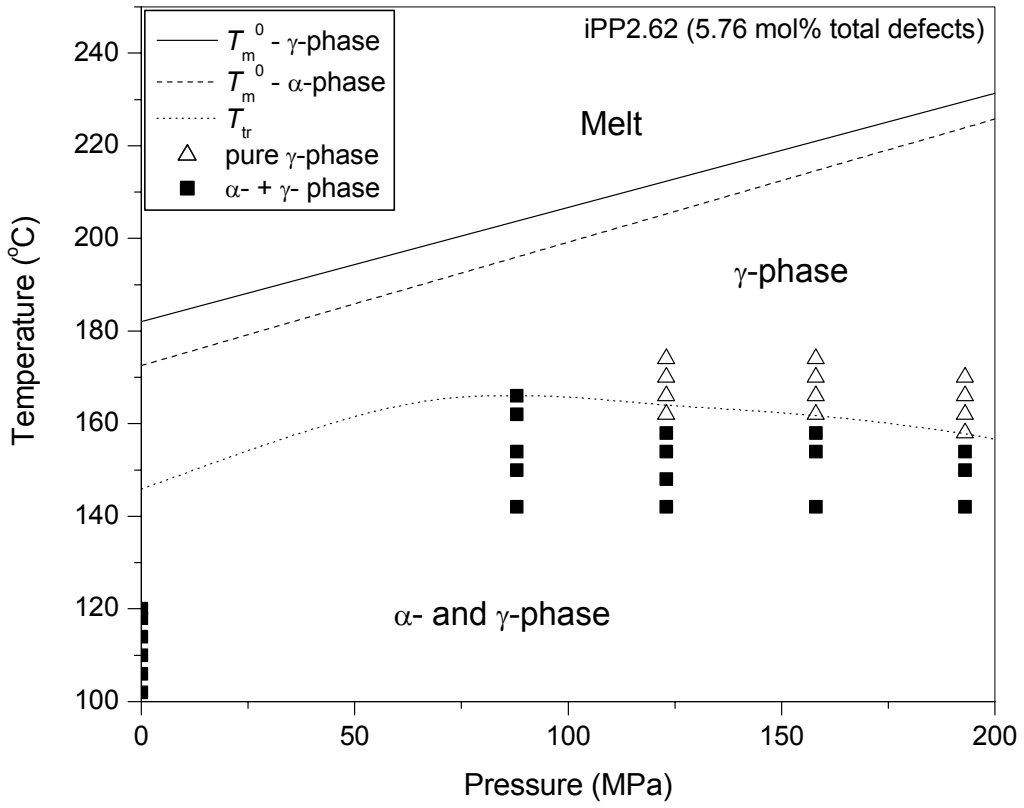

Figure 5.3.22. Temperature–pressure phase diagram for copolymer with total defect content of 5.76 mol% (2.62 mol% ethylene).

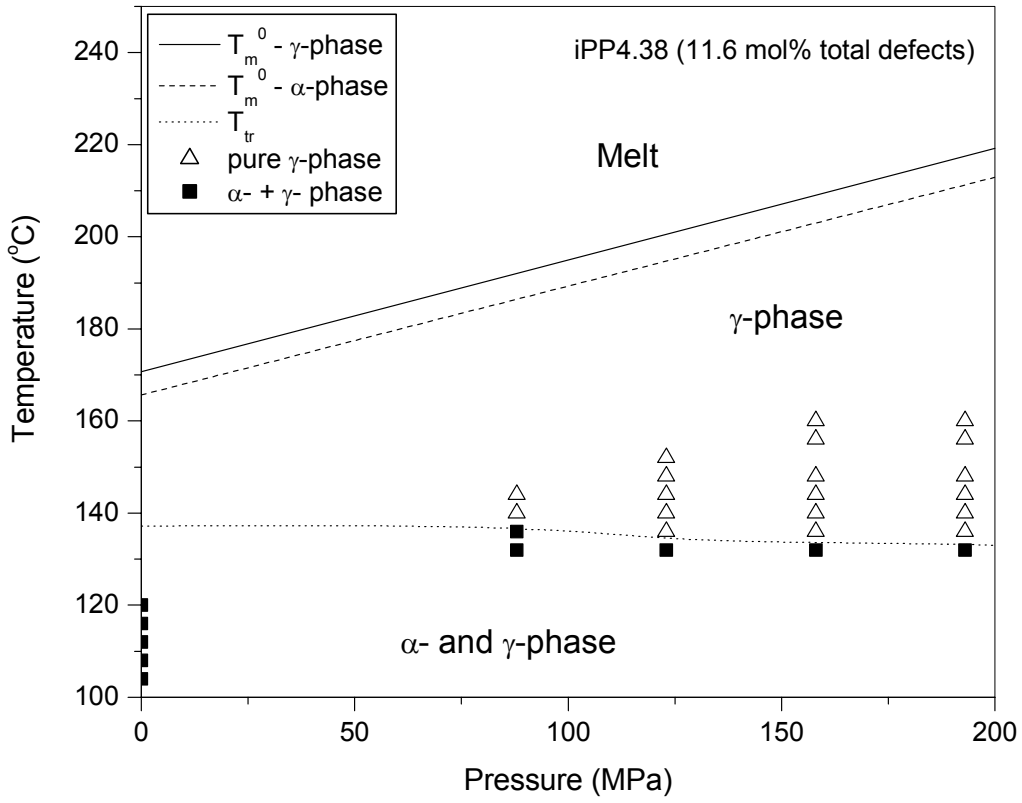

Figure 5.3.23. Temperature–pressure phase diagram for copolymer with total defect content of 11.60 mol% (4.38 mol% ethylene).

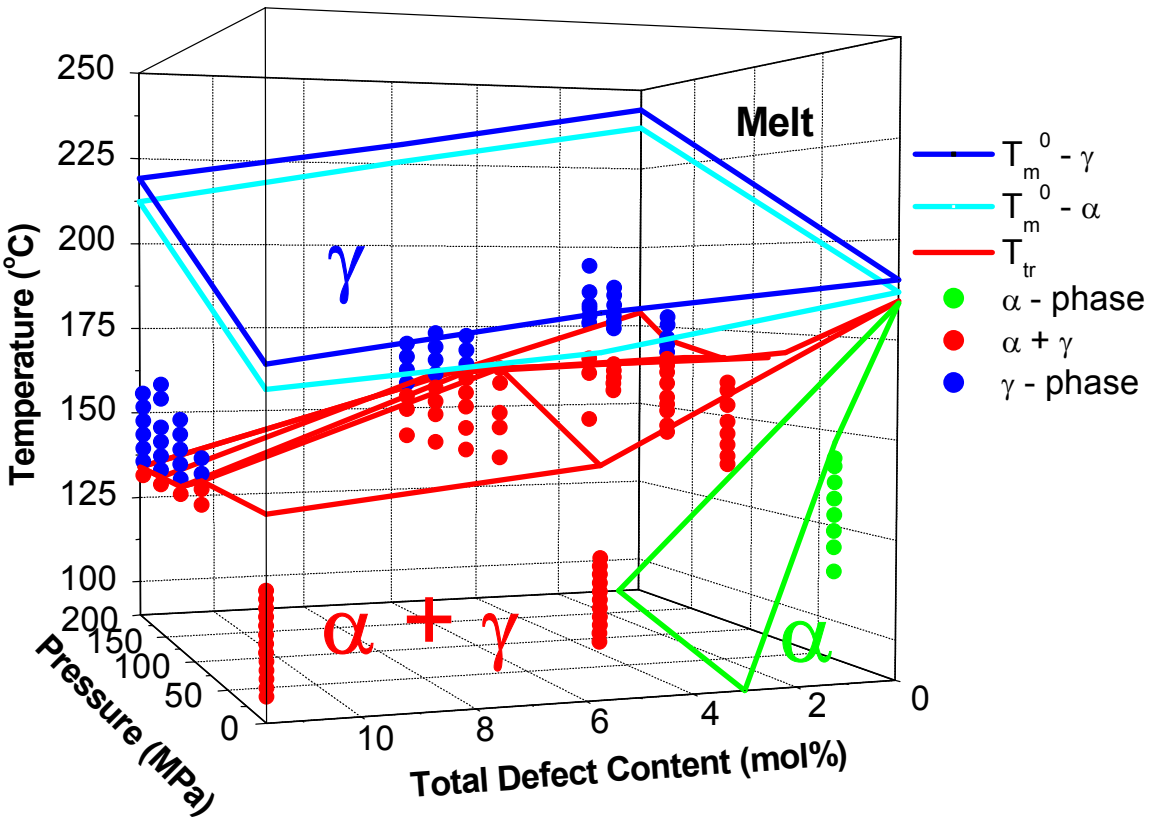

Figure 5.3.24. Temperature–pressure–composition phase diagram for *i*–PP.

Table 5.3.3. T_m^0 of α– and γ–phases, and the T_{tr} between these phases for defect free *i*–PP obtained from Figure 5.3.24.

p (MPa)	$T_{m,\alpha}^0$ (^oC)	$T_{m,\gamma}^0$ (^oC)	T_{tr} (^oC)
atmospheric	186.9	189.9	184.7
75	206.1	209.9	169.7
125	218.8	222.9	166.6
175	231.6	235.8	171.2
200	238.0	243.7	179.2

6. CONCLUSIONS

A series of studies have been conducted to investigate the isothermal crystallization of random propylene–ethylene copolymers with low ethylene content at atmospheric and high pressures. Copolymers were fractionated and their microstructure characterized in terms of an average propylene, ethylene and *meso* runs. The defect type and content plays a crucial role in understanding the crystallization behavior and polymorphism of the propylene–ethylene copolymers.

6.1. Thermal Behavior

Propylene–ethylene copolymers showed complex multiple melting behavior characterized by the presence of two or three melting endotherms. The area under the lower melting endotherms increased with increasing ethylene content and crystallization temperature. Using high temperature WAXD studied it was proved that the multiple endotherms are due to the melting of two different polymorphic crystals, α– and γ–phase crystals. Consequently, the low–temperature endotherms in the DSC melting curves were assigned to the melting of the γ–crystals, while the high–temperature endotherm was assigned to the melting of the α–crystals. Also, the lowest broad melting endotherm that occured at temperatures below the crystallization temperatures was shown to be due to the melting of the material which did not crystallize at these higher crystallization temperatures even for very long crystallization times, but crystallized into γ–phase crystals during the quenching. Based on this melting peak assignment it was possible to calculate the content of the γ–phase from the DSC endotherms, which was consistent with the findings from the WAXD study.

Equilibrium melting temperature of the α– and γ–phase of propylene–ethylene copolymers crystallized at atmospheric pressure were determined from SAXS, WAXD

and DSC experiments using the Gibbs–Thompson approach. It was shown that T_m^0 of both phases decreases with increasing defect content.

6.2. Crystallization at atmospheric pressure

The linear growth rates of random propylene–ethylene copolymers crystallized at atmospheric pressure were found to be dependent on the copolymer composition. The increase in the ethylene and total defect content drastically decreased spherulite growth rates. It was shown that in contrast with the *i*–PP homopolymer, copolymers with less than 11 mol% ethylene and 22 mol% total defects crystallize in three different regimes corresponding to three different crystallization temperature ranges. Copolymer iPP15.57 with 15.57 mol% ethylene and 33.35 mol% total defects exhibited only two crystallization regimes, namely regimes III and II.

For these copolymers the regime III to II transition temperature corresponded to the crystallization temperature at which the γ–crystal content exceeded 50 %. Therefore, the regime III/II transition was assigned to the change in the crystal growth front, from α–crystal (110) growth plane to (001) of the γ–orthorhombic crystal. Also, the regime III/II transition temperature decreased with increasing defect content for both sets of copolymers.

For samples that showed evidence of regime I (iPP2.62, iPP4.38 and iPP10.45), the regime II/I transition was dependent on the degree of supercooling irrespective of the copolymer characteristics. The regime II/I transition was always observed at a degree of supercooling of 53 ^{o}C. Observations using polarized light microscopy indicated that there were changes in the spherulite morphology with decreasing degree of supercooling. For these three copolymers at $\Delta T \leq 53$ ^{o}C the morphological features change from distinct positive to predominantly mixed spherulites, with more open and coarse spherulite texture.

Independent determination of the fold surface free energy, σ_e, and the composition dependence of the equilibrium melting temperature via SAXS and DSC measurements showed that the copolymers exhibited complex behavior based on their molecular weight and defect content. Values of σ_e increased with decreasing molecular weight, while for the two sets of copolymers with comparable molecular weights, the fold surface free energy of both α– and γ–phase decreased with increasing defect content. In addition, γ–phase had lower values of σ_e when compared with the α–phase. The higher fold surface free energy for the lower molecular weight copolymers was attributed to the contribution of the chain ends to the crystal–amorphous surface. The decrease of the γ–phase σ_e was assigned to the partial stress relief in the folds due to the inclination of the polymer chains in its orthorhombic unit cell.

6.3. Cocrystallization behavior

Three models of copolymer crystallization were evaluated in this study: the Flory's total exclusion, Sanchez–Eby's uniform inclusion and the equilibrium defect inclusion models. It was shown that for the copolymers with lower defect content, that is ethylene content ≤ 5 mol% and total defect content ≤ 12 mol%, Flory's total exclusion model fairly well predicts the equilibrium melting point depression. However, SAXS studies indicate that even for these copolymers partial inclusion of the defects (~ 10 %) has to take place in order to account for the copolymer lamellar thickness. In the higher defect content range the experimental values are higher than the calculated values using Flory equation. These copolymers are better represented with Sanchez–Eby's uniform inclusion model, which agrees well with their SAXS crystal thickness analysis. The independent evaluation of the excess free energy of defect incorporation, ε, from the decrease in the observed heat of fusion with defect content lead to values of ε that were an obvious overestimation.

6.4. Formation of γ–phase at high pressure

In this study it has been shown that the γ–phase content increases with the increasing crystallization temperature and the defect content in the propylene–ethylene copolymers. This confirms the premise that short isotactic sequences in the *i*–PP chains promote the development of the γ–crystals. However, at atmospheric pressure in the studied crystallization temperature range pure γ–phase crystals were never observed. Although it has been shown that infinite crystals of γ–form are slightly more stable than the α–form, kinetically α–crystals are favored at low supercoolings.

Analogous to the *i*–PP homopolymer crystallization, elevated pressures enhanced the formation of the γ–phase crystals. With increased crystallization pressure and temperature the concentration of γ–phase crystals increased for constant defect content. However, the presence of ethylene and stereo–defects in the copolymer chains greatly influenced the development of the pure γ–crystals. It was shown that increasing defect content shifts the onset of pure γ–phase formation in these propylene–ethylene copolymers to lower crystallization temperatures. Crystallization at pressures above 88 MPa and temperatures above 140 ^{o}C of copolymer with 11.6 mol% total defects led to pure γ–form regardless of the crystallization pressure. Also, copolymers crystallized at high pressures developed unique non-spherulitic morphology due to the presence of pure γ-orthrorhombic crystal structure

6.5. Pressure–temperature–composition phase diagram

Polymorphism and melting studies performed on the propylene–ethylene copolymers as a function of crystallization pressure enabled the modification of the existing α–γ phase diagram of *i*–PP homopolymer. Clapeyron equation and Gibbs free

energy approach were used to evaluate the thermodynamic parameters of the α– and γ–crystal forms of the copolymers at atmospheric and high pressures. As a result, a temperature–pressure–composition phase diagram was constructed. *i*–PP homopolymer used in the original study was considered a stereo–copolymer with 1.26 mol% defects. This three–dimensional phase diagram enabled the extrapolation of the equilibrium melting temperatures of both phases, as well as the transition temperature, to zero defect content. Using this extrapolation method T_m^0 of the α–phase (186.9 ^oC) and γ–phase (189.9 ^oC) were obtained for defect free *i*–PP.

7. FUTURE WORK

7.1. High pressure kinetics studies

Study of the crystallization kinetic of the random propylene–ethylene copolymers at high pressures. It would be of interest to determine how crystallization pressure will affect the crystallization regimes for the random copolymers. Linear growth rates and kinetic parameters can be compared with the atmospheric studies to generate a complete model of the crystallization of these copolymers.

7.2. Additional diffraction studies

Propylene–ethylene copolymers with low ethylene content used in this study exhibited bimodal lamellar thickness distribution when crystallized at low degrees of supercooling. Additional SAXS studies performed at different elevated temperatures should shed more light on the reason behind this behavior and to complement the high temperature WAXD studies. Also, it would be of interest to conduct SAXS experiments at the crystallization temperatures to evaluate the thickness of the lamellae to avoid the interference of the crystallization on quenching. Additionally, simultaneous SAXS and WAXD studies to study comparatively the development of the lamellar thickness and the formation of the α– and γ– phases should contribute to better understanding of the evolution of both phases.

7.3. Additional morphology studies

Propylene-ethylene copolymers exhibited unusual non-spherulitic morphology when crystallized at atmospheric pressure. More detailed studies of the morphology is needed using optical microscopy and TEM, as well as its correlation with the crystallization kinetics.

7.4. Computer Simulation

For better understanding of the cocrystalization model of the propylene–ethylene copolymers it would be of interest to conduct computer simulation calculations of the ethylene unit incorporation in *i*–PP crystal. The results from these simulations coupled with the already published results for stereo–defect incorporation in the *i*–PP crystals will contribute to more accurate determination of whether individual defects are incorporated in the crystals.

REFERENCES

1. *Encyclopedia of Polymer Science & Engineering*, v13, 464 1985.
2. Yeh, P., Birley, A.W., Hemsley, D.A., *Polymer* **26** 1155 (1985).
3. Ficher, H.K., Walker, D.A., *Plast. Rubber Process Appl.* **14** 103 (1990).
4. Balow, M.J., in *Handbook of Polypropylene and Polypropylene Composites*, Karian, H.G., Ed., Marcel Dekker, Inc: New York, 8, 1999.
5. Galli, P., Haylock, J.C., Simonazzi, T., In *Polypropylene: Structure, Blends and Composites*, Karger-Kocsis, J., Ed., Chapman & Hall: London, Vol. 2 1995.
6. Mezghani, K., PhD Dissertation, University of Tennessee, 1996.
7. Hermann, K., Gerngoss, O., Abitz. Z., *Phys. Chem.* **10** 371 (1930).
8. Till, P.H., *J. Polym. Sci*. **24** 301 (1957).
9. Keller, A., *Phil. Mag*. **2** 1171 (1957).
10. Fischer, E.W., *Z. Naturforsch*. **12a** 753 (1957)
11. Geil, P.H., *Polymer Single Crystals*, New York:Willey, 1963.
12. Flory, P.J., *J. Am. Chem. Soc*. **84** 2857 (1962).
13. Glotin, M., Mandelkern, L., *Coll. Polym. Sci*. **260** 182 (1982).
14. Phillips. P.J., in *Handbook of Crystal Growth*, Hurle, D.T.J., Ed: Vol.2 1994.
15. Keith, H.D., Padden, F.J., *J. Appl. Phys*. **34** 2409 (1963).
16. Bassett, D.C., *Principles of Polymer Morphology*, Cambridge University Press, Cambridge, 1981.
17. Bassett, D.C., in *Critical Reviews in Solid State and Materials Sciences*, 12 97 (1994).
18. Khoury, F., Passaglia, E., in *Treatise on Solid State Chemistry, Plenum Press* Vol. 3 (1976).
19. Natta, G., *J. Polym. Sci*. **16** 143 (1955).
20. Natta, G.J., Corradini, P., Ganis P., *Makromol. Chem.* **39** 238 (1960).
21. Natta, G.J., Corradini, P., *Nuovo Cimento, Suppl*. **15** 40 (1960).
22. Keith, H.D., Padden, F.J., Walter, N.M., Wickoff, H.W., *J. Appl. Phys*. **30** 1485 (1959).
23. Turner-Jones, A., Aizlewood, J.M., Beckett, D.R., *Makrom. Chem*. **75** 134 (1964).
24. Addink, E.J., Beintema, J., *Polymer* **2** 185 (1961).

25. Phillips, P.J., Mezghani, K., in *Polymeric Materials Encyclopedia*, Salamone, J.C. Ed: CRC Press, Boca Ratton, Vol 9, 6637, (1996).
26. Hikosaka, M., Seto, T., *Polym. J*. **5** 111 (1973).
27. Padden, F.J., Keith, H.D., *J. Appl. Phys*. **30** 1479 (1959).
28. Norton, D.R., Keller, A., *Polymer* **26** 704 (1985).
29. Olley, R.H., Bassett, D.C., *Polymer* **30** 399 (1989).
30. Lotz, B., Wittmann, J.C., *J. Polym. Sci., Polym. Phys. Ed*. **24** 1541 (1986).
31. Lotz, B., Wittmann, J.C., Lovinger, A.J., *Polymer* **37** 4979 (1996).
32. Basset, D.C., Olley, R.H., *Polymer* **25** 935 (1984)
33. Meille, S.V., Ferro, D.R., Bruckner, S., Lovinger, A.J., Padden, F.J., *Macromolecules* **27** 2615 (1994).
34. Asano, T., Fujiwara, Y., *Polymer* **19** 99 (1978).
35. Varga, J., *J. Thermal. Anal*. **31** 165 (1986).
36. Pae, K.D., Morrow, D.R., Sauer, J.A., *Nature* **211** 514 (1966).
37. Kardos, J.L., Christiansen, W., Baer, E., *J. Polym. Sci., Part A-2* **4** 777 (1966).
38. Campbell, R.A., Phillips, P.J., Lin, J.S., *Polymer* **34** 4809 (1993).
39. Mezghani, K., Phillips, P.J., *Polymer* **38** 5725 (1997).
40. Morrow, D.R., Newman, B.A., *J. Appl. Phys*. **39** 4944 (1968).
41. Alamo, R.G., Kim, M.H., Galante, M.J., Isasi, J.R., Mandelkern, L., *Macromolecules* **32** 4050 (1999).
42. Zimmermann, H.J., *J Macromol. Sci, Phys*. **B32** 141 (1993).
43. Mezghani, K., Phillips, P.J., *Polymer* **36** 2407 (1995).
44. Laihonen, S., Gedde, U.W., Werner, P.E., Martinez-Salazar, J., *Polymer* **38** 361 (1997).
45. Zhang, J., Shen, K., Na, S., Fu, Q., *J. Polym. Sci: Part B: Polym. Phys*. **42** 2385 (2004).
46. Bruckner, S., Meille, S.V., *Nature* **340** 455 (1989).
47. Meille, S.V., Bruckner, S., Porzio, W., *Macromolecules* **23** 4114 (1990).
48. Thomann, R., Wang, C., Kressler, J., Mulhaupt, R., *Macromolecules* **29** 8425 (1996).

49. Lotz, B., Graff, S., Wittman, J.C., *J. Polym. Sci. Polym. Phys. Ed*. **24** 2017 (1986).
50. Lotz, B., Graff, S., Straupe, C., Wittman, J.C., *Polymer* **32** 2902 (1991).
51. Gailey, J.A., Ralston, P.H., *SPE Trans*. **4** 29 (1964).
52. Bodor, G., Grel, M., Kallo, A., *Faserforschung und Textiltechnik* **15** 527 (1964).
53. Miller, R.L., *Polymer* **1** 135 (1960).
54. Zannetti, R., Celotti, G., Armigliato, A., *Eur. Polym. J*. **6** 879 (1970).
55. Corradini, P., Petraccone, V., De Rosa, C., Guerra, G., *Macromolecules* **19** 2699 (1986).
56. Wunderlich, B., *Macromolecular Physics*, Academic Press: New York, Vol 2. 1976.
57. Hoffman, J.D., Lauritzen, J.I., *J. Res. Natl. Bur. Stand*. **65A** 297 (1961).
58. Lauritzen, J.I., Hoffman, J.D., *J. Appl. Phys*. **44** 4353 (1973).
59. Hoffman, J.D., Davis, G., Lauritzen, J.I., in *Treatise on Solid State Chemistry*, Plenum Press Vol. 3 (1976).
60. Hoffman, J.D., Miller, R.L., Marand., H., Roitman., D.B., *Macromolecules* **25** 2221 (1992).
61. Hoffman, J.D., Miller, R.L., *Polymer* **38** 3151 (1997).
62. Phillips, P.J., *Rep. Prog. Phys*. **53** 549 (1990).
63. Flory, P.J., *Trans. Faraday Soc*. **51** 848 (1955).
64. Sanchez, I., Eby, R.K., *J. Res. Natl. Bur. Stand*. **77A** 353 (1973).
65. Sanchez, I., Eby, R.K., *Macromolecules* **8** 638 (1975).
66. Hoffman, J.D., Weeks, J.J., *J. Res. Natl. Bur. Stand*. **66A** 13 (1962).
67. Hoffman, J.D., Weeks, J.J., *J. Chem. Phys*. **37** 1723 (1962).
68. Mezghani, K., Campbell, R.A., Phillips, P.J., *Macromolecules* **27** 997 (1994).
69. Starkweather, H.W., Van-Catledge, F.A., MacDonald, R.N., *Macromolecules* **15** 1600 (1982).
70. Shin, Y-W., Uozumi, T., Terano, M., Nitta, K., *Polymer* **42** 9611 (2001).
71. Turner-Jones, A., *Polymer* **12** 487 (1971).
72. Laihonen, S., Gedde, U.W., Werner, P-E., Westdahl, M., Jaaskelainen, P., Martinez-Salazar, J., *Polymer* **38** 371 (1997).

73. Feng, Y., Jin, X., Hay, J.N., *Polym. J.* **30** 215 (1998).
74. Marigo, A., Marega, C., Zannetti, R., *Makromol. Chem*. **190** 2805 (1989).
75. Busico, V., Corradini, P., Rosa, C., Benedetto, E., *Eur. Polym. J*. **21** 239 (1985).
76. Hosoda, S., Nomura, H., Gotoh, Y., Kihara, H., *Polymer* **31** 1999 (1990).
77. Monasse, B., Haudin, J.M., *Colloid Polym Sci*. **266** 679 (1988).
78. Feng, Y., Hay, J.N., *Polymer* **39** 6589 (1998).
79. Avella, M., Martuscelli, E., Volpe, G., *Makromol. Chem*. **187** 1927 (1986).
80. Alamo, R.G., VanderHart, D.L., Nyden, M.R., Mandelkern, L., *Macromolecules* **33** 6094 (2000).
81. Perez, E., VanderHart, D.L., Chris, B., Howard, P.R., *Macromolecules* **20** 78 (1987).
82. Hosoda S., Hori, H., Yada, K., Nakahara, S., Tsuji, M., *Polymer* **43** 7451 (2002).
83. Zhao, Y., Vaughan, A.S., Sutton, S.J., Swingler, S.G., *Polymer* **42** 6599 (2001).
84. Weng, J., Olley, R.H., Bassett, D.C., Jääskeläinen, P., *J. Polym. Sci: Part B: Polym. Phys*. **42** 3318 (2004).
85. Cham, P.M., Marand, H., *Polymeric Materials: Science and Engineering*, *Pro*c. *Am. Chem. Soc. Div. of Polym*. **67** 365 (1992).
86. Foresta, T., Piccarolo, S., Goldbeck-Wood, G., *Polymer* **42** 1167 (2001).
87. Hosier, I.L., Alamo, R.G., Esteso, P., Isasi, J.R., Mandelkern, L., *Macromolecules* **36** 5623 (2003).
88. Bhateja, S.K., Pae, K.D., *J. Macromol. Sci. Revs. Macromol. Chem*. **C13** 77 (1975).
89. Sauer, J.A., Pae, K.D., *J. Appl. Phys*. **39** 4959 (1968).
90. Morrow, D., *J. Macromol. Sci.-Phys*. **B3** 53 (1969).
91. Pae, K.D., *J. Polym. Sci*. **A-2** 657 (1968).
92. Mezghani, K., Phillips, P.J., *Polymer* **39** 3735 (1998).
93. Zambelli, A., Locatelli, P., Bajo, G., Bovey, F.A., *Macromolecules* **8** 687 (1975).
94. Zambelli, A., Locatelli, P., Provasoli, A., Ferro, D.R., *Macromolecules* **13** 267 (1980).
95. Grant, D.M., Paul, E.G., *J. Am. Chem. Soc*. **86** 2984 (1964).
96. Busico, V., Cipullo, R., *Prog. Polym. Sci*. **26** 443 (2001).

97. Carman, C.J., Tarpley Jr., A.A., Goldstein, J.H., *Macromolecules* **6** 719 (1973).
98. Randall, J.C., *J. Polym. Sci., Polym. Phys. Ed*. **13** 901 (1975).
99. Busico, V., Cipullo, R., Corradini, P., Landriani, L., Vacatello, M., Segre, A.L., *Macromolecules* **28** 1887 (1995).
100. Bovey, F.A., *Polymer Conformation and Configuration*, Academic, New York, 1969.
101. Wilkes, C.E., Carman, C.J., Harrington, R.A., *J. Polym. Sci*. **C43** 237 (1973).
102. Hayashi, T., Inoue, Y., Chujo, R., Asakura, T., *Polymer* **29** 1848 (1988).
103. Cheng, H.N., Bennett, M.A., *Makrom. Chem*. **188** 2665 (1987).
104. Randall, J.C., *JMS –Rev. Macromol. Chem. Phys*. **C29** 201 (1989).
105. Cheng, H.N., *Macromolecules* **17** 1950 (1984).
106. Randall, J.C., *Polymer Sequence Determination,* Academic Press, New York, 1977.
107. Vonk, C.G., *Makromol. Chem., Makromol. Symp*. **15** 215 (1988).
108. Strobl, G.R., Schneider, M.J., *J. Polym. Sci., Polym. Phys*. **18** 1361 (1980).
109. Vonk, C.G., Kortleve, G., *Kolloid-Z. Z. Polym* **220** 19 (1967).
110. Randall, J.C., *J. Polym. Sci., Polym. Phys. Ed*. **14** 1693 (1976).
111. Natta, G., Corradini, P., Cesari, M., *Atti. accad. nazl. Lincei, Rend. classe sci. fis. mat. e nat*. **22** 11 (1957).
112. Olley, R.H., Bassett, D.C., *Polymer* **23** 1707 (1982).
113. Carman, C.J., Wilkes, C.Z., *Rubb. Chem. Technol*. **44** 781 (1971).
114. (a) Hayashi, T., Inoue, Y., Chujo, R., Asakura, T, *Polym. J*. **20** 107 (1988). (b) Hayashi, T., Inoue, Y., Chujo, R., Asakura, T, *Polym. J.* **20** 895 (1988).
115. http://www.mestrec.com/MestRe-C.html
116. Ruland, W., *J. Appl. Cryst*. **4** 70 (1971).
117. Koberstein, J.T., Morra, B., Stein, R., *J. Appl. Cryst*. **13** 34 (1980).
118. Vonk, C.G., *J. Appl. Cryst*. **6** 81 (1973).
119. Ruland, W., *Colloid Polym. Sci*. **255** 417 (1977).
120. Goderis, B., Reynaers, H., Koch, M.H.J., Mathot, V.B.F., *J. Polym. Sci: Part B*: *Polym. Phys*. **37** 1715 (1999).
121 Schreiber, S., PhD Dissertation, University of Tennessee, 1998.

122. Angelloz, C., Fulchiron, R., Douillard, A., Chabert, B., Fillit, R., Vautrin, A., David, L., *Macromolecules* **33** 4138 (2000).
123. Tritto, I., Fan, Z.Q., Locatelli, P., Sacchi, M.C., Camurati, I., Galimberti, M., *Macromolecules* **28** 3342 (1995).
124. Koenig, J.L., *Chemical Microstructure of Polymer Chains*, New York: Wiley, 1980.
125. Zannetti, R., Busi, P.,Guidetti, *Eur. Polym. J.* **19** 757 (1983).
126. Auriemma, F., De Rosa, C., *Macromolecules* **35** 9057 (2002).
127. Ferro, D.R., Bruckner, S., Meille, S.V., Ragazzi, M., *Macromolecules* **25** 5231 (1992).
128. Alamo, R.G., Mandelkern, L., *Macromolecules* **24** 6480 (1991).
129. Bruckner, S., Phillips, P.J., Mezghani, K., Meille, S.V., *Macromol. Rapid Commun*. **18** 1 (1997)
130. Cheng, S.Z.D., Janimak, J.J., Zhang, A., Hsieh, E.T., *Polymer* **32** 648 (1991).
131. Balta-Calleja, F.J., Vonk, C.G., *X-Ray Scattering of Synthetic Polymers*, Elsevier, 1989.
132. Defoor, F., Groeninckx, G., Reynaers, H., Schouterden, P., Van der Heijden, B., *Macromolecules* **26** 2575 (1993).
133. Flory, P.J., Yoon, D.Y., Dill, K., *Macromolecules* **17** 862 (1984).
134. Yoon, D.Y., Flory, P.J., *Macromolecules* **17** 2260 (1984).
135. Triolo, A., Lin, J.C., Triolo, R., *Physica A* **249** 362 (1998).
136. Triolo, A., Lin, J.C., Wignall, G.D., Triolo, R., *Polymer* **41** 3751 (2000).
137. Marigo, A., Marega, C., Saini, R., Camurati, I., *J. Appl. Polym Sci*. **79** 375 (2001).
138. Stribeck, N., Alamo, R.G., Mandelkern, L., Zachmann, H.G., *Macromolecules* **28** 029 (1995).
139. Martinez-Salazar, J., Cuesta, M.S., Balta Calleja, F.J., *Collid. Polym. Sci*. **265** 239 (1987).
140. Kim, M.-H., Phillips, P.J., Lin, J.S., *J. Polym. Sci: Part B: Polym. Phys*. **38** 154 (2000)
141. Farmer, B.L., Eby, R.K., *Polymer* **20** 363 (1979).
142. Martuscelli, E., Pracella, M., Crispino, L., *Polymer* **24** 693 (1983)

143. Wendling, J., Suter, U.W., *J. Comput. Aided Mater. Design* **7** 1 (2000).
144. De Carvalho, B., Bretas, R.E.S., *J. Appl. Polym. Sci*. **68** 1159 (1998).
145. Tseng, H., Phillips, P.J., *Macromolecules* **18** 1565 (1985).
146. Tanaka, N., *Thermochim. Acta* **374** 1 (2001).
147. Cheng, S.Z.D., Janimak, J.J., Zhang, A., Cheng, H.N., *Macromolecules* **23** 298 (1990).
148. Phillips, P.J., Edwards, B.C., J. *Polym. Sci: Polym. Phys. Ed*. **14** 377 (1976)
149. Zoller, P., Fakhreddine, Y.A., *Thermochim. Acta* **238** 397 (1994).
150. Starkweather, H.W., Zoller, P., Jones, G.A., Vega, A.J., *J. Polym. Sci. Polym. Phys. Ed*. **20** 751 (1982).
151. Starkweather, H.W., Zoller, P., Jones, G.A., *J. Polym. Sci. Polym. Phys. Ed*. **21** 256 (1983).
152. Starkweather, H.W., Zoller, P., Jones, G.A., *J. Polym. Sci. Polym. Phys. Ed*. **22** 1615 (1984).

VITA

Anita Dimeska was born in Skopje, Republic of Macedonia, on June 9, 1967. She attended University "Sts. Cyril and Methodius" in Skopje, R. Macedonia, and received her B.S. degree in Chemical Engineering with concentration in Basic Organic and Polymer Engineering in 1991, and M.S. degree in Chemical Engineering in 1995. In August of 1997 she entered the Doctoral program in Polymer Engineering at the University of Tennessee, Knoxville. She successfully defended her dissertation on November 23, 2004, and will graduate in May of 2005.